An Engineering Perspective on Invasive Fish Control: A Study of Bubble Curtain Deterrent Systems to Control Carp Movement

A DISSERTATION
SUBMITTED TO THE FACULTY OF
UNIVERSITY OF MINNESOTA
BY

Daniel Patrick Zielinski

IN PARTIAL FULFILLMENT OF THE REQUIREMENTS
FOR THE DEGREE OF
DOCTOR OF PHILOSOPHY

Vaughan Voller, Miki Hondzo

July 2013

Acknowledgements

First and foremost, I would first like to thank my advisors Vaughan Voller and Miki Hondzo for their considerable guidance and support, and from whom I gathered a great deal of inspiration and fount of original ideas. I also extend a special thanks to Peter Sorensen for his support, bottomless insights, and above all patience for an engineer in once unfamiliar territories of fisheries management. I would also like to thank Chris Paola for his time and energy spend as the chair of my review committee, and Kimberly Hill for accepting to fill in on my preliminary exam committee on short notice.

Financial support over the years has come from the Minnesota Environmental and Natural Resources Trust Fund as recommended by the Legislative-Citizen Commission on Minnesota Resources (LCCMR) and Ramsey-Washington Metro Watershed District. Additionally, I would like to thank the friends and family of Alvin G. Anderson for their considerable honor and support of textbooks.

I would also like to thank Zachary Sudman and Brian Moe for their tireless efforts to help construct and maintain the Kohlman Creek bubble curtain, and Justine Koch, Reid Swanson, and all others who did all the hard work to collect carp for my field tests. Without your help, much of this work would not have been possible. Many thanks to the students, faculty, and staff at Saint Anthony Falls Laboratory (SAFL) and Sorensen lab group for making me feel at ease no matter which campus I was working from.

Most importantly, I would like to thank my family for their support and words of encouragement along this long and winding journey towards my PhD. I am especially grateful to my parents who made many long trips to provide emergency childcare when I

had an important deadline, conference, or other commitment to manage. Finally, I am eternally thankful for my loving wife, Amanda. Without her support and limitless patience, none of this would have been possible.

Dedication

I dedicate this dissertation to my loving wife, Amanda, inquisitive daughter, Lorelai, and adventurous son Kaeden. Only with their unending support, patience and unflinching positive attitude was I able to reach this goal.

Abstract

The objective of this research was to investigate the ability of bubble curtain deterrent systems to inhibit the movement of invasive fish. Bubble curtains, which consist of a wall of bubbles (e.g. produced by forcing air through perforated pipes), fall into the category of behavioral deterrent systems that rely on aversive stimuli (e.g. sound and light) to guide fish in taxon specific manners. These systems provide advantages over physical/mechanical screens because they do not restrict fluid flow or negatively impact navigation. Bubble curtains are particularly appealing, because they are less expensive than other electrical or sonic barriers, are easily maintained, safe, and produce complex acoustic and hydrodynamic stimuli which may be optimized to deter fish movement. However, few studies have examined whether or how bubble curtains might work. In three studies, the common carp (*Cyprinus carpio*), a cyprinid responsible for water quality degradation in shallow water ecosystems, was used to investigate how bubble curtains influence fish behavior and might be optimized. First, through a laboratory experiment, two different bubble curtains were shown to reduce passage of common carp by 75-80% in both up- and down-stream directions. These findings also suggested that avoidance behaviors were attributed to fluid motion and sound stimuli. Second, a field test demonstrated that the performance of a bubble curtain under natural conditions was consistent with laboratory results, blocking 57±12% of downstream swimming carp, versus 75-80% in the laboratory. Third, a fish movement model based on diffusion theory and phonotaxic response was derived. In a novel application, a

stability analysis of the fish movement model demonstrated that acoustic stimuli produced by the bubble curtains can be sufficient to disrupt movement (i.e. deter passage) of common carp. Overall, I have shown through rigorous experimental and holistic quantitative analysis that bubble curtains can indeed deter common carp movement, but improvements must be identified in order for bubble curtains to remain a viable management tool in the future.

Table of Contents

Acknowledgements i
Dedication iii
Abstract iv
Table of Contents vi
List of Tables x
List of Figures xii
Chapter 1: Introduction 1
1 Overview of behavioral deterrent systems and the role in invasive fish management 1
1.1 Fish guidance technologies for invasive fish 2
1.2 Common carp as a model invader 5
1.3 Mathematical modeling of behavioral deterrent systems 6
2 Objectives and structure of this dissertation 8
Chapter 2: Laboratory experiments demonstrate that bubble curtains can effectively inhibit movement of common carp 11
1 Introduction 12
2 Materials and Methods 15
2.1 Experimental setup 15
2.2 Statistical analysis 22
3 Results 24
3.1 Tests of simple bubble curtains 24
3.2 Influence of sensory fields on efficacy of bubble curtain 27
4 Discussion 31
5 Conclusion 34
Chapter 3: Field test of an optimized bubble curtain deterrent system for common carp 35
1 Introduction 36
2 Materials and Methods 38
2.1 Study Site 38
2.2 Bubble curtain system components 41
2.3 PIT tag interrogation system 43
2.4 Experimental design 44
2.5 Statistical Analysis 48
3 Results 48
3.1 Downstream movement tests 48
3.2 Upstream movement tests 50

4 Discussion 51
5 Conclusion 54
Chapter 4: Mathematical evaluation of behavioral deterrent systems to disrupt fish movement 55
1 Introduction 56
2 Materials and Methods 60
2.1 Experimental set-up and animals 60
2.2 Data Collection 61
2.3 Movement Analysis 62
3 Model 66
3.1 Model Description 66
3.2 Stability Analysis 71
3.3 Parameter Estimation 73
4 Results 75
5 Discussion 82
6 Conclusions 85
Chapter 5: Conclusions and Future Work 86
Bibliography 90
Appendix A: Additional sound pressure level spectrum measurements 103
Appendix B: Acoustic and hydrodynamic fields generated by individual bubble curtains 104
1 Introduction 104
2 Materials and Methods 104
3 Results 105
Appendix C: Analysis of step-size distributions for evidence of Lévy flight movement patterns 111
1 Introduction 111
2 Methods 113
3 Results and Discussion 115
Appendix D: The control volume weighted flux scheme (CVWFS) for non-local diffusion and its relationship to fractional calculus 119
1 Introduction 121
2 Derivation of the CVWFS 123
3 Criteria for choosing CVWFS weights 127
4 Connection of CVWFS to the fractional calculus 129
4.1 Power-law Weights 129
4.2 The CVWFS approximates the Caputo Derivative 132
4.3 Relationship between the CVWFS and Grünwald approximations 132
5 Generalization of the CVWFS 134

5.1 Arbitrary Skew 134
5.2 Boundary Conditions 134
5.3 Transients 135
6 Testing and results 137
6.1 A Simple Steady State Problem 137
6.2 A Problem with a Prescribed Flux Boundary and Source 138
6.3 A Transient Problem 140
7 Conclusions 142
Addendum: A brief outline of fractional calculus 143
Appendix E: A random walk solution for fractional diffusion equations 147
1 Introduction 148
2 Fractional Diffusion 151
3 Random Walk Processes 151
3.1 A Particle Random Walk Scheme 153
3.2 An Initial Test Problem 155
3.3 A Domain Shift Random Walk Scheme 157
4 Analysis of the Domain Shifting Random Walk Scheme 158
4.1 What fractional diffusion equation is solved? 158
4.2 Effect of scale and number of steps 159
5 Verification of the Domain Shifting Random Walk Scheme 160
6 Solution in a Non-Cartesian Domain 161
7 Conclusions 162
Appendix F: The control volume weighted flux scheme (CVWFS) for two-dimensional, two-sided Caputo fractional diffusion equations 167
1 Introduction 168
2 Overview of the CVWFS 171
3 Alternative Weights 173
4 Extension of CVWFS to 2D Caputo Fractional Diffusion Equations 175
5 Testing and Results 178
5.1 Comparison of Weighting Schemes 178
5.2 2D Steady State Problems 180
5.3 A Transient Problem 182
5.4 Two-Sided Problem 184
6 Conclusions 186
Appendix G: A Control Volume Finite Element Method with Spines for Two-Dimensional Fractional Diffusion Equations 188
1 Introduction 189
2 Overview of CVWFS 192
3 Numerical approach for a fractional CVFEM 194

4 Testing and Results 201
4.1 2D Steady State Problem 201
4.2 Two Sided Problem 206
4.3 Annulus Problem 207
5 Conclusions 208

List of Tables

Table 3-1. Date and number of fish released in down- and up-stream movement tests of the bubble curtain in Kohlman Creek. During downstream movement tests the carp placed above the bubble curtain were the test group, while fish placed below were the control group. Conversely, during upstream movement tests the carp placed below the bubble curtain were the test group while fish placed above were the control group. 44

Table 3-2. Efficacies of the bubble curtain system during up- and down-stream movement tests. P_{test} is the proportion of the test group that crossed the bubble curtain while ON, while $P_{control}$ is the proportion of the control group that is expected to cross in the absence of the bubble curtain. The test statistic, *z*, is for assessing whether the proportion of carp passing through the bubble curtain P_{test} is different than the proportion expected to pass without the bubble curtain $P_{control}$ 49

Table 4-1. Description of three bubble curtains investigated by Zielinski et al. (2013) to inhibit common carp movement in a laboratory channel and the maximum sound pressure at 200 Hz. 61

Table 4-2. Net downstream flux of carp between control and bubble curtain trials, maximum sound pressure gradient, and effective concentration used to estimate the repulsion rate $\omega = \frac{-q_{ds}}{N\frac{\partial P}{\partial x}}$. 75

Table 4-3. Efficacies of the bubble curtain systems reported by Zielinski et al. (2013), and the statistical significance of observed reductions using a Mann-Whitney test with Dunn-Sidak correction for multiple comparisons. The bubble curtain efficacy is a measure of percent reduction in crossings between control and bubble-curtain trials. 79

Table B-1. Summary of the physical properties of the individual pipes studied in the straight flume under variable air and water flow. The porous pipe was a polyethylene pipe with 25 micron pores over the entire surface, while the perforated pipe was a PVC pipe drilled with 1mm holes at intervals of 1 cm. Water depth was maintained at 25 cm.....106

Table C-1. Evidence ratios and goodness-of-fit results 117

Table D-1: Comparison of Grünwald weights and CVWFS coefficients $\alpha = 0.5$ 133

Table E-1. Absolute total difference between analytical and domain shifting scheme. 159

Table F-1: Alternative normalized weights for CVWFS 174
Table F-2: L-infinity norm for CVWFS approximate solution to the one-dimensional fractional diffusion problem in Equation (25) utilizing each alternative weight in Equations (7)-(9) 179
Table F-3: Maximum absolute error of CVWFS approximation using alternative weights on grid spacing of $\Delta x = \Delta y = 0.025$ 181
Table G-1. The L^1, L^2, and L^∞ errors, following equation (28), of the fractional CVFEM with spines for equation (24) with $\alpha = 0.3, 0.5, 0.7$ 203
Table G-2. The L^1, L^2, and L^∞ errors and CPU time (s) of the fractional CVFEM with spines for equation (24) with $\alpha = 0.3, 0.5, 0.7$ for $\delta = 2^{-5}$ for increasing evaluation step size, Δx and Δy, by setting the numerator in equation (15) to 1δ, 2δ, and 4δ 205
Table G-3. The L^1, L^2, and L^∞ errors and CPU time (s) of the fractional CVFEM with spines for equation (24) with $\alpha = 0.3, 0.5, 0.7$ and $\delta = 2^{-5}$ using one, two, and three Gauss-node evaluation points. 206

List of Figures

Figure 2-1. Schematic of behavioral trial tank with approximate location of bubble curtain and PIT tag interrogation system (PIT antennas are labeled Ant #1-4). The outside diameter of the tank is 3 m and the inside diameter is 1 m, and water depth is 25 cm. 17

Figure 2-2. Plan view schematic of bubble curtain and speaker arrangements tested: a). fine-bubble; b) graded-bubble; c) coarse-bubble; d) speaker array; e) speaker array/fine-bubble systems. The darkened area is filled by plastic mesh, preventing fish passage along tank edge. Water flow is from left to right at 5 cm s^{-1}. See Figure 2-1 for further details of curtain positioning in the circular tank. 19

Figure 2-3. Total number of up- and down-stream passages made by common carp for each test (e.g. curtain type). Dashed lines separate trial groups compared with Kruskal-Wallis and Mann-Whitney tests. Control trials are spaced in chronologic order to illustrate how consistent carp behavior was over the entire study; however, in comparison to the bubble curtain designs, the controls were combined into a universal control group. Note, the coarse-bubble trial is shown repeatedly for clarity of trials being statistically analyzed. Statistical significance was determined by Mann-Whitney pair-wise comparisons with Dunn-Sidak correction for multiple comparisons. Box plots illustrate data quartiles, mean, median (squares) and whiskers represent minimum and maximum values. *P<0.05, **P<0.01, ***P<0.001 26

Figure 2-5. Plan view of sound pressure field in dB (ref 1 μPa) in the behavioral trial tank at a depth of 12.5cm at 200Hz with the coarse-bubble system. The bubble curtain is located to the right of the center of the tank, perpendicular to the y-axis centered at a radial distance of 0 cm. The background SPL at 200Hz was ~80dB (ref 1 μPa). The shaded area denotes the approximate location of the coarse-bubble system. 28

Figure 2-4. Sound pressure level power spectrum in the behavioral trial tank during coarse-bubble (solid black line), graded-bubble (solid blue line), and fine-bubble (solid red line) trials and the common carp hearing threshold documented by Popper (1972) (dashed black line). Bubble curtain sound data was obtained at the center of the bubble curtain, 5 cm above the channel bottom. 29

Figure 2-6. Sound Pressure Level (SPL) contours in dB (re 1μPa) at 200 Hz for the a) coarse-bubble, b) speaker array, and c) speaker array/fine-bubble systems in the test channel along a straight line through the center of the

bubble curtain (flow is left to right). Axes are normalized by the depth *D*=25cm and the barrier is centered about x/D=0. Approximate locations of speakers and bubble diffusers are shown for each configuration. 30
Figure 3-1. Map of the location of the Phalen Chain of Lakes in Minnesota, USA with headwaters and main lakes denoted (top panel) and location of the bubble curtain in Kohlman Creek (bottom panel): (1.) Bubble curtain, (2.) Temporary fish screen, concrete weir, and PIT tag antenna, and (3.) PIT tag antenna attached to culvert under Hwy 61. Photo obtained from Ramsey Count GIS Map Viewer 40
Figure 3-2. Plan view schematic of the bubble curtain system in Kohlman Creek with locations of release points for each movement test (top panel), and photograph of bubble curtain system and dock support structure, looking upstream (bottom panel). Photograph by author. 42
Figure 3-3. Proportion of test and control carp that swam downstream over one cycle of bubble curtain operation. The start time for the downstream movement tests was approximately 14:00 hr. Dark and light bars at the bottom indicated night and day. 50
Figure 3-4. Proportion fish from test and control groups to swim upstream towards the headwaters region over the 24hr test period. The bubble curtain was ON throughout each test. The start time for the upstream movement tests was approximately 12:00 hr. Dark and light bars at the bottom indicated night and day. 51
Figure 4-1. Plan view schematic of test channel, bubble curtain location, and PIT tag antennas (Ant #1-4). The distance between antennae is 1.57 m. Note positive movement is in the downstream direction. 62
Figure 4-2. Analysis of carp ensemble movements during control trials (N=24) consisting of net displacement of individuals, variance about the mean drift position (with (—) and without (--) the highly mobile individual), and mean drift position (without highly mobile individual). Note a positive displacement denotes a downstream movement and negative denotes upstream movement. 65
Figure 4-3. Sound pressure profile for 200Hz signal generated by the coarse-bubble curtain along with the theoretical acoustic pressure profile using the shallow water attenuation Eq. (12) (solid line). Measurements were made at depths of 5.0 cm (□), 12.5 cm (○), and 20.0 cm (Δ) along the centerline of the test channel. The center of the bubble curtain is located at $x = 0$ cm and edge of bubble curtain at $x = 25$ cm. Note the flattened sound pressure gradient within the bubble curtain ($x < 25$ cm). 70

Figure 4-4. Spatial evolution of the amplification factor from Eq. (18) for fine-bubble (—), graded-bubble (--), and coarse-bubble (—) curtains tested by Zielinski (2011) and Zielinski et al. (2013). The leading edge of the bubble curtain is located at x=0. The system is globally unstable if the amplification factor is positive, and stable if negative. 77
Figure 4-5. Movement analysis of carp ensemble movements during a) fine-; b) graded- ; and c) coarse-bubble curtain trials. Note a positive displacement denotes a downstream movement and negative denotes upstream movement. See Table 4-1 for description of bubble curtains. 78
Figure 4-6. Results of the stability analysis for bioacoustic fish fence investigated by Taylor et al. (2005). The amplification factor is calculated at the bubble curtain because the maximum sound pressure gradient occurs close to the sound source. A minimum sound pressure level (SPL) of 145 dB (re 1μPa) at 200Hz is necessary to result in instability growth. 81
Figure A-1. Sound pressure power spectrum in the tank during coarse-bubble trials. Measurements are provided along the centerline of the tank at a clockwise angle a). 0°, b). 45°, c). 180°, and d). 270° at a depth of 12.5 cm above the bottom of the tank. 103
Figure B-1. Flow topology (top) and Reynolds shear stress (N m^{-2}) in the XY plane (bottom) for perforated diffuser pipe (1 mm holes spaced at 1 cm) with an air flow rate of 2.5 $Ls^{-1}m^{-1}$ in a straight flume under a) 0 cm s^{-1} and b) 20 cm s^{-1} cross flow (from right to left). Axes are normalized by the depth D=25 cm and the barrier is centered about x/D=0. 108
Figure B-2. Sound pressure level power spectrum in the straight flume during use of the perforated diffuser pipe (1mm holes spaced at 1cm) at an air flow rate of 2.5$Ls^{-1}m^{-1}$. The measurement is taken at a depth of 20cm, 5cm away from the diffuser pipe. 109
Figure B-3. Sound Pressure Level (SPL) contours dB (re 1 μPa) created by the perforated pipe (1 mm holes spaced at 1 cm) with an air flow rate of 2.5 $Ls^{-1}m^{-1}$ in a straight flume under a) 0 cm s^{-1} and b) 20 cm s^{-1} cross flow (from right to left). Axes are normalized by the depth D=25 cm and the diffuser pipe is centered about x/D=0. 110
Figure C-1. Rank vs. frequency plots of common carp movement data for fish #1, 2, 4, and 18 and model predictions between a and b. Black circles denote actual ranked step size frequency for each fish. The three model fits are power-law (red line), truncated power-law (blue line), and exponential (black line), ...118
Figure D-1. Grids for calculating diffusion flux. a local diffusion, b non local diffusion. 125

Figure D-2. Schematic of channel model for non-local diffusion. The diffusion flux at *x* for a given channel is determined by a constant multiplied by the slope at the down-stream termination of the channel.....127
Figure D-3: Convergence of sum of weights *S*(*n*) to unity when $\alpha = 0.5$ 131
Figure D-4: Convergence of weight W_1 to unity and weight W_2 to zero as $\alpha \to 1$ 131
Figure D-5 CVWFS applied to steady state problem. Lines are analytical solutions, open squares are CVWFS solutions with 40 space steps, closed triangles are CVWFS solution with 20 space steps.....138
Figure D-6. Predictions of fractional diffusion ($\alpha = 0.5$) steady state with a fixed flux q_{val} and source term; line analytical solution, open squares CVWFS predictions. 140
Figure D-7. Predictions for fractional transient diffusion equation at time $t = 1$. Solid squares $\alpha = 0.2$, open squares $\alpha = 0.5$, solid triangles $\alpha = 0.8$. 141
Figure E-1. PDF of Lévy distribution generated by equation (7) for various values of (α, β) with $\gamma = 1.0$. (Figure modified from Schumer *et al.* (2009) Figure 7). 153
Figure E-2. Demonstration of the a). particle random walk and b). *domain shifting* random walk scheme for an arbitrary domain with Dirichlet boundary conditions ϕ_1 (blue) and ϕ_2 (red) after 3-steps. 155
Figure E-3. Particle Random walk solution of equation (9) for $\alpha = 0.5, \beta = 1$ with exact solution for $\beta = 1$ and $\beta = -1$. 156
Figure E-4. Solution to equation (9) with domain shifting random walk scheme ($\gamma = 0.005, \alpha = 0.5, \beta = 1.0$) along with the analytical solution.....158
Figure E-5. Solution to equation (12 and 14) $(\alpha_x = 0.3, \alpha_y = 0.7)$ with domain shifting random walk scheme ($\gamma = 0.005, N = 10000$) along with the analytical solution along the line of symmetry. 161
Figure E-8. Profiles for annulus problem along $\theta = \pi / 2$ and $\theta = 0$ radii with domain shifting random walk scheme ($\gamma = 0.0005, N = 4000$) for fractional diffusion case $\alpha_x = 0.3, \alpha_y = 0.7$ and $\beta_x = \beta_y = 0$. 163
Figure E-6. Circular annulus problem a). domain and boundary conditions and b.) comparison of domain shifting random walk scheme ($\gamma = 0.0001, N = 4000$) predicted profiles and analytical solution for integer diffusion case— $\alpha_x = \alpha_y = 1$. 165
Figure E-7. Profiles for annulus problem along $\theta = \pi / 2$ and $\theta = 0$ radii with domain shifting random walk scheme ($\gamma = 0.0005, N = 4000$) for fractional diffusion case $\alpha_x = 0.3, \alpha_y = 0.7$ and $\beta_x = -1, \beta_y = 1$ 166

Figure F-1: Grids for calculating diffusion flux in one-dimension with a). local diffusion and b). non-local diffusion (Figure modified from Voller et al. Figure 1 (Voller et al., 2011)). Fluxes from the W-west and E-east are noted at node *I,J*. 172
Figure F-2: Grid for calculating diffusion flux in two-dimensions. Subscripts on ℓ indicate direction of non-localities. Fluxes from N-north, S-south, E-east, W-west are noted at node *I,J*. 175
Figure F-3: CVWFS and random walk solution to steady state problems. Values presented along the line of symmetry (x=0, y=0 to x=1,y=1). 182
Figure F-4: CVWFS and exact solution to transient problem. Values presented along the line of symmetry (x=0, y=0 to x=1, y=1). 184
Figure F-5: CVWFS and domain-shifting scheme solution to two-sided problem. Values presented along the line of symmetry (x=0, y=0 to x=1, y=1). 186
Figure G-1. Unstructured mesh of linear triangular elements with (a) control volume for node *i* inside the domain, (b) typical region of support in element *P*, and (c) control volume for node *i* on the boundary. 195
Figure G-2. Evaluation of fractional gradient at Gauss Point (GP2), on face 2 of a region of support (dark shaded area) about control volume *i* using method of spines in the coordinate directions. Δx and Δy denote the spacing between evaluation points (○) where the local gradient is calculated and used in the CVWFS to approximate the fractional gradient. Domain boundary is labeled as Γ. Only the left sided fraction derivative is considered (i.e. weighted sum of local gradients to the *west* and *north* of GP2). 197
Figure G-3. a) Unstructured mesh with $\delta = 2^{-5}$ (2048 elements) used for the fractional CVFEM and b). profiles of CVFEM with spines and analytical solution – equation (27) – for two-dimensional fractional diffusion problem described by equation (24). Values presented along the line of symmetry (x=0, y=0 to x=1, y=1) for non-locality measures $\beta_x, \beta_y = 1$ and $\alpha_x, \alpha_y = 0.3, 0.5, 0.7$. 204
Figure G-4. Fractional CVFEM with spines and CVWFS solution to a two-sided problem, equation (29) with $\alpha_x = 0.8, \alpha_y = 0.6$ and $\beta_x, \beta_y = 0$. Values presented along the line of symmetry (x=0, y=0 to x=1, y=1). 207
Figure G-5. (a) Domain and boundary conditions for the circular annulus problem – adapted from Zielinski and Voller (2013a) – and (b) solution profiles along radii $\theta = 0$ and $\theta = \pi/2$, with domain shifting scheme ($\gamma = 0.00025$) and CVFEM for the fractional diffusion case $\alpha_x = 0.8, \alpha_y = 0.6$ and $\beta_x = -1, \beta_y = 1$ 210

Chapter 1: Introduction

1 Overview of behavioral deterrent systems and the role in invasive fish management

Introduction and proliferation of harmful non-native species is arguably one of the most pressing environmental issues in fisheries management. Invasive fish have the potential to threaten native species, local biodiversity, habitat, and ecosystem functions (Britton et al., 2011; Vitule et al., 2009). Irreversible ecological and economic damage may occur if appropriate control measures are not taken to minimize the spread and impact of invasive fish. Current management strategies generally focus on prevention of non-native fish introduction or suppression and control of established populations to acceptable levels (Britton et al., 2011, Lodge et al., 2006). A common thread between strategies is the reliance on barriers to limit fish movement. The alternative of using barriers to block invasive fish is one of the most effective and efficient management strategy (Lodge et al., 2006); however, this is not always an option due to unintended consequences of the barrier technology available (i.e. loss of navigability, block native species, health and safety risks). The latter use employs barriers to reduce secondary spread or recruitment to and from established populations to augment local management strategies (i.e. targeted removals) (Britton et al., 2011; Bajer and Sorensen, 2010). Unlike terrestrial invaders, fish movement is often restricted to well-defined waterways where dispersal can be predicted and sometimes blocked (Kolar and Lodge, 2002; Noatch

and Suski, 2012). Thus, development of sustainable and inexpensive barrier solutions is crucial for effective management of invasive fish.

1.1 Fish guidance technologies for invasive fish

Fish guidance technologies fall into one of two categories: 1) mechanical or physical barriers; and 2) behavioral (non-physical) deterrent systems. Mechanical or physical barriers include dams, screens, or traps that prevent fish passage through physical obstruction. Although effective, these systems impede water flow, are difficult and expensive to maintain, and can even increase fish mortality due to impingement in some cases (Noatch and Suski, 2012; Swanson et al., 2005). Alternatively, behavioral deterrent systems, which utilize deterrent stimuli like sound or light to guide fish, have been suggested for sites where mechanical or physical barriers are not well suited (Popper and Carlson, 1998; Noatch and Suski, 2012). The main advantage of behavioral deterrent systems is the potential to deter fish movement in taxon-specific manners without obstructing water flow; however, the lack of physical obstruction emphasizes the need to understand how each stimulus impacts individual species movements under a range of behavioral states.

Although a number of stimuli have been identified as potential deterrents to fish movement (see full lists in Zielinski (2011) and Noatch and Suski (2012)), relatively few have been shown to successfully control invasive fish movement under laboratory or field conditions (Zielinski et al., 2013; Ruebush et al., 2012; Taylor et al., 2006; Dawson et al., 2006; Swink, 1999; Holliman et al. 2011; Clarkson, 2004). The most prevalent system is the electrical barrier, which consists of grouped electrodes placed in water that impart

electrical energy to fish which results in taxis, immobilization, or death (Reynolds, 1996; Noatch and Suski, 2012). Examples of successful barriers include the blockage of sea lamprey, *Petromyzon marinus,* spawning migrations in the Great Lakes (Swink, 1999) and upstream spread of bighead, *Hypophthalmichthys nobilis,* and silver, *Hypophthalmichthys molitrix,* carp in the Chicago Sanitary and Ship Canal (Holliman et al. 2011). Electrical barriers have been shown to be effective at stopping upstream movement, but are as yet unproven for use against downstream movement (i.e. if a fish becomes immobilized, the current will carry the fish past the barrier), lack species specific action, require high operation and maintenance costs, and are particularly susceptible to power outages (Clarkson, 2004).

Another behavioral deterrent system shown to influence invasive fish movement is a multi-component system comprised of sound, light, and bubble curtain stimuli. Taylor et al. (2005) found a proprietary system, coined the bioacoustic fish fence or 'BAFF' (Fish Guidance Systems, UK) repelled up to 90% of passage attempts by bighead carp in a shallow concrete channel. Ruebush et al. (2012) also suggested silver carp were deterred by the BAFF in a branch of the Illinois River, but lacked sufficient controls to quantify the level of deterrence. Additionally, the BAFF system has been shown effective at guiding salmonid movements away from high mortality routes in the Sacramento-San Joaquin River Delta, USA, (Perry et al. 2012) and River Frome, UK (Welton et al. 2002). Although, multi-component systems show promise to control invasive fish movements, the technology is in its infancy and can be prohibitively expensive.

Fisheries managers have limited resources available for management activities (Vander Zaden and Olden, 2008); therefore, development of simple and inexpensive deterrent alternatives must be a priority. The motivation behind this work was driven by the need to find an inexpensive, yet effective means to control movement of common carp, *Cyprinus carpio*, between shallow interconnected water bodies. A behavioral deterrent of particular interest is the bubble curtain, which consists of a wall of bubbles produced by forcing air through perforated pipes. Bubble curtains are inexpensive, require relatively little maintenance, and generate complex sound, visual, and hydrodynamic fields which can be optimized to deter fish without obstructing water flow.

A number of studies have reported on the effectiveness of bubble curtains across a range of applications, including laboratory studies of <1 m long systems to full scale field trials at power plants with bubble curtains extending nearly 100 m (Brett and MacKinnon, 1953; Kuznetsov, 1971; Zweiacker et al., 1977; Liebermann and Muessig, 1978; Stewart, 1982; Patrick et al., 1985; Sager et al., 1987; Welton et al., 1997; EPRI, 1998; Sprott, 2001; EPRI, 2004; Dawson et al., 2006). It is difficult to make any collective assessment of bubble curtains using this data because these tests were performed in disparate systems, with different management goals, and targeted different fish species; however, there was sufficient evidence to suggest bubble curtains may indeed be capable of deterring fish movement. Additionally, many of the studies neglected to quantify relevant physical fields (i.e. sound or turbulence) needed to assess what factors influence bubble curtain performance or explain observed behaviors for targeted species. Despite the number of laboratory and field studies to date, the

mechanisms behind how or why these systems work are still unknown. This leads to the first **key objective** of this thesis work: **to develop a bubble curtain system that inhibits movement of common carp and identify the biologically relevant stimuli likely to influence fish movement.**

1.2 Common carp as a model invader

The common carp, hereafter termed carp, is a large benthic cyprinid native to the Caspian Sea region of Eastern Europe which was introduced to North America in the late 1870's (Balon, 1995). Over time, carp have spread widely and become one of the most successful invaders around the world (Lever, 1996). In regions where carp reach high densities, such as Midwestern North America and Southern Australia, carp are responsible for reduced biodiversity, water quality degradation, and destruction of aquatic plants (Koehn, 2004; Weber and Brown, 2009; Bajer et al., 2009). Furthermore, carp exhibit many of the traits predicted for a successful invasive species: wide environmental tolerance, early sexual maturity, short generation time, rapid growth, highly fecund, mobile, and broad diet (Koehn, 2004). This has made carp one of the world's 100 worst invaders (Lowe et al., 2000), target of countless management schemes (Weber and Brown, 2009), and ideal candidate for evaluating the efficacy of novel behavioral deterrent systems.

Carp reach high densities in regions with abundant and interconnected unstable habitat (i.e. water bodies susceptible to hypoxic conditions). Unstable habitat, such as inundated floodplains, backwaters, wetlands, or shallow lakes, provide predator free spawning habitat for carp that primarily inhabit connected stable habitat (e.g. deep

normoxic lakes or rivers). For example, in Midwestern North America, carp often inhabit stable, deep, normoxic lakes for much of the year but leave them to enter interconnected unstable, shallow lakes to spawn, so the latter areas frequently serve as recruitment 'hotspots' (Bajer and Sorensen, 2010). Great ecological benefit would be gained if the movement between deep lakes and spawning habitat were controlled; however, extant barrier technologies are not well suited for the low-head conditions typical of the interconnecting streams. Bubble curtains could provide a targeted, safe, and inexpensive alternative for sites where reduction, not total elimination of movement, is the management goal.

1.3 Mathematical modeling of behavioral deterrent systems

Mathematical models are powerful tools that provide clear frameworks by which complex fish behavior can be studied (Okubu and Levin, 2001). Despite recent experimental advances in behavioral deterrents for controlling fish movement, only a few studies have attempted to model how fish movements are impacted by deterrent stimuli (Goodwin et al. 2006; Lemasson et al., 2008, Perry et al., 2012). By understanding not just what factors influence fish movement, but how those movements are impacted, behavioral deterrent systems may be improved. Thus, fish movement models can be used, albeit cautiously, to help make informed management decisions regarding the implementation and design of behavioral deterrent systems. In practice, models can simulate how target and non-target species respond to various behavioral deterrents under a suite of environmental conditions over long periods of time, all scenarios that are difficult and prohibitively expensive to test experimentally. This leads to the second **key**

objective of this thesis work: **to develop a mathematical model to describe fish movement in the vicinity of a behavioral deterrent system**.

Mathematical models of organism movement are often based on diffusion theory (Skellam, 1951; Holmes et al., 1994; Codling et al., 2008; Okubo and Levin, 2001), where an individual's movement is represented as a random walk. In its simplest form, a random walk process consists of an ensemble of walkers taking a series of steps (of constant or variable size) in random, unbiased, directions. At the long time limit, the spatial distribution of walkers can be represented by the classical diffusion equation. In turn, if the step direction is biased, or the walkers tend to move in a preferred direction, the continuum approximation is the advection-diffusion equation. Here, the directional bias is introduced at the individual level or by external advection (e.g. fluid flow) (Codling et al., 2008; Codling et al., 2010). Advection-diffusion models have been used to describe the spatial distribution of numerous fish species (Zabel et al., 1997; Skalski and Gilliam, 2003; Sparrevohn et al., 2002; Sibert et al., 1999), and constitutes a natural basis for a continuum description of fish movement near a deterrent system, due to the need to stop directed fish movements (e.g. spread of an invasive species or migration).

The most critical component of modeling fish movement near a deterrent system is the avoidance function that links fish behavior to deterrent stimuli. A successful behavioral deterrent is one that elicits an avoidance response from target fish (Noatch and Suski, 2012; Popper and Carlson, 1998), which depends on the magnitude and gradient of the signal and sensitivity of corresponding sensory systems. The gradient is especially critical in generating a directional response. Thus, an advection-diffusion model

modified with a repulsion function garnered by a density dependent behavioral response to the stimuli gradient will be used to describe fish movement. The resulting advection-diffusion-reaction equation is conceptually similar to well studied chemotaxis models used to describe bacterial movement responding to chemical gradients (Hillen and Painter, 2009). The repulsive function does not explicitly include any sensory capacities of the fish, but relates a known stimuli source (in the case of bubble curtains, sound pressure) to the repulsive response observed in laboratory trials.

2 Objectives and structure of this dissertation

This dissertation is divided into two parts. Part I (**chapters 2 and 3)** discuss the experimental evaluation of different bubble curtains to inhibit common carp movement in a shallow laboratory channel and stream in Maplewood, Minnesota, USA. The fundamental design of bubble curtains, characterization of relevant stimuli fields, and results of laboratory and field tests are presented.

In **chapter 2**, the common carp was used to examine the performance of three different bubble curtains (fine-, graded-, and coarse-bubble) and acoustically enhanced systems to inhibit fish movement in a shallow laboratory channel. Additionally, hydrodynamic and acoustic fields generated by the bubble curtains were quantified. Further testing with speaker arrays and lighting are used to investigate the role of individual sensory stimuli to cause carp avoidance.

Follow up work in **chapter 3** expands on the work in **chapter 2** by testing the efficacy of a graded-bubble curtain in a stream draining a common carp spawning and nursery habitat. The objective of this study was to 1) validate the results for the graded-

bubble curtain from **chapter 2** under natural conditions, and 2) assess the potential use of bubble curtains as a carp management tool. Carp movement was monitored in the stream by a custom PIT tag interrogation system, allowing for separate tests for upstream swimming carp during spawning migrations and downstream swimming carp.

Part II (**chapters 4 and appendix C-G**) focuses primarily on the development of mathematical models to describe fish movement in the vicinity of behavioral deterrent systems and relevant numerical formulations of anomalous transport processes. In **chapter 4**, an advection-diffusion equation, incorporating a stimuli specific repulsive flux, is coupled with calculation of the generated stimulus field in order to model fish movement near a behavioral deterrent system. A stability analysis of this model is then used to determine the effectiveness of a bubble curtain to disrupt the natural, un-impeded, movement of fish in a laboratory channel. Results from the laboratory trials in **chapter 2** are used to parameterize and verify the stability analysis predictions.

The population level analysis of common carp movement in **chapter 4**, revealed carp may be exhibiting movement patterns consistent with Lévy flight processes (i.e. foraging hypothesis that assumes organisms disperse anomalously as a result of movement lengths chosen from distributions with heavy power-law tails). Therefore, **appendix C** expands upon this notion and uses modern statistical methods to test whether the movement length distributions of common carp, introduced in **chapter 2,** exhibit power-law decaying tails. Evidence of power-law distributions would suggest that fractional-diffusion models may better predict fish dispersal in this case. Here, the

fractional-diffusion equation is the stable limit approximation of random walks with power-law distributed step-sizes.

An objective of this work is to understand how such models work, thus requiring extensive supporting studies aimed at understanding the construction and operation of fractional-diffusion models. These studies led to significant advances in the application of fractional calculus transport models resulting in a number of archival papers in the relevant literature. These papers are presented in **appendix D-G** of this dissertation. Although these studies do not contribute directly to inferences of behavior or control of invasive fish; they are intended to present an alternative description for anomalous diffusive transport relevant to organism dispersal.

Chapter 2: Laboratory experiments demonstrate that bubble curtains can effectively inhibit movement of common carp

D.P. Zielinski, V.R. Voller, J.C. Svendsen, M. Hondzo, A.F. Mensinger, P. Sorensen
Laboratory experiments demonstrate that bubble curtains can effectively inhibit movement of common carp, Submitted to *Ecological Engineering*, April 22, 2013.

Although bubble curtains have been proposed many times as practical and inexpensive solutions to hinder the movement of invasive fish, few studies have examined why or how they might work. By understanding how bubble curtains influence fish behavior, management tools could be developed to control movement of invasive fish. In this study, the common carp (*Cyprinus carpio* L.) was used to examine the performance of three different bubble curtains (fine-, graded-, and coarse-bubble) and acoustically enhanced systems in an indoor channel. Trials revealed that the graded- and coarse-bubble systems reduced common carp passage across the curtain by 75-85% in both up- and down-stream directions. Concurrent acoustic field measurements revealed that these bubble curtains generated sound near 200 Hz at approximately 130dB (ref 1 μPa), well above the common carp hearing threshold. Further testing with speaker arrays and lighting indicated that carp avoidance to the bubble curtain involved responses to sound and fluid motion rather than visual cues. Although field tests are warranted, our results suggest that bubble curtains may be a viable and inexpensive deterrence system to limit common carp movement.

1 Introduction

Fish guidance technologies have long been part of fisheries management efforts to control invasive fishes (Taft, 2000; Lavis et al., 2003; Noatch and Suski, 2012). Physical or mechanical barriers (i.e. dams, screens, or traps) can be effective at stopping both up- and down-stream movement of invasive fish; however, these barriers can be extremely difficult and expensive to maintain because of clogging. Consequently, 'behavioral barriers', which utilize stimuli such as sound and light to target fish sensory systems and guide fish in taxon-specific manners, have been suggested for sites where mechanical or physical barriers are not well suited (Popper and Carlson, 1998; Noatch and Suski, 2012). A behavioral barrier of particular interest is the bubble curtain, which produces a wall of bubbles (e.g. by forcing air through perforated pipes). Bubble curtains are inexpensive, require relatively little maintenance, and generate complex sound, visual, and hydrodynamic fields which may be optimized to deter fish without obstructing water flow.

Initial development of bubble curtain technologies was driven by both commercial fishing (Kuznetsov, 1971), and the need to find alternative solutions to reduce fish impingement at power generation facilities (Taft, 2000; Michaud and Taft, 2000). Although laboratory and field studies have reported some fish to be deterred by bubble curtains, studies did not quantify sound fields or other physical characteristics needed to assess the factors driving the effectiveness of the barrier systems (Brett and MacKinnon, 1953; Kuznetsov, 1971; Zweiacker et al., 1977; Liebermann and Muessig, 1978; Stewart, 1982; Sager et al., 1987; EPRI, 1998; Sprott, 2001; Welton et al., 2002;

EPRI, 2004; Dawson et al., 2006). Further, some studies have reached contradictory conclusions (Patrick et al., 1985; Welton et al., 1997). One example of this scenario concerns the possibility of light/visual cues from bubble curtains to cause fish deterrence. While Patrick et al. (1985) suggested bubble curtains act as a visual deterrent due to a ~20% greater avoidance by gizzard shad (*Osmerus mordax*), alewife (*Alosa pseudoharengus*), and smelt (*Dorosoma cepedianum*) to a bubble curtain under low light than in darkness; however, Welton et al. (1997) described just the opposite and suggested that Atlantic salmon smolt (*Salmo salar*) were deterred more during night than daytime trials (42% compared to 0%). Alternatively, Kuznetsov (1971) suggested fish respond to the acoustic fields generated by bubble curtains based on observations of nighttime commercial fishing. Overall, studies appear to suggest that bubble curtains inhibit fish movement, but the factors within a bubble curtain that actually affect fish behavior remains unclear. Importantly, no studies have attempted to partition the influence of sound, visual, and hydrodynamic fields on fish behavior.

By understanding how bubble curtains influence fish behavior, management tools could be developed to control movement of invasive fish. Bubble curtains may influence fish visual, auditory, and lateral line systems by generating sound, tactile (e.g. fluid flow), and visual stimuli. Sound is generated by bubbles as they detach from the diffuser (Leighton and Walton, 1987; Leighton, 1994; Lin et al., 1994), which at the continuum limit (the curtain of bubbles works as a collection of coupled oscillators) results in low frequency (<1000Hz) sound emissions (Nicholas et al., 1994; Manasseh et al., 2004). The radiating sound field is comprised of longitudinal particle motion and local pressure

oscillations. For all teleost fish, the inner ear detects the particle motion component of the sound wave; however, ostariophysian fish (including common carp) have an anatomical link between swim bladder and inner ear which provides indirect audition of the pressure component as well (Popper and Fay, 2011). Rising bubble plumes also generate turbulence with distinct recirculation currents that are dependent on the upward velocity and density of the bubble plume (Brevik and Kristiansen, 2002; Soga and Rehmann, 2004). The mechanosensory lateral line is the main sensory system for hydrodynamic signals (Webb et al., 2008). Finally, bubble curtains may serve as a visual barrier by obscuring a fish's line of sight past the barrier (Patrick et al., 1985; Sager et al., 1987).

The present study investigated the impact of a bubble curtain on common carp (*Cyprinus carpio* L.), a cyprinid responsible for degrading water quality in shallow water ecosystems (Weber and Brown, 2009). In Midwestern North America, common carp, hereafter termed carp, often inhabit stable, deep, normoxic lakes for much of the year but leave them to enter interconnected unstable (susceptible to hypoxic conditions), shallow lakes to spawn, so the latter areas frequently serve as recruitment 'hotspots' (Bajer and Sorensen, 2010). Reducing or stopping the migration of adult fish to spawning habitat or young carp back to the stable lakes could dramatically decrease recruitment. Existing barrier technologies are not well suited for the conditions characteristic of streams connecting stable and unstable lakes which typically have low hydraulic head. Bubble curtains could provide a targeted, safe, and inexpensive alternative for sites involving downstream movement of small fishes, especially in waters where reduction, not total

elimination of movement, is the management goal. Furthermore, a behavioral barrier employing acoustic stimuli – such as the bubble curtain – may be potentially useful for targeting carp because of their relatively broadband hearing (50-3000Hz) and sensitivity (>65dB re: 1 μPa)(Popper, 1972).

The main objectives of the present study were to: 1) develop and test the efficacy of a bubble curtain to inhibit carp movement under controlled laboratory conditions; 2) identify the acoustic and hydrodynamic flow fields generated by the bubble curtain; and 3) determine the effect of visual and auditory components of the bubble curtain to inhibit movement. This study appears to represent the first attempt to quantify the biologically relevant stimuli fields generated by a bubble curtain that inhibits fish movement.

2 Materials and Methods

2.1 Experimental setup

Common carp (mass: 204±77g; total length: 259±29mm. (mean±S.D.)) were caught in Lake St. Catherine, MN, USA by electrofishing in July 2010 and transported to the laboratory, where the carp were maintained in large tanks supplied with continuously flow-through 20°C well water. Carp were fed pellets (Silver Cup, Utah) once a day between 10.00 h and 16.00 h.

Passive integrated transponder (PIT) tags (OregonRFID, OR, USA) were implanted into one third of the fish. Carp were anesthetized in a 0.05% solution of buffered tricaine methanesulfonate (MS222), a 5 mm incision was made between their pelvic and pectoral fins and the 23 mm-long half duplex PIT tag placed inside their body

cavity. Incisions were allowed to heal for three weeks (Skov et al., 2005) prior to the experiments and tagging resulted in no mortality. The remaining carp were left untreated. All experimental procedures were approved by the University of Minnesota Institutional Animal Care and Use Committee.

Experiments were performed in a round tank (3 m diameter) provided with an insert to create a circular channel (I.D. 1 m x O.D. 3 m) and water depth of 25 cm (Figure 2-1). Water was supplied to the channel through a submerged pipe, producing an average 5 cm s^{-1} current. Carp were tested in groups of three to facilitate natural shoaling behavior. To track carp movement, a PIT antenna array was constructed using the Oregon RFID Multi-Antenna HDX reader, powered by a 12-V deep cycle marine battery. Each antenna consisted of 5 turns of 16 gauge solid wire (1 m x 0.3 m hoop), tuned to an inductance of ~60-80 μH. All antennas were connected to tuning modules, which were connected to the PIT reader by twin coaxial cable. Each time a tagged carp passed through an antenna, the time of passage, PIT identification number, antenna number, and time between detections were logged onto a memory card for analysis. The antennas were equally spaced (~1.6 m) along the circular channel at the quarter points, centered about the bubble curtain (Figure 2-1). Manual testing indicated that the detection probability of each antenna was > 99%.

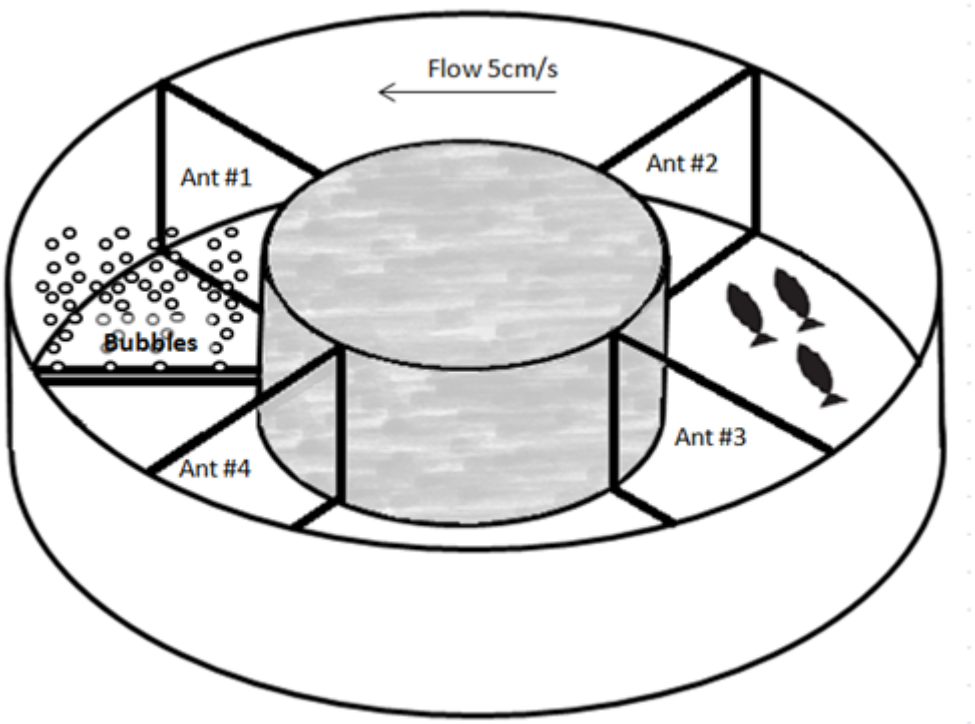

Figure 2-1. Schematic of behavioral trial tank with approximate location of bubble curtain and PIT tag interrogation system (PIT antennas are labeled Ant #1-4). The outside diameter of the tank is 3 m and the inside diameter is 1 m, and water depth is 25 cm.

2.1.1 Tests of simple bubble curtains

Responses of carp to three different bubble curtain systems were tested. Bubble curtain systems varied in size, configuration, and air supply to help identify features influencing fish behavior. The first system was a fine-bubble system comprised of two 2.5 cm diameter porous polyethylene pipes (Genpore, PA, USA). These pipes had an average pore size of 25 microns over their entire surface. The pipes were placed 30 cm apart on the bottom of the test channel (Figure 2-2a). Two S41 regenerative air-blowers (Aquatic Ecosystems, FL, USA), in series, were used to supply 5.6 L s^{-1} m^{-1} of air at 28

kPa. This configuration was similar to the systems investigated by Welton et al. (1997) and Patrick et al. (1985), with the difference being the use of two pipes instead of just one.

The second system was a graded-bubble system comprised of six 2.5 cm diameter pipes. The system produced incrementally larger bubbles across the length of the system (Figure 2-2b), employing one porous polyethylene pipe (~25 micron pores), four PVC pipes with 1 mm diameter holes spaced at 1 cm, and one PVC pipe with 3 mm diameter holes spaced at 5 cm. Pore sizes increased in the downstream direction. The total air flow was 30.1 L s^{-1} m^{-1} at 5kPa in the drilled PVC pipes and 28 kPa in the porous pipe. The total width of the system was 50 cm. The increasing bubble size produced by the graded-bubble system was chosen to provide an increasingly adverse stimuli field across the length of the barrier.

The third system was a coarse-bubble (CB) system comprised of a grid layout of 2.5 cm diameter PVC pipes with 3 mm holes spaced at 5 cm over the entire surface (Figure 2-2c). This layout provided bubble curtains that were both perpendicular and parallel to the water flow, and reduced the potential for fish to maneuver through gaps in the curtain. The air flow was increased to 108.0 L s^{-1} m^{-1} at 5 kPa, by using four S41 regenerative air blowers in parallel. The total width of the system was 50cm.

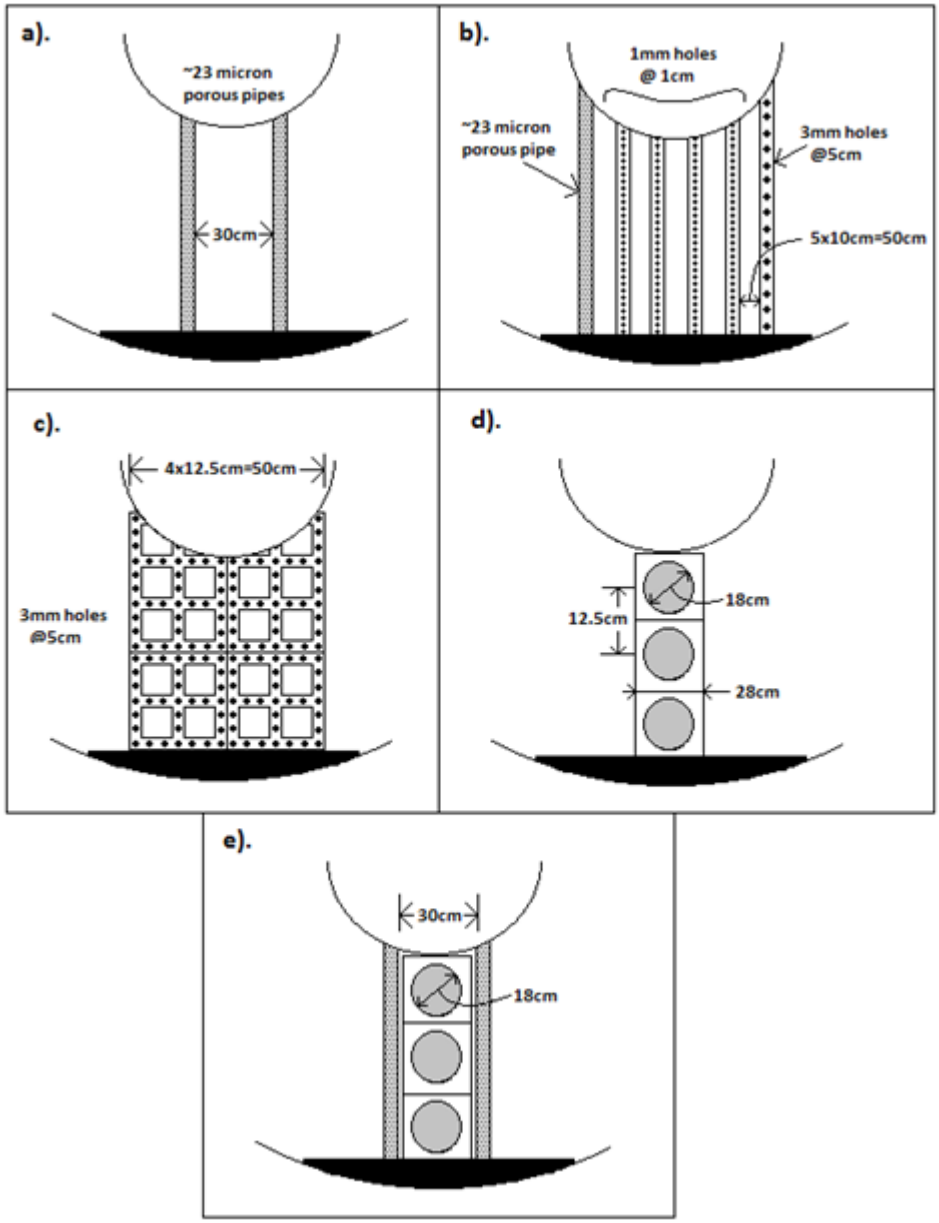

Figure 2-2. Plan view schematic of bubble curtain and speaker arrangements tested: a). fine-bubble; b) graded-bubble; c) coarse-bubble; d) speaker array; e) speaker array/fine-bubble systems. The darkened area is filled by plastic mesh, preventing fish passage along tank edge. Water flow is from left to right at 5 cm s^{-1}. See Figure 2-1 for further details of curtain positioning in the circular tank.

Behavioral trials were conducted between 20.00 and 6.00 h with all lights off in the testing facility and a black tarp covering the circular tank so that no light was visible,

minimizing the role of any visual stimulus. For each trial, one PIT tagged and two untagged carp were selected at random, placed into the circular channel, and allowed to acclimate for 10 min before the trial began. Tests included trials with the bubble curtain on and off, the latter constituting a control trial. Carp were removed from the circular channel after 7 h of data collection and placed into separate holding tanks to eliminate any re-testing. Each set of trials was conducted no sooner than 3 weeks after the conclusion of the previous trial. All behavioral trials with the bubble curtains turned on had a sample size N=7, except the graded-bubble system had N=8. Control trials were performed before and after each set of behavioral trials (subsets of N=8, 7, 3, and 6 for a total sample size of N=24) to ensure carp behavior remained consistent along the entire experimental period (Figure 2-3).

2.1.1.1 Properties of the bubble curtain

The sound pressure field encountered by the carp during trials was mapped at depths of 5, 12.5, and 20 cm above the bottom of the tank. Measurements were taken at a resolution of 10 cm in the quadrant of each barrier and 25 cm in the rest of the tank. In this study, descriptions of the acoustic field are restricted to sound pressure measurements.

Acoustic pressure measurements were obtained using a miniature (50 mm length, 9.5 mm diameter) BK 8103 hydrophone (Bruel & Kjær, Denmark). This hydrophone has a frequency range of 0.1 Hz to 180 kHz and a sensitivity of approximately -211 dB ref 1 V/ μPa. The output signal from the hydrophone was amplified by a 144L low noise voltage amplifier (DL instruments, NY, USA) and fed into a National Instruments SC-

2345 signal conditioning board. A custom LabVIEW program (National Instruments, TX, USA) was written to control and record from the conditioning board, and a custom Matlab (Mathworks, MA, USA) program was written to analyze and transform the pressure waveform into the frequency domain. At each measurement location, ten signal ensembles were averaged to improve the signal-to-noise ratio. The hydrophone data record was 10.0 s in duration and was sampled at 100 kHz.

2.1.2 Testing the role of sound and light stimuli on the efficacy of a bubble curtain

Once the coarse-bubble system was identified as the most effective bubble curtain, we investigated the influence of sound and light on the efficacy of the coarse-bubble system. To accomplish this, responses of carp to an illuminated coarse-bubble system, speaker array system, and bubble curtain system supplemented with a speaker array were tested as outlined below.

2.1.2.1 Visual stimuli

Trials using the coarse-bubble system were performed between 20.00 to 6.00h with three 40W 120V (Sylvania, MA, USA) light bulbs installed approximately 1.0 m above the water surface to illuminate the circular channel (average surface illumination: 370 lx). These data were compared to data collected in darkness.

2.1.2.2 Sound stimuli

Bubble curtains create visual and flow fields in conjunction with sound. To test the role of sound alone, a speaker array was used in place of the coarse-bubble system. The speaker array system comprised of two UW30 underwater speakers (Electrovoice,

MN, USA) on either side of an AQ339 underwater speaker (Clark Synthesis, CO, USA) (Figure 2-2d). The signal was a 10 s recording of the sound produced by the coarse-bubble system which was set to loop continuously. Acoustic pressure measurements were performed to ensure that the maximum sound pressure level (SPL) generated by the speaker array closely matched those created by the coarse-bubble system, thereby creating a bubble curtain stimulus without bubbles or turbulence.

2.1.2.3 Sound and bubble stimuli

Another trial used a bubble curtain that was supplemented with a speaker array to investigate whether adding a sound field to a weak bubble curtain impacted carp movement. Addition of the bubble curtains provided some fluid flow and influenced the acoustic field by acting as a resonant amplifier (Manasseh et al., 2004) re-transmitting the sound generated by the speaker array. The speaker array/fine-bubble system was a combination of the fine-bubble and speaker array system (Figure 2-2e). The signal of the speaker array/fine-bubble system was a 10 s recording of the coarse-bubble system set to maintain the same the maximum SPL. Acoustic mapping was used to quantify any differences in the acoustic field dynamics between the coarse-bubble, speaker array, and speaker-array/fine-bubble systems.

2.2 Statistical analysis

A Shapiro-Wilk test determined that the numbers of crossings over each bubble curtain system during control and bubble curtain trials were not normally distributed, so nonparametric tests were required (Conover, 1980). A Kruskal-Wallis test (Conover,

1980) was then used to compare differences between the number of passages in the up- and down-stream direction between the bubble curtain and control trials (e.g. fine-bubble, graded-bubble, and coarse-bubble, and control groups), the visual stimuli trials (e.g. coarse-bubble group with and without light), and speaker array trials (e.g. coarse-bubble, speaker array, and speaker array/fine-bubble groups). The average number of passages in each direction was used to compare the efficacy of each bubble curtain design. When the Kruskal-Wallis test suggested significance ($P<0.05$), Mann-Whitney pair-wise comparisons with Dunn-Sidak correction for multiple comparisons were performed to determine which pair differed. A Kruskal-Wallis test was also used to confirm that the control trials (no bubble curtains) did not change over time (so we could combine them into a universal control group). Additionally, the total activity of the carp over the entire test period was quantified by summing the number of times a carp passed through any consecutive antenna. A Kruskal-Wallis test was used to compare the total activity levels between all trials to assess whether the bubble curtains impacted all carp movement in the tank or just passage over the bubble curtain.

The efficacy (E) of each bubble curtain was calculated for each dataset in the following manner:

$$E = 100\% \cdot \left(1 - \frac{N_{curtain}}{N_{control}}\right)$$

Where $N_{curtain}$ is the mean number of carp passages through the curtain while it is on (test trials) and $N_{control}$ is the mean number of carp passages over the curtain while it is off (control trials).

3 Results

3.1 Tests of simple bubble curtains

Carp tended to swim in the downstream direction nearly twice as often as in the upstream direction during the control trials (Mann-Whitney U-test: $P<0.01$) (Figure 2-3). When compared, all control trials had the same number of passages in the both directions over time (Kruskal-Wallis: $P>0.05$) (Figure 2-3). The average number of crossings during each control test was 60[28.5, 80] (mean[1st, 3rd quartiles]) and 90[64, 126] in the up- and down-stream direction.

A difference in the number of passages in the up- and down-stream direction was found among the bubble curtains trials (Kruskal-Wallis: $P<0.001$, both directions) (Figure 2-3). While the fine-bubble curtain was not found to reduce the number of passages in either direction (38[23, 61] upstream and 31[8, 51] downstream), the graded-bubble curtain reduced passage by 78% (Mann-Whitney U-test: $P<0.05$, 20[2, 30]) in the downstream direction and 72% (Mann-Whitney U-test: $P<0.05$, 16[5.5, 36]) in the upstream directions. The coarse-bubble curtain was the most effective system, resulting in a downstream efficacy of 87% (Mann-Whitney U-test: $P<0.001$, 11[1, 24]), and upstream efficacy of 82% (Mann-Whitney U-test: $P<0.005$, 10[0, 21]). Additionally, there were two graded-bubble and three coarse-bubble curtain tests that had zero crossings in the downstream direction.

The swimming activity of the carps was unaffected by the bubble curtains. The total number of crossings between consecutive antennae (total activity) between bubble curtain and control trials did change (Kruskal-Wallis: $P<0.05$), but a reduction was

observed during the graded-bubble trial (46% reduction, Mann-Whitney U-test: $P<0.01$). No additional change in the total activity was observed over all other trials, resulting in a mean number of times carp passed between any two antennae at ~1000/test period (or nearly 3 m traveled every 30 s).

3.1.1 Identifying the characteristic sound field of a bubble curtain

The bubble curtains investigated in this study generated a broad spectrum acoustic field with a peak frequency between 100 Hz and 300 Hz (Figure 2-4). The contour plot of the sound pressure field in the behavioral tank at 200 Hz for the coarse-bubble system was typical for all bubble curtains (Figure 2-5). The sound pressure contours at 200 Hz for the fine-bubble and graded-bubble systems displayed similar characteristics (i.e. no extraneous sound away from the bubble curtain and rapid attenuation in the near field). The maximum sound pressure level (SPL) between 100-300 Hz was 120 dB (ref 1 μPa) for the fine-bubble system. The up- and down-stream maximum SPL between 100-300 Hz was found to be 100 and 130 dB (ref 1 μPa) for the graded-bubble system, resulting from increased size of bubbles along the length of the system. The maximum SPL between 100-300 Hz of the coarse-bubble system was 134 dB (re 1 μPa). Power spectrum plots of the SPL generated by the coarse-bubble system at additional locations in the tank are provided in Appendix A and B, along with additional acoustic and hydrodynamic field measurements of single pipe bubble curtains under varying depth, air-flow, and water flow obtained in an earlier pilot study.

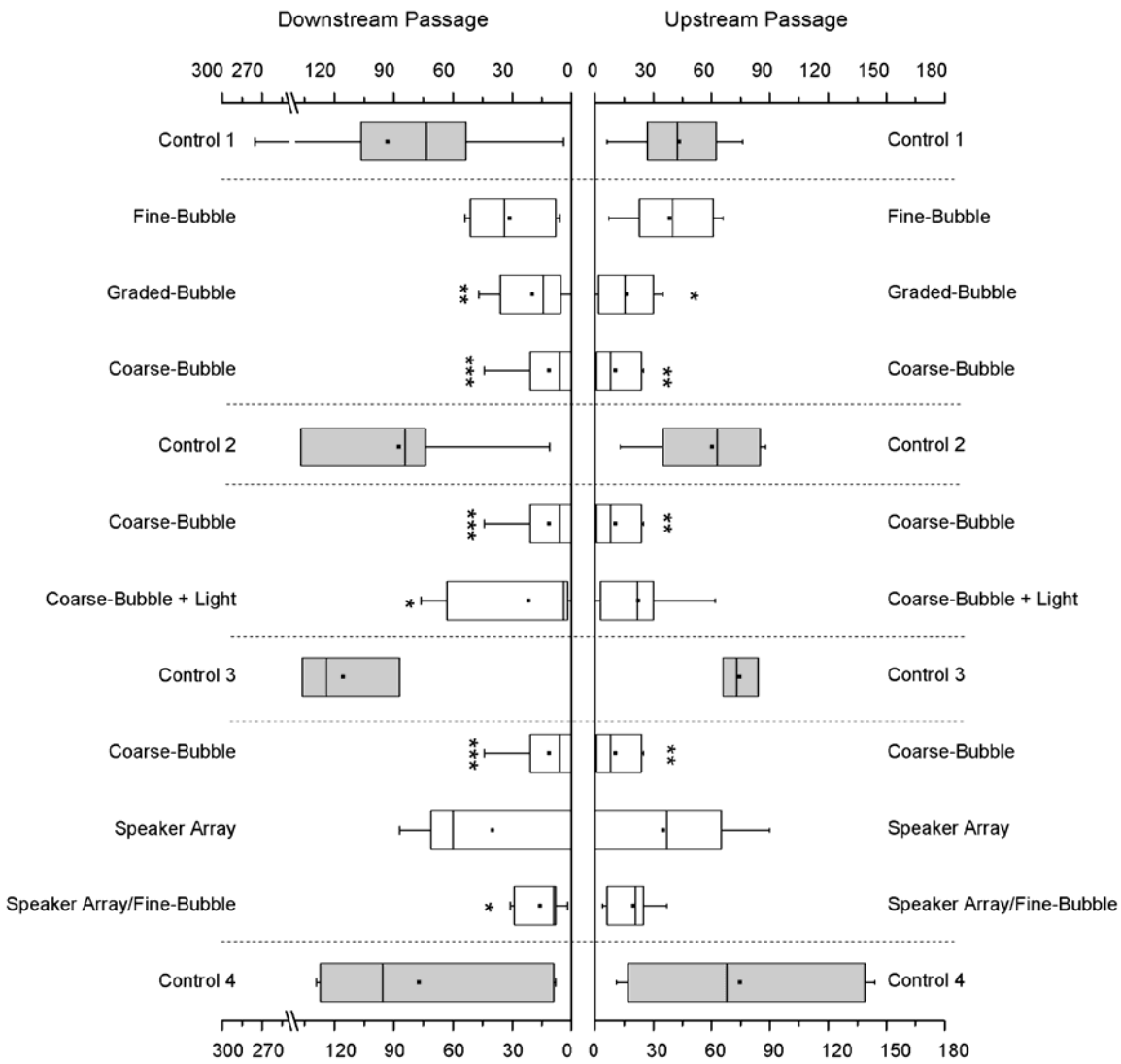

Figure 2-3. Total number of up- and down-stream passages made by common carp for each test (e.g. curtain type). Dashed lines separate trial groups compared with Kruskal-Wallis and Mann-Whitney tests. Control trials are spaced in chronologic order to illustrate how consistent carp behavior was over the entire study; however, in comparison to the bubble curtain designs, the controls were combined into a universal control group. Note, the coarse-bubble trial is shown repeatedly for clarity of trials being statistically analyzed. Statistical significance was determined by Mann-Whitney pair-wise comparisons with Dunn-Sidak correction for multiple comparisons. Box plots illustrate data quartiles, mean, median (squares) and whiskers represent minimum and maximum values. *P<0.05, **P<0.01, ***P<0.001

3.2 Influence of sensory fields on efficacy of bubble curtain

The number of passages over the coarse-bubble system while well lit was not found to be different in the up- or down-stream direction compared to the dark trial (Mann-Whitney U-test: P>0.05, 22[3, 30] and 22[2, 63]) (Figure 2-3). Likewise, no differences in the number of up- or down-stream passages were found between the coarse-bubble, speaker array, and speaker array/fine-bubble trials (Kruskal-Wallis: P>0.05) (Figure 3-3). The speaker array/fine-bubble system resulted in a reduction of passage similar to the coarse-bubble system in both the up- and down-stream directions (16[6, 25] and 19[8, 29]).

An area of high sound pressure was concentrated near the speaker array with a maximum SPL between 100-300 Hz for the speaker array and speaker array/fine-bubble system of 134 dB (ref 1 μPa) (Figure 2-6). The sound pressure field attenuated radially away from the speaker array system (Figure 2-6b), while the sound pressure field generated by the speaker array/fine-bubble system remains elevated between the fine-bubble diffusers located x/D =0.3 on either side of the speakers at approximately 125 dB (ref 1 μPa) at 200 Hz (Figure 2-6b), before attenuating rapidly in the channel wise direction similar to that of the coarse-bubble system (Figure 2-6a). In addition to introducing a tactile stimulus, the presence of the fine-bubble curtain serves to re-orient the sound pressure gradient produced by the speaker array alone.

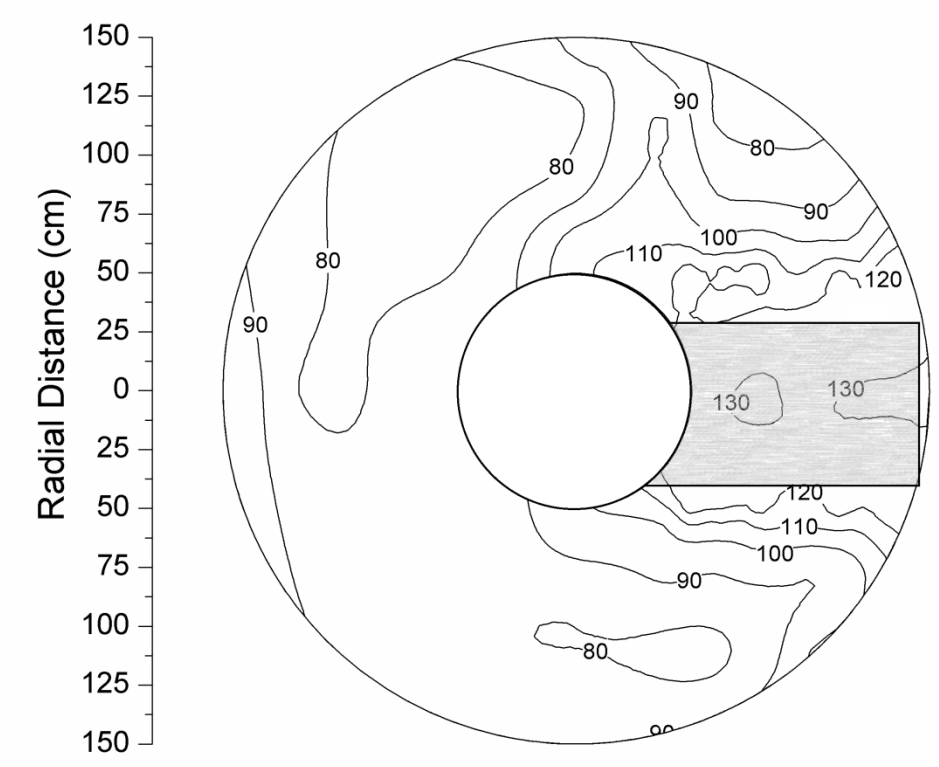

Figure 2-5. Plan view of sound pressure field in dB (ref 1 μPa) in the behavioral trial tank at a depth of 12.5cm at 200Hz with the coarse-bubble system. The bubble curtain is located to the right of the center of the tank, perpendicular to the y-axis centered at a radial distance of 0 cm. The background SPL at 200Hz was ~80dB (ref 1 μPa). The shaded area denotes the approximate location of the coarse-bubble system.

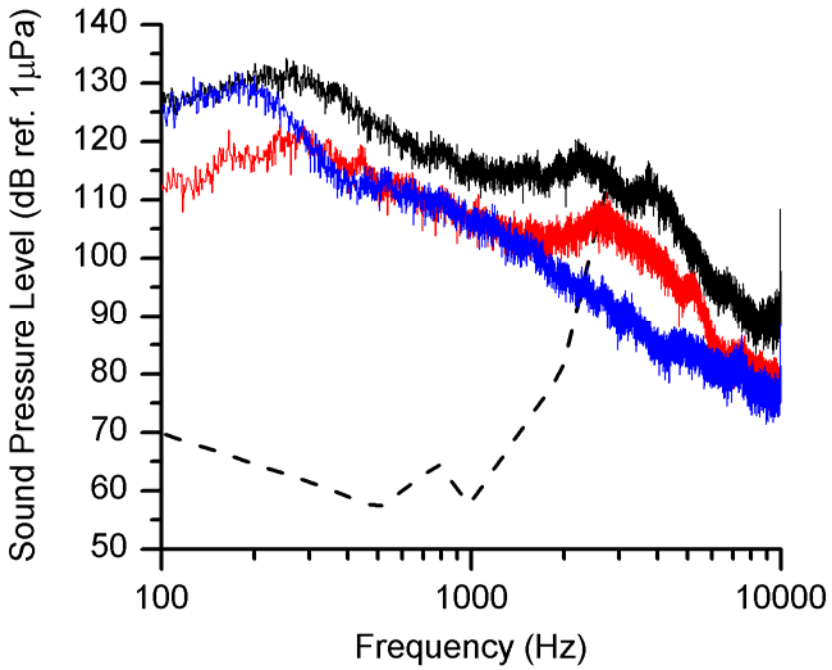

Figure 2-4. Sound pressure level power spectrum in the behavioral trial tank during coarse-bubble (solid black line), graded-bubble (solid blue line), and fine-bubble (solid red line) trials and the common carp hearing threshold documented by Popper (1972) (dashed black line). Bubble curtain sound data was obtained at the center of the bubble curtain, 5 cm above the channel bottom.

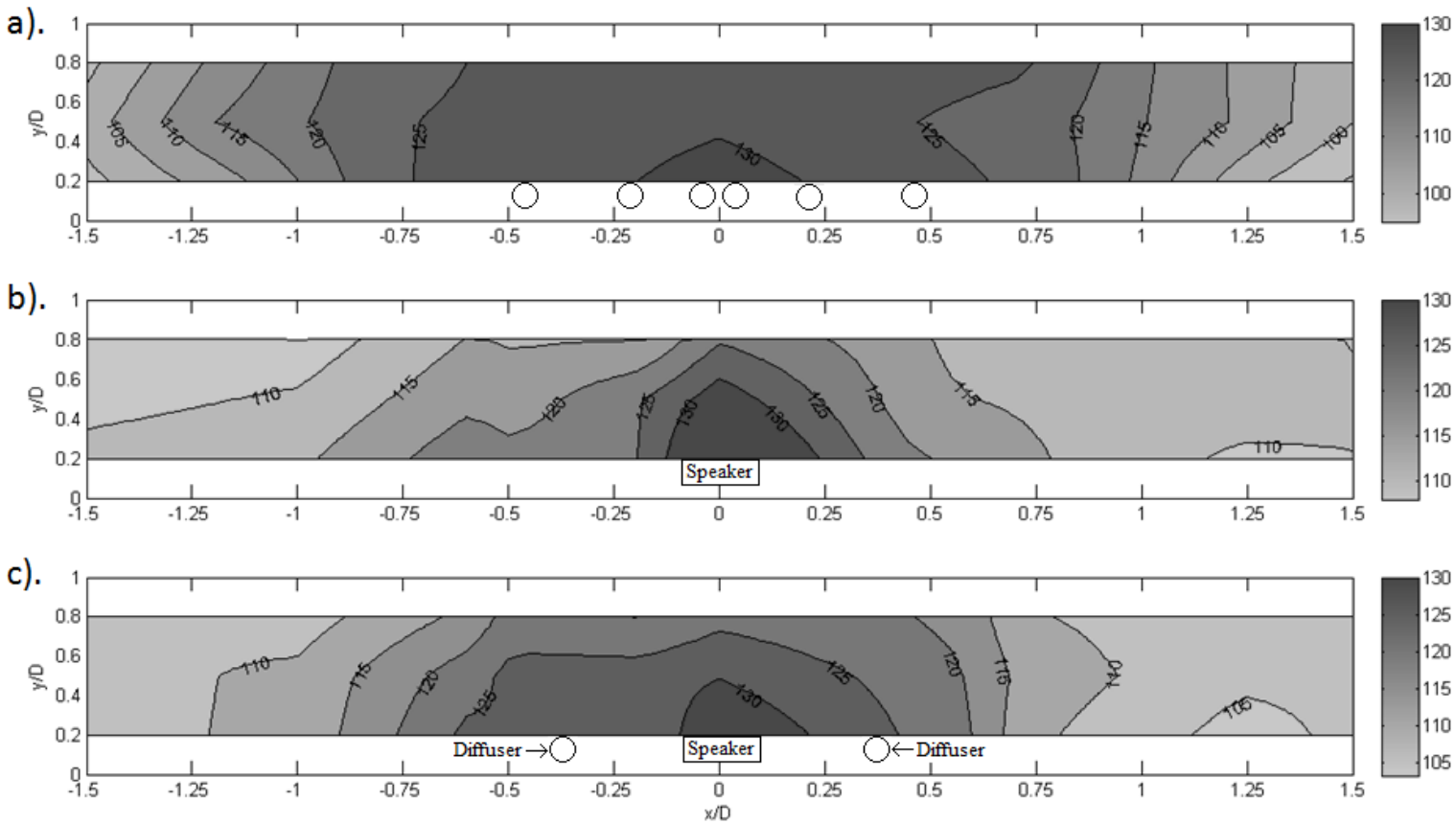

Figure 2-6. Sound Pressure Level (SPL) contours in dB (re 1μPa) at 200 Hz for the a) coarse-bubble, b) speaker array, and c) speaker array/fine-bubble systems in the test channel along a straight line through the center of the bubble curtain (flow is left to right). Axes are normalized by the depth *D*=25cm and the barrier is centered about x/D=0. Approximate locations of speakers and bubble diffusers are shown for each configuration.

4 Discussion

This study demonstrated that common carp exhibit strong behavioral responses to bubble curtains in shallow water. The graded-bubble and coarse-bubble systems produced similar efficacies and reduced 75-85% of the number of crossing attempts made by common carp in the behavioral tank. Behavioral trials including speaker arrays and lighting indicated that sound and hydrodynamic fields influenced common carp movement more than visual cues from the bubble curtains.

Results of the speaker array and speaker array/fine-bubble trials suggest that avoidance behavior near a bubble curtain, is most likely a response to some combination of stimuli (hydrodynamic and acoustic), and not just an individual stimulus or characteristic (e.g. sound amplitude). Although the speaker array exhibited the same maximum sound pressure level of the coarse-bubble system, it did not match the level of passage reduction observed for both the coarse-bubble and speaker array/fine-bubble systems. Interestingly, the inclusion of the fine-bubble curtain to the speaker array resulted in an efficacy similar to that of the bubble curtain systems (upstream 67%, downstream 82%). As expected, the bubble curtains acted as resonant amplifiers which re-oriented the sound pressure gradient in a stream-wise direction, rather than attenuating radially. A more abrupt change in the sound pressure field along with improved efficacy appears to suggest that the transmission of sound through a bubble curtain, providing tactile and auditory stimuli, may play a role in carp avoidance.

Sound, a variable not addressed in earlier bubble curtain studies, appears in part to influence carp deterrence from a bubble curtain. Graded-bubble and coarse-bubble

systems generated sound pressure levels well above the carp hearing threshold, and were sufficiently loud (roughly 30-40dB (ref 1 μPa) above background) to prevent sound masking due to 'cocktail party' effects, a phenomena where the target signal is masked by background sounds (Popper and Carlson, 1998). Although bubble sizes differed between curtain designs, the primary frequency of sound emitted from the bubble curtains remained < 300Hz as result of collective oscillations of bubbles, reduced sound of speed in the bubble-water mixture, and restrictive channel dimensions (Lamarre and Melville, 1994; Nicholas et al., 1994). Although sound is not solely responsible for deterrence behaviors, the sound produced by these bubble curtains was biologically relevant and likely to influence carp passage.

The sound pressure field generated by each bubble curtain was observed to attenuate rapidly (i.e. exhibit a high sound pressure gradient), an important feature for acoustic deterrents because it reduces the risk of fish from acclimating to the sound source. Rapid attenuation observed during the bubble curtain trials was a result of the shallow water 'cutoff phenomena' for low frequency sound, which states that sound at a frequency less than the cutoff frequency (a depth dependent frequency at which sound propagates infinitely ~ 3 kHz for open water at a depth of 25 cm) will decrease exponentially with distance (Urick 1975, Akamatsu et al. 2002). The attenuation rate of sound at 200 Hz for each bubble curtain was ~107 dB/m (ref 1 μPa), in close agreement with the predicted value of 109 dB/m (ref 1 μPa) based on theoretical calculations for shallow water sound attenuation by Akamatsu et al. (2002). On a biologically relevant length scale, carp would not be expected to detect the presence of the bubble curtain via

sound pressure, at the depths investigated, more than two body lengths away because the sound pressure level reduces to background levels within that distance. However, an increase in depth would lower the cut-off frequency and allow sound at lower frequencies to propagate further. Thus, decreasing the sound pressure gradient and potentially decreasing efficacy. Currently, it remains unclear whether acoustic pressure or acoustic particle motion dominates the carp's response to a sound field (Popper and Fay, 2011).

Indeed, our finding of sound and fluid flow stimuli influencing carp movement through a bubble curtain is purely correlative. In order to definitively quantify the role of sound and fluid motion, further paired trials that isolate each stimuli field is needed. The most logical option for reducing/eliminating the influence of tactile stimuli could be accomplished by ablating the lateral line; however, results may be confounded since the role of the lateral line in sensing acoustic particle motion is unknown in carp.

A minimal reduction in efficacy to limit downstream passage (87% to 75%) was observed during the illuminated coarse-bubble trial. Had the bubble curtain acted as a visual deterrent, an increase in efficacy would have been expected for the illuminated case similar to what Mussen and Chech Jr. (2012) observed for lit and unlit fish screen trials. This finding suggests that, at least for common carp, the role of visual cues to deter passage through a bubble curtain is limited.

We have good confidence in our experimental setup due to a consistent activity level and steady control trial passage rate throughout the entire testing period. Here, a stable activity level indicates that decreases in the number of passages were from avoidance of the bubble curtain and not a function of decreased activity.

5 Conclusion

This research represents the first effort to relate bubble curtain characteristics to fish deterrence. Our findings indicate that under laboratory conditions (25 cm deep and low flow), bubble curtains provide a simple and inexpensive, yet effective means to reduce common carp passage up to 80% in the up- and down-stream direction. Although the results of this study may not be fully translatable to field conditions, they do provide important insight on the responses of common carp to bubble curtains. In the future, *in-situ* experiments of these bubble curtains should be performed to determine the efficacy for inhibiting common carp movement under natural conditions. We recommend that improvement of bubble curtains should be based on enhancing hydrodynamic and acoustic cues rather than visual cues.

Chapter 3: Field test of an optimized bubble curtain deterrent system for common carp

A bubble curtain deterrent system was installed in a stream draining a common carp (*Cyprinus carpio*) spawning and nursery habitat to confirm results of an earlier laboratory study, and assess its potential management tool. The bubble curtain blocked 57±12% of downstream swimming carp, versus 80% in the laboratory. In contrast, the bubble curtain blocked less than 20% of upstream swimming common carp. Despite this reduction in performance, field results appear consistent with findings from a laboratory study. This study suggests that the bubble curtain may not be sufficient for management efforts as a cross stream barrier; however, simple improvements (e.g. use as a deflection screen or adding other deterrents) could make it a comparably inexpensive and practical management tool for controlling downstream movement of common carp in shallow, low head systems where reduction of movement, not elimination, is the goal.

1 Introduction

Management strategies for invasive fish often require the use of barriers to reduce movement (Britton et al., 2011, Lodge et al., 2006); however, extent barrier technologies (e.g. electrical barriers or mechanical screens) can be expensive and difficult to maintain. Since resources are often limited for fisheries management activities (Vander Zaden and Olden, 2008), there is a clear need for inexpensive new barrier technologies. Bubble curtain deterrent systems, consisting of a wall of bubbles (e.g. created by forcing air through a perforated pipe) have been suggested as a potential solution (Zielinski et al., 2013; Popper and Carlson, 1998). Bubble curtains are relatively inexpensive compared to other behavioral deterrents (e.g. electrical or sonic barriers), easily maintained, safe, and produce complex acoustic and hydrodynamic stimuli that appear to deter fish movement (Kuznetsov, 1971; Stewart, 1982; Patrick et al, 1985; Welton et al., 1997, Noatch and Suski, 2012; Zielinski et al., in review). Additionally, they can function in low head and shallow water conditions, which most physical/mechanical barriers are ill suited.

Recently, Zielinski et al. (2013) identified two different bubble curtain systems that reduced 75-85% up- and down-stream passage of invasive common carp (*Cyprinus carpio*) in a laboratory test channel, and attributed avoidance to both sound and fluid motion stimuli. These bubble curtains produced sound pressure levels of ~130 dBs (ref. 1 μPa) at peak frequencies between 100-300 Hz, which was critical because common carp have relatively broadband hearing (50-3000Hz) and sensitivity (>65 dB (ref 1μPa)) (Popper, 1972). Although laboratory investigations of bubble curtain and other

behavioral deterrents provide useful insights into the response of fish to such stimuli (Stewart, 1982; Patrick et al., 1985; Sager et al., 1987; Welton et al., 1997; Taylor et al, 2005; Dawson et al., 2006), relatively few studies have successfully observed the same level of deterrence in the field (Liebermann and Muessig, 1978; EPRI, 1998; Ruebush et al, 2012). The primary objective of this study was to field test the bubble curtain developed by Zielinski et al. (2013) in order to validate laboratory results.

We tested a bubble curtain to inhibit movement of common carp, one of the world's most destructive aquatic invasive species (Weber and Brown, 2009; Lowe et al., 2000). First introduced to North America in the late 1870's, common carp, hereafter termed carp, have spread widely and become successful invaders around the world (Lever, 1996). Studies have shown that carp reach especially high densities in regions with abundant unstable (susceptible to hypoxic conditions) habitat that may function as potential nursery areas (Koehn 2004; Bajer and Sorensen, 2010). Bajer and Sorensen (2010) demonstrated that in interconnected systems of lakes in Midwestern North America (Minnesota) carp tend to inhabit stable, deep, normoxic lakes for much of the year but leave them to enter interconnected unstable, shallow lakes to spawn, so the latter areas frequently serve as recruitment 'hotspots'. Limiting the movement of carp between lakes and nursery habitat could drastically reduce recruitment. Extant barrier technologies are not well suited for the low-head conditions typical of interconnecting streams; therefore, bubble curtains could be an inexpensive and effective alternative for these sites, where reduction, not total elimination of fish movement, is the management goal (Zielinski et al, 2013; Popper and Carlson, 1998).

In this study, we conducted a field test of a laboratory optimized bubble curtain system in a stream that drains a common carp spawning and nursery habitat with the objectives of 1) validating laboratory results of Zielinski et al. (2013) under natural conditions; and 2) assessing the potential use of bubble curtains as a carp management tool. For this, a field scale bubble curtain was constructed and installed in a stream in central Minnesota, USA. Carp were captured from local populations both up- and down-stream of the bubble curtain, implanted with Passive Integrated Transponder (PIT) tags, and transplanted into the stream to test the bubble curtain system. A PIT tag interrogation system was installed to monitor carp movement in the stream and calculate efficacy of the bubble curtain system.

2 Materials and Methods

2.1 Study Site

We tested the effectiveness of a bubble curtain deterrent system in Kohlman Creek, Maplewood, MN, approximately 15 km north of St. Paul. (45°01’36”N 93°02’48”W) (Figure 3-1). Kohlman Creek is located in the middle of the Phalen Chain of Lakes which is comprised of eight interconnected lakes (Figure 3-1). The headwater region (upstream of bubble curtain), consisting of Markham Pond, Casey Lake, and Upper Basin/Willow Lake, is carp nursery for the entire system, supporting nearly 30,000+ young of year (YOY) carp in 2010 and prone to experience hypoxic conditions during winter (Osborne, 2012). The main lakes (downstream of bubble curtain) are stable lakes which lack YOY carp, but have high densities of adult carp. Site selection was based on five factors: 1) carp are abundant in the system; 2) Kohlman Creek creates

a natural bottleneck for carp movement in up- and down-stream directions; 3) a downstream water control structure and temporary fish screen facilitate controlled releases of upstream swimming adults; 4) close proximity to power supply for electrical components and room for equipment storage, and; 5) was requested by the watershed manager in an attempt to stop both upstream downstream movement of carp. Our initial plans were to place the bubble curtain at the exit of Markham Pond to reduce the movement of young carp out of the headwater region, a scenario that promoted the laboratory trials in Zielinski et al., (2013). The watershed manager, however, requested the bubble curtain be placed in Kohlman Creek to also stop the upstream migration of adults towards the headwater region for spawning, a scenario not considered in the laboratory testing. During bubble curtain testing, Kohlman Creek was ~10 m wide, maintained a ~0.75 m thalweg depth, and had flow velocities less than 0.5 m/s. A temporary fish screen, installed downstream of the bubble curtain, (Figure 3-2) was used to help collect naturally upstream moving adults in the spring of 2013.

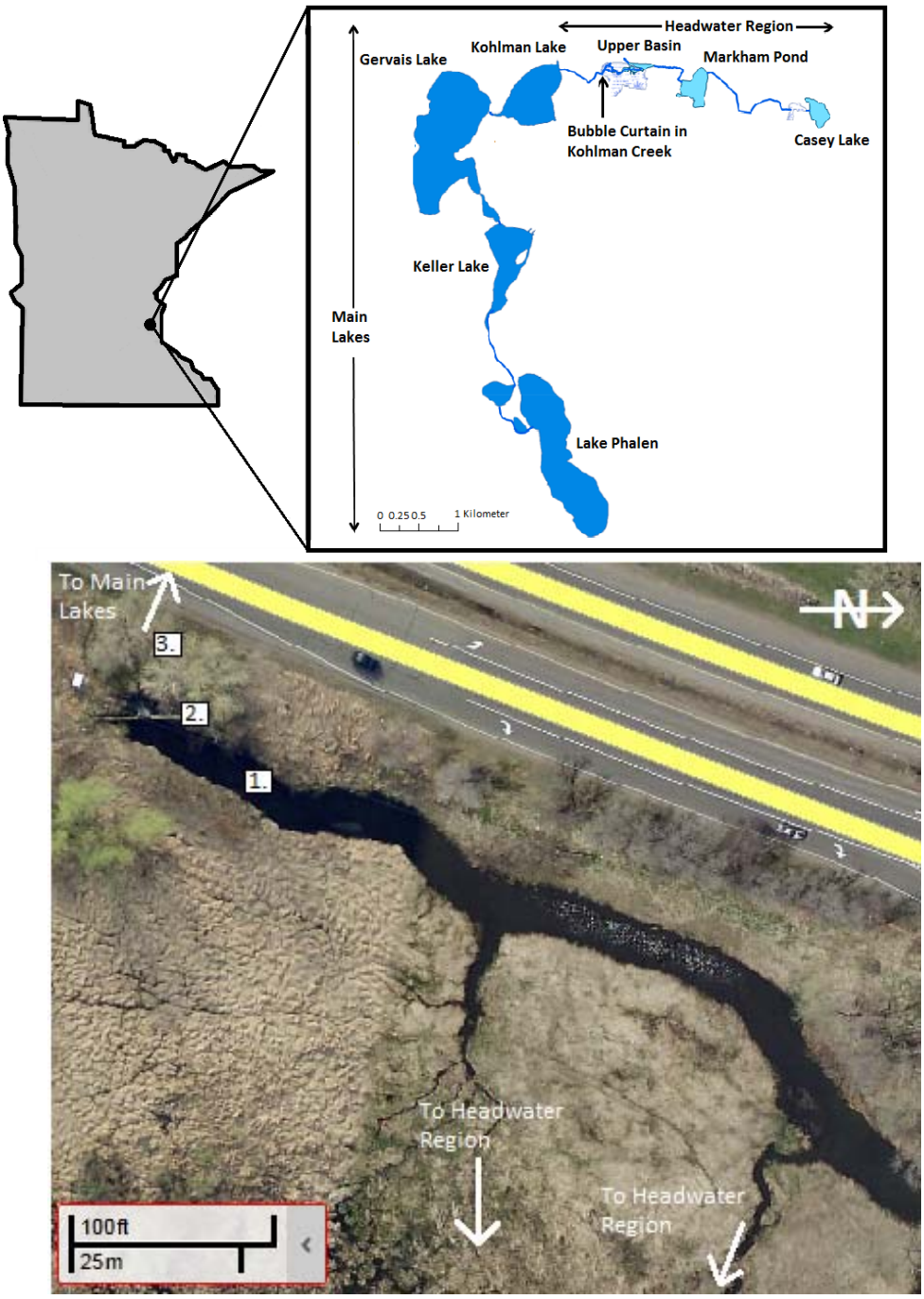

Figure 3-1. Map of the location of the Phalen Chain of Lakes in Minnesota, USA with headwaters and main lakes denoted (top panel) and location of the bubble curtain in Kohlman Creek (bottom panel): (1.) Bubble curtain, (2.) Temporary fish screen, concrete weir, and PIT tag antenna, and (3.) PIT tag antenna attached to culvert under Hwy 61. Photo obtained from Ramsey Count GIS Map Viewer

2.2 Bubble curtain system components

We designed and constructed a 4m long bubble curtain deterrent system, based on the design of the graded-bubble curtain evaluated by Zielinski et al. (2013). Although the coarse-bubble curtain (Zielinski et al., 2013) was the best performing system in the laboratory, it required nearly 4 times as much air as the graded-bubble curtain without a significant difference in performance. Prior to installation of the bubble curtain, the stream bed was armored with geotextile fabric and coarse aggregate to prevent erosion underneath, and three dock structures were constructed as anchors for the bubble curtain (components designed and installed under supervision of Barr Engineering, Minnesota, USA).

The bubble curtain system comprised of six 3.75 cm PVC pipes (Figure 3-2), each perforated with 3 mm diameter holes spaced at 5 cm. Two 10 cm diameter PVC pipes with six 3.75 cm outlets were used as an air-manifold, evenly distributing air to each pipe. System components were fixed on to a four meter long steel frame that was situated at a 45° angle to the flow of Kohlman Creek, submerged, and anchored to the dock structures (Figure 3-2). Regenerative blowers were housed in a custom aluminum shelter on the west bank of Kohlman Creek. Air was routed through two 7.5 cm flexible HDPE pipes down to the bank and attached to each manifold. Two S61 regenerative air-blowers (Aquatic Ecosystems, FL, USA) in series supplied 15 L s^{-1} m^{-1} of air to the barrier at 25 kPa. Space under the support docks was screened off with 1 cm square plastic mesh, preventing fish from bypassing the bubble curtain. Additionally, underneath each dock structure was a custom v-trap (one upstream facing and one

downstream facing) to collect any carp that were deflected parallel to the bubble curtain. The total cost of the bubble curtain systems was ~$20,000 ($5000 for bubble curtain and $15,000 for infrastructure).

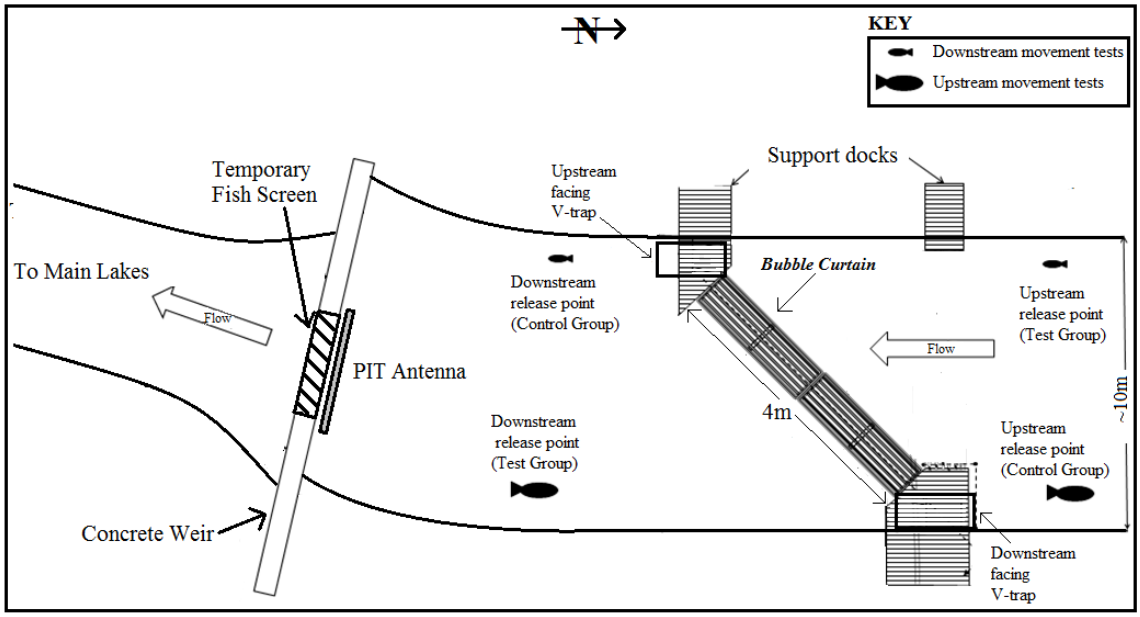

Figure 3-2. Plan view schematic of the bubble curtain system in Kohlman Creek with locations of release points for each movement test (top panel), and photograph of bubble curtain system and dock support structure, looking upstream (bottom panel). Photograph by author.

2.3 PIT tag interrogation system

To help estimate the efficacy of the bubble curtain, we monitored carp movement in Kohlman Creek using a PIT tag interrogation system (OregonRFID, OR, USA). The PIT tag interrogation system was constructed using the Oregon RFID Multi-Antenna HDX reader, powered by 110V electrical service which was converted to 12V DC using a power inverter. Originally, four PIT antennas were to be installed up- and down-stream of the bubble curtain; however, significant interference by overhead power lines prevented the installment of antennas upstream of the bubble curtain. Thus, we were limited to placing PIT antennas at the concrete weir and nearby downstream culvert (Figure 3-1). We could not monitor carp movement upstream of the bubble curtain with the PIT tag system.

The weir antenna consisted of 2 turns, with continuous wire spacing of 9 mm, of 12-gauge threaded wire (1 m x 2.5 m loop), tuned to an inductance of ~50 μH. The culvert antenna consisted of 1 turn, in a figure-eight configuration, of 8-gauge threaded wire (2 x 0.75 m x 2.5 m loops stacked vertically), tuned to an inductance of ~75 μH. Both antennas were connected to tuning modules, which were connected to the PIT reader by twin coaxial cable. Each time a tagged carp passed through an antenna, the time of passage, PIT identification number, and antenna number were logged onto a memory card for analysis. The antennas were spaced approximately 7 m apart. Antenna operation was checked daily during tests.

2.4 Experimental design

In order to calculate the efficacy of the bubble curtain to block carp movement, we conducted two sets of movement tests with carp caught from local populations. The collected fish were individually marked and released in Kohlman Creek where their movements were monitored as they attempted to cross the bubble curtain. Downstream movement tests were carried out August-November 2012 and June-July 2013, while the upstream movement tests were carried out in May 2013 (Table 3-1).

Table 3-1. Date and number of fish released in down- and up-stream movement tests of the bubble curtain in Kohlman Creek. During downstream movement tests the carp placed above the bubble curtain were the test group, while fish placed below were the control group. Conversely, during upstream movement tests the carp placed below the bubble curtain were the test group while fish placed above were the control group.

	Above Bubble Curtain		**Below Bubble Curtain**		
Start Date	**n**	**Total Length (mm, ±SD)**	**n**	**Total Length (mm, ±SD)**	**Source**
Downstream Movement Tests					
		Test Group		*Control Group*	
07/23/2012	7	329±17	6	324±28	Markham Pond
07/26/2012	9	321±13	4	354±54	Casey Lake
08/01/2012	11	347±33	5	322±28	Casey Lake
11/02/2012	10	318±31	5	325±19	Markham Pond
06/10/2013	15	342±19	5	332±8	Markham Pond
08/02/2013	9	339±89	5	352±9	Upper Basin
Total	**61**	**334±41**	**30**	**334±28**	
Upstream Movement Tests					
		Control Group		*Test Group*	
05/15/2013	3	565±68	7	600±44	Kohlman Creek
05/19/2013	3	653±79	7	619±27	Kohlman Creek
05/21/2013	3	611±56	7	669±53	Kohlman Creek
05/30/2013	3	642±17	7	657±48	Kohlman Creek
Total	**12**	**618±62**	**28**	**636±50**	

Similar to the evaluation given by Welton et al. (2003) the efficacy, E, is calculated as

$$E = 100\% \cdot \left(1 - \frac{P_{test}}{P_{control}}\right) \quad (1)$$

where P_{test} is the observed ratio of carp that cross the bubble curtain while ON, and $P_{control}$ is the proportion of carp expected to cross the bubble curtain while OFF.

2.4.1 Downstream movement tests

Downstream movement tests were conducted using carp collected from the headwater region (Markham Pond, Casey Lake, and Upper Basin) that we hypthesized would try to move downstream into the main lakes. Carp were caught by electrofishing and released into Kohlman Creek near the bubble curtain for testing (Table 3-1). All captured fish were measured for length (mm), surgically implanted with a 23 mm PIT tag, and released ~5 m above or below the bubble curtain (Figure 3-2).

For downstream movement tests, P_{test} is the proportion of carp released above the bubble curtain that passed downstream through the bubble curtain while ON, and $P_{control}$ is the proportion of carp released below the bubble curtain that swam downstream un-impeded by the bubble curtain (Figure 3-2). It was assumed that, $P_{control}$ represents the expected ratio of test carp to swim downstream in the absence of a bubble curtain.

Bubble curtain operation was cycled on and off every 24 hrs during the tests. Alternating bubble curtain operation not only allowed for evaluation of bubble curtain performance, but downstream passages while the bubble curtain was OFF provided

further evidence the headwater carp were motivated to move downstream. Each test period continued until all carp move downstream, out of Kohlman creek, but no longer than 4 days (2 cycles of bubble curtain operation). The temporary fish screen was open during all downstream movement tests.

The primary metric for evaluating bubble curtain efficacy to inhibit downstream movement is the PIT tag detections at the antennas downstream of the bubble curtain. Only one antenna is required for these tests since any detection of carp released above the bubble curtain indicates a crossing. As a result, the culvert antenna was used only as a back-up to the concrete weir antenna. In order to account for potential PIT tag rejection, fatality, predation from birds, or missed antenna detection, only carp detected by the PIT antennas are used in the evaluation of bubble curtain performance.

2.4.2 Upstream movement tests

Upstream movement tests were conducted using carp collected from Kohlman Creek, immediately downstream of the temporary fish screen. Collection and testing of these fish only occurred at times when natural upstream migration occurred, thus ensuring carp were motivated to challenge the bubble curtain. Fish were trapped between the temporary fish screen and a custom net and caught by electrofishing, then transplanted further upstream in Kohlman Creek for testing. These carp were typically captured along with 20-100 additional carp trying to move upstream at the temporary screen. All fish captured for testing were measured for length (mm), implanted with a 23 mm PIT tag, marked with reflective ribbon tied to the anterior spine of the dorsal fin (control and test fish received different colors) for visual monitoring, and released ~5 m

up- and down-stream of the bubble curtain (Figure 3-2). Based on age-length relationships, the carp used in upstream testing, larger than 550 mm TL, were age-2+. These carp were also examined to identify sex and maturational condition by gently squeezing the fish. In total, 18 males and 22 females were selected for testing the bubble curtain against upstream movement. These tests only lasted 24 hrs because all fish were observed either crossing the bubble curtain or leaving the stream entirely before 24 hrs elapsed.

For upstream movement tests, P_{test} was the proportion of carp released below the bubble curtain that passed upstream through the bubble curtain while ON, and $P_{control}$ is the proportion of carp released above the bubble curtain and moved more than 15 m upstream un-impeded by the bubble curtain (Figure 3-2). Again, it was assumed that $P_{control}$ represented the expected ratio of test carp to swim upstream in the absence of a bubble curtain.

Since PIT antennas could not be installed upstream of the bubble curtain, we had to rely on visual monitoring to track carp movement. The locations of marked carp were visually monitored by an observer that walked the entire length of Kohlman Creek (~130 m) twice every 3 hrs after the start of each test, during daylight hours. In addition to visual monitoring, any downstream movement (i.e. carp returning to the main lakes) was monitored by the PIT antennas. In the event of lost ribbon or PIT tag loss/fatality, only fish observed in the stream or detected by the PIT antennas was included in the evaluation of the bubble curtain performance.

2.5 *Statistical Analysis*

A statistical test for assessing whether the proportion of carp passing through the bubble curtain is different than the proportion expected to pass without the bubble curtain is given by the test statistic *z* with Yates continuity correction (Fleiss et al., 2003).

$$z = \frac{\left(P_{control} - P_{test} - 0.5m\right)}{\sqrt{mP\left(1-P\right)}} \tag{2}$$

where $m = \left(1/n_{test} + 1/n_{control}\right)$ and $P = \left(n_{test}P_{test} + n_{control}P_{control}\right)/N$. Here, n_{test} and $n_{control}$ are the total sample size of carp used to test the bubble curtain and controls, and $N = n_{test} + n_{control}$. In this way, *z* is referred to the normal standard distribution which is equivalent to the one-sided test version of a standard 2x2 contingency table Chi-squared test (Fleiss et al., 2003). When the Chi-squared test suggested significance (P<0.05), a Mantel-Haenzel Chi-squared test, χ^2_{assoc}, for significance of the overall degree of association was performed to ensure that bubble curtain performance was constant over each time.

3 Results

3.1 *Downstream movement tests*

During tests in 2012 and 2013, 84% (51 of 61) of PIT tagged carp passed downstream during the downstream movement tests. In total, 17 of 51 ($P_{test} = 0.33$) carp from the test group (placed above the bubble curtain) swam downstream through the bubble curtain while ON. In contrast, 20 of 25 ($P_{control} = 0.77$) carp from the control group (placed below the bubble curtain) swam downstream into the main lakes. The

efficacy (percentage decrease in expected passage) of the bubble curtain to block downstream movement of common carp in Kohlman Creek is 57±12% (±SE) (P<0.001) (Table 3-2). Efficacy of the bubble curtain was consistent across each test period (Mantel-Haenzel Chi-squared, $\chi^2_{assoc} = 10.6$, P<0.001).

Carp from the control and test groups typically did not pass downstream until after dark (Figure 3-3); however, one test carp did cross the bubble curtain within two hours of the test start (~1400 hrs). Within the first 24 hrs, 57% (n=15) of the control group carp swam downstream, while only 25% (n=13) of the test group swam downstream through the bubble curtain. No carp were collected in the upstream facing v-trap during the downstream movement tests.

Table 3-2. Efficacies of the bubble curtain system during up- and down-stream movement tests. P_{test} is the proportion of the test group that crossed the bubble curtain while ON, while $P_{control}$ is the proportion of the control group that is expected to cross in the absence of the bubble curtain. The test statistic, *z*, is for assessing whether the proportion of carp passing through the bubble curtain P_{test} is different than the proportion expected to pass without the bubble curtain $P_{control}$.

Movement Test	While the bubble curtain is ON, Number of carp (out of total) swimming		Proportions	Efficacy (%)	*Z*
	Downstream	Upstream			
Downstream Movement Test					
Test Group(n_{test})	17(51)		P_{test} =0.33	57	3.62*
Control Group ($n_{control}$)	20(26)		$P_{control}$ =0.77		
Upstream Movement Test					
Test Group (n_{test})		14(19)	P_{test} =0.74	16	0.28
Control Group ($n_{control}$)		7(8)	$P_{control}$ =0.88		

* Denotes P<0.001

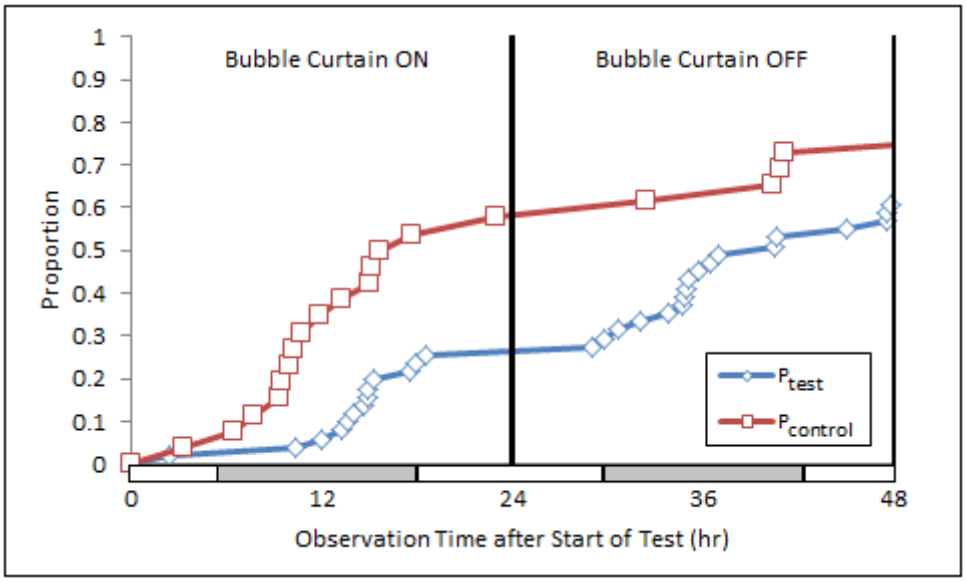

Figure 3-3. Proportion of test and control carp that swam downstream over one cycle of bubble curtain operation. The start time for the downstream movement tests was approximately 14:00 hr. Dark and light bars at the bottom indicated night and day.

3.2 Upstream movement tests

During the upstream movement tests 35 of 40 carp were visually observed passing upstream or detected by the PIT tag system passing downstream. Additionally, the test on 05/19/2013 was terminated after 4 hrs due to severe flooding in Kohlman Creek that prevented visual observations. In total, 14 of 23 ($P_{test} = 0.74$) carp from the test group (placed below the bubble curtain) swam upstream through the bubble curtain while ON. Similarly, 7 of 8 ($P_{control} = 0.88$) carp from the control group (placed above the bubble curtain) swam upstream towards the headwater region. The control carp were generally observed in small tributaries approximately 50 to 75 m upstream of the release point (Figure 3-1). Bubble curtain efficacy for blocking upstream movement of carp is

16±11% (P > 0.05) (Table 3-2). The significance of association test was not preformed because upstream tests did not reveal any significant level of blockage over 24 hrs. Although the bubble curtain was unable to ultimately block upstream movement of common carp, the bubble curtain did delay more than 50% of adult carp upstream passage by 6 hrs (Figure 3-4). Only one carp was collected in the downstream facing v-trap during the upstream movement tests.

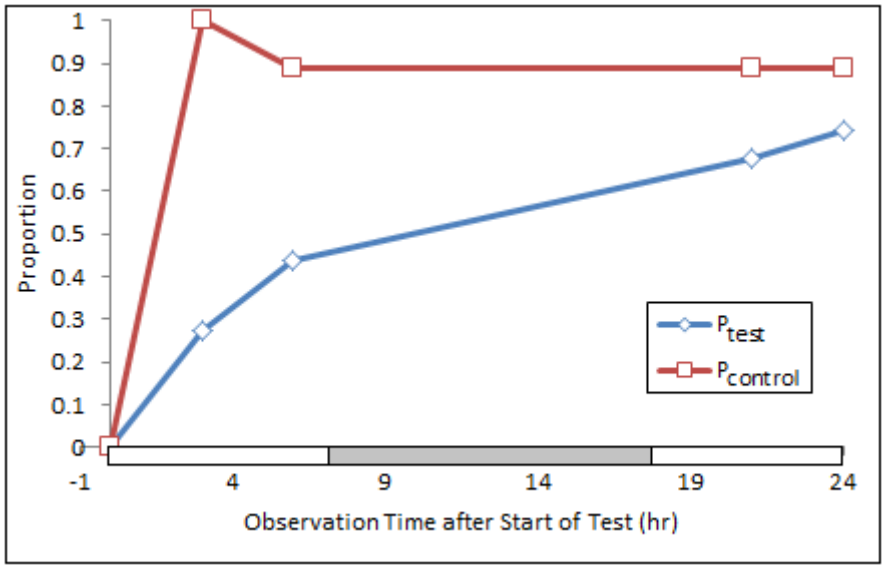

Figure 3-4. Proportion fish from test and control groups to swim upstream towards the headwaters region over the 24hr test period. The bubble curtain was ON throughout each test. The start time for the upstream movement tests was approximately 12:00 hr. Dark and light bars at the bottom indicated night and day.

4 Discussion

This study found a bubble curtain reduced downstream movement of common carp in the field by 57±12%. Although our finding was less than the 75-80% efficacy reported from laboratory studies (Zielinski et al., 2013), the field test results were consistent with laboratory observations in that a significant portion of the test group were deterred by the bubble curtain. Different conditions/procedures at the field site and

laboratory experimental set-up may have contributed to the apparent difference. In Kohlman Creek, any downstream swimming carp deterred by the bubble curtain were unable to return to the headwaters region because a sheet pile weir, located 200 m upstream of the bubble curtain, and prevented fish passage out of Kohlman Creek under normal flows. Such a restriction could artificially decrease efficacy by increasing the number of times carp challenge and subsequently cross the bubble curtain. Additionally, the efficacy reported in Zielinski et al. (2013) may have been artificially elevated because efficacy was measured to be a reducing in crossing, not percentage of fish blocked as reported in this study. Overall, the field study offers some confidence towards obtaining tractable results in future laboratory investigations of alternative deterrent systems following the protocol used by Zielinski et al., (2013).

In contrast, results of upstream movement tests revealed that the bubble curtain had negligible impact (efficacy < 20%) on stopping upstream migrating carp. In fact, the bubble curtain only delayed upstream passage by 6hrs for half the test carp. The carp used for upstream movement tests were approximately twice as large as those tested in the laboratory (Zielinski et al., 2013) and downstream movement tests and due to spawning pressure, highly motivated to swim upstream. Although we expected a decreased blockage rate during upstream movement tests, the results suggest that the bubble curtain is not effective against carp migrating upstream for spawning. In general, carp placed above the bubble curtain (control group) were observed far upstream (> 100 m), near the sheet pile weir, within 1-2 hrs after the test started; while carp placed below the bubble curtain (test group) remained downstream or returned to the main lakes. Over

the first two fish observations (at 3 and 6 hrs) several upstream passage attempts from test carp were observed being repelled at the bubble curtain. Additionally, two test carp were observed jumping over the bubble curtain to pass upstream. Albeit anecdotal, these observations combined with delay of movement suggests that highly motivated and mobile carp are somewhat deterred by bubble curtains.

The bubble curtain was operated on a 24 hr cycle throughout the testing periods without any major problems. Although severe flooding in June 2013 prematurely ended the second upstream test (i.e. water depth and turbidity made visual observations impossible), the integrity of the bubble curtain did not appear to be compromised during high water events or by debris; in fact several observed passage attempts of upstream swimming carp were repelled at the bubble curtain during high water. In contrast, the downstream temporary fish screen required regular cleaning or removal to prevent additional flooding. The effort required for routine maintenance of the downstream fish screen emphasizes the desirability of deterrent systems that are unaffected by debris and flood flows.

Our findings suggest that the optimized bubble curtain is not yet sufficient for widespread use in fisheries management; however, a minimal increase in efficacy of 10-15% may make it an attractive option to stop downstream movement. One potential solution is to change the orientation of the bubble curtain to provide fish an escape route away from the deterrent, reducing the chance for repeated crossing attempts. For this reason, most behavioral deterrents are used as deflection screens, not a cross-stream barrier (Perry et al., 2012; Taylor et al., 2005; Welton et al., 2002). Another way to

increase the efficacy may be to integrate other cost effective deterrents like strobe lights. Indeed, the low cost and reliable operation preserves the position of bubble curtain as a potential management tool provided suitable improvements are found.

5 Conclusion

This study demonstrated that a laboratory optimized bubble curtain blocks 57±12% of downstream swimming common carp in a shallow stream, which was less than the reported value of 75-80% from laboratory studies. Additionally, the bubble curtain did not stop upstream movement of migrating carp (efficacy < 20%). Although the reported efficacy may be insufficient for management efforts now, simple modifications like repositioning or additional deterrent stimuli to improve efficacy by 10-15% may make bubble curtains a realistic management tool for sites where reduction, not total elimination, of movement is the goal.

Chapter 4: Mathematical evaluation of behavioral deterrent systems to disrupt fish movement

D.P. Zielinski, M. Hondzo, V.R. Voller. Mathematical evaluation of behavioral deterrent systems to disrupt fish movement. Submitted to *Ecological Modeling*, June 18, 2013.

Although behavioral deterrent systems, directed at exploiting fish sensory systems, are common place in fisheries management, little is understood about the link between imposed sensory signals (e.g., sound intensity) and the resulting fish movements. Here, an advection-diffusion equation, incorporating a stimuli specific repulsive flux, is coupled with calculation of the generated stimulus field in order to model fish movement near a behavioral deterrent system. A stability analysis of this model is then used to determine the effectiveness of a deterrent stimulus to disrupt the natural movement of fish. Results of laboratory experiments of a bubble curtain to inhibit common carp, *Cyprinus carpio* L., movement are used to develop the model and verify stability analysis predictions. This experimental data demonstrates that the acoustic stimulus (sound pressure levels) produced by bubble curtain systems can be sufficient to disrupt the natural movement of carp, i.e. inhibit fish passage. In addition, it is shown that the stability analysis can identify the minimum sound pressure level from an alternative bubble/acoustic deterrent system required to inhibit fish movement. This coupling of a movement model and stability analysis could find general application in the assessment of behavioral deterrent systems, in particular at field sites where long term physical testing may be impractical.

1 Introduction

Recent progress in fish guidance technologies has focused on the development of behavioral deterrent systems, which utilize stimuli such as sound, light, electricity, turbulence, or combination thereof to guide fish movement in taxon-specific manners (Noatch and Suski, 2012, Lavis et al., 2003). Examples include devices designed to inhibit or block the spread of invasive fish (Ruebush et al., 2012; Conover et al., 2007; Taylor et al., 2005; Stokstad, 2003; Verrill and Berry, 1995) or divert migrating fish to safer routes (Perry et al., 2012; Welton et al., 2002; Taft, 2000; Michaud and Taft, 2000; Welton et al., 1997). These systems differ from alternative mechanical or physical barriers by not obstructing water flow (Noatch and Suski, 2012). Realizing this benefit, however, requires a sufficient understanding of how fish react to individual deterrent stimuli used in available technologies. Although a number of studies have observed fish avoidance to a variety of stimuli (see review by Noatch and Suski, 2012), there are relatively few studies that attempt to model how fish movements are altered by such systems (Lemansson et al., 2008; Goodwin et al., 2006). Furthermore, the potential impact on fish movement outside of targeted species or under varying environmental conditions is not well understood. Thus, improvement and expansion of the design of behavioral deterrent systems requires an understanding of not only what factors influence movement, but how movements are impacted. To address this shortfall the aim here is to develop an advection-diffusion-reaction model to describe fish movement within the stimulus field created by a behavioral deterrent system. The utility of this model will be enhanced by employing a stability analysis aimed to predict the required level of the

stimulus (e.g., sound pressure) that will disrupt the natural movement of fish and make the system effective.

Mathematical models of organism movement are often based on diffusion theory (Codling et al., 2008; Okubo and Levin, 2001; Holmes et al. 1994; Skellam, 1951), where each individual's movement is assumed to follow Brownian motion. Although rudimentary in detail, diffusion models provide a clear framework for understanding more complex behaviors. The classic diffusion model in a homogenous population is a continuum approximation of simple isotropic random walks (Codling et al., 2008), where the area spread of individuals is linear in time. This simple model can be extended to account for a biased drift motion with the addition of an advective component. The resulting advection-diffusion model is a continuum approximation of a biased random walk, where a directional bias is introduced at the individual level or by external field such as a flow current direction (Codling et al., 2010; Codling et al., 2008). Advection-diffusion models of this nature have been used to describe the spatial distribution of numerous fish species (Skalski and Gilliam, 2003; Sparrevohn et al., 2002; Sibert et al., 1999; Zabel et al., 1997), and constitute a natural basis for a continuum description of fish movement near fish guidance systems.

The impact of behavioral deterrent systems on fish movement requires that an aversive stimulus is produced (Noatch and Suski, 2012; Popper and Carlson, 1998) which can be exploited to block or merely direct fish away from targeted areas. The measure of how effective a stimulus is at causing an avoidance response relies upon the sensitivity of the corresponding sensory system and magnitude and gradient of the generated stimulus

field. In this model, the advection-diffusion equation is modified to include a repulsive (or negative taxis) function in order to capture the behavioral response to the gradient of the stimulus. The resulting model for fish movement is the well studied advection-diffusion-reaction (ADR) equation, where the reaction term describes the avoidance response to a deterrent stimulus. In systems where individuals undergo diffusion and reaction behaviors, "diffusion-induced instability" can arise. We hypothesize that instabilities in the governing ADR are indicative of a disruption in fish movement, resulting in a successful deterrent system. In this study, a stability analysis is used to predict what conditions are necessary for a behavioral deterrent system to inhibit fish movement.

Modeling work is supported by observations of a laboratory trial investigating the behavior of common carp, *Cyprinus Carpio* L., in the vicinity of bubble curtains, created by forcing air through perforated pipes arranged on the stream bed. The acoustic field is thought to be an important deterrent stimulus in such systems (Zielinski et al., 2013; Zielinski, 2011; Kuznetsov, 1971). Sound is generated as the bubbles detach from the perforations and are re-transmitted by the bubble curtain, creating a distinct wall of bubbles and rapidly attenuated sound. Since the sound pressure fields generated by bubble curtains can be readily measured and—in shallow water—readily described using a waveguide model (Akamatsu et al. 2002), a phonotaxic repulsion term can be constructed. Here a system of equations is formed by coupling the ADR with the equation for sound propagation. The resulting model could have worthwhile applications beyond deterrent systems for common carp. Similar bubble curtain and acoustic

deterrent systems have also shown promise in stopping the spread of the invasive bighead carp, *Hypophthalmichthys nobilis* R, (Ruebush et al, 2012; Taylor et al., 2005) and directing Atlantic salmon, *Salmo salar* L., smolt migration (Welton et al., 2002), areas of study where predictive models are crucial for management decisions. Expanding beyond fish guidance technologies, development of a fish movement model with phonotaxic response may be useful in studies of larval reef fish attraction, whose orientation is thought to be influenced by reef sounds (Staaterman et al., 2012; Simpson et al., 2005; Codling et al., 2004).

This paper is laid out as follows. First, results of a laboratory investigation on common carp movement near three different bubble curtains and statistical analysis of their movement are presented. The following section derives an advection-diffusion-reaction model to predict fish movement in the vicinity of a bubble curtain. Next, the governing equation for the sound field is introduced. It is then demonstrated how a stability analysis can be used to identify the intensity of stimulus (sound pressure level) required for an effective deterrent system. Results of the laboratory trial are used to assess the findings of the stability analysis. A demonstration of model flexibility is also provided by using the stability analysis to back-calculate the sound pressure level produced by an effective, commercially available acoustic deterrent system. The work concludes with a discussion on how environmental and biological variations may impact bubble curtain effectiveness. Ultimately, this paper provides a description of fish movement near a behavioral deterrent system that can be used as a building block for developing large scale models in which larger temporal and spatial scale impacts of

behavioral deterrent systems can be investigated, or in streamlining the design of physical trials.

2 Materials and Methods

2.1 Experimental set-up and animals

The responses of common carp, *Cyprinus carpio* L. (hereafter termed carp), to three separate bubble curtains systems were monitored as described in Zielinski et al. (2013) and Zielinski (2011). Experiments took place in a circular tank with an insert which created a circular test channel (inner diameter 1.0 m, outer diameter 3.0 m) with a water depth of 25 cm (Figure 4-1). Continuously supplied well water, maintained at 20°C, provided a background water flow of 5 cm/s. Trials were conducted over night with fish movements recorded during a 7h period. For each trial, three carp were placed in the tank, and allowed to acclimate for 10 min before the trial began. A set of control trials (no bubbles) with a total sample size of N=24 were performed along with three sets of bubble curtain trials. Carp were exposed to a fine-bubble (N=7), graded-bubble (N=8), and coarse-bubble (N=7) curtain system, each incrementally more robust than the prior (e.g. greater air-flow rate, curtain thickness, and sound pressure level) (Table 4-1).

Table 4-1. Description of three bubble curtains investigated by Zielinski et al. (2013) to inhibit common carp movement in a laboratory channel and the maximum sound pressure at 200 Hz.

Name	Description	Maximum Sound Pressure Level (Pa)
Fine-bubble	Two 2.5 cm dia. porous polyethylene pipes (~25 micron pores) spaced 30cm apart.	1.0
Graded-bubble	Six 2.5 cm diameter pipes (one porous polyethylene pipe, four PVC pipes with 1 mm dia. holes spaced at 1 cm, and one PVC pipe with 3 mm dia. holes spaced at 5 cm), with a total thickness of 50 cm.	3.2
Coarse-bubble	Grid layout of 2.5 cm diameter PVC pipes with 3mm holes spaced at 5 cm over the entire surface, with a total thickness of 50 cm.	5.1

2.2 Data Collection

Carp movements were monitored by a Passive Integrated Transponder (PIT) tag system (www.oregonrfid.com), consisting of four antennae placed at quarter points around the channel (Figure 4-1). The PIT antennas marked detections when a focal fish passed through, but no data was obtained regarding the channel-width position or depth. Position data were converted to displacement distances, *x,* by adding or subtracting the centerline distance between antennae, ~1.57 m, in accordance with the direction of passage (e.g., upstream is negative, downstream is positive). For each test, one PIT-tagged carp and two non-tagged carp were placed in the channel because the PIT system can only detect one tag at a time. Two non-tagged carp were included to reduce stress in the focal fish and promote natural behavior in the test channel, but only the movement of the focal fish was monitored.

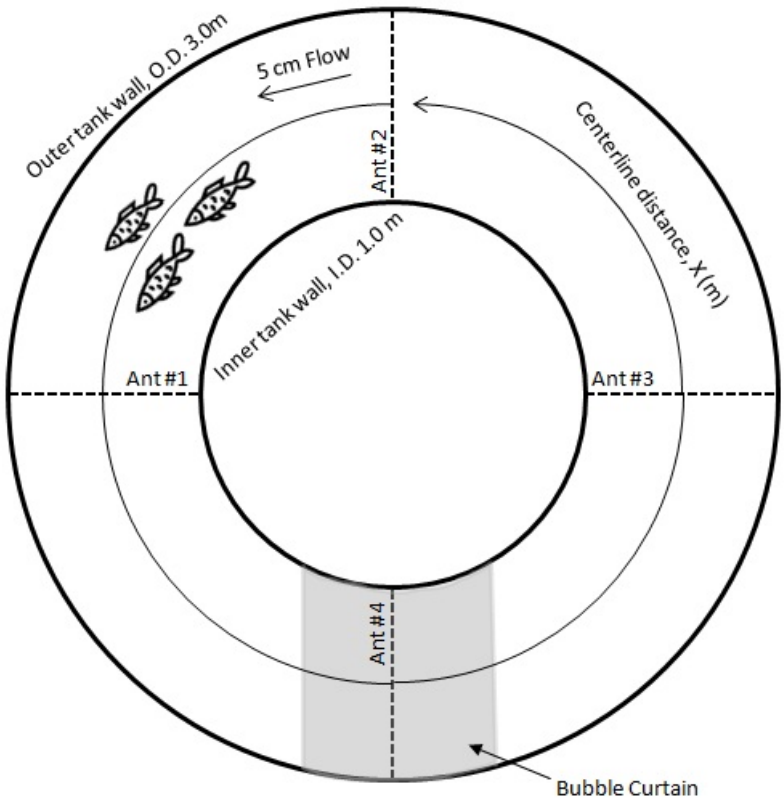

Figure 4-1. Plan view schematic of test channel, bubble curtain location, and PIT tag antennas (Ant #1-4). The distance between antennae is 1.57 m. Note positive movement is in the downstream direction.

2.3 Movement Analysis

The spatial spread of carp during control and bubble curtain trials was analyzed through time. This analysis assumed the entire ensemble of carp are released simultaneously from a single point and allowed to spread as independent, non-interacting individuals. The mean drift position, $E(x)$, of the ensemble was calculated in the following manner (Codling et al., 2008)

$$E(x) = \int_{-\infty}^{\infty} xN(x,t)dx \qquad (1)$$

where $N(x,t)$ denotes the density of carp through space *x*, and time *t*. Upon plotting the mean drift position, the slope of the line was used to estimate the drift, or advection coefficient, μ. Similarly, the variance about the mean drift position was calculated using (Codling et al., 2010; Codling et al., 2008)

$$Var = E(x^2) - E(x)^2 \tag{2}$$

where $E(x^2)$ is the mean square displacement about the origin. In a normal diffusive process, variance grows linearly in time following the standard relationship of

$$Var \sim 2Dt \tag{3}$$

where D is the diffusion coefficient.

Movement of carp between tests was assumed to be independent; however, within each test, three carp were able to interact. Presently, no assessment of social interaction within each test can be made. A test similar to that suggested by Bode et al. (2012), however, could be performed to assess what level of social interaction is present in a carp aggregation. A strong social group may subsequently act to reduce the spatial distribution of the carp, whereas weak social interactions may lead to greater spread.

2.3.1 Spatial spread of carp during control trials

Carp exhibited a downstream bias during the control trials (Figure 4-2a). The displacement of the majority of individuals fit within in a finite range of displacement distances; however, one individual followed a nearly ballistic trajectory, travelling more than 3 times farther than any other carp. The variance of the entire ensemble movements increased with time as $\sim t^{1.99}$ (Figure 4-2). A power-law relationship does not fit the

trend predicted by normal diffusion (i.e., spread increases linearly in time), suggesting carp may exhibit anomalous behaviors. In this case, organisms are thought to spread faster than what is expected in normal diffusion (i.e. super-diffusion) (Viswanathan et al., 2011). However, if the highly mobile individual is removed from the ensemble, the resulting variance increases linearly with time (Figure 4-2b). A linear regression of the variance of ensemble movements, without the highly mobile individual, can explain 99% of observed behavior. Hence, a model assuming normal diffusive behavior is sufficient to describe natural movement of carp in the test channel, consistent with other diffusion based models developed for fish movements (Sparrevohn et al., 2002; Skalski and Gilliam, 2000; Zabel et al., 1997). Further investigation into anomalous behavior possibly presented by the carp movements falls outside the scope of this paper (see Viswanathan et al. (2011) and Edwards (2011) for full discussion, and see Appendix C for step-size analysis of carp movements for evidence of power-law decaying tails).

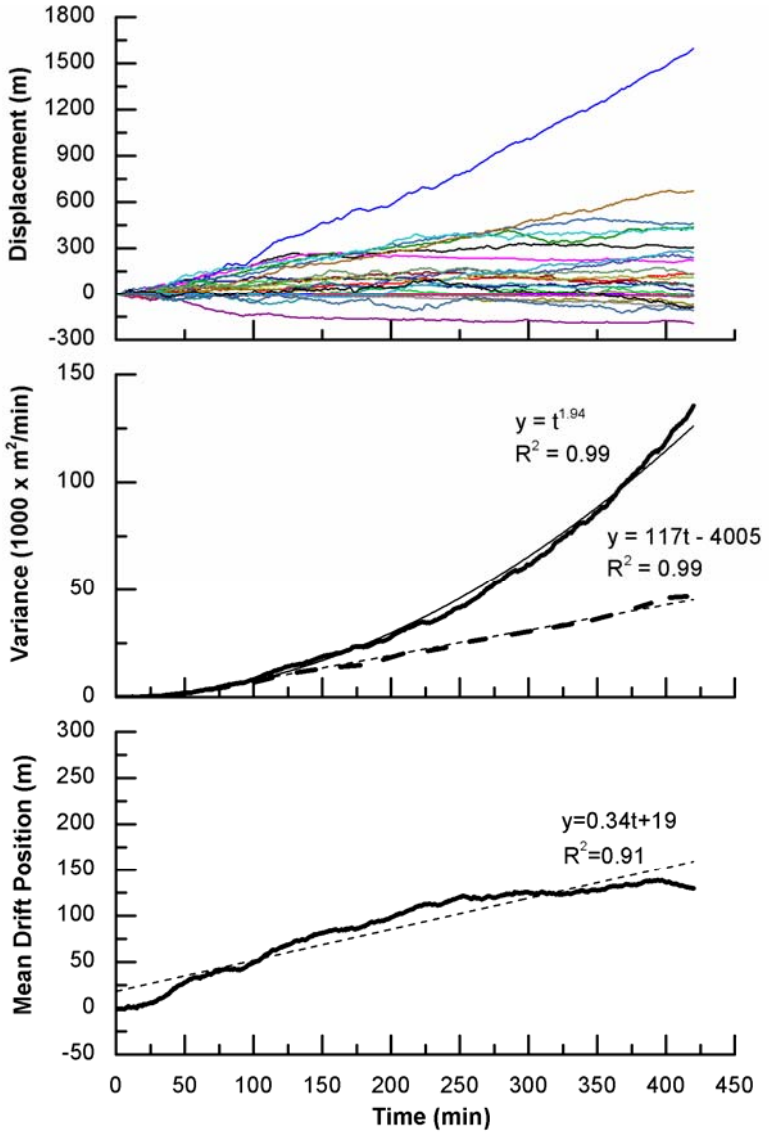

Figure 4-2. Analysis of carp ensemble movements during control trials (N=24) consisting of net displacement of individuals, variance about the mean drift position (with (—) and without (--) the highly mobile individual), and mean drift position (without highly mobile individual). Note a positive displacement denotes a downstream movement and negative denotes upstream movement.

3 Model

3.1 Model Description

Once insight into the natural carp movement (no bubble curtain) in the test channel was gained, a mathematical model to describe carp movement in the vicinity of the bubble curtain was constructed. The model consists of one equation to describe fish movement in a stimulus field and another to describe the stimulus field.

3.1.1 Modeling Fish Movement

Based on the findings of the spatial spread of carp during control trials, a standard advection-diffusion model was used to describe the undeterred, or natural, movement of carp. Assuming the individual carp form a non-interacting ensemble (e.g. individuals move independently), movement can be approximated by a biased Brownian motion that satisfies the following partial differential equation:

$$\frac{\partial N}{\partial t} = -\frac{\partial}{\partial x}\left(q_{AD}\right) \tag{4}$$

Here the flux of carp in the x-direction is given by

$$q_{AD} = \mu N - D\frac{\partial N}{\partial x} \tag{5}$$

For a hypothetical instantaneous release of individuals, N_o, from a single point, the fundamental solution of Eq. (4) and (5) is the normal distribution, with a mean shifted to $x = \mu t$ and variance $2Dt$

$$N(x,t) = \frac{N_o}{2\sqrt{\pi Dt}} \exp\left(\frac{-(x-\mu t)^2}{4Dt} \right) \tag{6}$$

The advection term, μ , represents individually initiated movement in response to fluid flow (e.g. positive rheotaxis observed in Figure 4-2). For simplicity, both advection and diffusion coefficients were assumed to be spatially independent.

The critical component of modeling fish interaction with a deterrent stimulus is capturing the avoidance response and subsequent impact on movement patterns. Effectiveness of a deterrent system depends on the magnitude and gradient of the stimulus field as well as the sensitivity of corresponding sensory systems. For example, sharp gradients are preferred because fish may acclimate to a gradually varying stimulus, thus reducing any level of deterrence. In the case of bubble curtains, the acoustic field is thought to be an influential stimulus for interrupting movement of carp (Zielinski, 2011; Zielinski et al., 2013) due to the intensity of the sound generated by the bubble curtain and increased sensitivity to sound exhibited by carp. Here, carp avoidance appears to be a result of phonotaxis, or acoustically directed motion. Mathematically, a phonotaxic repulsion term can be developed in a similar fashion to classical chemotaxis models (Hillen and Painter, 2009) where an organism's tendency to move towards or away from a stimuli source follows the stimulus gradient. Assuming that the flux of fish will increase with the number of fish *N(x,t)* present, we can take the phonotaxic flux, q_p ,to be

$$q_p = -\omega N \frac{\partial P}{\partial x} \tag{7}$$

where ω, is the acoustic attraction/repulsion rate, Pa m^{-1} min^{-1}, which is a measure of the tendency to move towards or away from a sound source, and *P(x,t)* is the sound pressure through space *x* and time *t*. When the repulsion rate is combined with the sound pressure gradient, the resultant term is akin to a repulsive velocity term.

As Eq. (7) represents a phonotaxic flux similar to diffusive and advective flux of Eq. (5), the two can be combined to generate a total flux term:

$$q_{total} = q_{AD} + q_p \tag{8}$$

Thus a basic advection-diffusion-reaction equation to model fish movement in the vicinity of a bubble curtain is generated by substituting Eq. (8) into Eq. (4):

$$\frac{\partial N}{\partial t} = -\mu \frac{\partial N}{\partial x} + D \frac{\partial^2 N}{\partial x^2} + \omega N \frac{\partial^2 P}{\partial x^2} + \omega \frac{\partial N}{\partial x} \frac{\partial P}{\partial x} \tag{9}$$

3.1.2 Modeling the Sound Field

In order to evaluate the Eq. (9) for carp movement in the vicinity of a bubble curtain, the corresponding sound field must be described. The acoustic wave equation for one-dimension is given as:

$$\frac{\partial^2 P}{\partial x^2} = \frac{1}{c^2} \frac{\partial^2 P}{\partial t^2} \tag{10}$$

where c is the speed of sound (1500m/s). Assuming a pressure-release boundary condition exists, the solution to Eq. (10) can be written as a linear combination of sinusoidal waves (Akamatsu et al., 2002). However, simplifications to Eq. (10) can be made since the trials occurred in shallow water, and the target sound pressure component occurs at a low frequency. First, the bubble curtains generate sound at a peak frequency

below the resonant (or cutoff) frequency *f* of the tank as determined by Akamatsu et al. (2002):

$$f_{cutoff} = \frac{c}{2h} \tag{11}$$

where h is the water depth. Following the shallow water "cutoff phenomena", the low frequency components of the sound wave attenuate exponentially. Therefore, the only acoustical mode that can survive is the smallest mode, resulting in the simplified solution to Eq. (10)

$$P = P_o 10^{-\left(\frac{1-x}{L}\right)} \exp(-i2\pi ft) \tag{12}$$

where P_o is the source level of sound produced by the bubble curtain at $x = 0$, and L is the theoretical attenuation length – distance at which the sound pressure level decays by 20 dB – for a shallow-water system (Akamatsu et al., 2002)

$$L(f) = \frac{550}{f_{cutoff} \times \sqrt{1 - \left(\frac{f}{f_{cutoff}}\right)^2}} \tag{13}$$

Detailed measurement of the sound pressure field in the test channel during each bubble curtain trial was used to validate the waveguide model in Eq. (12). Sound pressure measurements were obtained using a miniature BK 8103 hydrophone (Bruel & Kjær, Demark) and processed using customized LabVIEW (National Instruments, TX, USA) and Matlab (Mathworks, MA, USA) programs. Measurements were taken at depths of 5, 12.5, and 20 cm below the water surface at a resolution of 10 cm. The sound

pressure level produced by each bubble curtain exhibited rapid attenuation at a peak frequency of ~200 Hz (Table 1). For example, sound produced by the coarse-bubble curtain decayed to background levels (0.01 Pa) within 50 cm of the edge of the bubble curtain, in close agreement with the theoretical prediction of Eq. (12) (Figure 4-3). Furthermore, the observed attenuation length of the 200 Hz sound component (18.7 cm) was also in close agreement with that predicted by Eq. (13) (18.4 cm). Although sound pressure decreased in the vertical direction within the bubble curtain, the sound pressure gradient near the edge of the bubbles (x = 25 cm) was similar for all depths (Figure 4-3).

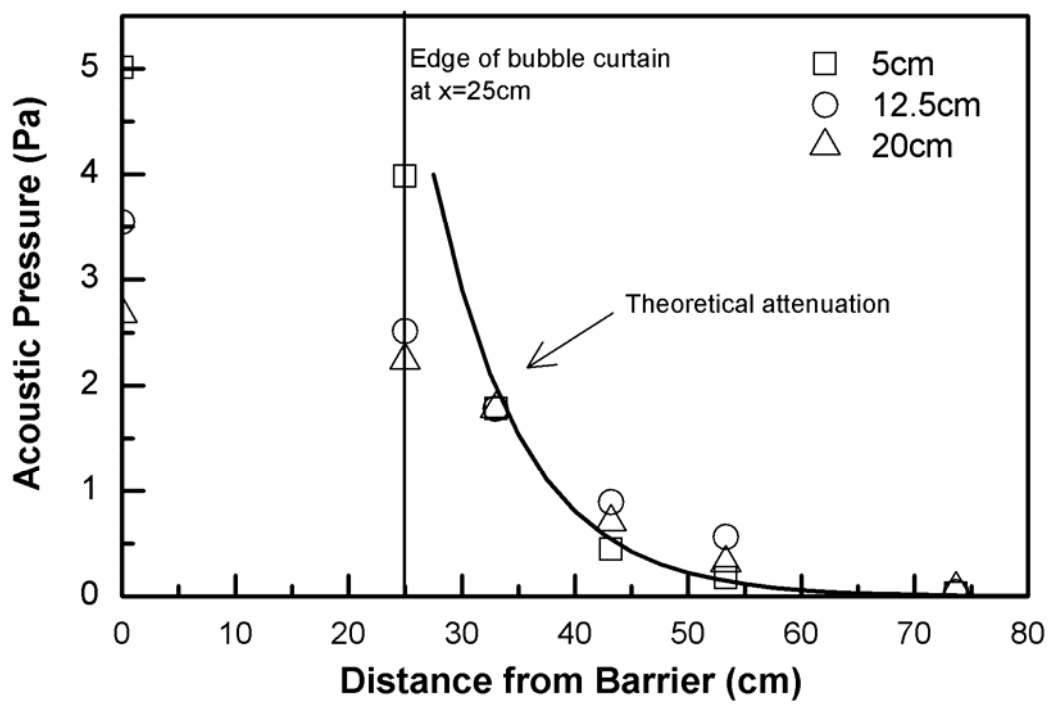

Figure 4-3. Sound pressure profile for 200Hz signal generated by the coarse-bubble curtain along with the theoretical acoustic pressure profile using the shallow water attenuation Eq. (12) (solid line). Measurements were made at depths of 5.0 cm (□), 12.5 cm (○), and 20.0 cm (Δ) along the centerline of the test channel. The center of the bubble curtain is located at x = 0 cm and edge of bubble curtain at x = 25 cm. Note the flattened sound pressure gradient within the bubble curtain (x < 25 cm).

It should be noted that the graded-bubble curtain produced an additional sound gradient across the width of the barrier by using gradually larger bubbles across the length of the system—the upstream sound pressure was 0.1 Pa and downstream was 3.2 Pa. However, for this analysis the sound field was simplified by only considering the stronger signal, as the maximum pressure gradient is generated by the attenuation of the higher signal.

3.2 Stability Analysis

Behavioral deterrent systems, such as the bubble curtains discussed here, are designed to inhibit movement of fish by disrupting natural movement patterns by means of non-physical or mechanical deterrent stimuli. The natural movement of carp is governed by a diffusive process, Eq. (4), which trends towards homogenous distributions and increased solution stability. When individuals undergo diffusion and reaction transport (interaction with each other or environmental stimulus), so called diffusion-induced instability can arise (Okobu and Levin, 2001). Here, the strength of the reaction term overpowers the diffusion process and serves to destabilize the solution. In the case of behavioral deterrents, the natural diffusive spread of carp is considered to be an equilibrium state and the repulsive response to the stimulus field induces instabilities that can grow or diminish over time and space. In this way, a stability analysis of Eq. (9) and (12) can reveal what conditions if any, are required for instability growth and disruption to natural movement. Here, infinitesimal perturbations of the carp concentration are introduced into the governing equations to investigate the stability of the system about an equilibrium state. In the event of perturbation growth, the system is unstable, which we

hypothesize is indicative of deterred movement. Alternatively, a perturbation decay indicates that the system is stable, resulting in failed deterrence.

The steady state of Eq. (9) is found by setting the spatial and temporal derivatives of the carp concentration to zero, and substituting in the equilibrium concentration $N = \hat{N}$. The single spatially uniform state of Eq. (9) is

$$\omega \hat{N} \frac{\partial^2 P}{\partial x^2} = 0 \tag{14}$$

which is assumed to be stable with respect to homogenous perturbations. To examine the stability of the uniform steady state, infinitesimal perturbations are introduced to the carp concentration. Only concentration perturbations are considered because the acoustic stimulus was assumed to be constant. Here, the perturbation, $\varepsilon_N(x,t)$, is written in the form

$$N = \hat{N} + \varepsilon_N \tag{15}$$

Substituting Eq. (15) into Eq. (9), using Eq. (14), and linearizing the equation, the perturbation evolution equation for this system results

$$\frac{\partial \varepsilon_N}{\partial t} = -\mu \frac{\partial \varepsilon_N}{\partial x} + D \frac{\partial^2 \varepsilon_N}{\partial x^2} + \omega \varepsilon_N \frac{\partial^2 P}{\partial x^2} + \omega \frac{\partial \varepsilon_N}{\partial x} \frac{\partial P}{\partial x} \tag{16}$$

where the acoustic pressure is described by Eq. (12). It is sufficient to assume the solution to Eq. (16) takes the form of an oscillating wave function

$$\varepsilon_N(x,t) = A_N e^{\sigma t + iqx} \tag{17}$$

to examine the stability of Eq. (16). In Eq. (17) A_N is the perturbation amplitude at $t = 0$, σ is the amplification factor, and $q = \frac{\pi}{\lambda}$ is the wave number. Notice that if σ is real and positive, perturbations grow exponentially with time, indicating the equilibrium state is unstable. Substituting Eq. (17) into Eq. (16) and dividing through by $A_N e^{\sigma t + iqx}$ results in the equation for spatial evolution of the amplification factor

$$\sigma(x) = -iq\mu - q^2 D + \omega \frac{\partial^2 P}{\partial x^2} + iq\omega \frac{\partial P}{\partial x} \tag{18}$$

However, the real part of Eq. (18) is the critical component because the sign of σ reveals if the perturbations grow or diminish over time and space. In Eq. (18) the advection rate does not impact global stability; rather the stability at a given wave number is governed by the diffusive rate, repulsion rate, and curvature of the acoustic pressure.

3.3 Parameter Estimation

In order to evaluate Eq. (18) for the three bubble curtains investigated by Zielinski et al. (2013) and Zielinski (2011), parameters introduced in previous sections must be estimated. Advection and diffusion coefficients for natural carp movements were estimated from the mean drift position and variance (Figure 4-2). Parameters estimates were obtained from carp movements without the highly mobile individual. The slope of the mean drift position regression describes the average rate of movement of the ensemble, or advective rate (μ=0.34 m min^{-1}). Similarly, the diffusion coefficient was estimated using Eq. (3) with slope of the variance of ensemble movements (D=58.5 m^2/min).

The spatial distribution of carp during bubble curtain trials were used to estimate the acoustic attraction/repulsion rate ω. Acoustic attraction/repulsion was estimated by relating the net downstream flux of fish between control and bubble curtain trials to the concentration of fish present and sound pressure gradient. As the graded- and coarse-bubble curtain trials resulted in net downstream movement of carp, albeit limited, we can estimate the phonotaxic flux by subtracting the downstream flux during bubble curtain trials from the control trials. The fine-bubble curtain trials were not used for parameter estimations as the carp were not found to be significantly deterred, see Section 4 for more details. The downstream flux was calculated by taking the sum of carp passages across the bubble curtain in the downstream direction over 7hrs (# of carp crossing/(area of antenna x 7hr)). An effective concentration was estimated by dividing the number of fish per trial by the total area covered by the ensemble (Table 4-2). Based on Eq. (7), the repulsive flux (or reduction in downstream movement) increases when the sound pressure gradient or concentration increases by the average rate ω=0.6 m^2/Pa·min. Note that a negative downstream flux in Table 4-3 signifies motion in the upstream direction, or a repulsive flux.

Table 4-2. Net downstream flux of carp between control and bubble curtain trials, maximum sound pressure gradient, and effective concentration used to estimate the repulsion rate $\omega = \frac{-q_{ds}}{N\frac{\partial P}{\partial x}}$.

Bubble Curtain	Net downstream flux (#/m^2·min)	Maximum $\partial P/\partial x$ (Pa/m)	Concentration, N (#/m^3)	Repulsion rate, ω (m^2/Pa·min)
Graded-Bubble	-16.2	39.6	0.5	0.8
Coarse-Bubble	-15.8	62.7	0.6	0.4

An encounter rate is important to define for establishing the wavelength of perturbations in the stability analysis. The encounter rate, k (# of attempts/min), was estimated by summing the number of times each group of carp attempted to cross the bubble curtain over the 7 hr test period (k=0.15 #/min average). Note that the encounter rate was converted to an effective wavelength, λ (m), by dividing the average speed of the carp, which is assumed to be equal to the advection rate μ, by k (λ=2.3 m).

4 Results

A base condition using the parameters estimated from laboratory trials was performed to assess whether the stability analysis adequately predicts bubble curtain effectiveness. The base condition includes the acoustic pressure generated by fine-, graded-, and coarse-bubble curtains along the test channel centerline to a distance two times the depth away, assuming exponential attenuation , Eq. (12), with a water depth of 25 cm. The leading edge of the bubble curtain was assumed to be located at $x=0$ and generated a constant sound pressure throughout the water column. The bubble curtain

edge is set as a boundary because the sound pressure across the curtain width is approximately constant, resulting in no additional repulsive flux using Eq. (7).

Positive amplification factors, indicative of instability growth, are predicted at a distance of *0.5 x depth* for graded- and coarse-bubble curtains, but not for the fine-bubble curtain (Figure 4-4). This suggests that the graded- and coarse-bubble curtains are most likely to disrupt carp movement. Results of the displacement, variance, and mean drift positions of carp movements during bubble curtain trials are consistent with the stability analysis prediction (Figure 4-5). The breakdown of spreading rates between bubble curtain and control trials indicates a distinct behavioral change in carp movement. In particular, the graded- and coarse-bubble curtains reduced the spreading rate by an order of magnitude in comparison to control trials. In contrast, the variance of ensemble movements near the fine-bubble curtain exhibited possible anomalous, yet monotonic spreading, suggesting the fine-bubble curtain that had little to no impact on carp movement (Zielinski et al., 2013). Observed reductions in up- and down-stream passages made between the control and bubble curtain trials (Table 4-3), provides further evidence that the stability analysis correctly predicted that the graded- and coarse-bubble curtain were the most effective. Overall, the graded- and coarse-bubble curtains were found to reduce carp passage by >75%, while the fine-bubble curtain provided no statistically significant reduction.

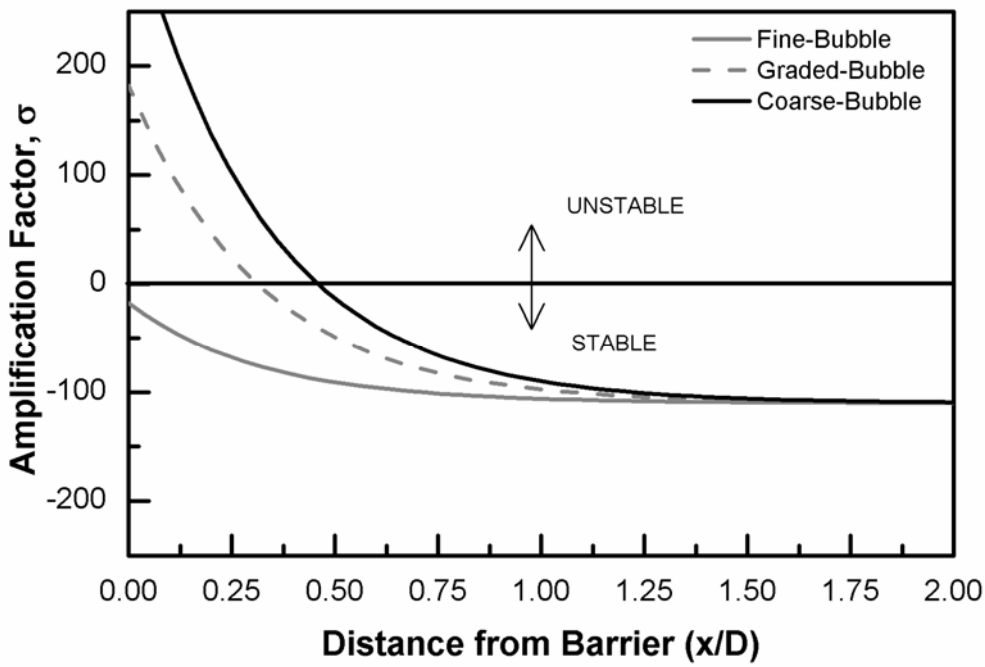

Figure 4-4. Spatial evolution of the amplification factor from Eq. (18) for fine-bubble (—), graded-bubble (--), and coarse-bubble (—) curtains tested by Zielinski (2011) and Zielinski et al. (2013). The leading edge of the bubble curtain is located at x=0. The system is globally unstable if the amplification factor is positive, and stable if negative.

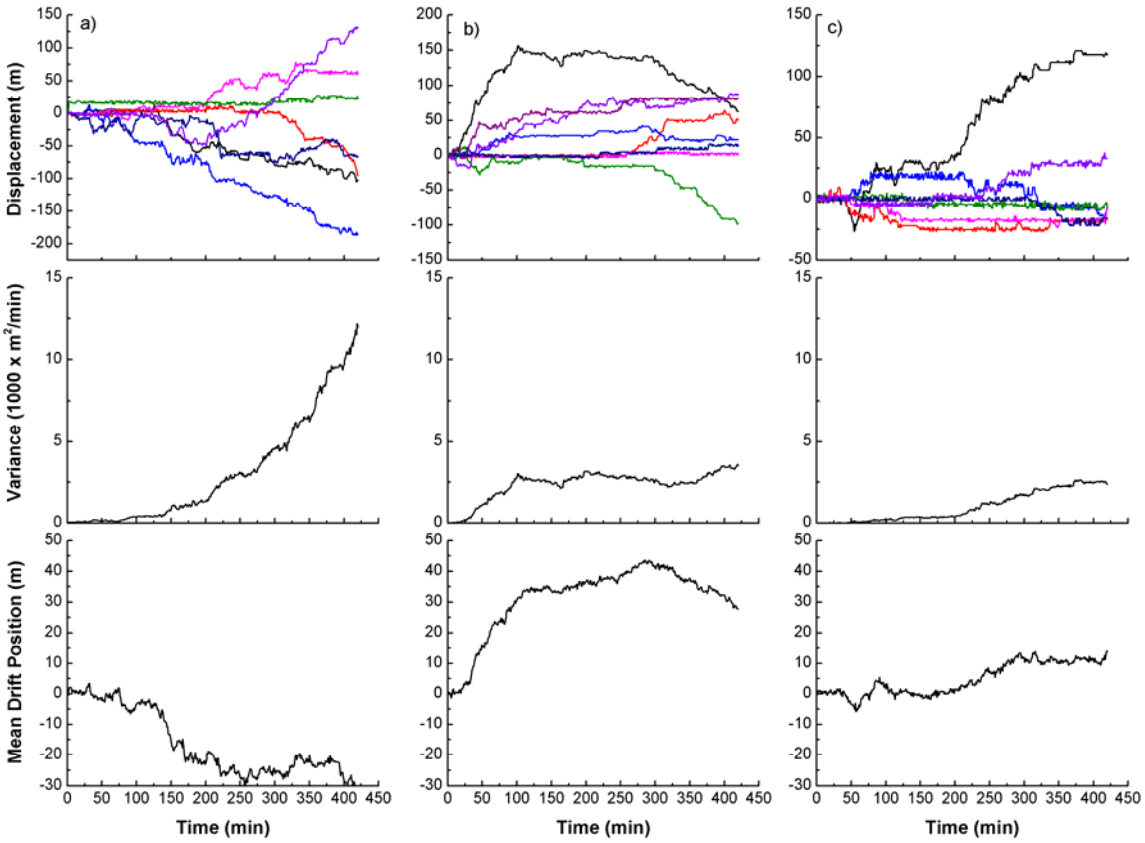

Figure 4-5. Movement analysis of carp ensemble movements during a) fine-; b) graded- ; and c) coarse-bubble curtain trials. Note a positive displacement denotes a downstream movement and negative denotes upstream movement. See Table 4-1 for description of bubble curtains.

Table 4-3. Efficacies of the bubble curtain systems reported by Zielinski et al. (2013), and the statistical significance of observed reductions using a Mann-Whitney test with Dunn-Sidak correction for multiple comparisons. The bubble curtain efficacy is a measure of percent reduction in crossings between control and bubble-curtain trials.

Bubble Curtain	Downstream Efficacy (%)	Upstream Efficacy (%)
Fine-bubble	65 ($P > 0.05$)	36 ($P > 0.05$)
Graded-bubble	78 ($P < 0.01$)	72 ($P < 0.05$)
Coarse-bubble	87 ($P < 0.001$)	82 ($P < 0.01$)

As expected, the higher acoustic output from the graded- and coarse-bubble curtains resulted in greater disruption of carp movement. Using the results of the base condition model, the minimum wavelength that results in a positive amplification factor for each bubble curtain was 2.5, 1.4, and 1.1 m. Thus, the coarse-bubble curtain would be expected to interrupt carp movement up to an encounter rate of ~0.3 #/min, or one passage attempt every 3 min.

A common objective of analyzing the stability of organism movement models is to study the formation of patterns in nature. In this way, a destabilizing variable (e.g. predator or food) causes a uniformly distributed population to aggregate into groups (e.g. schooling or spatial patchiness). Thus, we expect in the case of the graded- or coarse-bubble curtain systems the physical representation of instability would manifest as a grouping of fish a distance of $0.25 - 0.5\ x\ depth$ away from the bubble curtain. Theoretically, fish grouping near the bubble curtain could be observed; however, the

experimental method used in the study did not allow for such an observation, nor do we expect a group of fish to stay indefinitely near the bubble curtain. Rather, the impact of instability is observed in the diminished growth of variance and mean position of the ensemble.

An additional test condition was performed based on the results of the Taylor et al. (2005) investigation of a bioacoustic behavioral fish guidance system on bighead carp. The system consisted of a speaker and air bubble curtain placed in a 24.7 m long raceway with 11 bighead carp per trial over a 6h period. Taylor et al. (2005) reported that 95% of all passage attempts were repelled by this system. In contrast to the base condition, the maximum SPL generated by the barrier was not know *a priori*; therefore, the stability analysis was used to predict the necessary sound pressure level to cause instability growth. The resulting sound pressure level was then compared to sound characteristics of the same system reported by other studies. Taylor et al. (2005) reported that the sound pressure produced by the sound projector reduced exponentially. Again, rapid attenuation predicted by Eq. (12) and (13) would be expected for all sound generated by this system under the resonant frequency of 1230 Hz, because these experiments occurred in 61 cm of water and utilized a sound signal between 20-2000 Hz. Bighead carp and common carp have similar hearing capabilities (Taylor et al., 2005; Popper, 1972; Lovell et al., 2006) and possibly similar behaviors, so the advective, diffusive, and repulsion rate found for common carp were used again for this model. The encounter rate presented by Taylor et al. (2005) (284 attempts/(6h x 3 trials)) results in an effective wavelength of λ =1.4 m. Using a typical signal frequency of 200 Hz, the attenuation distance can be

obtained by Eq. (13) (L = 45.3 cm), indicating that for this depth the sound decays much slower than that in the previous trials (L = 18.4 cm). The stability analysis predicts that a source sound pressure level of 145 dB (re 1μPa) would be sufficient to cause instability growth, which is under the reported maximum sound pressure level of 170 dB (re 1μPa), reported by Perry et al. (2012) and Welton et al. (2002) (Figure 6).

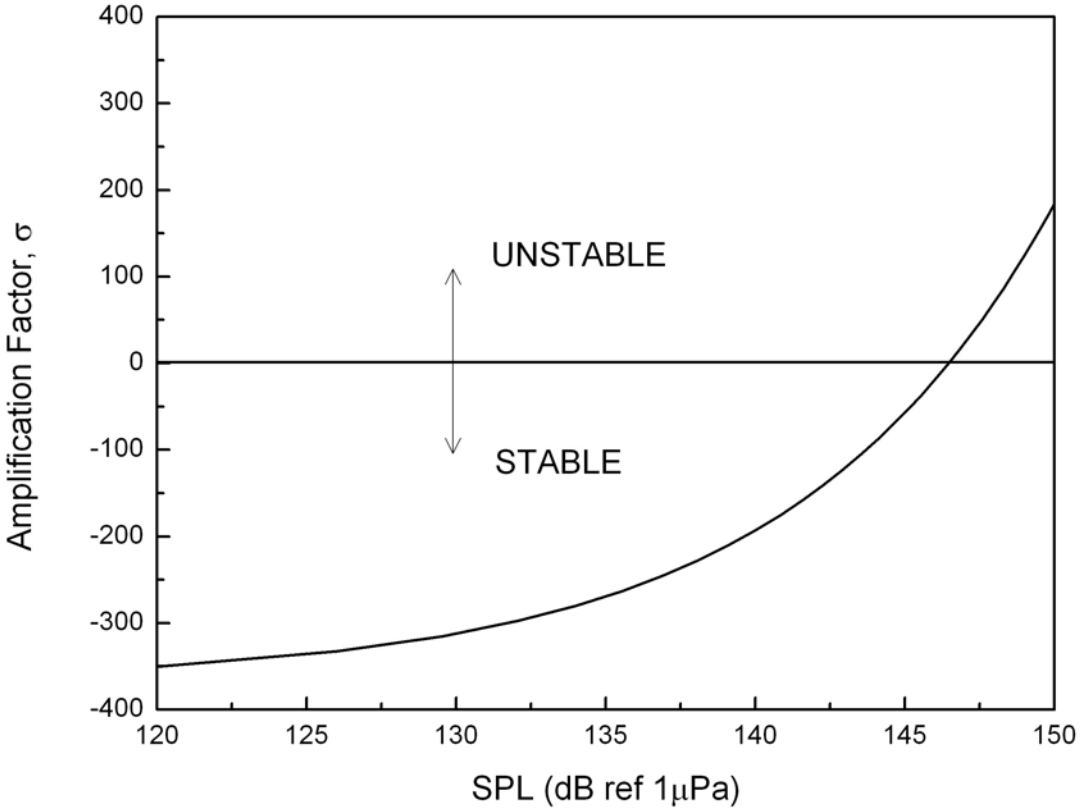

Figure 4-6. Results of the stability analysis for bioacoustic fish fence investigated by Taylor et al. (2005). The amplification factor is calculated at the bubble curtain because the maximum sound pressure gradient occurs close to the sound source. A minimum sound pressure level (SPL) of 145 dB (re 1μPa) at 200Hz is necessary to result in instability growth.

5 Discussion

This work represents the first attempt at modeling fish movement in the vicinity of a bubble curtain/ acoustic deterrent system. Furthermore, a novel application of stability analysis was presented as a way to predict the impact of a deterrent system to disrupt fish movement patterns. Predictions of fish deterrence by the stability analysis were corroborated by results from bubble curtain trials described in Zielinski et al. (2013) and Zielinski (2011). The stability analysis also suitably predicted the minimum sound signal strength produced by a bubble/ speaker system, studied by Taylor et al. (2005), required to deter bighead carp movement.

The equation for evolution of the amplification factor, Eq. (18), suggests that the ability of a behavioral deterrent system with temporally constant deterrent stimuli to disrupt the natural movement pattern of fish is dependent on the diffusive rate of the species and strength of the repulsive reaction. Although the impact of the advection rate is neglected in this stability analysis, conditions certainly exist where strong water flow may overwhelm any fish escape attempt and push the fish past the barrier. The current model assumes that the advection and diffusion exhibited by the fish is self initiated and dependent on flow direction (rheotaxis) but not flow strength. Adequate performance under variable hydraulic conditions is paramount to the behavioral deterrent systems and presents an argument as to why these types of systems are not expected to be 100% effective at blocking fish passage (Noatch and Suski, 2012).

Additionally, Eq. (18) provides insight into the range of conditions that a certain deterrent stimulus can be expected to disrupt fish movement. In the context of an

acoustic deterrent, the important factors governing the strength of the repulsive response are hearing sensitivity, behavior, water depth, and signal characteristics. A complicating factor relating to sound detection is that carp are capable of detecting both acoustic particle motion and sound pressure. Sensitivity to each component is thought to be dependent on the distance away from the sound source in addition to physiological adaptations (Popper and Fay, 2011). Currently, the sound component that carp respond to in proximity to a bubble curtain is unknown. In this study, however, sound pressure was used as a proxy for acoustic stimulus in the movement model due to the unique ability of carp to detect sound pressure across a great distance and relative ease of measurement. Certainly, the hearing threshold for sound pressure or particle motion can be obtained from well-established techniques (Zeddies et al., 2012; Radford et al., 2012; Lugli and Fine, 2007; Lovell et al., 2006), but quantifying the response of fish to the detected sound is much more difficult as a similar signal may generate diverse reactions from different species, i.e. Dawson et al. (2006) observed eurasian ruffe, *Gymnocephalus cernuus* L., to be mildly attracted to a bubble curtain while Patrick et al. (1985) observed alewife, *Alosa pseudoharengus*, smelt, *Osmerus mordax,* and gizzard shad, *Dorosoma cepedianum*, to be repelled by a similar bubble curtain. Thus, as the attraction/ repulsive rate is expected to be species and stimuli dependent, this model could be used to predict the impact of specific stimuli on guiding other target and non-target species once sufficient parameters are estimated. Future work could include determining repulsion rates to other deterrent stimuli such as light, turbulence, or electricity.

Water depth is also important to the transmission of the acoustic signal. In depths less than 1 m, sound components less than 750 Hz decrease exponentially away from the barrier according to Eq. (12) and (13) and higher frequency components will attenuate following the inverse square law (Akamatsu et al., 2002). Thus, as depths increase, the attenuation rate and pressure gradient will decrease. For example, the model suggests that the graded- and coarse-bubble curtains will only be effective up to depths less than 0.5 m, assuming the encounter rates remain similar to that in the laboratory. At greater depths, the sound pressure gradient decreases. To combat the flattening of the pressure gradient, two options are available 1) increase the maximum sound pressure or 2) artificially increase the pressure gradient. As shown by Welton et al. (2002), bubble curtain systems driven by speakers are capable of generating much higher sound pressure than by bubbles alone. Because bubble plumes propagate sound more efficiently than water alone (Manasseh et al., 2004; Nicholas et al., 1994), the resulting acoustic field is anisotropic, which can be utilized to modify the pressure gradient generated by an underwater speaker array. The combined use of bubble curtains and speaker arrays are already utilized by bioacoustic behavioral deterrent systems (Perry et al., 2012; Ruebush et al., 2012; Taylor et al., 2005; Welton et al., 2002). Another contributing issue to shallow water attenuation is the signal frequency. The range of the signal frequency must be within the species hearing range, often containing frequencies below 1 kHz. However, if higher frequencies are used, common carp are capable of detecting sound up to 5 kHz (Popper, 1972), the attenuation is much more gradual, resulting in diminished pressure gradients.

6 Conclusions

A mathematical model was presented to describe the movement of fish in the vicinity of a behavioral deterrent system and examine what conditions would be required to disrupt natural movement patterns of fish. A stability analysis performed on a movement model of common carp near a bubble curtain aptly predicted instability growth as a result of acoustic repulsion (phonotaxis) for two of the bubble curtains investigated by Zielinski et al. (2013) and Zielinski (2011). This type of model could be used as the basis of large scale stochastic models or other spatial population dynamics models to predict deterrent system performance over time, or used to investigate the impact of alternative movement patterns on performance. Even though this model was only validated for acoustic deterrents on carp, other behavioral deterrents and species could be examined with the inclusion of appropriate stimuli and species specific repulsion rates.

Chapter 5: Conclusions and Future Work

Unchecked proliferation of invasive fish could lead to irreversible ecological and economic damages around the world. Behavioral deterrent systems, and bubble curtains in particular, are an inexpensive management tool that could control movement of invasive fish, such as common carp. Most studies on bubble curtain systems focus on passage results, while virtually ignoring relevant stimuli produced by such systems. Thus, a problem of interest is to develop a bubble curtain system that inhibits movement of invasive fish, identify the biologically relevant stimuli likely to influence fish movement, and develop a mathematical model to describe fish movement in the vicinity of a behavioral deterrent system. This thesis research provides detailed methodologies and results from laboratory, field scale, and mathematical studies to help understand and quantify the ability of bubble curtain systems to inhibit common carp movement.

The main findings of this thesis research can be summarized as:

- **Chapter 2** demonstrated that the graded- and coarse-bubble curtain reduced common carp passage by ~80% in both up- and down-stream directions in a 25 cm deep laboratory channel. Concurrent stimuli measurements indicated that bubble curtains produce sound well above the common carp hearing threshold. Furthermore, results of carp movement and stimulus field (e.g. fluid flow, sound) measurements indicated that sound and fluid motion, rather than visual cues, are responsible for carp deterrence.
- **Chapter 3** demonstrated that under field conditions, the performance of the graded-bubble curtain system was reasonably consistent with laboratory results,

blocking 57±12% of downstream swimming carp, versus 75-80%in the laboratory. In contrast, the bubble curtain did not block upstream passage of carp (efficacy was less than 20%); in fact the system appeared to merely delay passage by ~6hrs. However, due to the comparably low cost and reliable operation, bubble curtains could still be used as a management tool to control downstream movement of carp in low head shallow waterways if simple alterations (i.e. repositioning or additional deterrents) can improve efficacy by 10-15%.

- **Chapter 4** provided a fish movement model based on diffusion theory and linked observed deterrence behaviors to phonotaxic responses. Thus, demonstrating that the acoustic stimulus produced by bubble curtains can be sufficient to disrupt movement of carp (i.e. deter fish passage). A stability analysis of the resulting model was shown to aptly predict which bubble curtain system, investigated in **chapter 2**, would inhibit carp passage. Additionally, it was demonstrated that disruptions to normal movement patterns near a behavioral deterrent system arise in the movement model as diffusion-induced instabilities.

The previous findings were only possible through rigorous experimental investigations and holistic quantitative analysis. The research provides a crucial step in the development and possible implementation of bubble curtains in real-world management efforts. Differing from previous bubble curtain studies, this research sought to 1) understand bubble curtain mechanics, 2) relate relevant deterrent stimuli to observed behavioral responses, and 3) use laboratory measurements to develop predictive mathematical models. Overall, bubble

curtains can indeed deter common carp movement, but improvements must be identified in order for bubble curtains to remain a viable management tool in the future.

This research provides crucial insight into bubble curtain function and common carp dispersal behaviors, but it also raises many new questions and potential directions for future research. These include:

- Identifying tractable, inexpensive solutions to improving bubble curtain function in the field. Our findings in **chapter 2** suggest that additional improvements to bubble curtain systems should focus on hydrodynamic and acoustic stimuli; therefore, continued testing of dual-element systems (i.e. bubbles plus sound) is needed.
- Study the impact of bubble curtains on other invasive fish. Recently, silver carp (*Hypophthalmichthys molitrix*) and bighead carp (*Hypophthalmichthys nobilis)* upstream progress in the Mississippi River and towards the Great Lakes has emphasized the need for safe barrier technologies that do not impede navigation. Since silver carp and bighead carp are just as sensitive (if not more) to sound, bubble curtains could have great potential to help control movement of both species in shallow waters (i.e. tributaries). Indeed, a laboratory study to investigate the use of bubble curtains to help control silver carp and bighead carp movement in Mississippi River tributaries will be underway this fall at the newly formed Minnesota Aquatic Invasive Species Research Center.

- Understand and quantify how alternative movement patterns impact performance of behavioral deterrent systems. Indeed, dispersal traits are not expected to be homogenous across an entire population, as a result the classical diffusion model in **chapter 4** may no longer be valid in such cases. For this situation, multi-state (Skalski and Gilliam; 2003), continuous(Gurarie et al., 2009), and Lévy flight models (Meerschaert, 2012; Petrovskii et al., 2008; Zhang et al., 2007c) have been suggested. Using the movement framework in **chapter 4**, additional fish movement models could be generated that are better suited to predict barrier performance under heterogeneous dispersal.

Bibliography

Akamatsu, T., Okumura, T., Novarini, N., Yan, H.Y., (2002) Empirical refinements applicable to the recording of fish sounds in small tanks. J. Acoust. Soc. Am. 112, 3073-3082.

Aoki, Y. Sen, M., Paolucci, S., (2008) Approximation of Transient Temperatures in Complex Geometries using Fractional Derivatives. Heat Transfer 44, 771-777.

Bajer, P., Sorensen, P. (2010) Recruitment and abundance of an invasive fish, the common carp, is driven by its propensity to invade and reproduce in basins that experience winter-time hypoxia in interconnected lakes. Biological Invasions 12, 1101-1112.

Bajer, P., Sullivan, G., Sorensen, P., (2009) Effects of a rapidly increasing population of common carp on vegetative cover and waterfowl in a recently restored Midwestern shallow lake. Hydrobiologia 632, 235-245.

Balon, E.K. (1995) Origin and domestication of the wild carp, Cyprinus carpio: from Roman gourmets to the swimming flowers. Aquaculture 129, 3–48.

Beer, G., Smith, I., Duenser, C., (2008) The boundary element method with programming: for engineers and scientists, Springer, New York, USA.

Benson, D.A., Wheatcraft, S.W., Meerschaert, M.M. (2000a) Application of a fractional advection-dispersion equation. Water Resources Research, 36, 1403-1412.

Benson, D.A., Wheatcraft, S.W., Meerschaert, M.M. (2000b) The fractional-order governing equation of Lévy Motion. Water Resources Research, 36, 1413-1423.

Bode, N.W.F., Franks, D.W., Wood, A.J., Piercy, J.J.B., Croft, D.P., Codling, E.A., (2012) Distinguishing social from non-social navigation in cohesive animal groups. American Naturalist 179, 621-632.

Bradford, M.J., Taylor, G.G., (1997) Individual variation in dispersal behaviour of newly emerged chinook salmon (Oncorhynchus tshawytscha) from the Upper Fraser River, British Columbia. Can. J. Fish Aquat. Sci. 52, 1585-1592.

Brett, J.R., MacKinnon, D., (1953) Preliminary experiments using lights and bubbles to deflect migrating young spring salmon. J. Fish. Res. Bd. Can. 10, 548-559

Brevik, I., Kristiansen, Ø., (2002) The flow in and around air-bubble plumes. International Journal of Multiphase Flow 28, 617-634.

Britton, J.R., Gozlan, R.E., Copp, G.H. (2011) Managing non-native fish in the environment. Fish and Fisheries 12, 256-274.

Bueno-Orovio, A., Kay, D., Burrage, K., (2012) Fourier spectral methods for fractional-in-space reaction-diffusion equations. Journal of Computational Physics, Eprint available from: http://eprints.maths.ox.ac.uk/1551/.

Burrage, K., Hale, N., Kay, D., (2012) An Efficient Implicit FEM Scheme for Fractional-in-Space Reaction-Diffusion Equations. SIAM Journal on Scientific Computing, 34, A2145-A2172.

Clarkson, R.W., (2004) Effectiveness of Electrical Fish Barriers Associated with the Central Arizona Project. North American Journal of Fisheries Management 24, 94-105.

Codling, E.A., Bearon, R.N., Thorn, G.J., (2010) Diffusion about the mean drift location in a biased random walk. Ecology 91, 3106-3113.

Codling, E.A., Plank, M.J., Simon, B., (2008) Random walk models in biology. Journal of the Royal Society Interface 5, 813-34.

Codling, E.A., Hill, N.A., Pitchford, J.W., Simpson, S.D., (2004) Random walk models for the movement and recruitment of reef fish larvae. Marine Ecology Progress Series 279, 215-224.

Conover, G., Simmonds, R.,Whalen, M. (editors), (2007) Management and control plan for bighead, black, grass, and silver carps in the united states, Washington D.C.: Asian Carp Working Group, Aquatic Nuisance Species Task Force.

Conover, W. J., (1980) Practical Nonparametric Statistics, John Wiley & Sons, New York, NY. 493 pp.

Cote, J., Fogarty, S., Weinersmith, K., Brodin, T., Sih, A., (2010) Personality traits and dispersal tendency in the invasive mosquitofish (Gambusia affinis). Proc. R. Soc. B. 277, 1571-1579.

Dawson, H.A., Reinhardt, U.G., Savino, J.F., (2006) Use of Electric or Bubble Barrier to Limit the Movement of Eurasion Ruffe (Gymnocephalus cernuus). J. Great Lakes Res. 40-49.

Diethelm,K., Ford, N.J., Freed, A.D., Luchko, Y., (2005) Algorithms for the fractional calculus: A selection of numerical methods. Computer Methods in Applied Mechanics and Engineering 194, 743-773, 2005.

Diethelm, K., (1997) Generalized compound quadrature formulae for finite-part integrals. IMA

Journal of Numerical Analysis, 17, 479-493.

Ding, Z., Xiao, A., Li, M., (2010) Weighted Finite Difference Methods for a Class of Space Fractional Partial Differential Equations with Variable Coefficients, J. Comput. Appl. Math. 233, 1905-1914.

Edwards, A.M., (2011) Overturning conclusions of Lévy flight movement patterns by fishing boats and foraging animals. Ecology 92, 1247-1257.

Edwards, A.M., Phillips, R.A., Watkins, N.W., et al., (2007) Revisitng Lévy flight search patterns for wandering albatrosses, bumblebees and deer. Nature, 449, 1044-1048.

Electric Power Research Institute (EPRI), (2004) Chapter 22: Behavioral Methods, Fish Passage Manual Chapter Updates. Technical Report 1011448. Palo Alto, CA.

Electric Power Research Institute (EPRI), (1998) Evaluation of Fish Behavioral Barriers. Technical Report 109483. Palo Alto, CA.

Ervin,V.J., Roop, J.P., (2006) Variational formulation for the stationary fractional advection dispersion equation. Numerical Methods for Partial Differential Equations, 22, 558-576.

Fleiss J.L., (2003) Statistical Methods for Rates and Proportions, 3nd edn. New York: Wiley, 309 pp.

Foufoula-Georgiou, E., Ganti, V., Dietrich, W.E., (2010) A nonlocal theory of sediment transport on hillslopes. Journal of Geophysical Research: Earth Surface, 115, F00A16.

Fraser, D. F., Gilliam, J. F., Daley,M. J., Le, A. N., Skalski, G. T., (2001) Explaining leptokurtic movement distributions: intrapopulation variation in boldness and exploration. Am. Nat. 158, 124–135.

Ganti, V., Meerschaert, M.M., Foufoula-Georgiou, E., Viparelli, E. and Parker, G., (2010) Normal and anomalous diffusion of gravel tracer particles in rivers. Journal of Geophysical Research, 115, F00A12.

Goodwin, R., Nestler, J., Anderson, J., Weber, L., Loucks, D., (2006) Forecasting 3-d fish movement behavior using an eularian–lagrangian-agent method (elam). Ecol. Model. 192, 197–223.

Gurarie, E., Anderson, J.J., Zabel, R.W., (2009) Continuous models of population-level heterogeneity inform analysis of animal dispersal and migration. Ecology, 90, 2233-2242.

Haji-Sheikh, A. and Howell, J. R., (2006) Monte Carlo Methods, in Handbook of Numerical

Heat Transfer, Second Edition (eds W. J. Minkowycz, E. M. Sparrow and J. Y. Murthy), John Wiley & Sons, Inc., Hoboken, NJ, USA.

Hillen, T., Painter, K., (2009) A user's guide to PDE models for chemotaxis. J. Math. Biol. 58, 183-217.

Holliman, F.M, (2010) Operational Protocols for Electric Barriers on the Chicago Sanitary and Ship Canal: Influence of Electrical Characteristics, Water conductivity, Behavior, and Water Velocity on Risk for Breach by Nuisance Invasive Fishes. Smith-Root Inc. Final Report.

Holmes, E.E, Lewis, M.A., Banks, J.E., Veit, R.R., (1994) Partial differential equations in ecology: Spatial interactions and population dynamics. Ecology 75, 17-29.

Humphries, N.E., Queiroz, N., Dyer, J.R.M. et al. (2010) Environmentalcontext explains Lévy and Brownian movement patterns of marine predators. Nature, 465, 1066-1069.

Ilic, M., Liu, F., Turner, I., Anh, V., (2005) Numerical Approximation of a Fractional-In-Space Diffusion Equation. Fractional Calculus and Applied Analysis, 8, 323-341.

Jones, M.J., Stuart, I.G., (2009) Lateral movement of common carp (*Cyprinus cario L*) in a large lowland river and floodplain. Ecology of Freshwater Fish, 18, 72-82.

Jumyi, L., Mingyu, X., (2009) Some Exact Solutions to Stefan Problems with Fractional Differential Equations. J. Math. Anal. Appl. 351, 536-542.

Koehn, J.D., (2004) Carp (Cyprinus carpio) as a powerful invader in Australian waters. Freshw. Biol. 49:882–894.

Kolar, C. S., Lodge, D.M., (2002) Ecological predictions and risk assessment for alien fishes in North America. Science, 298, 1233-1236.

Kot, M., Lewis, M.A.,van den Driessche, P., (1996) Dispersal data and the spread of invading organisms. Ecology 77, 2027–2042.

Kundu, P., (1990) Fluid mechanics. San Diego: Academic Press.

Kuznetsov, Y.A., (1971) The behavior of fish in the zone affected by a curtain of air bubbles. In: A.P. Alekeseeu, (eds), Fish Behavior and Fishing Techniques. National Marine Fish Service, NOAA, National Technical Information Service Transactions, 71-50010: 103-110.

Lamarre, E., Melville, W.K., (1994) Void-fraction measurements and sound-speed fields in bubble plumes generated by breaking waves. J. Acoust. Soc. Am. 95 (3): 1317-1328.

Lavis, D. S, Hallett, A., Koon, E. M., McAuley, T., (2003) History of and advances in barriers

as an alternative method to suppress sea lampreys in the Great Lakes. Journal of Great Lakes Research 29 (Supplement1): 362–372.

Leiberman, J.T., Muessig, P.H., (1978) Evaluation of an air bubbler to mitigate fish impingement at an electric generating plant. Estuaries and Coasts 1 (2):129-132.

Leighton, T.G., (1994) The acoustic bubble. Academic Press, San Diego, CA. 913 pp.

Leighton, T.G., Walton, A.J., (1987) An experimental study of the sound emitted from gas bubbles in a liquid. European Journal of Physics 8, 98-104.

Lemasson, B. H., Haefner, J. W., Bowen, M. D., (2008) The effect of avoidance behavior on predicting fish passage rates through water diversion structures. Ecol. Model. 219, 178-188.

Lever, C., (1996) Naturalized fishes of the world. Academic Press, San Diego

Lin, J.N., Banerji, S.K., Yasuda, H., (1994) Role of interfacial tension in the formation and the detachment of air bubbles. Langmuir 10, 936-942.

Liu, F., Anh, V. and Turner, I., (2004) Numerical solution of the Space Fractional Fokker-Planck Equation, J. Comp. Appl. Math., 168, 209-219.

Liu, J., M. Xu, (2009) Some exact solutions to Stefan problems with fractional differential equations. Journal of Mathematical Analysis and Applications, 351, 536-542.

Lodge, D.M., Williams, A., MacIsaac, H.J. et al., (2006) Biological invasions: recommendations for US policy and management. Biological Invasions 16, 1035–2054.

Lovell, J.M., Findlay, M.M., Nedwell, J.R., Pegg, M.A., (2006) The hearing abilities of the silver carp (hypopthalmichthys molitrix) and bighead carp (aristichthys nobilis). Comparative Biochemistry and Physiology – Part A: Molecular & Integrative Physiology 143, 286-91.

Lowe, S., Browne, M., Boudjelas, S., De Poorter, M., (2000) 100 of the world's worst invasive alien species: a selection from the global invasive species database. Auckland, New Zealand: Invasive Species Specialist Group.12 pp.

Lugli, M., Fine, M.L., (2007) Stream ambient noise, spectrum and propagation of sounds in the goby padogobius martensii: Sound pressure and particle velocity. J. Acoust. Soc. Am. 122, 2881-92.

Lynch,V.E., Carreras, B.A., del-Castillo-Negrete, D., Ferreira-Mejias, K.M., Hicks, H.R., Numerical methods for the solution of partial differential equations of fractional order. Journal of Computational Physics, 192, 406-421, 2003.

Manasseh, R., Nikolovska, A., Ooi, A., Yoshida, S., (2004) Anisotropy in the sound field generated by a bubble chain. Journal of Sound and Vibration 278, 807-823.

Meerschaert, M.M., (2012) Fractional Calculus, Anomalous Diffusion, and Probability, in Fractional Dynamics,(Eds., Metzler, R. & Klafter, J.), World Scientific, Singapore, 265-284.

Meerschaert, M.M., Scheffler, H., Tadjeran, C., (2006) Finite difference methods for two-dimensional fractional dispersion equation. Journal of Computational Physics, 211, 249-261.

Meerschaert, M.M., Tadjeran, C., (2006) Finite difference approximations for two-sided space-fractional partial differential equations. Applied Numerical Mathematics, 56, 80-90.

Meerschaert, M.M., Tadjeran, C. (2004) Finite Difference Approximations for Fractional Advection–Dispersion Flow Equations. J. Comput. App. Math., 172, 65–77.

Meerschaert, M.M., Benson, D.A., Baeumer, B., (2001) Operator Lévy motion and multiscaling anomalous diffusion. Physical Review E, 63, 021112.

Metzler, R., Klafter, J., (2000), The random walk's guide to anomalous diffusion: a fractional dynamics approach. Physics Reports, 339: 1-77.

Michaud, D.T., Taft, E.P., (2000) Recent evaluations of physical and behavioral barriers for reducing entrainment at hydroelectric plants in the upper Midwest. Environmental Science and Policy 3 (1): 499-512.

Moroney, T., Yang, Q. (2013a) A banded preconditioner for the two-sided, nonlinear space-fractional diffusion equation. Computers & Mathematics with Applications. In Press.

Moroney, T., Yang, Q., (2013b) Efficient solution of two-sided nonlinear space-fractional diffusion equations using fast Poisson preconditioners. Journal of Computational Physics, 246, 304-317

Mussen, T.D., Cech Jr., J.J, (2012) The roles of vision and the lateral-line system in Sacramento splittail's fish-screen avoidance behaviors: Evaluating vibrating screens as potential fish deterrents. Environmental Biology of Fishes DOI10.1007/s10641-012-0094-2.

Nicholas, M., Roy, R.A., Crum, L.A., Oguz, H., Prosperetti, A., (1994) Sound emissions by a laboratory bubble cloud. J. Acoust. Soc. Am. 95 (6): 3171-3182.

Noatch, M.R., Suski, C.D., (2012) Non-physical barriers to deter fish movements. Environmental Reviews 20(1): 71-82.

Okubo, A., Levin, S.A., (2001) Diffusion and ecological problems: modern perspectives.

Springer, New York, NY. 467 pp.

Oldham, K.B., Spanier, J.,(1974) The fractional calculus. Academic Press, New York, USA.

Osborne, J.B., (2012) Distribution, abundance and overwinter survival of young-of-the-year common carp in a Midwestern watershed. University of Minnesota. MS Thesis, Minneapolis, MN.

Patrick, P.H., Christie, A.E., Sager, D., Hocutt, C., Stauffer Jr., J., (1985) Responses of fish to a strobe light/ air-bubble barrier. Fisheries Research 3, 157-172.

Perry, R.W., Romine, J.G., Adams, N.S., Blake, A.R., Burau, J.R., Johnston, S.V., Liedtke, T.L., (2012) Using a non-physical behavioral barrier to alter migration routing of juvenile Chinook salmon in the Sactamento-San Joaquin River Delta. River Research and Applications doi: 10.1002/rra.2628.

Petrovskii, S. Morozov, A., Li, B. (2008) On a possible origin of the fat-tailed dispersal in population dynamics. Ecologcial Complexity, 5, 146-150.

Piret, C., Hanert, E., (2013) A radial basis functions method for fractional diffusion equations. Journal of Computational Physics, 238, 71-81.

Podlubny, I., (1999) Fractional differential equations: an introduction to fractional derivatives, fractional differential equations, to methods of their solution and some of their applications. Academic Press, San Diego, USA.

Popper, A.N., (1972) Pure-tone auditory thresholds for carp, Cyprinis carpio. J. Acoust. Soc. Am. 52 (6): 1714-1717.

Popper, A.N., Carlson, T.J., (1998) Application of Sound and Other Stimuli to Control Fish Behavior. Transactions of the American Fisheries Society 127, 673-707.

Popper, A.N., Fay R.R., (2011) Rethinking sound detection by fishes. Hearing Research 273 (1–2) 25-36.

Radford, C.A., Montgomery, J.C., Caiger, P., Higgs, D.M., (2012) Pressure and particle motion detection thresholds in fish: A re-examination of salient auditory cues in teleosts. J. Exp. Biol. Doi:10.1242/jeb.073320.

Rehage, J.S., Sih, A., (2004) Dispersal behavior, boldness, and the link to invasiveness: a comparison of four Gambusia species. Biological Invasions, 6 379-391.

Reynolds, J.B., (1996) Electrofishing. In Fisheries Techniques, 2nd Edition. (Eds Murphy,B. R.,

Willis, D.W.). American Fisheries Society, Bethesda, MD. pp 221–253.

Roop, J.P., (2006) Computational aspects of FEM approximation of fractional advection dispersion equations on bounded domains in R^2. Journal of Computational and Applied Mathematics, 193, 243-268.

Ruebush, B.C.,Sass, G.G., Chick, J.H., Stafford, J.D., (2012) In-situ tests of sound-bubble-strobe light barrier technologies to prevent range expansions of Asian carp. Aquatic Invasions 7, 37-48.

Sager, D.R., Hocutt, C.H., Stauffer, J.R., (1987). Estuarine fish responses to strobe light, bubble curtains and strobe light/bubble-curtain combinations as influenced by water flow rate and flash frequencies. Fisheries Research 5, 383-399.

Scherer, R. , S.L. Kalla, L. Boyadjiev, B. Al-Saqabi, (2008) Numerical treatment of fractional heat equations. Applied Numerical Mathematics, 58, 1212-1223.

Schumer, R., Benson, D.A., Meerschaert, M.M., Wheatcraft, S.W., (2001) Eulerian derivation of the fractional advection–dispersion equation. Journal of contaminant hydrology, 48, 69-88.

Schumer, R., Meerschaert, M.M., Baeumer, B., (2009) Fractional advection-dispersion equations for modeling transport at the Earth surface. Journal of Geophysical Research, 114, F00A07.

Shen, C. Phanikumar, M.S., (2009) An efficient space-fractional dispersion approximation for stream solute transport modeling. Advances in Water Resources, 32, 1482-1494.

Sibert, J.R., Hampton, J., Fournier, D.A., Bills, P.J., (1999) An advection-diffusion-reaction model for the estimation of fish movement parameters from tagging data, with application to skipjack tuna (katsuwonus pelamis). Can. J. Fish. Aquat. Sci. 56, 925-938.

Silva, A.T., Santos, J.M., Ferreira, M.T., Pinheiro, A.N., Katopodis, C.K., (2001). Effect of water velocity and turbulence on the behavior of Iberian Barbell (Luciobarbus bocagei, Steindachner 1864) in an experimental pool-type fishway. River Res. Applic. 27: 360-373.

Simpson, S.D., Meekan, M.G., Montgomery, J.C., McCauley, R.D., Jeffs, A., (2005). Homeward Sound. Science 308, 221.

Skalski, G.T., Gilliam, J.F., (2000) Modeling diffusive spread in a heterogeneous population: A movement study with stream fish. Ecology 81, 1685-1700.

Skalski, G.T., Gilliam, J.F., (2003) A diffusion-based theory of organism dispersal in

heterogeneous populations. Am. Nat. 161, 441-458.

Skellam, J.G., (1951) Random dispersal in theoretical populations. Biometrika 38, 196-218.

Skov, C., Brodersen, J., Brönmark, C., Hansson, L.-A., Hertonsson, P., Nilsson, P.A., (2005) Evaluation of PIT-tagging in cyprinids. Journal of Fish Biology 67, 1195-1201.

Soga, C.L.M., Rehmann, C.R., (2004) Dissipation of turbulent kinetic energy near a bubble plume. Journal of Hydraulic Engineering 130(5): 441-448.

Sparrevohn, C.R., Nielsen, A., Stottrup, J.G., (2002) Diffusion of fish from a single release point. Can. J. Fish. Aquat. Sci. 59, 844-853.

Sprott, T., (2001) Preliminary Report on the Field Testing of an Air-Curtain Screen to Minimize Fish Passage onto Submerged Floating Drydocks. The National Shipbuilding Research Program. NSRP 0589.

Staaterman, E., Paris, C.B., Helgers, J., (2012) Orientation behavior in fish larvae: A missing piece to Hjort's critical period hypothesis. J. Theor. Biol. 304, 188-196.

Stewart, P., (1982) An investigation into the reactions of fish to electrified barriers and bubble curtains. Fisheries Research 1, 3-22.

Stokstad, E., (2003) Can well-timed jolts keep out unwanted exotic fish? Science 301, 157-159.

Swanson, C., Young, P.S., Chech Jr., J.J., (2005) Close Encounters with a Fish Screen: Integrating Physiological and Behavioral Results to Protect Endangered Species in Exploited Ecosystems. Transactions of the American Fisheries Society, 134, 1111-1123.

Swink, W.D., (1999) Effectiveness of an Electrical Barrier in Blocking a Sea Lamprey Spawning Migration on the Jordan River, Michigan. North American Journal of Fisheries Management, 19, 397-405.

Tadjeran, C., Meerschaert, M.M., (2006) A second-order accurate numerical method for the two-dimensional fractional diffusion equation Journal of Computational Physics, 220, 813-823.

Tadjeran, C., Meerschaert, M.M., Scheffler, H.P., (2006) A Second-Order Accurate Numerical Approximation for the Fractional Diffusion Equation. J. Comp. Phys. 213, 05-213.

Taft, E.P., (2000) Fish protection technologies: a status report. Environmental Science & Policy 3, 349-359.

Taylor, R.M., Pegg, M.A., Chick, J.H., (2005). Response of bighead carp to a bioacoustic

behavioral fish guidance system, Fish. Manage. Ecol. 12, 283-286.

Tudorache, C., Viaene, P., Blust, R., Vereecken, H., De Boek, G., (2008) A comparison of swimming capacity and energy use in seven European freshwater fish species. Ecology of Freshwater Fish, 17, 284-291.

Urick, R.J., (1975) Principles of Underwater Sound, McGraw-Hill, New York, NY. 423 pp.

VanderZanden, M.J., Olden, J.D., (2008) A management framework for preventing the secondary spread of aquatic invasive species. Can. J. Fish. Aquat. Sci. 65, 1512-1522.

Verrill, D.D., Berry, C.R., (1995) Effectiveness of an electrical barrier and lake drawdown for reducing common carp and bigmouth buffalo abundances. N. Am. J. Fish. Manage. 15, 137-141.

Viswanathan, G.M., da Luz, M.G.E., Raposo, E.P., Stanley, H.E. (Eds.), (2011) The physics of foraging: an introduction to random searches and biological encounters. Cambridge University Press, New York.

Vitule, J.R.S., Freire, C.A., Simberloff, D., (2009) Introduction of non-native freshwater fish can certainly be bad. Fish and Fisheries 10, 98–108.

Voller, V.R., (2009) Basic Control Volume Finite Element Methods for Fluids and Solids, World Scientfic, Singapore.

Voller, V.R., (2010) An exact solution of a limit case Stefan problem governed by a fractional diffusion equation. International Journal of Heat and Mass Transfer, 53, 5622-5625.

Voller, V.R., Paola, C., (2010) Can anomalous diffusion describe depositional fluvial profiles? Journal of Geophysical Research, 115, F00A13.

Voller, V.R., Paola, C., Zielinski, D.P., (2011) The Control Volume Weighted Flux Scheme (CVWFS) for Non-Local Diffusion and Its Relationship to Fractional Calculus. Numerical Heat Transfer B, 59, 421-441.

Voller, V.R., Ganti, V., Paola, C., Foufoula-Georgiou, E., (2012) Does the flow of information in a landscape have direction?, Geophysical Research Letters, 39, L01403.

Wang, Y., (2013) Anomalous transport in weakly heterogeneous geological porous media. Physical Review E 87, 032144.

Wang, H., Wang, K., (2011) An $O(N\log^2 N)$ alternate-direction finite difference method for two-dimensional fractional diffusion equations. Journal of Computational Physics, 230,

21:7830-7839.

Webb, J.F., Montgomery, J.C., Mogdans, J., (2008) Bioacoustics and the lateral line system of fishes. In: Webb, J.F., Fay, R.R., Popper, A.N. (eds) Fish bioacoustics, Springer Science+Business Media, New York, 17-48.

Weber, M. J., Brown, M. L., (2009) Effects of common carp on aquatic ecosystems 80 years after "carp as a dominant": ecological insights for fisheries management. Reviews in Fisheries Science 17(4): 524-537.

Welton, J.S., Beaumont, W.R.C., Clarke, R.T., (2002) The efficacy of air, sound and acoustic bubble screens in deflecting Atlantic salmon Salmo salar L., smolts in the River Frome, UK. Fisheries Management and Ecology 9: 11-18.

Welton, J.S., Beaumont, W.R.C., Ladle, M., Masters, J.E.G. (1997) Smolt trapping using acoustic techniques. Phase 1, literature review and initial investigation of acoustic bubble screens. Bristol: Environmental Agency, R&D Technical Report W66.

Weron, A., Weron, R., (1995) Computer simulation of Levy alpha-stable variables and processes, in Garbaczewski, P. (Ed.), Chaos: The Interplay Between Stochastic and Deterministic Behavior, Lect. Notes. Phys., Springer, Berlin, 457, 379-392.

Wrobel, L.C., Aliabadi, M.H., (2002) The boundary element method: Applications in thermo-fluids and acoustics, John Wiley and Sons, New York, USA.

Xicheng, L., Mingyu, X., Showel, W., (2007) Analytical solutions to the moving boundary problems with space–time-fractional derivatives in drug release devices. Journal of Physics A: Mathematical and Theoretical, 40, 12131.

Yang, Q., (2010) Novel analytical and numerical methods for solving fractional dynamical system. PhD Thesis, Queensland University of Technology. Australia.

Yang, Q., Liu, F., Turner, I., (2010) Numerical Methods for Fractional Partial Differential Equations with Riesz Space Fractional Derivatives. App. Math. Model 34, 200-218.

Yang, Q., Liu, F., Turner, I., (2010) Stability and Convergence of an Effective Numerical Method for the Time-Space Fractional Fokker-Planck Equation with a Nonlinear Source Term. International Journal of Differential Equations, 464321.

Yang, Q., Turner, I., Liu, F., Ilic, M., (2011) Novel Numerical Methods for Solving the Time-Space Fractional Diffusion Equation in Two Dimensions. SIAM Journal on Scientific Computing 33, 1159-1180.

Yong, Z., Benson, D., Meerschaert, M. Scheffler, H., (2006) On Using Random Walks to Solve the Space-Fractional Advection-Dispersion Equations. Journal of Statistical Physics, 123, 89-110.

Zabel, R.W., Anderson, J.J., (1997) A model of the travel time of migrating juvenile salmon, with an application to Snake River spring chinook salmon. N. Am. J. Fish. Manage. 17, 93-100.

Zeddies, D.G., Fay, R.R., Gray, M.D., Alderks, P.W., Acob, A., Sisneros, J.A., (2012) Local acoustic particle motion guides sound-source localization behavior in the plainfin midshipman fish, Porichthys notatus. J. Exp. Bio. 215, 152-160.

Zhang , Y., Benson, D.A., Reeves, D.M., (2009) Time and Space Nonlocalities Underlying Fractional-Derivative Models: Distinction and Literature Review of Field Applications. Advances in Water Resources, 32, 561-581.

Zhang, X., Crawford, J.W., Deeks, L.K., Stutter, M.I., Bengough, A.G., Young, I.M., (2005) A mass balance based numerical method for the fractional advection-dispersion equation: Theory and application. Water Resources Research 41, W07029.

Zhang, X., Johnson, S.N., Crawford, J.W., Gregory, P.J., Young, I.M., (2007c) A general random walk model for the leptokurtic distribution of organism movement: Theory and application. Ecological Modelling 200, 79-88.

Zhang, X., Lv, M., Crawford, J.W. and Young, I.M., (2007a) The impact of boundary on the fractional advection–dispersion equation for solute transport in soil: Defining the fractional dispersive flux with the Caputo derivatives. Advances in Water Resources, 30, 1205-1217.

Zhang, Y. D. Benson, M.M. Meerschaert, E.M. LaBolle, (2007b) Space-fractional advection-dispersion equations with variable parameters: Diverse formulas, numerical solutions, and application to the Macrodispersion Experiment site data. Water Resources Research, 43, W05439.

Zielinski, D.P., (2011) Bubble barrier technologies for common carp. University of Minnesota, MS Thesis, Minneapolis, MN.

Zielinski, D.P., Voller, V.R., (2012) Numerical Solutions of a Two-Dimensional Caputo Fractional Diffusion Equation", in B.H.V. Topping, (Editor), "Proceedings of the Eighth International Conference on Engineering Computational Technology", Civil-Comp Press, Stirlingshire, United Kingdom, paper 80, doi:10.4203/ccp.99.80.

Zielinski, D.P., Voller, V.R., (2013a) A random walk solution for fractional diffusion equations, International Journal of Numerical Methods for Heat and Fluid Flow, 23, 7-22.

Zielinski, D.P., Voller V.R. (2013b) The control volume weighted flux scheme (CVWFS) for two-dimensional, two-sided Caputo fractional diffusion equations, Submitted to Advances in Engineering Software, January 2013.

Zielinski, D.P., Voller, V.R., Svendsen, J.C., Hondzo, M., Mensinger, A.F., Sorensen, P., (2013) Laboratory experiments demonstrate that bubble curtains can effectively inhibit movement of common carp. Submitted to Ecological Engineering, April 22, 2013.

Zielinski, D.P., Hondzo, M., Voller, V.R. (2013a) Mathematical evaluation of behavioral deterrent systems to disrupt fish movement. Submitted to Ecological Modeling, June 18, 2013.

Zienkiewicz, O.C., Taylor, R.L., (1989) The finite Element Methods Vol. 1. Basic Formulations and Linear Problems. McGraw-Hill, London, England.

Zweiacker, P.J., Gaw, J.R., Green, E., Adams, C., (1997) Evaluation of an air-bubble curtain to reduce impingment at an electric generating station. Proceedings of the Annual Conference of SE Association Fish Wildlife Committee 31: 343-356.

Appendix A: Additional sound pressure level spectrum measurements

Supplementary Data 1 in:D.P. Zielinski, V.R. Voller, J.C. Svendsen, M. Hondzo, A.F. Mensinger, P. Sorensen. Laboratory experiments demonstrate that bubble curtains can effectively inhibit movement of common carp, Submitted to *Ecological Engineering*, April 22, 2013.

The following plot provides the SPL spectrum of the coarse-bubble curtain at select locations in the tank.

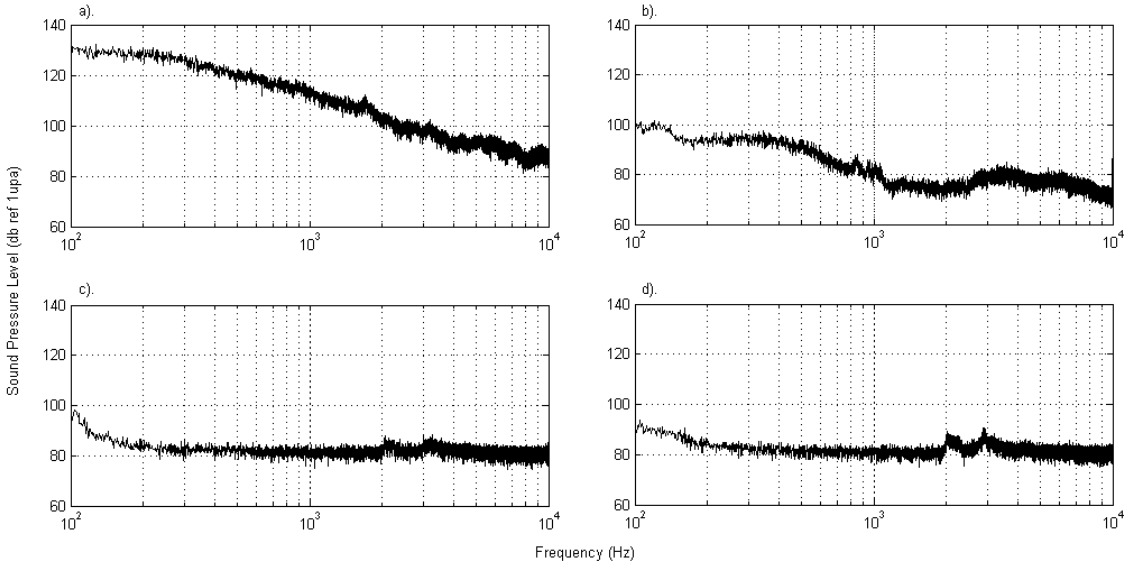

Figure A-1. Sound pressure power spectrum in the tank during coarse-bubble trials. Measurements are provided along the centerline of the tank at a clockwise angle a). 0°, b). 45°, c). 180°, and d). 270° at a depth of 12.5 cm above the bottom of the tank.

Appendix B: Acoustic and hydrodynamic fields generated by individual bubble curtains

Supplementary Data 2 in:D.P. Zielinski, V.R. Voller, J.C. Svendsen, M. Hondzo, A.F. Mensinger, P. Sorensen. Laboratory experiments demonstrate that bubble curtains can effectively inhibit movement of common carp, Submitted to *Ecological Engineering*, April 22, 2013.

1 Introduction

To identify the physical properties of the typical bubble curtain, while relating them to biological responses, measurements of the acoustic and fluid flow fields generated by the bubble curtains under varying conditions were performed. Initial measurements of the acoustic and hydrodynamic properties of individual bubble curtains were performed in a straight flume that was better suited to take precise measurements. These measurements were used to enhance our understanding of how the stimuli fields were influenced by changes in the air flow rate, bubbles size, and fluid flow and help inform the design of larger scale and more complex bubble curtain systems.

2 Materials and Methods

Initial measurements of the sensory stimuli created by a bubble curtain were performed in a straight flume (0.5 m wide x 0.92 m high x 10 m long). In order to isolate the typical sensory fields generated by a simple bubble curtain, two different bubble curtains employing differently spaced and sized bubbles were investigated. The bubble curtain systems consisted of either a porous polyethylene pipe (~25 micron pores) or perforated PVC pipe with 1 mm holes spaced at 1 cm. The bubble curtains were supplied between 2.5 and 2.8 $Ls^{-1}m^{-1}$ of air (approximately the air flow rate each pipe consumed in the fine- and graded-bubble systems discussed in the study). Measurements were taken for each bubble curtain under a depth of 25 cm, a depth expected in interconnecting streams between lakes in Midwestern North America. The impact of flow was also considered by subjecting each bubble curtain to mean channel velocities of 0.0, 10.0, and

20.0 cm s^{-1}. Photographs were taken of the bubble curtains to quantify the typical bubble size and the size and shape of the bubble curtain.

Velocity and acoustic pressure measurements were taken along the centerline plane parallel to the flume bottom at 5, 10, 15, and 20 cm at a distance of 5, 10, 25, 50, and 100 cm up- and down-stream of the bubble curtain. The velocity fields were characterized by measurements from a SonTek 16-Mhz MicroADV (Acoustic Doppler Velocimeter) (SonTek, CA, USA) mounted on a mobile instrument track. Instantaneous velocity measurements were taken at a frequency of 50 Hz. At this rate, 3000 instantaneous measurements of velocity were recorded for each sample point (n=40) for a sampling period of 60 s. The data were filtered and analyzed through SonTek software HorizonADV and WinADV. These measurements were used to quantify the time-averaged velocities, flow patterns, fluctuating velocities, and Reynolds shear stress. Velocity measurements were not made near the water surface (<5 cm) due to the size of the ADV instrument. In this study, the Reynolds shear stress (τ) was defined for the plane XY (Kundu, 1990) as:

$$\tau_{xy} = -\rho \overline{u'_x u'_y}$$

where ρ is the water density (1000 kg/m^3) and u' is the fluctuating velocity component in the *x* and *y* plane. The Reynolds stresses represent a shear stress that occurs when two water masses or layers of different velocities are parallel or adjacent to each other (Silva et al. 2011). Acoustic measurements were obtained using the same equipment and procedure outlined in the main document.

3 Results

The porous pipe generated bubbles between 1-2mm in diameter, while the perforated pipe formed 5mm diameter bubbles. The resonant frequencies of the bubbles using the equation for Minneart's frequency (Leighton; 1994) would be between 500-3000Hz.

Flow topology was not found to vary significantly between the porous or perforated pipes or air flow rates, thus for conciseness we limit our visual description (Figure B-1) to the perforated pipe at an air flow rate of 2.5 $Ls^{-1}m^{-1}$. Velocity

measurements taken in the straight flume revealed that the flow field was dominated by recirculation cells, rotating about a center located 1-2 times the depth away from either pipe at both air flow rates (Figure B-1). In addition, water velocities were found to be lower near the water surface than near the channel floor. Although not recorded with the ADV, complimentary flow away from the bubble curtains was visually observed at the water surface during all experiments. In general, the porous pipe generated higher water velocities when compared to the perforated diffuser pipe (Table B-1). Under no fluid flow conditions, the velocity field was symmetric about the bubble curtain with a maximum velocity of 15 cm s^{-1} (Table B-1) (Figure B-1a). However, when subjected to a main channel velocity of 20.0 cm s^{-1}, the recirculation cells elongate on the downstream side and compress on the upstream side of the bubble curtain (Figure B-1b).

Table B-1. Summary of the physical properties of the individual pipes studied in the straight flume under variable air and water flow. The porous pipe was a polyethylene pipe with 25 micron pores over the entire surface, while the perforated pipe was a PVC pipe drilled with 1mm holes at intervals of 1 cm. Water depth was maintained at 25 cm.

Bubble Curtain	Water Velocity (cm s^{-1})	Air flow rate ($Ls^{-1}m^{-1}$)	Maximum Velocity (cm s^{-1})	Maximum Reynolds stress (N m^{-2})	Maximum SPL (dB ref. 1 μPa)
Porous Pipe	0	2.5	16	4.2	100
	0	2.8	17	4.7	112
	10	2.5	16*	1.3	98
	20	2.5	20*	2.9	98
Perforated Pipe	0	2.5	12	2.5	120
	0	2.8	13	2.5	125
	10	2.5	20*	1.9	120
	20	2.5	20*	3.0	120

*maximum velocities influenced by background flow in the channel

Reynolds shear stresses in the XY plane differed between the porous or perforated pipes at each air flow rate; however, the stresses did not increase with air flow rate (Table B-1). The Reynolds shear stress increased near the water surface without flow in the channel, where it reached values > 1.5 N m^{-2} (Figure B-1a) as a result of surface outflow. In contrast, the Reynolds shear stress decreased near the bottom of the channel, where it reached values < 0.5N m^{-2}. When subjected to a main channel velocity of 20.0cm s^{-1},

high Reynolds shear stresses are observed further downstream of the bubble curtain, where values > 3N m^{-2} (Figure B-1b) were reached.

The bubble curtains investigated in this pilot study generated a broad spectrum acoustic field with a peak frequency between 100 Hz and 300 Hz (Figure B-2). The perforated diffuser pipe generated higher SPLs in the straight flume experiments compared to the porous pipe (Table B-1). The maximum SPL field generated by the perforated pipe under 2.5 $Ls^{-1}m^{-1}$ air flow rate (Figure B-3) illustrates the typical propagation of sound away from the bubble curtain under main channel velocities of 0.0 cm s^{-1} and 20.0 cm s^{-1}. The background SPL was measured to be 62 dB (re 1 μPa) under no flow and 65 dB (re 1 μPa) under 20.0 cm s^{-1} water velocity. Although the bubble curtains subjected to main channel velocities experienced angular deformations in the downstream direction of 18° and 33° (at 10.0 cm s^{-1} and 20.0 cm s^{-1} respectively) (Figure B-3), the maximum SPL generated by the perforated pipe was not altered by the main channel velocity, instead the sound pressure contours shifted downstream as a result of bubble curtain deformation (Figure B-3b).

To our knowledge, this study is the first attempt to quantitatively measure the stimuli fields generated by bubble curtains in relation to fish guidance. The hydrodynamic investigation detailed in the Supplementary Data revealed that average velocities created by similar sized bubble curtains do not exceed those expected in carp habitats (Jones and Stuart, 2007) and were within the sustained (aerobic) swimming capacity of common carp (Tudorache et al., 2008). In addition, the Reynolds shear stresses generated by a single perforated, or porous diffuser pipe were low enough to avoid causing injury but may still be able to cause some fish disorientation or displacement. Silva et al. (2012) found that Reynolds shear stresses between 0.02 N m^{-2} and 73.4 N m^{-2} were the main factor that explained passage success for a similar sized cyprinid. However, for bubble curtains high stresses were only observed near the water surface, or not at all on the upstream side of the bubble curtain when subjected to some cross flow. The lack of high water velocities and significant turbulence that occupies the full water column reduces the potential of hydrodynamic forces as a main influence on fish movement through a bubble curtain.

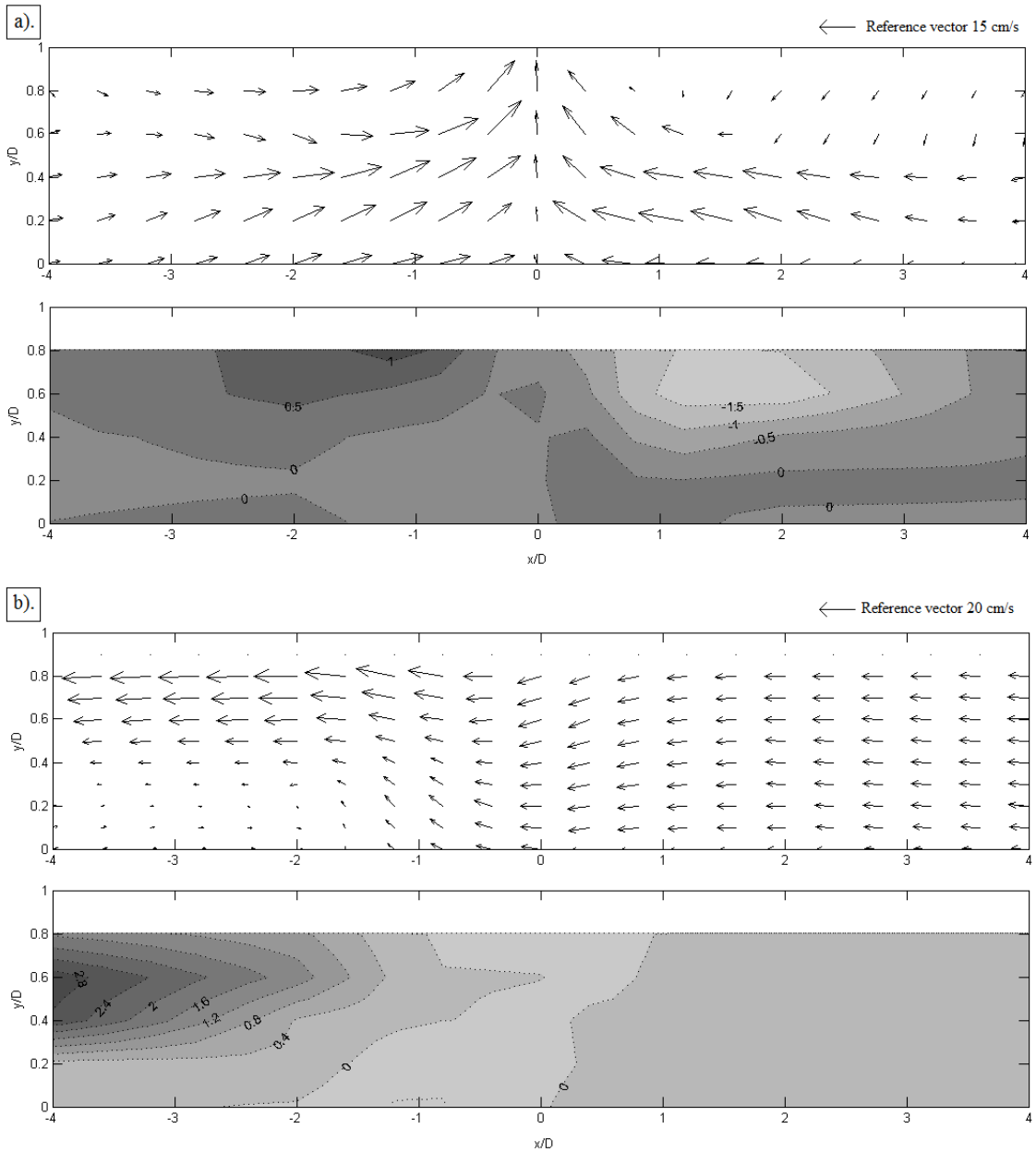

Figure B-1. Flow topology (top) and Reynolds shear stress (N m^{-2}) in the XY plane (bottom) for perforated diffuser pipe (1 mm holes spaced at 1 cm) with an air flow rate of 2.5 $Ls^{-1}m^{-1}$ in a straight flume under a) 0 cm s^{-1} and b) 20 cm s^{-1} cross flow (from right to left). Axes are normalized by the depth *D*=25 cm and the barrier is centered about x/D=0.

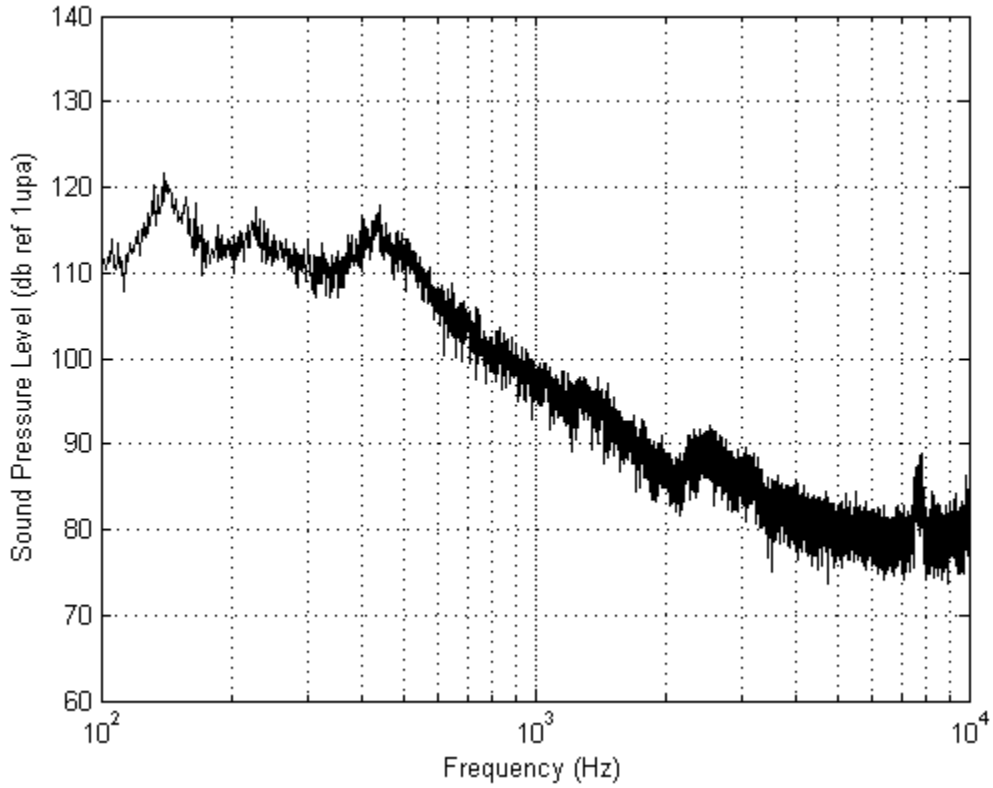

Figure B-2. Sound pressure level power spectrum in the straight flume during use of the perforated diffuser pipe (1mm holes spaced at 1cm) at an air flow rate of $2.5Ls^{-1}m^{-1}$. The measurement is taken at a depth of 20cm, 5cm away from the diffuser pipe.

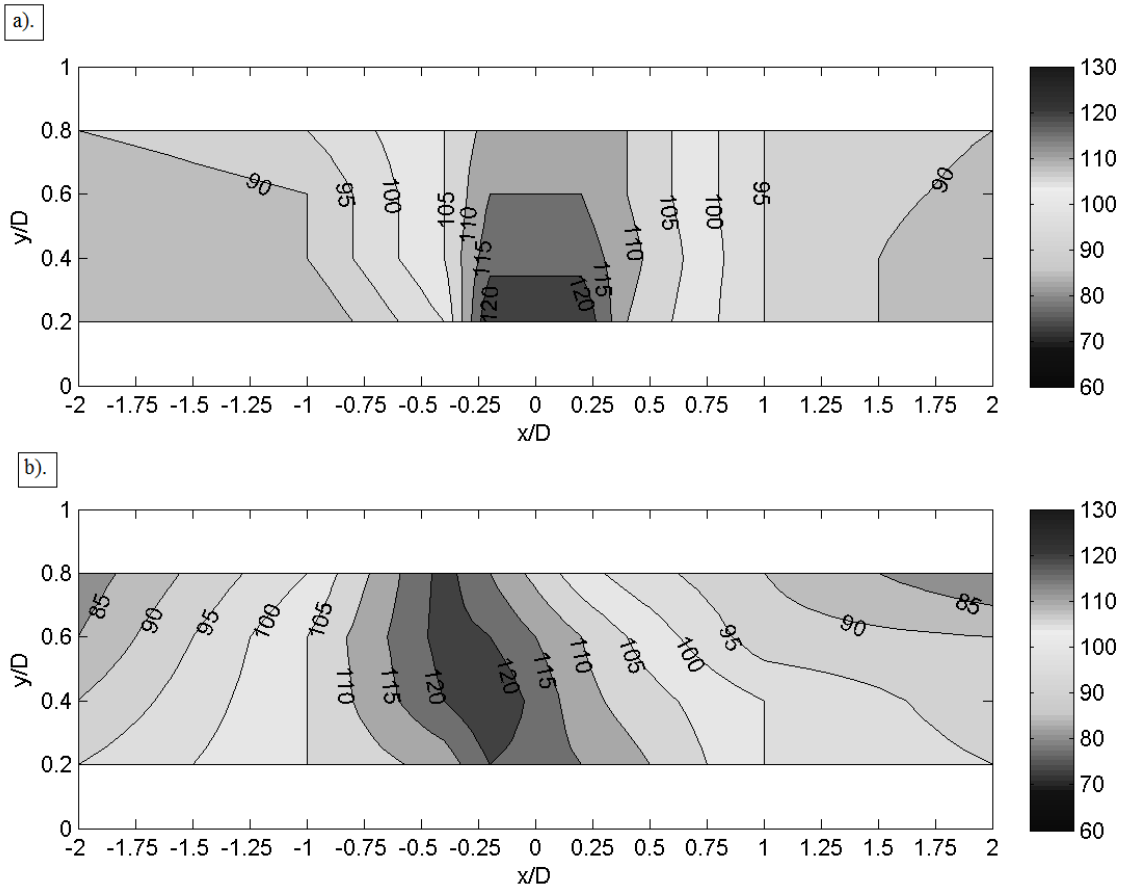

Figure B-3. Sound Pressure Level (SPL) contours dB (re 1 μPa) created by the perforated pipe (1 mm holes spaced at 1 cm) with an air flow rate of 2.5 $Ls^{-1}m^{-1}$ in a straight flume under a) 0 cm s^{-1} and b) 20 cm s^{-1} cross flow (from right to left). Axes are normalized by the depth *D*=25 cm and the diffuser pipe is centered about x/D=0.

Appendix C: Analysis of step-size distributions for evidence of Lévy flight movement patterns

1 Introduction

Classical diffusion models provide a standard theoretical tool by which patterns of fish movement are compared (Okobu and Levin, 2001; Gurarie et al., 2009). Built on principles in physics, the classical diffusion equation is a continuum approximation of an ensemble of particles undergoing isotropic random walks (i.e. Brownian motion). The primary assumption underlying classical diffusion is that individuals or particles move independently and homogenously disperse. Unlike transport of passive particles, dispersal traits are often highly variable among living organisms of the same species (Kot et al., 1996). Differences among individual size, age, gender, and maturity can cause variation in movement characteristics, but Fraser et al. (2001) and Rehage and Sih (2004) have suggested that differences among behavioral traits may also influence dispersal and, in certain cases, species invasiveness. Indeed, several fish movement studies have observed dispersal distances that diverge from being normally distributed, as expected for homogenous spreading, to being leptokurtically distributed (i.e. high density of dispersers near the mean and tails of the distribution) (Cote et al., 2010; Rehage and Sih, 2004; Fraser et al., 2001; Skalski and Gilliam, 2000; Bradford and Taylor, 1997). In these cases, an assumption of Gaussian (normally distributed) spreading will underestimate the arrival time of the dispersal front. Hence, understanding how heterogeneous dispersal traits impact fish movement is critically important to fisheries management, and in particular the control of invasive fish.

At high levels of intra-species variability, dispersal traits can no longer be homogenized across a population and the classical diffusion model becomes invalid for predicting population dispersal. For this situation, multi-state diffusion models (Skalski and Gilliam, 2000 and 2003), gamma-variance process (Gurarie et al., 2009), and fractional-diffusion models (Meerschaert, 2012; Viswanathan et al., 2011; Petrovskii et al., 2008; Zhang et al., 2007c) have been suggested for capturing variation in dispersal

distances taken by a population. Multi-state diffusion models partition a population into distinct subgroups (e.g. slow vs. fast swimmers, model each as independent populations with classical diffusion models, and the superposition of multiple Gaussian dispersals results in a leptokurtic distribution of dispersal distances (Skalski and Gilliam, 2000 and 2003). In contrast, Gurarie et al. (2009) proposed to model heterogeneities by assuming a given movement parameter (e.g. diffusion or advection coefficient) varies within a population according to a continuous gamma distribution. Although these methods recover leptokurtic distributions, the underlying dispersal mechanism is still subject to classical diffusion theory.

An alternative to these heterogeneous dispersal models are fractional-diffusion models. Several studies have suggested that anomalous diffusion (i.e. spreading not consistent with normal diffusive processes) can be replicated by Lévy flights (i.e. random walk process where step-sizes are selected from distributions with heavy power-law tails) which are approximated by fractional-diffusion equations at the stable limit (Viswanathan et al., 2011). In contrast to the multi-state model, this method assumes all individuals follow the same behavioral rules, and heterogeneities arise from population level step size distributions rather than individual differences. A prominent characteristic of organisms performing Lévy flights is non-linear growth of variance. Although substantial evidence has been collected to suggest anomalous dispersal in organisms (Viswanathan et al. ,2011; Humphries et al., 2010), Lévy motion remains a highly controversial topic in movement ecology as evidence of earlier claims of Lévy motion have been refuted (Edwards et al., 2007; Edwards, 2011).

The effects of heterogeneous dispersal are particularly important in the development and assessment of new behavioral deterrent systems, which rely on aversive stimuli like sound and light to guide fish in taxon specific manners. Zielinski et al. (2013) recently demonstrated that a bubble curtain deterrent system can inhibit the movement of invasive common carp, *Cyprinus carpio*, and later illustrated through stability analysis of a diffusion based movement model that disruption of movement patterns, hypothesized as being indicative of a successful bubble curtain, depends on organism diffusion and repulsive response to the bubble curtain (Zielinski et al., 2013a).

Although the classical advection-diffusion equation used by Zielinski et al. (2013a), was capable of predicting dispersal of 23 out of 24 focal fish, the dispersal traits of the remaining fish, which moved in nearly ballistic fashion, was excluded from analysis. Specifically, the displacement of the remaining fish over time suggested possible anomalous behavior (e.g. the fish traveled ~3 times farther than all other fish and caused non-linear growth of dispersal variance $\sim t^{1.94}$, in Figure 2 in Zielinski et al., 2013a). Therefore, the movement data of common carp in the vicinity of a bubble curtain (Zielinski et al., 2013) are re-analyzed to test whether the anomalous dispersal is a result of a Lévy process. Modern likelihood and Akaike information criterion (AIC) (Edwards et al., 2007) are used to test whether the step-size distributions exhibit power-law or exponentially decaying tails.

2 Methods

The step-size analysis outlined here follows modern statistical methods for model selection introduced by Edwards et al. (2007) and Edwards (2011). First, two power-laws and one exponential distribution are fit to common carp movement data using likelihood tests, and the optimal distribution is selected using AIC relative likelihood ratios. Next, the goodness-of-fit test of the optimal distribution is found by comparing with common carp step-size distributions to assess the goodness-of-fit. This analysis is performed for movement lengths at the individual level.

If an organism performs a Levy flight, the step-size distribution will have a power-law decaying tail. Because the Levy foraging hypothesis (Viswanathan et al., 2011) is only concerned with the shape of the distribution tail (i.e. large movements), the probability density function for a power-law distribution of steps greater than a minimal step size a is

$$f(x) = (\mu - 1)a^{\mu-1}x^{-\mu} \quad x \geq a \tag{1}$$

where $1 < \mu \leq 3$ is the power-law exponent, and the log-likelihood function is

$$\log\left[L(\mu|\text{data } \mathbf{x})\right] = n\log(\mu - 1) + n(\mu - 1)\log a - \mu\sum_{j=1}^{n}\log x_j \tag{2}$$

Here, a is estimated from binned step-sizes as the start of power-law decay of the distribution. In this form, a power-law distribution allows for the selection of rare, but extremely large step sizes. At the stable limit of a Levy flight, with step-sizes chosen from equation (1), the fractional-diffusion equation can be used to approximate dispersal. Recently, this concept has been applied to the study of non-Gaussian spreading in fluid and sediment transport processes (See Appendix D-G for extensive discussions on numerical modeling techniques for fractional diffusion). However, living organisms are not able to perform infinitely large step lengths. Therefore, a truncated form of equation (1) must be defined such that a maximum step-size, b, is set for organism dispersal (Edwards, 2011)

$$f(x) = \frac{(\mu - 1)}{\left(a^{1-\mu} - b^{1-\mu}\right)} x^{-\mu} \quad x \in [a, b] \tag{3}$$

And log-likelihood function

$$\log\left[L(\mu | \text{data } \mathbf{x})\right] = n \log(\mu - 1) - n \log\left(a^{1-\mu} - b^{1-\mu}\right) - \mu \sum_{j=1}^{n} \log x_j \tag{4}$$

In equation (3), b is set as the maximum step size observed by each common carp. In contrast, if an organism performs a normal random walk (Gaussian spreading) the step-size distribution will exhibit an exponential tail. The probability density function for the simplest form of an exponential tail form movement lengths greater than a is

$$f(x) = \lambda e^{-\lambda(x-a)} \quad x \geq a \tag{5}$$

where λ is the rate of exponential decay and the log-likelihood function

$$\log\left[L(\lambda | \text{data } \mathbf{x})\right] = n \log \lambda + n\lambda a - \lambda \sum_{j=1}^{n} x_j \tag{6}$$

A truncated exponential tail distribution need not be considered because the distribution described by equation (5) decays fast enough that extremely large step lengths are exceedingly rare.

Appropriate maximum likelihood estimates (MLE) for μ and λ and Akaike's information criterion (AIC) are calculated for the step-size distributions of each fish

individually and combined as an ensemble (Edwards et al., 2007). The AIC for each model is

$$AIC_i = -2\log\left[L_i\left(\theta_i \middle| data\mathbf{x}\right)\right] + 2K_i \tag{7}$$

where $\theta_1 = \theta_2 = \mu$, $\theta_3 = \lambda$ and K_i is the number of parameters estimated from the data $(K_i = 2)$. Once MLEs of model parameters are derived, each model was plotted on a log-log rank-frequency plot to visually inspect the fit of each model.

Next, following the approach by Edwards et al., (2011), evidence ratios of AIC were computed for each model and normalized such that the model with an evidence ratio of 1 was considered to be the best fit for the data. Finally, a chi-squared goodness-of-fit test was performed for the best fit model to test whether the data are consistent with the best model (Conover, 1980). A model was considered to be consistent with observed step-sizes when $p \geq 0.05$.

3 Results and Discussion

Zielinski et al. (2013a) demonstrated that that when all common carp are included in the movement analysis, variance grows non-linearly in time which suggests possible anomalous (i.e. Lévy-like) behaviors. Therefore, the step-size distribution, at a time scale of 1 min, for each fish is calculated and tested using the approach outlined in Section 2. Table C-1 lists the maximum/minimum step size, evidence ratios, MLE parameter and goodness-of-fit statistics for the most supported model. In addition, Figure C-1 shows the raw data and model fits for fish #1, 2, 4, and 18 (i.e. cases where the best fit model was consistent with movement data) on a rank vs. frequency plot. Although one fish (#3) appeared to move in a nearly ballistic manner in Figure 4-2a of Zielinski et al. (2013a) there was little variation between maximum step lengths (6.3-17.3 m) employed by each fish.

The power-law model was not the best fit model for any of the fish; in fact the evidence ratio was below 100 only for fish #20 and #15. The limited range of fish movement (i.e. less than an order of magnitude difference between a and b) may have contributed to the lack of support for this model. Additionally, the power-law model

allowed for movement lengths far exceeding the maximum observed distances, and thus could not be supported by the data. Based on these findings, an unbounded power-law and formal fractional-diffusion equation should not be used to model the dispersal of these fish.

In contrast, the truncated power-law model was the best fit model for ten of the fish, and received mild support from two more fish (#19 and #22). Because the truncated power-law model supported nearly half of the movement data collected, a power-law model, albeit not the unbounded form in equation (1), may still be a good model for this data set. Indeed, the goodness-of-fit tests show that the truncated power-law is consistent with movement data for fish #2 $(P = 0.073)$ and #4 $(P = 0.18)$. The MLE of these two fish exhibited a power-law relationship of order $\mu = 2.7$, equating to a Lévy index $\alpha = \mu - 1 = 1.7$ (Viswanathan et al., 2011) which is close to the normal distribution limit of $\alpha = 2$. The MLE exponent does not follow the expected relationship for variance growth in Figure 4-2a (Zielinski et al., 2013a), where $Var \sim t^{3-\alpha}$; however, this was expected since the MLE exponent was estimated on the individual level, not the population level of the variance.

The exponential model was the best fit model for the remaining fourteen fish. Based on evidence ratios, the exponential model may be a good model for this data; however, goodness-of-fit test suggest otherwise. The *P*-values in Table 1 only exceed $P > 0.01$ for fish #18 and #1. Although the exponential model was not consistent with movement data for any of the fish, the MLE value was relatively constant, $\lambda \sim 0.4$, across data in which it was the best fit. At the population level, the exponential model the best fit based on evidence ratios, but the goodness-to-fit test indicated that it was not consistent with movement data.

Overall, the likelihood and AIC analysis approach did not uncover sufficient evidence to support a comprehensive Lévy flight model for common carp movement in a laboratory tank. Instead, limited support for truncated Lévy flights was observed for two of the common carp. Viswanathan et al. (2011) argued that support for truncated power-laws may still imply an underlying Lévy process because singularities, such as infinitely

large movement lengths, are impossible to observe in physical systems. However, the lack of a single explanatory model for each fish highlights dispersal traits, even in populations as small as the group considered here, are not homogenous. Lack of support for power-law models in the AIC approach suggests for the majority of fish, the step-size distribution did not exhibit heavy, power-law tails. In fact, exponential model preference along with power-law exponent MLEs near the normal limit, $\mu = 3$, provides further evidence that common carp may disperse according to a classical diffusion model.

Table C-1. Evidence ratios and goodness-of-fit results

			Evidence ratios			MLE	Goodness-of-fit best model	
Fish	*a*	*b*	P	TP	Exp	μ/λ	*n*	*P*
1	1.7	11.0	10^{19}	10^{3}	**1.0**	0.39	152	0.013
2	1.4	9.4	10^{4}	**1.0**	10^{11}	2.63	270	0.073
3	1.7	11.0	10^{71}	**1.0**	10^{9}	1.02	324	10^{-43}
4	1.4	9.4	640	**1.0**	10^{12}	2.79	241	0.18
5	2.1	14.1	10^{19}	10^{11}	**1.0**	0.46	210	0
6	2.5	17.3	10^{4}	590	**1.0**	0.50	176	0
7	0.9	6.3	10^{28}	10^{9}	**1.0**	0.77	264	0
8	1.4	9.4	10^{4}	**1.0**	10^{17}	2.65	292	0.003
9	1.7	11.0	10^{29}	3200	**1.0**	0.36	206	10^{-9}
10	1.4	9.4	10^{11}	**1.0**	10^{9}	2.07	321	0.002
11	1.7	11.0	10^{31}	10^{4}	**1.0**	0.35	207	10^{-20}
12	1.4	9.4	10^{7}	**1.0**	10^{10}	2.39	315	0.009
13	1.4	9.4	10^{19}	**1.0**	10^{8}	1.73	344	0.024
14	1.7	11.0	10^{26}	3300	**1.0**	0.36	191	10^{-7}
15	1.4	9.4	41	**1.0**	10^{8}	3.18	266	0
16	1.9	12.6	10^{35}	1000	**1.0**	0.30	241	10^{-29}
17	1.7	11.0	10^{38}	**1.0**	75	1.02	220	10^{-19}
18	1.9	12.6	10^{21}	10^{8}	**1.0**	0.41	193	0.020
19	1.2	7.9	10^{5}	9.0	**1.0**	0.98	258	0
20	1.4	9.4	88	**1.0**	10^{8}	1.41	273	0.008
21	2.1	14.1	10^{23}	470	**1.0**	0.30	219	10^{-7}
22	1.7	11.0	10^{23}	9.0	**1.0**	0.34	165	10^{-5}
23	2.4	15.7	10^{19}	110	**1.0**	0.28	217	10^{-4}
24	2.4	15.7	10^{18}	10^{6}	**1.0**	0.34	213	10^{-5}

Notes: The model with the most support has an evidence ratio of 1.0 (shown in bold). Sample size is *n* and *P* is the value for the goodness-of-fit tests (Chi-squared test, Conover, 1980) for the model with evidence ratio 1.0. If $P > 0.05$ then the best fit model is considered to be consistent with the observed step-size distribution.

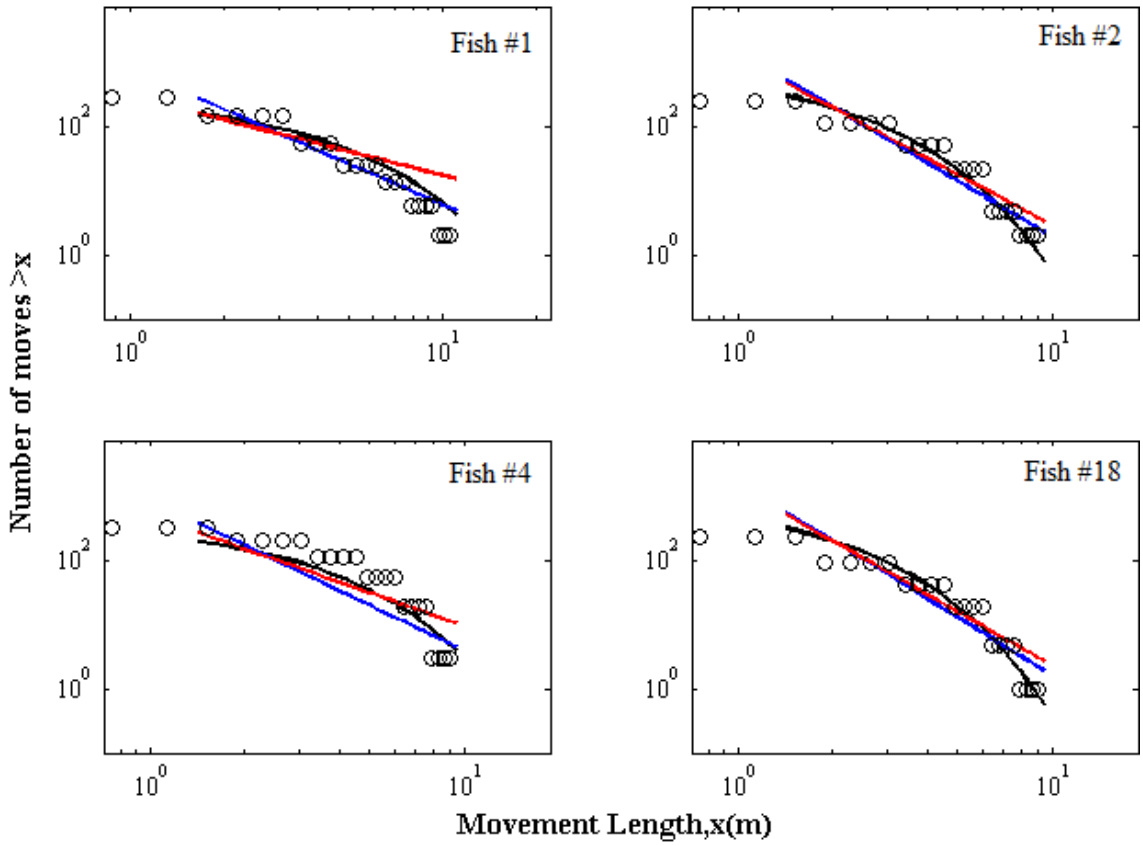

Figure C-1. Rank vs. frequency plots of common carp movement data for fish #1, 2, 4, and 18 and model predictions between a and b. Black circles denote actual ranked step size frequency for each fish. The three model fits are power-law (red line), truncated power-law (blue line), and exponential (black line),

Appendix D: The control volume weighted flux scheme (CVWFS) for non-local diffusion and its relationship to fractional calculus

Published as: Voller, V.R., Paola, C. and Zielinski, D.P. (2011), The Control Volume Weighted Flux Scheme (CVWFS) for Non-Local Diffusion and Its Relationship to Fractional Calculus, *Numerical Heat Transfer B,* **59**, 421-441.

In diffusion transport, the flux at a point is typically modeled in terms of the local gradient of a potential. When heterogeneities are present this local model can break down and it may be more appropriate to model the diffusion flux as a weighted sum of gradients present throughout the domain. Here a discrete non-local flux model—consistent with control volume implementations—is developed. This scheme is referred to as the Control Volume Weighted Flux Scheme (CVWFS). The key component is the modeling of the diffusion flux at a given control volume face in terms of a weighted sum of gradients at that face and at faces up- and down- stream. Criteria for choosing the weights are proposed. This results in numerical solution schemes where the coefficient matrix is diagonally dominant, has positive off-diagonal elements, and zero row sums. For a particular power-law weighting scheme it is shown how the CVWFS is related to the definition of the Caputo fractional derivative and the one-shift Grünwald approximation of the Riemann-Liouville fractional derivative. On developing transients and boundary condition treatments, the accuracy and suitability of the CVWFS scheme is demonstrated by solving a number of problems governed by Caputo fractional diffusion equations.

NOMENCLATURE

c	specific heat
${}_0^C D_x^\alpha$	Caputo fractional derivative from the left in [0,1]
${}_x^C D_1^\alpha$	Caputo fractional derivative from the right in [0,1]
g	Grünwald weight
k	conductivity
ℓ	heterogeneity length scale
q	flux
s	source
t	time
T	temperature
W	weight
x	space
$\frac{\partial^\alpha}{\partial x^\alpha}$	fractional derivative operator from the left
$\frac{\partial^\alpha}{\partial(-x)^\alpha}$	fractional derivative operator from the right
α	fractional order or locality
β	skew in pdf
Δt	time step
Δx	space step
$\Delta\tau$	pseudo time step
θ	CVWFS coefficient
μ	weight correction
ρ	density

Subscripts

I	node I
in	in face
out	out face
val	specified value

Superscripts

L	Derivative from left
R	Derivative from right

1 Introduction

It is well known that diffusion processes can be represented by random walk models with step lengths chosen from a suitable probability density functions (pdf). With a Gaussian pdf—where the probability of taking a step of a given size decays exponentially with its length—a random walk process leads to a diffusion flux $\boldsymbol{q}(\boldsymbol{x})$ modeled as the product of a constant and the potential gradient at a local point (Metzler and Klafter, 2000), e.g., for thermal diffusion in the x-direction

$$q(x=a) = -k\left.\frac{\partial T}{\partial x}\right|_{x=a} \tag{1}$$

where k is the thermal conductivity and T is temperature. On setting the divergence of this flux equal to source and transient terms the general one-dimensional thermal diffusion equation can be formed,

$$\rho c\frac{\partial T}{\partial t} = \frac{\partial}{\partial x}\left(k\frac{\partial T}{\partial x}\right) + s(x,T) \tag{2}$$

where a constant density ρ and specific heat c have been assumed.

In the presence of heterogeneities (Zhang et al., 2009; Schumer et al., 2009; Benson et al., 2000) —spatial regions over which physical properties differ from background average values—the link between a Gaussian distribution and the diffusion flux may no longer be valid. If the heterogeneities occur at all scales, up to and including the domain scale, transport occurs via non-local (anomalous) diffusion (Zhang et al., 2009; Schumer et al., 2009; Metzler and Klafter, 2000; Benson et al., 2000). In such systems the diffusion flux at a point can not be expressed in terms of a local potential gradient. Further, in order to statistically characterize the diffusion process, the Gaussian pdf needs to be replaced with the more general Lévy pdf; a distribution which exhibits "heavy" power law decaying tails. Such a distribution allows for the finite probability of selecting extreme step lengths in a random walk process (Metzler and Klafter, 2000), leading to a non-local diffusion flux that can be compactly expressed in terms of a fractional potential gradient (Zhang et al., 2009; Meerschaert and Tadjeran, 2006)

$$q = -k\frac{1+\beta}{2}\frac{\partial^{\alpha}T}{\partial x^{\alpha}} + k\frac{1-\beta}{2}\frac{\partial^{\alpha}T}{\partial(-x)^{\alpha}} \tag{3}$$

Neglecting any non-local time behaviors, use of this flux in a heat balance leads to a so called "fractional diffusion" equation

$$\rho c\frac{\partial T}{\partial t} = \frac{\partial}{\partial x}\left(k\frac{1+\beta}{2}\frac{\partial^{\alpha}T}{\partial x^{\alpha}} - k\frac{1-\beta}{2}\frac{\partial^{\alpha}T}{\partial(-x)^{\alpha}}\right) + s(x,T) \tag{4}$$

In (3) and (4), as fully described in the appendix, $\frac{d^{\alpha}T}{dx^{\alpha}}$ and $\frac{d^{\alpha}T}{d(-x)^{\alpha}}$ are general fractional derivatives from the left and right respectively, the possible non-integer order of the derivative $0 < \alpha \le 1$ is a measure of the non-locality ($\alpha = 1 \equiv \text{local diffusion}$), and $1 \ge \beta \ge -1$ is a measure of the skewness that distorts the associated Lévy distribution so that the heavier tail is on the right ($\beta > 0$) or left ($\beta < 0$).

Applications of fractional diffusion equation to heat transfer problems associated with the form in (4) have been presented in recent literature. Aoki, Sen, and Paolucci (2008) develop approximate solutions of heat transfer in complex geometries in which the fractional order of the time derivative depends on the Biot number. Jumyi and Mingyu (2009) and Voller (2010) present solutions of the Stefan melting problem expressed in terms of fractional space and time derivatives.

The recent literature has also made significant numerical analysis advances in treating fractional derivative equations (Yang et al., 2010; Ding et al., 2010; Zhang et al., 2007a; Meerschaert and Tadjeran, 2006; Tadjeran et al., 2006; Meerschaert and Tadjeran, 2004; Liu et al., 2004). A well investigated route to appropriate finite difference solutions is through using the one-shift Grünwald approximation of the Riemann-Liouville fractional derivative (Meerschaert and Tadjeran, 2006; Tadjeran et al., 2006; Meerschaert and Tadjeran, 2004) (see definitions in appendix). Here an alternative to the one-shift Grünwald approximation is used to arrive at a solution scheme for diffusion equations with the general form of (4). The key feature in this alternative is that it is based on a physical construct for non-local diffusion which can be directly implemented at the level of a control volume discretization.

The starting point for derivation of the alternative scheme is to recognize that, in a standard control volume method, the diffusion flux at the face of a given control volume is approximated in terms of the potential gradient across that face. In the proposed physical construct, the non-local diffusion flux is modeled as a weighted sum of the potential gradient across the local face and potential gradients at control volume faces located both up- and down- stream of the local face. This approach of modeling the non-local flux is referred as the Control Volume Weighted Flux Scheme (CVWFS). Due to the physical nature of its derivation, the CVWFS directly provides the numerical machinery for a control volume solution (Voller, 2009) of fractional diffusion equations. Further, with the specification of criteria for choosing the weights, the resulting coefficient matrix of the CVWFS exhibits desirable properties for the construction of robust and stable solutions, in particular diagonal dominance, positive off diagonal entries, and row sums of zero.

A link between the proposed CVWFS and the elements of fractional calculus is achieved through the use of a particular set of power-law weights. In the first place, it is shown that the CVWFS representation of a flux approximates a Caputo fractional derivative (defined in the appendix). Secondly it is noted that the coefficients resulting from a CVWFS closely match the weights in the one-shift Grünwald approximation of the Riemann-Liouville fractional derivative of order $\alpha + 1$. These findings allow for the development of effective CVWFS solutions for a range of steady and transient Caputo fractional diffusion equations with the general form given in (4).

2 Derivation of the CVWFS

As opposed to starting from theory and working toward an approximate method for accounting for non-local diffusion, we first develop an approximate scheme from first principals and then show how the elements of this scheme are related to theoretical descriptions of non-local behaviors. This serves the important advantage of starting with an intuitive model of non-local diffusive transport that will underpin later theoretical constructions, such as fractional derivatives, with a more immediate physical analog.

The first step is to consider the control volume approximation of a simple steady state diffusion process. At internal points of a one-dimensional domain the governing equation is,

$$-\frac{d}{dx}(q) = 0 \tag{5}$$

where q is the x-component of the heat flux. Neglecting, for now, the specification and treatment of boundary conditions, we seek a control volume finite difference scheme for the solution of (5). Based on the grid design shown in Figure D-1 the appropriate scheme at node I is

$$\frac{q_{in-I} - q_{out-I}}{\Delta x} = 0 \tag{6}$$

where the fluxes shown are respectively evaluated at the in and out faces of the Ith control volume. If any heterogeneities present are at scale below the control volume size Δx, the face heat fluxes can be expressed in terms of the local gradient, i.e., $q = -k\frac{dT}{dx}$. In this way, using standard finite difference approximations for the *in* and *out* fluxes, the scheme (6) can be written in the familiar control volume form

$$\frac{1}{\Delta x}\left[k_{in-I}\frac{T_{I-1} - T_I}{\Delta x} - k_{out-I}\frac{T_I - T_{I+1}}{\Delta x}\right] = 0 \tag{7}$$

By contrast, in non-local diffusion, due to heterogeneities in the system occurring at length scales larger than the approximating control volume, the flux at a point is not fully determined by the local gradients.

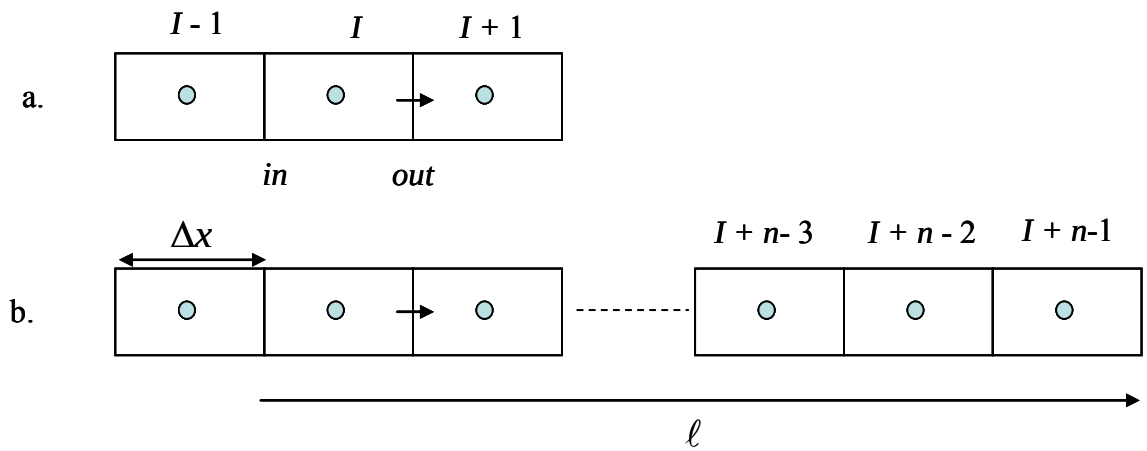

Figure D-1. Grids for calculating diffusion flux. a local diffusion, b non local diffusion

One candidate model for non-local diffusion is to imagine, at each x-location, a unit width occupied by a set of channels, see Figure D-2. To represent the system heterogeneities the channels are assigned varying lengths in the range $0 \le L \le \ell$, where $\ell >> \Delta x$. Within this model, a particular version of non-local diffusion is realized by assuming that the diffusion flux in a given channel is controlled by the gradient at the downstream termination of the channel. In this way, the fluxes in (6) are written as a weighted average of the gradients evaluated at control volume faces downstream of node *I,* i.e.,

$$q_{in-I}^{R} = k_{in-I} \sum_{j=1}^{n} W_j \left[\frac{T_{I+j-2} - T_{I+j-1}}{\Delta x} \right]$$
$$q_{out-I}^{R} = k_{out-I} \sum_{j=1}^{n-1} W_j \left[\frac{T_{I+j-1} - T_{I+j}}{\Delta x} \right] \qquad (8)$$

where $n\Delta x = \ell$, W_j is the fraction of channels, passing through location *x*, that terminate at distance $j\Delta x$ downstream (to the Right), see Figure D-1b. We refer to the scheme in (8) as the Control Volume Weighted Flux Scheme (CVWFS).

Note the calculation of the *out*-flux associated with node *I* in (8) involves one less term than the corresponding *in*-flux calculation; a devise that ensures positive coefficients and

thereby improves the properties of the resulting numerical scheme. When (8) is used in the flux balance (6) the following discrete form of the diffusion term is generated

$$-\frac{\partial}{\partial x}(q^R) \approx \frac{q^R_{in-I} - q^R_{out-I}}{\Delta x} \approx \frac{1}{\Delta x}\left[k_{in-I}\sum_{j=1}^{n} W_j\left[\frac{T_{I+j-2} - T_{I+j-1}}{\Delta x}\right] - k_{out-I}\sum_{j=1}^{n-1} W_j\left[\frac{T_{I+j-1} - T_{I+j}}{\Delta x}\right]\right] \tag{9}$$

Equation (9) represents the way in which the CVWFS is programmed in a control volume scheme. For analysis, however—assuming a constant thermal conductivity k—it is also useful to write the CVWFS in the alternative form

$$-\frac{\partial}{\partial x}(q^R) \approx \frac{1}{\Delta x^{\alpha+1}}\sum_{j=0}^{n} \theta_j T_{I+j-1} \tag{10}$$

Where the CVWFS coefficients are given by

$$\begin{aligned}
\theta_0 &= kW_1\Delta x^{\alpha-1} \\
\theta_1 &= k(-2W_1 + W_2)\Delta x^{\alpha-1} \\
\theta_j &= k(W_{j-1} - 2W_j + W_{j+1})\Delta x^{\alpha-1}, \quad 2 \le j \le n-1 \\
\theta_n &= k(W_{n-1} - W_n)\Delta x^{\alpha-1}
\end{aligned} \tag{11}$$

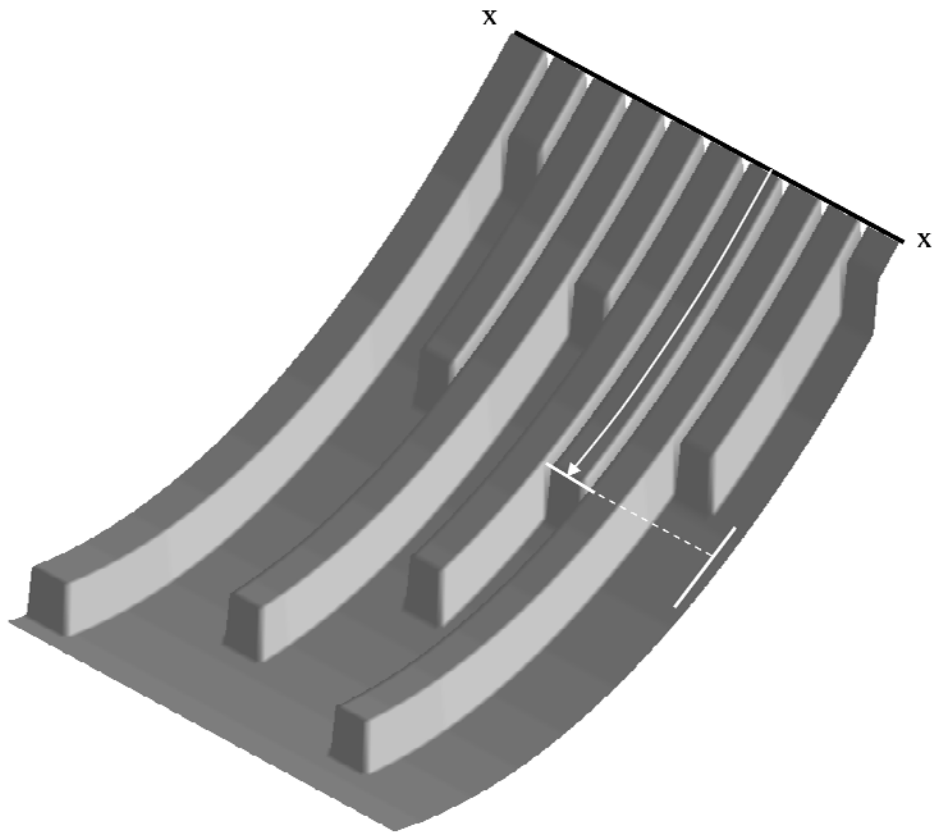

Figure D-2. Schematic of channel model for non-local diffusion. The diffusion flux at *x* for a given channel is determined by a constant multiplied by the slope at the down-stream termination of the channel

3 Criteria for choosing CVWFS weights

For the equations (8) to (11) to be valid and workable the weights, W_j have to satisfy the following criteria

Criterion 1, Weighted Average:

Since (8) is a weighted average the sum of weights has to be unity

$$S(n) = \sum_{j=1}^{n} W_j \approx 1\,, \tag{12}$$

with

$$0 \le W_j \le 1, \quad \forall j \tag{13}$$

Criterion 2, Diagonal Dominance:

In the setting of a numerical solution (10) can be viewed as the Ith row in a matrix equation $\boldsymbol{AT} = \boldsymbol{b}$. In the numerical solution of a steady state problem an iterative solver of this system will converge if $\boldsymbol{A}$ is diagonally dominant, requiring satisfaction of the condition

$$|\theta_1| \ge |\theta_0| + \sum_{j=2}^{n} |\theta_j| \tag{14}$$

If the weights are chosen such that they decrease monotonically,

$$W_j \ge W_{j+1}, \quad \forall j \tag{15}$$

and have negative "curvature"

$$W_{j-1} - 2W_j + W_{j+1} \ge 0, \quad \forall j \tag{16}$$

all the coefficients on the right hand side of the inequality (14) are non-negative and the sum of the off-diagonal terms can, assuming without loss of generality that $\Delta x = 1$, be calculated as

$$\theta_0 + \sum_{j=2}^{n} \theta_j = 2kW_1 - kW_2 = -\theta_1 \tag{17}$$

thereby satisfying the diagonally dominate condition. Note also, with the conditions in (15) and (16), (i) the only negative coefficient in (10) will be the coefficient for the diagonal term T_I, and (ii) the row sum of coefficients $\sum_{j=o}^{n} \theta_j = 0, \forall n$, these are important properties for the construction of conserving and stable solution schemes.

Criterion 3, Convergence to Locality:

Using the α locality index defined following (4), in the limit of $\alpha \to 1$, Eqs. (8) must recover the local flux definition, i.e.,

$$\lim_{\alpha \to 1} W_1 = 1$$
$$\lim_{\alpha \to 1} W_{j \neq 1} = 0 \tag{18}$$

Criterion 4, Convergence to full nonlocality:

Finally, in the full nonlocal limit, of $\alpha \to 0$, Eqs. (8) no longer represents a gradient, and all the weights should reduce to the constant $W = \Delta x$.

In using these criteria it is emphasized that, in addition to a correct weighting and recovery of locality, any resulting CVWFS scheme is guaranteed to exhibit the key numerical properties of diagonally dominance, positive off-diagonal coefficients, and zero row sums.

4 Connection of CVWFS to the fractional calculus

4.1 Power-law Weights

With the proposed CVWFS any choice of weights that satisfy the three part criteria will represent a workable non-local diffusion treatment. In order to provide a verification of the CVWFS, however, it is necessary to select valid weights that can be shown to provide a connection to the fractional calculus (see addendum). Such a step will allow for CVWFS solutions to be verified against available analytical solutions of fractional diffusion equations. With this objective in mind and assuming a re-scaling that sets the heterogeneity length-scale to $\ell = 1$, $\Delta x = 1/n$, the following power-law weights are proposed

$$W_j = (1-\alpha)[(j-\mu)\Delta x]^{-\alpha}\Delta x \tag{19}$$

with

$$0 < \mu = \left[1 - \Gamma(1-\alpha)^{-\frac{1}{\alpha}}\right] < 1 \tag{20}$$

where $\Gamma(x)$ is the gamma function. This choice of weights satisfies the required criteria, in particular:

1. They represent a valid weighted average, i.e., $0 \le W_j \le 1$ and through the concept of a Riemann sum

$$\lim_{n\to\infty}\sum_{j=1}^{n} W_j = (1-\alpha)\int_0^1 \eta^{-\alpha}\, d\eta = 1. \tag{21}$$

   On reference to Figure D-3 where the value of the sum $S(n) = \sum_{j=1}^{n} W_j$ ($\alpha = 0.5$) is plotted against *n*, it is seen that the average condition in (21) is rapidly approached even at quite small values of *n*.

2. The weights decrease monotonically and it can readily be confirmed for any choice of $0 < \alpha \le 1$ that they satisfy the diagonal dominance criteria in (17).
3. The weights satisfy the convergence to locality. This is demonstrated in Figure D-4 which, for the case of $n = 20$, plots the values of $W_1(\alpha)$ and $W_2(\alpha)$ in the range $.5 \le \alpha < 1$; the approach of $W_1 \to 1$ and $W_2 \to 0$ as $\alpha \to 1$ is clearly seen. Hence, using the monotonic decreasing nature of the weights ($W_j \ge W_{j+1}$), it can be concluded that as $\alpha \to 1$ locality, as defined in (18), is recovered.
4. The weights satisfy the convergence to nonlocality criterion, i.e. in the limit $\alpha \to 0$, all the weights approach the constant value Δx.

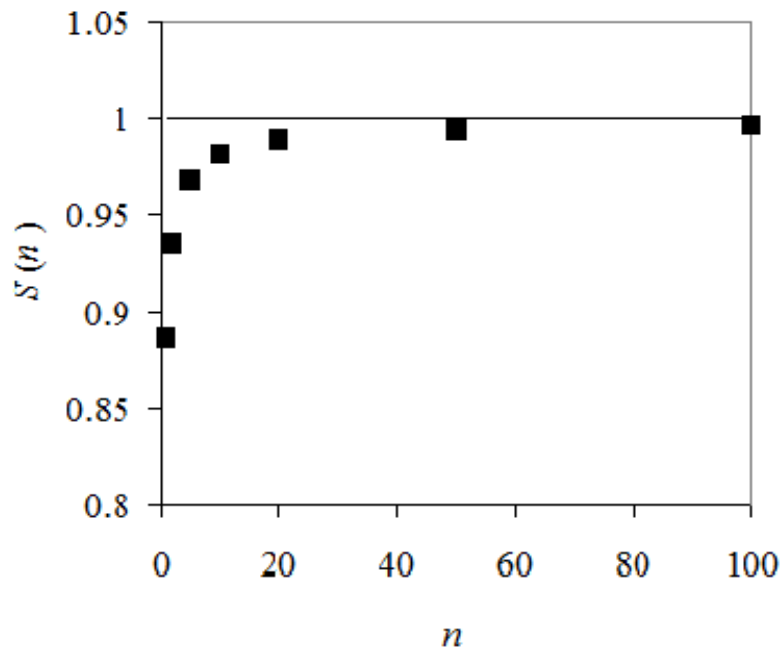

Figure D-3: Convergence of sum of weights $S(n)$ to unity when $\alpha = 0.5$

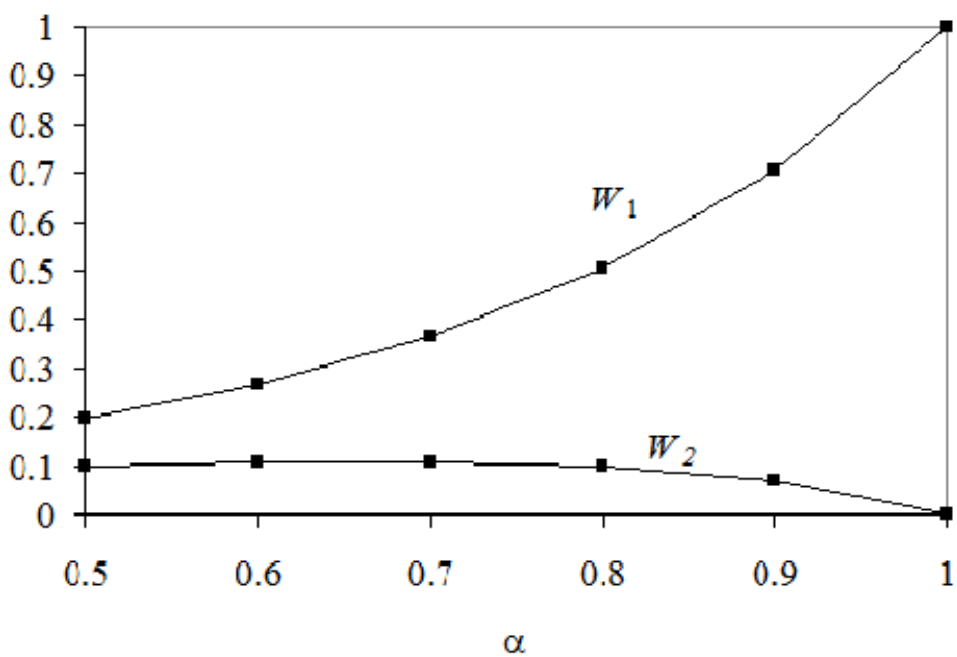

Figure D-4: Convergence of weight W_1 to unity and weight W_2 to zero as $\alpha \to 1$

4.2 *The CVWFS approximates the Caputo Derivative*

With the weights of (19) the CVWFS general non-local diffusion flux in (8) can be written as

$$q^R = k(1-\alpha)\sum_{j=1}^{n}[(j-\mu)\Delta x]_j^{-\alpha}\left[\frac{T_{I+j-1}-T_{I+j}}{\Delta x}\right]\Delta x \tag{22}$$

If the right hand is treated as a Riemann sum we arrive at

$$\underset{\lim n\to\infty}{q^R} = -k(1-\alpha)\int_0^1 \eta^{-\alpha}\frac{\partial}{\partial\eta}T(x+\eta)\,d\eta \tag{23}$$

which, on using the variable transform $\eta = \xi - x$, becomes

$$\underset{\lim n\to\infty}{q^R} = -k(1-\alpha)\int_x^{x+1}(\xi-x)^{-\alpha}\frac{\partial}{\partial\xi}T(\xi)\,d\xi \tag{24}$$

On reference to the appendix, it can be observed that the right-hand side of (24) has the form of the right-hand Caputo fractional derivative of order $0<\alpha\le 1$. Hence, within a multiplicative constant, the CVWFS flux in (22) can be viewed as an approximation of the right-hand Caputo fractional derivative, formally

$$q^R \approx k(1-\alpha)\Gamma(1-\alpha)\,{}_x^C D_{x+1}^{\alpha}(T) \tag{25}$$

4.3 *Relationship between the CVWFS and Grünwald approximations*

With the power-law weights (19) and a constant conductivity

$$k = \frac{1}{(1-\alpha)\Gamma(1-\alpha)} \tag{26}$$

we can use equation (25) in (10) to arrive at the following approximation for the heat balance based on a right-hand Caputo fractional flux

$$-\frac{\partial}{\partial x}[{}_x^C D_{x+1}^{\alpha}(T)] \approx \frac{1}{\Delta x^{\alpha+1}}\sum_{j=0}^{n}\theta_j T_{I+j-1} \tag{27}$$

This is observed to have the same form as the right-hand one-shift Grünwald formula for approximating the right-hand Riemann-Liouville fractional derivative of order $\alpha+1$, i.e., from (A13) in the addendum

$$\frac{\partial^{\alpha+1}T}{\partial(-x)^{\alpha+1}} \approx \frac{1}{\Delta x^{\alpha+1}} \sum_{j=0}^{n} g_j T_{I+j-1} \tag{28}$$

an approximation which is the key component in many previous proposed schemes for the numerical solution of non-local diffusion processes governed by a fractional derivative equation (Meerschaert and Tadjeran, 2006; Tadjeran et al., 2006; Meerschaert and Tadjeran, 2004). As noted in the appendix, the Caputo and Riemann-Liouville derivatives are, in general, not equivalent. Never the less, due to the similarities in the forms in (27) and (28), it is instructive to explicitly explore the relationship between the CVWFS and Grünwald approximations. Table D-1 compares the first 10 CVWFS coefficients (θ in (27)) and Grünwald weights (g in (28)) for the case $\alpha = 0.5$.

Table D-1: Comparison of Grünwald weights and CVWFS coefficients $\alpha = 0.5$

J	θ	g
0	1.0000	1.0000
1	1.5086	1.5000
2	0.3878	0.3750
3	0.0600	0.0625
4	0.0226	0.0234
5	0.0114	0.0117
6	0.0067	0.0068
7	0.0043	0.0044
8	0.0030	0.0030
9	0.0021	0.0022

Although not exact, there is a very close match between these values—an observation that can be made for all choices of $0 < \alpha \leq 1$. In this light, it is reasonable to assume that the proposed CVWFS will retain all of the desirable numerical properties that have been previously established for the one-shift Grünwald approximation (Meerschaert and Tadjeran, 2006; Tadjeran et al., 2006; Meerschaert and Tadjeran, 2004). We feel that this is a key property and attribute of the proposed CVWFS weighting scheme, a property which is not found when alternating power-law weighting schemes—which do not use the correction (20)—are used for finite-difference approximations of the Caputo derivatives, e.g., (Voller and Paola, 2010). Note also from Table D-1, for later use, that

for all values of $0 < \alpha \le 1$

$$\theta_1 \approx g_1 = -(1+\alpha) \tag{29}$$

5 Generalization of the CVWFS

5.1 Arbitrary Skew

The "channel" physical analog used to derive the CVWFS assumed that the diffusion flux at a point x was due to the slopes at channel terminations. We could also take the opposite view and assume that the flux is controlled by the slopes at the channel initiation. With this assumption the CVWFS will set

$$\begin{aligned} q^L_{in-I} &= k_{in-I} \sum_{j=1}^{n-1} W_j \left[\frac{T_{I-j} - T_{I+1-j}}{\Delta x} \right] \\ q^L_{out-I} &= k_{out-I} \sum_{j=1}^{n} W_j \left[\frac{T_{I+1-j} - T_{I+2-j}}{\Delta x} \right] \end{aligned} \tag{30}$$

In a similar manner to the analysis presented immediately above, with the power law weights of (19), this choice can be shown to be related to the left hand Caputo derivative (A4) via

$$q^L \approx -k(1-\alpha)\Gamma(1-\alpha)\ {}_{x-1}^{C}D_x^{\alpha}(T) \tag{31}$$

and, with the appropriate definition of k, to the one-shift Grünwald formula. In this way the CVWFS approximation for the general fractional diffusive term is

$$\frac{\partial}{\partial x}\left(-\frac{1+\beta}{2} q^L - \frac{1-\beta}{2} q^R \right) \approx \frac{1+\beta}{2} \frac{q^L_{in-I} - q^L_{out-I}}{\Delta x} + \frac{1-\beta}{2} \frac{q^R_{in-I} - q^R_{out-I}}{\Delta x} \tag{32}$$

where $-1 < \beta < 1$ weights between down- and up- stream contributions to the non-local flux, the right (R) fluxes are calculated with (8), the left (L) fluxes are calculated with (30).

5.2 Boundary Conditions

In problems on a bounded domain $0 \le x \le 1$, to avoid accessing values that lie outside of the domain, the CVWFS fluxed in (8) and (30) are calculated with the truncated summations

$$q_{in-I}^{R} = k_{in-I} \sum_{j=1}^{n+2-I} W_j \left[\frac{T_{I+j-2} - T_{I+j-1}}{\Delta x} \right]$$
$$q_{out-I}^{R} = k_{out-I} \sum_{j=1}^{n+1-I} W_j \left[\frac{T_{I+j-1} - T_{I+j}}{\Delta x} \right] \tag{33a}$$

$$q_{in-I}^{L} = k_{in-I} \sum_{j=1}^{I-1} W_j \left[\frac{T_{I-j} - T_{I+1-j}}{\Delta x} \right]$$
$$q_{out-I}^{L} = k_{out-I} \sum_{j=1}^{I} W_j \left[\frac{T_{I+1-j} - T_{I+2-j}}{\Delta x} \right] \tag{33b}$$

where a grid of $n+1$ equally spaced grid points is assumed with node points 1 and $n+1$ located on the domain boundaries. The definitions in (33) retain the key numerical properties of diagonal dominance, positive off-diagonal coefficients and zero row sums.

With the definitions in (33) fixed value boundary conditions can be readily imposed by fixing the nodal temperatures T_1 and T_{n+1} to the appropriate given values. When fixed flux conditions are required the face fluxes are still calculated with (33) with an iterative update applied to determine the boundary nodal values T_1 and T_{n+1}. For example, in a steady state problem employing a pseudo transient iterative solution, a prescribed flux q on the left boundary would involve the following first order iterative update at node 1

$$T_1 = T_1 + (\Delta\tau / \Delta x)(q - \tfrac{1+\beta}{2} q_{out-1}^{L} - \tfrac{1-\beta}{2} q_{out-1}^{R}) \tag{34a}$$

where $\Delta\tau$ is the pseudo time step. At node $n+1$ the update would be

$$T_{n+1} = T_{n+1} + (\Delta\tau / \Delta x)(\tfrac{1+\beta}{2} q_{in-n+1}^{L} + \tfrac{1-\beta}{2} q_{in-n+1}^{R} - q) \tag{34b}$$

5.3 Transients

In using Grünwald weights previous researchers (Meerschaert and Tadjeran, 2006; Tadjeran et al., 2006; Meerschaert and Tadjeran, 2004) have developed stable transient time and space schemes for fractional diffusion equations based on explicit and implicit (Crank-Nicolson) time integration. In developing a transient CVWFS we initially opt for a more straightforward time explicit approach which is first order in time and

second order in space. On assuming constant density and specific heat, and no anomalous behavior in time, this scheme can be written as

$$T_I^{new} = T_I + \frac{\Delta t}{\rho c}\left[\frac{1+\beta}{2}\frac{q_{in-I}^L - q_{out-I}^L}{\Delta x} + \frac{1-\beta}{2}\frac{q_{in-I}^R - q_{out-I}^R}{\Delta x}\right] \tag{35}$$

Where, Δt is the time step, the superscript *new* refers to values at the new time level, and the fluxes on the right hand side are calculated with old time values using (8) and (30) in infinite domains or the truncated summations (33) in a finite domain.

A stability criterion can be established by considering an infinite domain and using (11) to rewrite the scheme in (35) as

$$T_I^{new} = T_I + \frac{1}{\rho c}\frac{\Delta t}{\Delta x^{\alpha+1}}\left[\frac{1+\beta}{2}\sum_{j=0}^{n}\theta_j T_{I+1-j} + \frac{1-\beta}{2}\sum_{j=0}^{n}\theta_j T_{I+j-1}\right] \tag{36}$$

Based on known behaviors in the numerical solution of local diffusion it is assumed that (36) will provide a stable solution provided that all of the coefficients on the right hand side are positive. Via the construction of the CVWFS, see (11), the only possible negative coefficient is the coefficient for T_I which has the form

$$a_I = 1 + \frac{1}{\rho c}\frac{\Delta t}{\Delta x^{\alpha+1}}\theta_1 \tag{37}$$

If the power-law weights in (19) are used, a constant conductivity assumed, and the approximation in (29) employed (37) becomes

$$a_I \approx 1 - \frac{k}{\rho c}\frac{\Delta t}{\Delta x^{\alpha+1}}\Gamma(1-\alpha)(1-\alpha)(1+\alpha) \tag{38}$$

On forcing $a_I \geq 0$ this provides an equation to determine the stability limit on the choice of time step. For example if $k/\rho c = 1/\Gamma(1-\alpha)(1-\alpha)$ the time step is restricted to be

$$\Delta t < \frac{\Delta x^{1+\alpha}}{1+\alpha}, \tag{39}$$

matching the stability criterion more formally derived for explicit schemes based on Grünwald weights (Ding et al., 2010; Meerschaert and Tadjeran, 2006). The aforementioned explicit scheme will provide a stable solution for any value Δx and Δt

that satisfy equation (39). In the testing of the scheme, the consequences of changing the values of Δx and Δt, while still satisfying (39), will be investigated.

6 Testing and results

6.1 A Simple Steady State Problem

The first test problem investigated is a simple steady state non-local diffusion problem in the domain $0 \le x \le 1$, with fixed boundary conditions $T(0) = 1$ and $T(1) = 0$. The general Caputo fractional diffusion equation for this problem is

$$\frac{\partial}{\partial x}\left(\frac{1+\beta}{2}{}_0^C D_x^\alpha T - \frac{1-\beta}{2}{}_x^C D_1^\alpha T\right) = 0 \tag{40}$$

With

$$T(0) = 1, \quad T(1) = 0 \tag{41}$$

In the limit case of $\beta = 1$ the solution of (40) and (41)—which can be checked by referring to the standard Caputo fractional derivatives listed in the addendum—is

$$T = 1 - x^\alpha \tag{42}$$

And in the limit case $\beta = -1$ the solution is

$$T = (1-x)^\alpha \tag{43}$$

Equations (40) and (41) are solved using the form of the CVWFS in (33) with the power-law weights of (19). The solution is arrived at by solving the transient CVWFS equation with a pseudo time step and marching to steady state. The pseudo time step is chosen to satisfy the stability criteria in (39) and to ensure a fit between the CVWFS and Caputo derivative the conductivity, specific heat, and density are arranged so that $k/\rho c = 1/\Gamma(1-\alpha)(1-\alpha)$.

Figure D-5 shows the CVWFS predictions for a number of values of α, β, and step size Δx. Where available, the predictions of the CVWFS, even down to quite coarse grid steps, are in excellent agreement with the analytical solutions in (42) and (43). An interesting solution is the symmetric case $\alpha = 0.5, \beta = 0$. Here, although predictions

approach a straight line there is still a clear non-linear trend near both boundaries. An analytical solution, however, is not available to confirm this behavior.

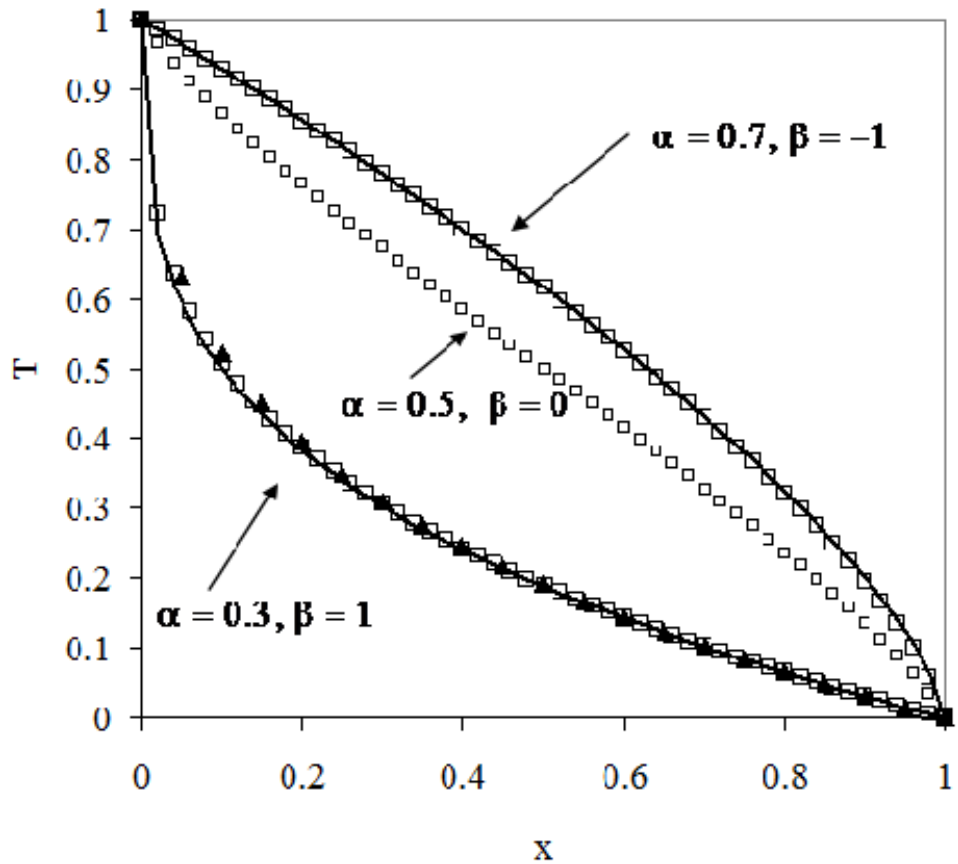

Figure D-5 CVWFS applied to steady state problem. Lines are analytical solutions, open squares are CVWFS solutions with 40 space steps, closed triangles are CVWFS solution with 20 space steps.

6.2 A Problem with a Prescribed Flux Boundary and Source

Related to recent work on sediment deposition [16], the following fully right hand Caputo fractional derivative problem with a flux boundary and source term is posed.

$$-\frac{\partial}{\partial x}\left({}_{x}^{C}D_{1}^{\alpha}T\right)=2, \quad 0\le x\le 1 \tag{44}$$

Two alternative boundary conditions are considered. The first places the flux condition on the upstream boundary

$${}_0^C D_1^\alpha(T) = q_{val}^L = 2 \quad \text{and } T(1) = 0 \tag{45a}$$

the second places it at the downstream boundary

$$T(0) = 1 \text{ and } {}_0^C D_1^\alpha(T) = q_{val}^R = -0.4 \tag{45b}$$

Note there is an intrinsic difference in these two choices. In the first the gradient at the prescribed flux boundary has no influence in the calculation of fluxes at internal points which, through the right-hand derivative, are only influenced by downstream gradients. In the second, case, however, the gradient at the prescribed flux boundary will be used in the calculation of all internal fluxes.

Using the standard Caputo derivatives in the appendix the analytical solution when (45a) is applied is

$$T = \frac{2}{\Gamma(\alpha+2)}(1-x)^{1+\alpha} + \frac{q_{val}-2}{\Gamma(\alpha+1)}(1-x)^{\alpha} \tag{46a}$$

with (45b) the solution is

$$T = 1 + \frac{2}{\Gamma(\alpha+2)}\left[(1-x)^{1+\alpha} - 1\right] + \frac{q_{val}}{\Gamma(\alpha+1)}\left[(1-x)^{\alpha} - 1\right] \tag{46b}$$

Once again a pseudo time stepping CVWFS approach is used to solve this problem.

$$T_I^{new} = T_I + \frac{\Delta\tau}{\rho c}\left[\frac{q_{in-I}^R - q_{out-I}^R - 2\Delta x}{\Delta x}\right] \tag{47}$$

where the fluxes on the right hand side are calculated using the weights of (19) in (33a) setting $k/\rho c = 1/\Gamma(1-\alpha)(1-\alpha)$. With condition (45a), reflecting the fixed flux condition and ½ sized control volume, the scheme at node 1 is modified as

$$T_1^{new} = T_1 + \frac{\Delta\tau}{\rho c}\left[\frac{q_{val}^L - q_{out-1}^R - \Delta x}{\Delta x}\right] \tag{48a}$$

With the downstream flux condition the scheme at node $n+1$ is modified as

$$T_{n+1}^{new} = T_{n+1} + \frac{\Delta\tau}{\rho c}\left[\frac{q_{in-n+1}^R - q_{val}^R - \Delta x}{\Delta x}\right] \tag{48b}$$

The CVWFS solutions, with $\Delta x = 0.05$ and $\alpha = 0.5$, are compared with the analytical solutions (46) in Figure D-6; these results indicate a close comparison between the CVWFS and the analytical solution.

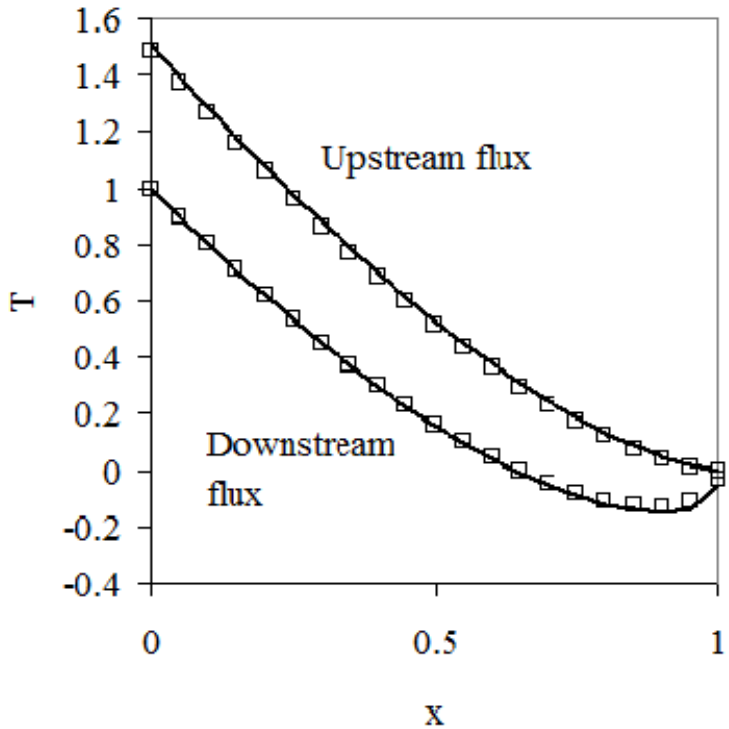

Figure D-6. Predictions of fractional diffusion ($\alpha = 0.5$) steady state with a fixed flux q_{val} and source term; line analytical solution, open squares CVWFS predictions.

6.3 *A Transient Problem*

Similar to the work in [9] the following transient problem is posed

$$\frac{\partial T}{\partial t} = \frac{\partial}{\partial x}\left(k^{*}\,{}_{0}^{C}D_{x}^{\alpha}T\right) - x^{3}(1+x)e^{-t} \tag{49}$$

with boundary conditions

$$T(0,t) = 0, \quad T(1,t) = e^{-t} \tag{50}$$

and initial condition

$$T(x,0) = x^{3} \tag{51}$$

If the conductivity is given by $k^{*} = \Gamma(4-\alpha)x^{\alpha+2}/30$ then (49)-(51) has the analytical solution

$$T(x,t) = x^{3}e^{-t} \tag{52}$$

At internal nodes the explicit CVWFS for this problem takes the form

$$T_I^{new} = T_I + \Delta t\left[\frac{q_{in-I}^L - q_{out-I}^L - \Delta x(x_I)^3(1+x_I)e^{-t}}{\Delta x}\right] \tag{53}$$

Where the fluxes on the left are evaluated using the power law weights of (19) in (33b) and a setting of $k = k^*/\Gamma(1-\alpha)(1-\alpha)$. Twenty five space step of $\Delta x = 0.04$ are used and, on noting that $k^* \le \frac{1}{5}$, a conservative interpretation of the stability criterion in (39) sets $\Delta t = 2.5\Delta x^2 = 0.004$. The time $t = 1$ predictions, using α values of 0.2, 0.5 and 0.8, are compared with the analytical solution (52) in Figure D-7. At large and intermediate values of α the agreement is good, e.g., $\alpha = 0.5$ the maximum absolute error between prediction and analytical is $\sim 3.8\times10^{-3}$ and at $\alpha = 0.8$ the error is $\sim 4.8\times10^{-4}$; this last value close to those reported in (Tadjeran et al., 2006). At lower values of α, errors do increase, e.g., $\alpha = 0.2$ the maximum error is $\sim 1.2\times10^{-2}$. The errors are reduced in this case, however, if small steps sizes are used; e.g., with ½ the step size $\Delta x = 0.02$ the maximum errors when $\alpha = 0.2$ is $\sim 6.2\times10^{-3}$.

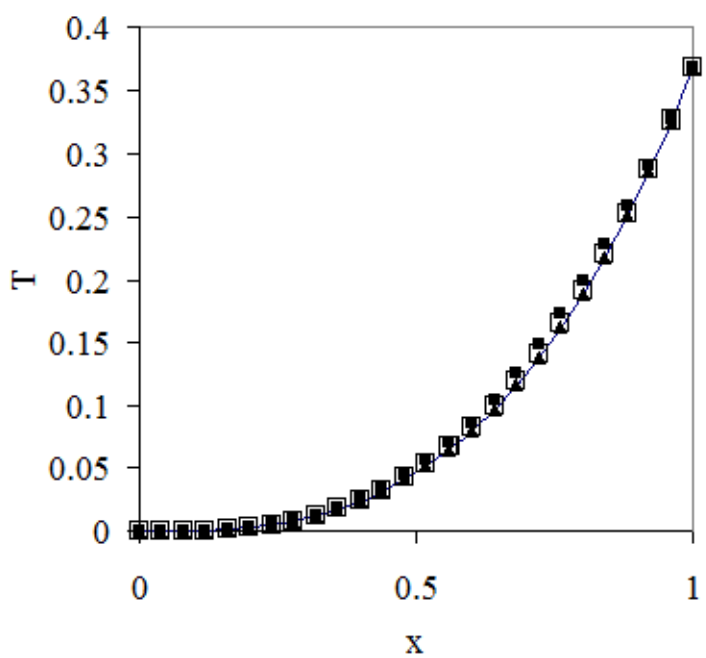

Figure D-7. Predictions for fractional transient diffusion equation at time $t = 1$. Solid squares $\alpha = 0.2$, open squares $\alpha = 0.5$, solid triangles $\alpha = 0.8$.

7 Conclusions

Non-local diffusion will occur in systems where the lengths of heterogeneities span all scales up to the domain size. Here a discrete model—referred to as the Control Volume Weighted Flux Scheme (CVWFS)—for numerical solution of non-local diffusion has been proposed. The key in this model is the assumption that the diffusion flux at a given location is proportional to a weighted average of the potential gradients throughout the domain. On devising criteria for choosing the weights in this construct, the resulting numerical solution scheme is shown to possess a number of critical numerical properties. In particular, the diffusion coefficient matrix is diagonally dominant, has strictly non-negative off diagonals coefficients, and has a zero coefficient sum along any given row. Further, the level of non-locality can be controlled by adjusting a single parameter, $0 < \alpha \leq 1$ (fully local). These attributes allow for the construction of flexible and robust control volume schemes that can be used to model non-local diffusion systems.

For a given choice of power law weights it has been shown that the CVWFS is an approximation of the Caputo fractional derivative of order α. From this finding, on identifying suitable boundary and transient treatments, the CVWFS has been used to solve a wide range of steady state and transient non-local diffusion problems governed by Caputo fractional derivatives. In all cases tested, solutions are stable and produce results that compare well with available analytical solutions.

Further analysis has shown that the CVWFS also closely approximates the previously investigated fractional derivative solution schemes based on the one-shift Grünwald approximation. Establishing the connection between the proposed CVWFS and the Grünwald approximation is an important result. In particular, this finding allows us to apply the extensive numerical analysis results for the Grünwald approximation to the CVWFS. It is important to recognize, however, that the CVWFS is an independent scheme in its own right with some significant different features:

1. The CVWFS as given by (33) is immediately applicable in a standard Control Volume scheme.

2. The CVWFS is derived from a discrete physical construct whereas the Grünwald is obtained from a theoretical generalization of the binomial expansion of integer order finite difference schemes. This difference is observed by noting that although the CVWFS coefficients provide a close match for the equivalent Grünwald weights the agreement is not precise.
3. The agreement between the CVWFS and Grünwald approximation is obtained for a specific choice of weights. The generality of the CVWFS allows for the realization of alternative approximations, based on different choices of weights, approximations that may be applicable to alternative non-local diffusion models.

Further work will explore the possibility of extending the CVWFS to two-dimensional and non-local time settings, investigating the possibilities of alternative weights, and making applications to more complex problems; e.g., fractional diffusion Stefan melting problems (Voller, 2010; Jumyi and Mingyu, 2009).

Addendum: A brief outline of fractional calculus

Through the properties of thick tailed Lévy pdf's and random walk processes it can be shown that non-local diffusion in a domain with a power-law distribution of heterogeneities can be described in terms of fractional derivatives (Zhang et al., 2009; Schumer et al., 2009). To make full use of this finding, however, it is important to have a basic knowledge of the sometimes subtle workings of the fractional calculus. The purpose of this brief appendix is to provide this knowledge. Further information and background can be found on refereeing to standard texts on fractional calculus, e.g., Podlubny (1998).

The first and perhaps most awkward element in fractional calculus is that there is not a unique definition for a fractional derivative. In terms of analytical definitions a sound starting point is the generalization of the Cauchy formula for repeated integration

$$I^n f(x) = \frac{1}{(n-1)!}\int_0^x (x-\xi)^{n-1} f(\xi)d\xi \qquad \text{(A1)}$$

to the non-integer case —referred to as Reimann-Liouville Integration

$$I^{\lambda} f(x) = \frac{1}{\Gamma(\lambda)} \int_0^x (x-\xi)^{\lambda-1} f(\xi) d\xi \tag{A2}$$

where λ is any real number $\lambda > 0$ and $\Gamma(\lambda)$ is the gamma function (note at integer values $\Gamma(n) = (n-1)!$). From here we can arrive at a fractional derivative of order α by taking the nth integer derivative of the fractional $\lambda = (n^{\text{th}} - \alpha)$ integral

$$\frac{\partial^{\alpha} f}{\partial x^{\alpha}} = \frac{1}{\Gamma(n-\alpha)} \frac{d^n}{dx^n} \int_0^x (x-\xi)^{n-1-\alpha} f(\xi) d\xi \tag{A3}$$

This definition is referred to as the left-hand Reimann-Liouville derivative. A problem in application is that, unless all of the integer derivatives of f vanish at $x = 0$, as the lower limit is approached ($x \to 0$) the right-hand side of (A3) becomes singular. This behavior can be regulized by defining the fractional derivative through taking the $\lambda = (n^{\text{th}} - \alpha)$ integral of the nth derivative of $f(x)$. The result is the left-hand Caputo derivative

$${}_0^C D_x^{\alpha} f = \frac{1}{\Gamma(n-\alpha)} \int_0^x (x-\xi)^{n-1-\alpha} \frac{d^n f(\xi)}{d\xi^n} d\xi \tag{A4}$$

which vanishes (= 0) as $x \to 0$. It is important to note that, unlike the integer case, in the fractional calculus the integral and derivative operators are non-commutative. Hence in general the Caputo and Riemann-Liouville fractional operators are not equivalent.

In addition to left-hand derivatives we can also define right-hand derivatives. In the domain $0 \le x \le 1$ the right-hand Reimann-Liouville and Caputo derivatives are

$$\frac{\partial^{\alpha} f}{\partial (-x)^{\alpha}} = \frac{(-1)^n}{\Gamma(n-\alpha)} \frac{d^n}{dx^n} \int_x^1 (\xi - x)^{n-1-\alpha} f(\xi) d\xi \tag{A5}$$

$${}_x^C D_1^{\alpha} f = \frac{(-1)^n}{\Gamma(n-\alpha)} \int_x^1 (\xi - x)^{n-1-\alpha} \frac{d^n f(\xi)}{d\xi^n} d\xi \tag{A6}$$

Particular derivatives of (A3) and (A4) can be calculated via the application of Laplace Transforms. For the case of Caputo (e.g., (Voller and Paola, 2010)) standard Caputo derivatives are

$${}_0^C D_x^{\alpha} C_0 = 0 \text{; where } C_0 \text{ is a constant} \tag{A7}$$

$${}_0^C D_x^\alpha x^\eta = \frac{\Gamma(\eta+1)}{\Gamma(\eta+1-\alpha)} x^{\eta-\alpha}\text{, for real value } \eta \geq 1 \geq \alpha > 0 \text{ or } 0 < \eta \leq \alpha \leq 1 \tag{A8}$$

(A8) providing the special cases for $\alpha > 0$

$${}_0^C D_x^\alpha x^{\alpha+1} = \Gamma(\alpha+2)x \tag{A9}$$

and

$${}_0^C D_x^\alpha x^\alpha = \Gamma(\alpha+1) \tag{A10}$$

Further in the interval $0 \leq x \leq 1$ it can be shown that (Voller and Paola, 2010)

$${}_x^C D_1^\alpha f = {}_0^C D_{1-x}^\alpha f \tag{A11}$$

providing a route for calculating standard right-hand Caputo derivatives.

In addition to the analytical definitions presented above there is an approximate definition referred to as the Grünwald approximation (Schumer et al., 2009). This approximation is arrived at by considering a grid of nodes equally space a distance Δx apart. Following arguments in (Schumer et al., 2009) using an initial forward difference followed by backward differences, the nth integer derivative at node I can be approximated as

$$\frac{d^n}{dx^n} f \approx \frac{1}{\Delta x^n} \sum_{j=0}^{n} (-1)^j \frac{n!}{j!(n-j)!} f_{I+1-j} \tag{A12}$$

where f_K, $I+1-n \leq K \leq I+1,$ are the nodal values of f. Once again this integer form can be generalized for non-integer cases to arrive at the so called one-shift Grünwald formula or approximation for a fractional derivative

$$\frac{d^{\alpha+1} f}{dx^{\alpha+1}} \approx \frac{1}{\Delta x^n} \sum_{j=0}^{n} g_j f_{I+1-j} \tag{A13}$$

where

$$g_j = \frac{(-1)^j \Gamma(\alpha+2)}{\Gamma(j+1)\Gamma(\alpha+2-j)} = \frac{\Gamma(j-\alpha-1)}{\Gamma(-\alpha-1)\Gamma(j+1)} \tag{A14}$$

are the Grünwald weights. The notation on the left of (A13) is correct since it can be shown that in the limit of $n \to \infty$ the approximation is for the left-hand Riemann-

Liouville derivative in (A3), e.g., see (Podlubny, 1998). The associated right-hand one-shift Grünwald formula is

$$\frac{d^{\alpha+1} f}{d(-x)^{\alpha+1}} \approx \frac{1}{\Delta x^n} \sum_{j=0}^{n} g_j f_{I+j-1} \tag{A15}$$

By its nature of coefficients multiplying nodal values (A13) and (A14) and/or (A15) provide a natural choice for developing finite difference schemes for solving problems expressed in terms of Riemann-Liouville fractional derivatives. Extensive numerical analysis by Meerschaert and co-workers (Meerschaert and Tadjeran, 2006; Tadjeran, 2006; Meerschaert and Tadjeran, 2004) has shown that a range of robust and stable fractional derivatives schemes based on the one-shift Grünwald can be constructed.

Appendix E: A random walk solution for fractional diffusion equations

Published as: Zielinski, D.P., Voller, V.R. (2013), A random walk solution for fractional diffusion equations, *International Journal of Numerical Methods for Heat and Fluid Flow*, **23**,1, 7-22, doi:10.1108/09615531311289088.

The purpose of this paper is to develop an alternative numerical approach for describing fractional diffusion in Cartesian and non-Cartesian domains using a Monte Carlo random walk scheme. The resulting domain shifting scheme provides a numerical solution for multi-dimensional steady state, source free diffusion problems with fluxes expressed in terms of Caputo fractional derivatives. The method described here follows a similar approach to random walk methods previously developed for normal (local) diffusion. The key differences from standard methods are (1) the random shifting of the domain about the point of interest with (2) shift steps selected from non-symmetric, power-law tailed, Lévy probability distribution functions. The domain shifting scheme is verified by comparing predictive solutions to known one-dimensional and two-dimensional analytical solutions for fractional diffusion problems, and applied to a problem of fractional diffusion in a non-Cartesian annulus domain. This is the first random walk scheme to utilize the concept of allowing the domain to undergo the random walk about a point of interest. Domain shifting scheme solutions of fractional diffusion in non-Cartesian domains provide an invaluable tool to direct the development of more sophisticated grid based finite element inspired fractional diffusion schemes.

1 Introduction

In developing computational approaches for the solution of general transport equations a standard test problem is the steady-state transport in an arbitrary two-dimensional domain Ω. If the chosen domain is homogeneous, isotropic, and static the transport can be modeled by a diffusion flux of the form

$$\boldsymbol{q} \sim -k\left(\frac{\partial \phi}{\partial x}, \frac{\partial \phi}{\partial y}\right) \tag{1}$$

where ϕ is a potential and k is a suitability dimensioned coefficient. The associated steady sate transport equation is

$$\nabla \cdot (-\mathbf{q}) = 0 \tag{2a}$$

Such that if the diffusion coefficient is constant the Laplace equation

$$\frac{\partial^2 \phi}{\partial x^2} + \frac{\partial^2 \phi}{\partial y^2} = 0 \tag{2b}$$

results. Through the use of unstructured finite element methods (FEM) (e.g., Zienkiewicz and Taylor, 1989; Voller, 2009) or boundary elements methods (BEM) (e.g., Wrobel and Aliabadi, 2002; Beer *et al.,* 2008) solving the Laplace problem in (2b) is a simple exercise, even in cases where the domain has an arbitrary shape. These methods develop solutions by working directly with discrete versions of the mathematical statements in equations (1) and (2). An alternative, more fundamental approach, which can be used when Dirichlet conditions are imposed on the boundary of Ω is to use a so-called Monte Carlo method (Haji-Sheikh and Howell, 2006). As described in more detail below, this approach rests on exploiting the theoretical connection between Brownian motion and diffusion (Metzler and Klafter, 2000). In specific cases where only information at limited points within the domain is required Monte Carlo solutions can be effective. Efficiency is quickly lost, however, once the number of points where information is required increases. As such Monte Carlo approaches are typically not deemed to be competitive with FEM or BEM solutions of (2).

An assumption in using the diffusion flux definition in equation (1) is that the largest length scale of heterogeneity is significantly smaller than the domain size; a situation that allows for homogenization and the evaluation of diffusion fluxes in terms of *local* gradients. In some situations, however the length scales of heterogeneities may occur at all scales, up to and including the size of the domain. Such a realization invalidates the homogenization process and requires a non-local treatment to evaluate the diffusion fluxes. Example systems where such treatments may be required are transport in porous media (Benson *et al.*, 2000a; Benson *et al.*, 2000b; Yong *et al.*, 2006; Zhang *et al.*, 2005; Zhang *et al.*, 2007b) and sediment transport in fluvial systems (Schumer *et al.*, 2009; Voller and Paola, 2010; Ganti *et al.*, 2010, Voller et al, 2012). If the heterogeneities are power-law distributed an appropriate non-local treatment can be developed in terms of so called fractional derivatives (Schumer *et al.*, 2009). As expanded on below, this approach accounts for the non-locality through modeling the diffusion fluxes in terms of fractional (non-integer) gradients for example, the components of the diffusion flux at a point are determined from

$$q_x \sim -\frac{1+\beta_x}{2}\frac{\partial^{\alpha_x}\phi}{\partial x^{\alpha_x}} + \frac{1-\beta_x}{2}\frac{\partial^{\alpha_x}\phi}{\partial(-x)^{\alpha_x}} \tag{3a}$$

and

$$q_y \sim -\frac{1+\beta_y}{2}\frac{\partial^{\alpha_y}\phi}{\partial y^{\alpha_y}} + \frac{1-\beta_y}{2}\frac{\partial^{\alpha_y}\phi}{\partial(-y)^{\alpha_y}} \tag{3b}$$

where $0 < \alpha_{x,y} \le 1$ is associated with the power-law of the heterogeneity distribution and $-1 < \beta_{x,y} < 1$ is the skew of this distribution between the up- and down-stream directions. An appropriate conceptualization of (3) is to associate the flux at a point as a weighted sum of gradients (first derivatives) located up- and down-stream of that point. In this way, a fractional diffusion version of the sample test problem governed by (2) can be constructed by using (3) as the definition of the flux vector in place of the definition of equation (1). A number of numerical methods, based on structured Cartesian grids, for solving a variety of transport equations that involve fractional derivatives have been proposed in the literature (Tadjeran and Meerschaert, 2007; Meerschaert *et. al.*, 2006; Liu

et al., 2004; Zhang *et al.*, 2005; Zhang *et al.*, 2007a, Voller et al., 2011). By contrast, due to the difficulty of representing the non-local fractional gradients, solutions in arbitrarily shaped domains using unstructured grids, have to-date not been constructed. It is noted, however, that in a similar manner to the connection between a Brownian motion and diffusion, there also exists a theoretical association between non-Brownian (i.e., Lévy motion) and fractional diffusion (Metzler and Klafter, 2000). This suggests that while fractional diffusion transport in arbitrary domains may not be currently amenable to FEM solutions technologies, it may be possible to develop Monte Carlo solutions. The objective of this paper is the development of such a Monte Carlo scheme.

In the next section, to provide appropriate background, a brief definition of fractional diffusion is provided. This section is followed by an explicit identification of the random particle motion associated with a fractional derivative. This identification allows for the development of a Monte Carlo solution approach. Two alternative Monte Carlo schemes are proposed. The first scheme, closely associated with conventional methods, employs a particle random walk process where successive steps in the walk are selected from the appropriate probability density function (pdf) associated with the order of the fractional derivative. It is shown, through a simple one-dimensional test problem that whereas this approach works well with an integer derivative (associated with a symmetric Gaussian pdf) it is not completely successful when the steps of the walk are chosen from the non-symmetric pdfs associated with fractional derivatives. This drawback is overcome by employing a novel Monte Carlo scheme, which, in contrast to previous particle motion approaches, is based around a sequence of random motions (shifts) of the problem domain itself. This approach, referred to as the *domain shifting method*, is verified by solving fractional diffusion transport—obtained by substituting the definition (3) into (2a)—in a square domain with Dirichlet boundary conditions, a problem which admits an analytical solution. The potential wider utility of the scheme is then demonstrated by solving a fractional diffusion problem in a circular annulus domain with fixed conditions imposed on the inner and outer boundaries; a problem that is currently beyond the reach of FEM and BEM approaches.

2 Fractional Diffusion

When (3) is used in (2), along with the additional assumption that the heterogeneities in the coordinate directions are statistically independent, see discussions by Tadjeran and Meerschaert (2007), the general non-local or fractional diffusion equation in two dimensions

$$\frac{\partial}{\partial x}\left[\frac{1+\beta_x}{2}\frac{\partial^{\alpha_x}\phi}{\partial x^{\alpha_x}}-\frac{1-\beta_x}{2}\frac{\partial^{\alpha_x}\phi}{\partial(-x)^{\alpha_x}}\right]+\frac{\partial}{\partial y}\left[\frac{1+\beta_y}{2}\frac{\partial^{\alpha_y}\phi}{\partial y^{\alpha_y}}-\frac{1-\beta_y}{2}\frac{\partial^{\alpha_y}\phi}{\partial(-y)^{\alpha_y}}\right]=0 \qquad (4)$$

results.

In a general setting there are a number of alternative definitions of the fractional derivatives in (4). A definition that carries a relatively easy physical interpretation and avoids singularities at the origin is the Caputo definition (Podlubny, 1999). In a domain extending from $0 \le x \le 1$, the left sided Caputo is expressed as a convolution integral obtained through constructing the fractional integral of an integer derivative, i.e.,

$$\frac{\partial^{\alpha}\phi}{\partial x^{\alpha}}=\frac{1}{\Gamma(1-\alpha)}\int_0^x (x-\xi)^{-\alpha}\frac{\partial\phi}{\partial\xi}d\xi \qquad (5)$$

where Γ is the gamma function. With this definition, it is observed that the flux at a given point x is no longer determined from the *local* gradient but rather via a *non-local* representation consisting of a weighted sum of the gradients *upstream* of x. Non-locality, however can extend over both the up- and down-stream regions. Hence in addition to defining an up-stream contribution (from the left) it is also necessary to define a down-stream contribution from the right in this way the right-sided Caputo is defined as

$$\frac{\partial^{\alpha}\phi}{\partial(-x)^{\alpha}}=\frac{-1}{\Gamma(1-\alpha)}\int_x^1 (\xi-x)^{-\alpha}\frac{\partial\phi(\xi)}{\partial\xi}d\xi \qquad (6)$$

3 Random Walk Processes

A well known result of statistical physics is that the spread of an initial pulse by random (Brownian) motion of particles takes the form of a Gaussian (pdf)—which is also

the fundamental solution of the transient diffusion equation. This observation provides a theoretical under-pinning for the use of a Monte Carlo (random walk) solution for the diffusion equation (2), with the step sizes of the walk selected from an appropriate Gaussian pdf (Haji-Sheikh and Howell, 2006).

Brownian motion is subject to the central limit theorem such that the mean of a sufficiently large sample of Brownian steps will be normally variable, i.e., a set of such means will form a Gaussian pdf with exponential decaying tails. In more general random motions, referred to as Lévy flights, the steps are not subject to the central limit theorem and the spreading of an initial pulse with particles undergoing such motions forms a Lévy pdf, characterized by the appearance of thick power-law decreasing tails—indicating the finite probability of extreme events. Analogous to the connection between the Gaussian pdf and diffusion, the Lévy pdf provides a fundamental solution for a transient fractional diffusion equation (Benson *et al*. 2000b; Liu *et al.* 2004; Meerschaert, 2012). This raises the possibility of constructing a random-walk solution for a fractional diffusion equation (4) by simply choosing step sizes Δ from an appropriate α -stable Lévy pdf.

An appropriate method for choosing such steps has been proposed by Weron and Weron (1995)

$$\Delta = \gamma S_{\alpha\beta}\left(\frac{-\ln u \cos\zeta}{\cos\left(\zeta - (\alpha+1)\left(\zeta + B_{\alpha\beta}\right)\right)}\right)^{\frac{\alpha}{\alpha+1}}\left(\frac{\sin\left((\alpha+1)\left(\zeta + B_{\alpha\beta}\right)\right)}{\cos\zeta}\right) + \eta$$

$$B_{\alpha\beta} = \frac{\tan^{-1}\left(\beta \tan\left(\frac{\pi(\alpha+1)}{2}\right)\right)}{\alpha+1} \tag{7}$$

$$S_{\alpha\beta} = \left[1 + \beta^2 \tan^2\left(\frac{\pi(\alpha+1)}{2}\right)\right]^{\frac{1}{2\alpha+2}}$$

where $\zeta = \pi(v - 1/2)$, and $u, v \in (0,1)$ are independent uniform random numbers. In equation (7) η is a shift parameter (taken as zero here), γ is a scale parameter, and α and β

are the previously defined non-locality parameters. A plot of the pdfs of step sizes obtained with (7) is shown in Figure E-1. Note that when $\beta = 1$, corresponding to the left hand Caputo derivative, the pdf is non-symmetric with a thick power-law tail extending to the right. When the skew parameter is $\beta = -1$, corresponding to the right hand derivative, the thick tail extends to the left. Also note, that in all cases independent of the value of β, as locality is approached, i.e., $\alpha \to 1$, the symmetric normal (Gaussian) pdf with exponentially decaying tails will result.

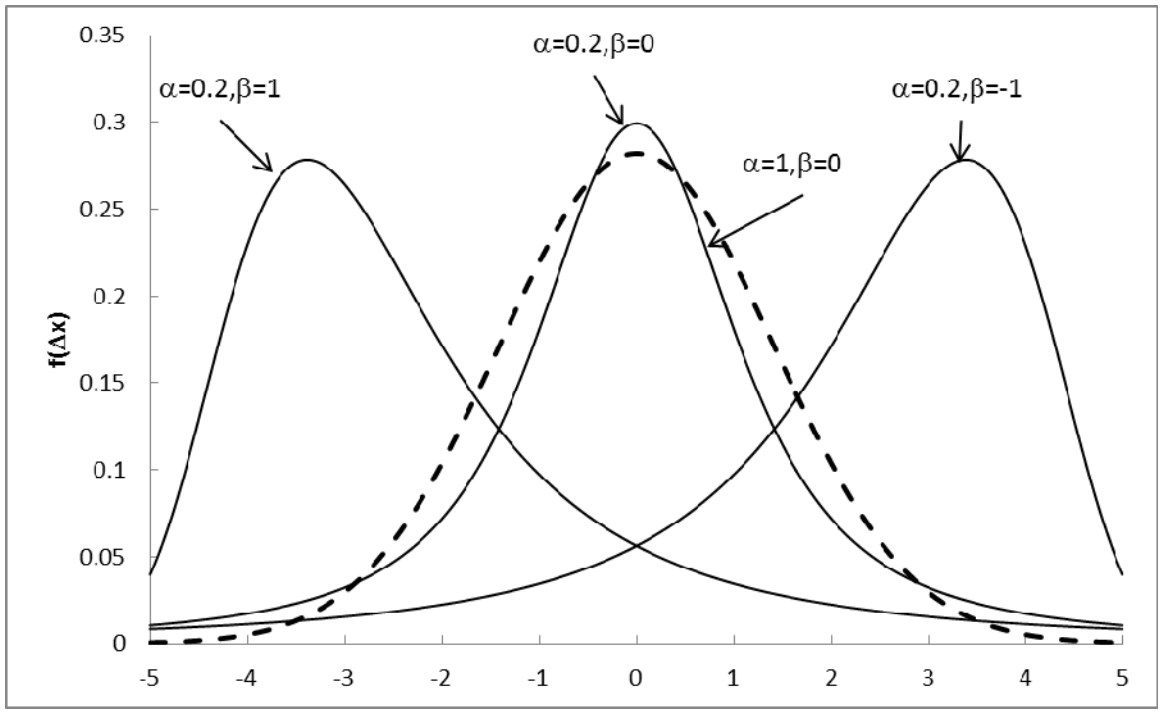

Figure E-1. PDF of Lévy distribution generated by equation (7) for various values of (α, β) with $\gamma = 1.0$. (Figure modified from Schumer *et al.* (2009) Figure 7).

3.1 A Particle Random Walk Scheme

Based on the connection between the non-Brownian motion defined by (7) and fractional diffusion, the following Monte Carlo scheme is derived by considering an arbitrary domain where the domain boundary is segmented into two parts with prescribed values ϕ_1 and ϕ_2 respectively. The scheme is constructed to find the potential value at a specified point P in Ω through the following steps:

1. A particle is placed at the point P.
2. This particle then undergoes a random walk that continues until the particle crosses a domain boundary.
3. This walk is constructed of successive steps $(\Delta x, \Delta y)$ chosen from equation (7) with a scale parameter γ chosen to be smaller than the domain size.
4. To ensure that a walk is not over influenced by a more heavily weighted tail (small α) in a given coordinate direction, the scale choices are set such that $\gamma_x \Rightarrow \gamma^{(1/1+\alpha_x)}$ and $\gamma_y \Rightarrow \gamma^{(1/1+\alpha_y)}$. Note, for a Gaussian pdf $\alpha = 1$, on associating γ with the variance, this choice will generate a scaling equal to the standard deviation.
5. The walk is terminated when the particle exits from the domain.
6. At this time the boundary crossed by the particle is tallied by an integer counter $m_i, i = 1,2$, and a new walk is started by repositioning the particle on point P.
7. After many walks the potential at point P is approximated as

$$\phi_P = \frac{m_1}{N}\phi_1 + \frac{m_2}{N}\phi_2 \tag{8}$$

A schematic of this scheme is shown in Figure E-2a. Note that in the case that $\alpha = 1$ this scheme is essentially identical to previous Monte Carlo random walk schemes found in the literature (see review in Haji-Sheikh and Howell, 2006). The key difference here is the generalization of the non-Gaussian pdf associated with fractional diffusion.

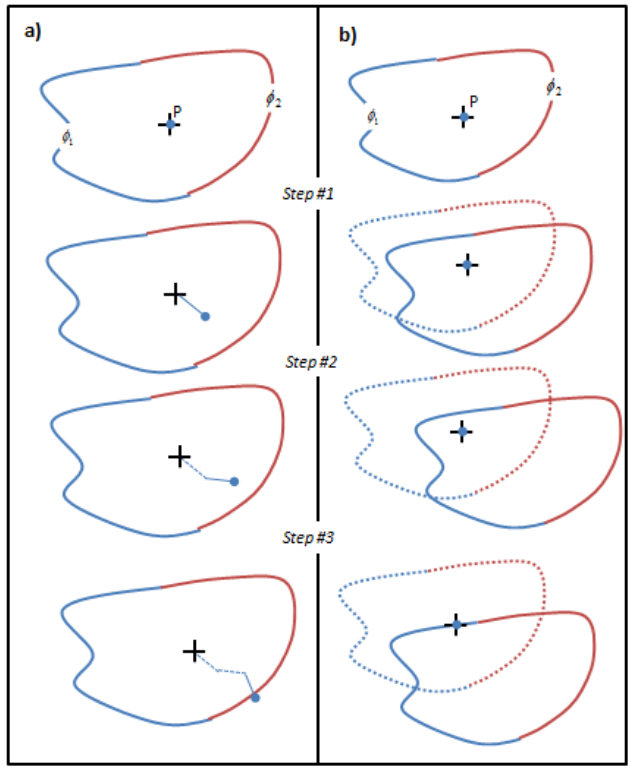

Figure E-2. Demonstration of the a). particle random walk and b). *domain shifting* random walk scheme for an arbitrary domain with Dirichlet boundary conditions ϕ_1 (blue) and ϕ_2 (red) after 3-steps.

3.2 An Initial Test Problem

A demonstration of the above particle random walk scheme difference is made by considering the one-dimensional fractional diffusion problem,

$$\frac{d}{dx}\left[\frac{1+\beta_x}{2}\frac{d^{\alpha_x}\phi}{dx^{\alpha_x}}-\frac{1-\beta_x}{2}\frac{d^{\alpha_x}\phi}{d(-x)^{\alpha_x}}\right]=0$$

$$\phi(0)=1,\quad \phi(1)=0 \tag{9}$$

This problem admits closed solutions, when the non-locality is directed fully downstream $\beta=-1$ the solution is $\phi=(1-x)^{\alpha}$, alternatively when the non-locality is directed fully up-stream $\beta=1$, the solution is $\phi=1-x^{\alpha}$. Direct use of the proposed particle random walk solution on this problem leads to an interesting inconsistency. Figure E-3 shows the

solution obtained for the points $x_i = i/10, i = 1,2,..9$ when $\alpha = 0.5, \beta = 1$ with N=4000 walkers used at each point and the scale parameter in (7) set as $\gamma = 0.005$. For this choice of fractional parameters the correct solution is $\phi = 1 - x^{\alpha}$ the particle random walk process, however, generates the solution $\phi = (1-x)^{\alpha}$. That is the particle random walk process using the Lévy distribution associated with the left hand derivative ($\beta = 1$) generates the solution corresponding to the right-hand derivative $(\beta = -1)$. In other words, for the particle random walk to work the skew used in generating the steps via (7) needs to be set as $\beta^* = -\beta$.

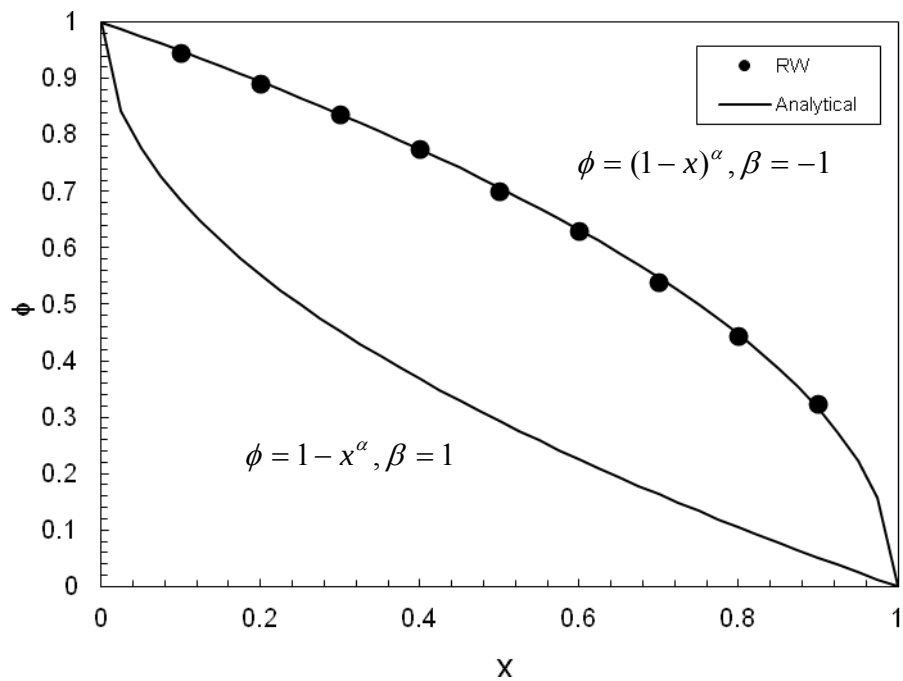

Figure E-3. Particle Random walk solution of equation (9) for $\alpha = 0.5, \beta = 1$ with exact solution for $\beta = 1$ and $\beta = -1$.

A hypothesis of what is happening here is that the proposed particle random walk assesses the *influence of the specified point on a given boundary*. Whereas a more physical realization would be to assesses *the influence of a given boundary on the specified point*. Clearly if the pdf in equation (7) is symmetric (e.g. a normal distribution associated with integer diffusion $\alpha = 1$) the influence of the point on the boundary or the

boundary on the point will be identical. When the pdf is non-symmetric however, i.e., fractional derivatives with $0 < \alpha < 1$ are in play, the test problem is indicating that the random walk process needs to operate in a mirror image mode such that *the influence of a given boundary on the specified point* is determined.

3.3 A Domain Shift Random Walk Scheme

An alternative scheme, which does essentially mirror the particle random walk scheme, is to determine the potential value at a specified point P in Ω through a succession of random steps that rigidly shifts the domain itself about a now *fixed* point *P*—see Figure E-2b. The particular steps in this so called *domain shift* method are as follows

1. The point P is placed at a specified point in the domain and its location is fixed.
2. The domain then undergoes a random rigid motion that continues until the point *P* falls outside of the current domain position.
3. As with the particle random walk the motion of the domain is constructed of successive steps $(\Delta x, \Delta y)$ chosen from equation (7).
4. As before, appropriate scaling is employed to reduce bias from thick tails.
5. The walk is terminated when the point *P* falls outside of the domain.
6. At this time the last boundary segment that crossed over the point is tallied by an integer counter $m_i, i = 1,2$, and a new domain shifting process is started by repositioning the domain to its original position.
7. After many such domain shifting processes the potential at point P is once again approximated by equation (8).

When equation (9) is re-solved by applying the domain shifting process (*N*=4000 realizations of the domain shift with steps generated using the values $\gamma = 0.005, \alpha = 0.5, \beta = 1$). The resulting solution, at points $x_i = i/10, i = 1,2,..9$, shown in Figure E-4, closely matches the expected analytical solution $\phi = (1-x)^{\alpha}$. A result that demonstrates that the proposed domain shifting process corrects the drawback of the

particle random walk scheme. That is, with domain shifting, the value of β used to generate the random walk step, matches the value in the associated fractional diffusion equation. Hence from this point on the domain shifting scheme will be the random walk process of choice in solving fractional diffusion equations.

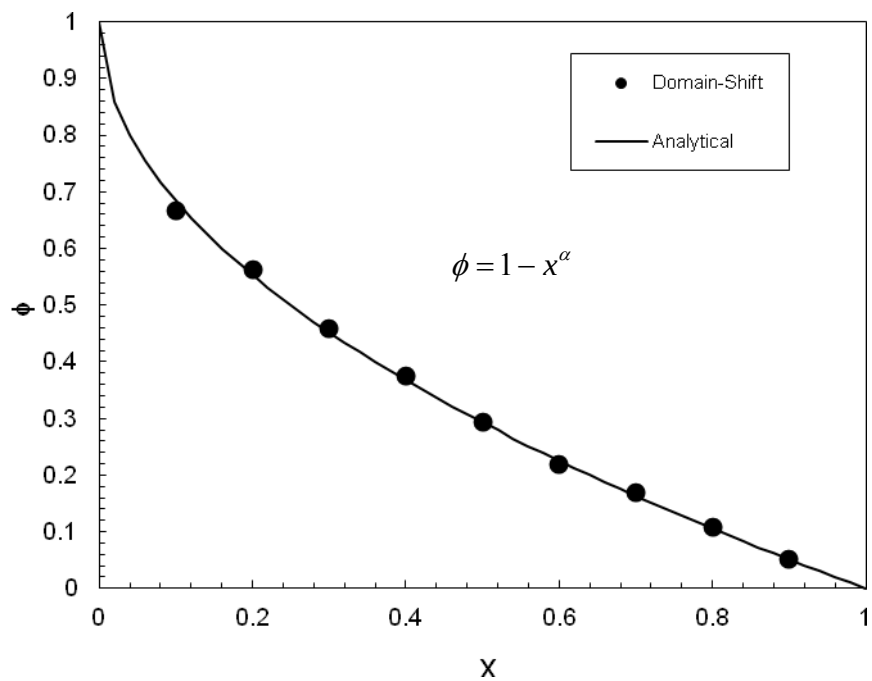

Figure E-4. Solution to equation (9) with domain shifting random walk scheme ($\gamma = 0.005, \alpha = 0.5, \beta = 1.0$) along with the analytical solution.

4 Analysis of the Domain Shifting Random Walk Scheme

Before the non-Cartesian domain feature of the domain shifting random walk scheme is demonstrated, it is worthwhile to investigate the basic components of the scheme.

4.1 What fractional diffusion equation is solved?

The analytical solution shown in Figure E-4 is obtained using the Caputo definition of the fractional derivative (see equation (5) and (6)). An alternative definition is the Riemann-Liouville, expressed as an integer derivative of a fractional integral (Podlubny, 1999), i.e., the left hand Riemann-Liouville derivative of order $0 < \alpha \le 1$ is

$$\left.\frac{d^{\alpha}\phi}{dx^{\alpha}}\right|^{RL} = \frac{1}{\Gamma(\alpha-1)}\frac{d}{dx}\int_{0}^{x}(x-\xi)^{-\alpha}\phi(\xi)d\xi \tag{10}$$

From Podlubny (1999), the following relationship can be obtained between the Caputo and Riemann-Liouville of order $0 < \alpha \leq 1$

$$\left.\frac{d^{\alpha}\phi}{dx^{\alpha}}\right|^{RL} = \frac{d^{\alpha}\phi}{dx^{\alpha}} + \frac{x^{-\alpha}}{\Gamma(1-\alpha)}\phi(0) \tag{11}$$

Thus the Riemann-Liouville differs from the Caputo by an additional term featuring the left-hand boundary condition. If this condition is $\phi(0) = 0$, the Caputo and Riemann-Liouville definition are equivalent. Note however, in the analytical solution in Figure E-4, the left-hand boundary condition is $\phi(0) = 1$. Hence it can be inferred from the predictions in Figure E-4, that the domain shift random walk, as expected through the particle motion theory, provides a solution to the Caputo defined fractional diffusion equation.

4.2 Effect of scale and number of steps

The solution of (9) shown in Figure E-4 can also be used to assess the effects of the scale parameter γ and number of random walk realizations *N*. Table E-1 provides the total absolute difference between the domain shifting random walk scheme and analytical solution evaluated over the chosen nine points by taking N=100, 1000, 10000 and γ=0.1, 0.01, 0.001. Note that increasing N and decreasing γ both tend to increase the accuracy of the domain shifting random walk scheme.

Table E-1. Absolute total difference between analytical and domain shifting scheme.

N	γ		
	0.1	0.01	0.001
100	0.35	0.30	0.37
1000	0.31	0.06	0.09
10000	0.27	0.06	0.03

5 Verification of the Domain Shifting Random Walk Scheme

The multi-dimensional operation of the domain shifting random walk scheme can be tested by considering the Caputo derivative version of the general steady state fractional diffusion problem in equation (4) in a square domain $(0 \le y \le 1, \quad 0 \le x \le 1)$. Two solutions have been obtained for the following boundary conditions using direct differentiation and substitution in (4) using standard Caputo fractional derivative relationships (Voller *et al*., 2011). With the boundary conditions

$$\begin{aligned} &\phi(x,0) = 1 - x^{\alpha_x} \\ &\phi(0,y) = 1 - y^{\alpha_y} \\ &\phi(x,1) = \phi(1,y) = 0 \end{aligned} \tag{12}$$

and pure left hand derivatives ($\beta_x = \beta_y = 1$) in (4), the analytical solution is

$$\phi(x,y) = \left(1 - x^{\alpha_x}\right)\left(1 - y^{\alpha_y}\right) \tag{13}$$

Alternatively, with the boundary conditions

$$\begin{aligned} &\phi(x,0) = (1-x)^{\alpha_x} \\ &\phi(0,y) = (1-y)^{\alpha_y} \\ &\phi(x,1) = \phi(1,y) = 0 \end{aligned} \tag{14}$$

and pure right-hand derivatives ($\beta_x = \beta_y = -1$) in (4), the analytical solution is

$$\phi(x,y) = (1-x)^{\alpha_x}(1-y)^{\alpha_y} \tag{15}$$

These solutions, for the case when $\alpha_x = 0.3$ and $\alpha_y = 0.7$, are checked against the domain shifting predictions (N= 10000, γ=0.005) for points along the line of symmetry (x=0, y=0 to x=1, y=1) in Figure E-5. The close agreement between prediction and analytical solution is sufficient to verify that the domain shifting random walk scheme provides an accurate solution to two-dimensional fractional diffusion equations.

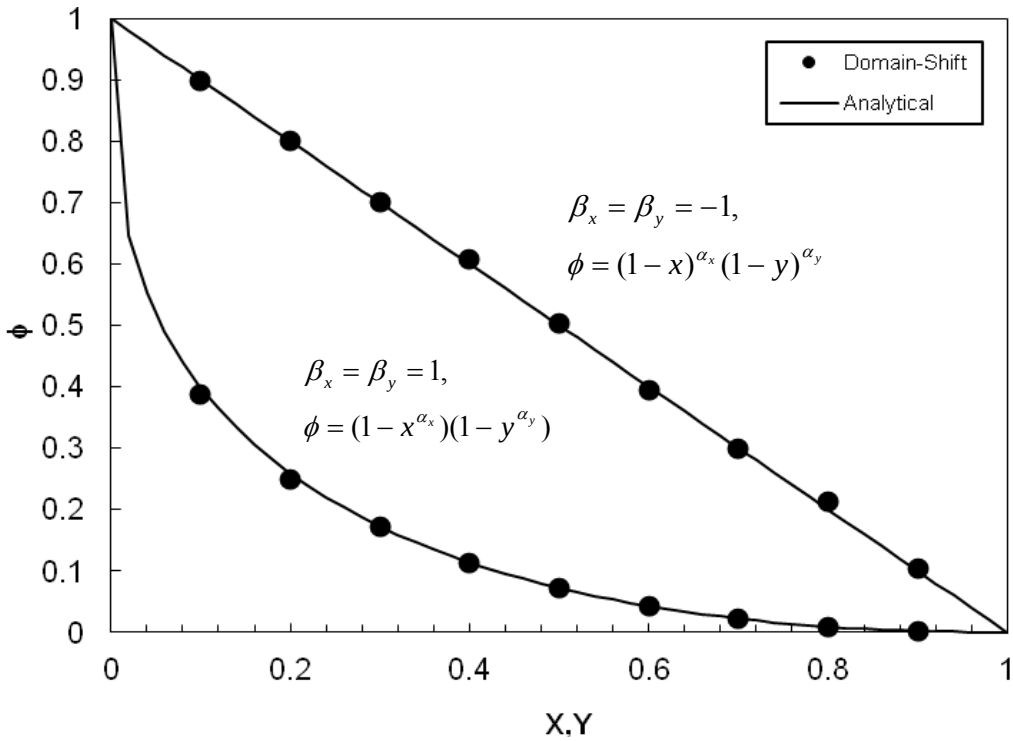

Figure E-5. Solution to equation (12 and 14) $(\alpha_x = 0.3, \alpha_y = 0.7)$ with domain shifting random walk scheme ($\gamma = 0.005, N = 10000$) along with the analytical solution along the line of symmetry.

6 Solution in a Non-Cartesian Domain

The ability of the proposed domain shifting random walk scheme to solve a steady state fractional diffusion problem in a non-Cartesian domain can be demonstrated by considering its application in a circular annulus domain consisting of an inner radius, $r = 1$ at $\phi = 1$, and outer radius, $r = 2$ at $\phi = 0$, see Figure E-6a. In the first instance a consistency check is made by using the domain shifting random walk to obtain predictions along the radii at $\theta = 0$ and $\theta = \pi/2$ in the non-fractional case ($\alpha_x = \alpha_y = 1$), see Figure E-6b. As expected these predictions closely match the known axisymmetric analytical solution for this case

$$\phi(r) = 1 - \frac{\ln(r)}{\ln(2)} \tag{16}$$

A test for a fractional case, using the same reference radii as the previous result, is provided in Figure E-7. Here the settings are $\alpha_x = 0.3, \alpha_y = 0.7$ and $\beta_x = -1, \beta_y = 1$, with domain shifting parameters $\gamma = 0.0005, N = 4000$. These predictions, driven by the non-local behavior embedded in the choice of the $\alpha's$ and $\beta's$, are clearly non-axisymmetric. It is important to note that this non-axisymmetric behavior is still retained in cases where symmetric Lévy distributions are used. To confirm this, Figure E-8 shows the domain shifting predictions, along the reference radii, for the previous problem of Figure E-7, but with the symmetric pdf settings $\beta_x = \beta_y = 0$.

7 Conclusions

The accurate description of diffusion in systems where the length scale of heterogeneities approaches the domain length scale may require non-local treatments. If the heterogeneous length scales are power-law distributed then an appropriate non-local model can be posed in terms of fractional derivatives. The essential feature in such models is that the flux at a given point is expressed as a weighted sum of potential gradients over a non-local neighborhood around the point. In Cartesian systems such non-local fluxes can be represented by generalizations of standard finite difference schemes. In non-Cartesian systems, however, it is much more difficult to construct discrete representations of non-local fluxes. In this paper an alternative to grid-based solutions—based on a Monte-Carlo random walk process—has been proposed for the solution of steady-state fractional diffusion problems in non-Cartesian domains. This solution is based on the established random-walk solution for the standard integer diffusion problem. The critical differences are (1) the selection of random walk steps from a non-symmetric, power-law tailed, Lévy distribution—a distribution theoretically related to the fundamental solution of fractional diffusion—and (2) a novel domain shifting approach that ensures the boundary influence on a given point of interest, correctly accounts for the non-symmetric nature of the Lévy distribution. Some restrictions do apply, however. In the first place the existing domain shifting random walk construction cannot currently

deal with problems that have source terms, boundary conditions involving a specified flux, or non-linear diffusivities.

In the current work this proposed solution approach has been verified by comparing predictive performance of the domain shifting random walk in the solution of one- and two-dimensional steady-state fractional diffusion problems with known analytical solutions. Beyond this, the ability of the domain shifting random walk has been demonstrated by the solution of steady state fractional diffusion in a non-Cartesian annulus domain. In this demonstration, the full generality of the factional diffusion is imposed by setting different values for the non-locality measures (level α and skew β) in the coordinate direction.

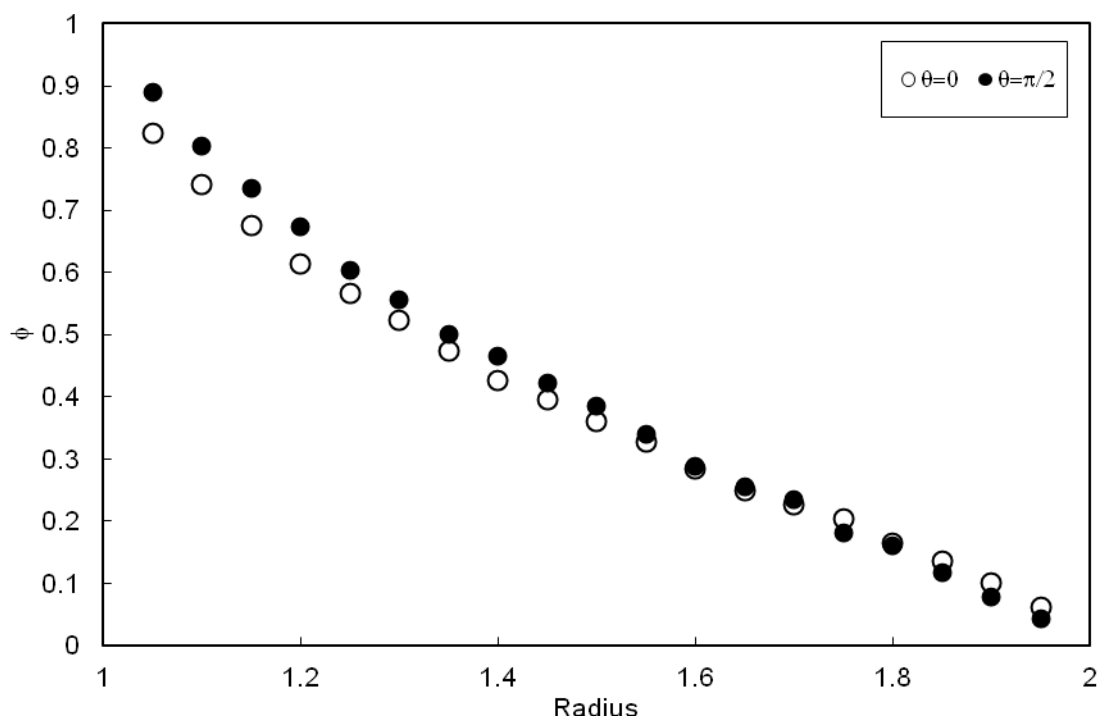

Figure E-8. Profiles for annulus problem along $\theta = \pi/2$ and $\theta = 0$ radii with domain shifting random walk scheme ($\gamma = 0.0005, N = 4000$) for fractional diffusion case $\alpha_x = 0.3, \alpha_y = 0.7$ and $\beta_x = \beta_y = 0$.

In closing the following comments are made about the domain shift predictions in non-Cartesian geometries. The verification of the domain shifting random walk in a two-

dimensional Cartesian domain, achieved by comparing with closed analytical solutions, is sufficient evidence that the scheme will provide valid solutions for general multi-dimensional fractional diffusion systems. This result justifies applying the mechanics of the domain shifting random walk to obtain predictions for non-Cartesian geometries such as the annulus geometry studied in this work. It is important to recognize, however, that in making this application, no explicit problem statement was made. Indeed, for a non-Cartesian geometry, it remains an open question as to what such a problem statement would be. Never the less, this does not detract from the fact that the domain shifting random walk does provide non-Cartesian domain predictions that systematically account for the level α and skew β of non-locality in a given diffusion system. In this way, domain shifting random walk predictions for steady-state, source free systems, with Dirichlet conditions, will provide an invaluable tool to direct the development of more sophisticated and generally applicable grid based FEM inspired schemes for fractional diffusion.

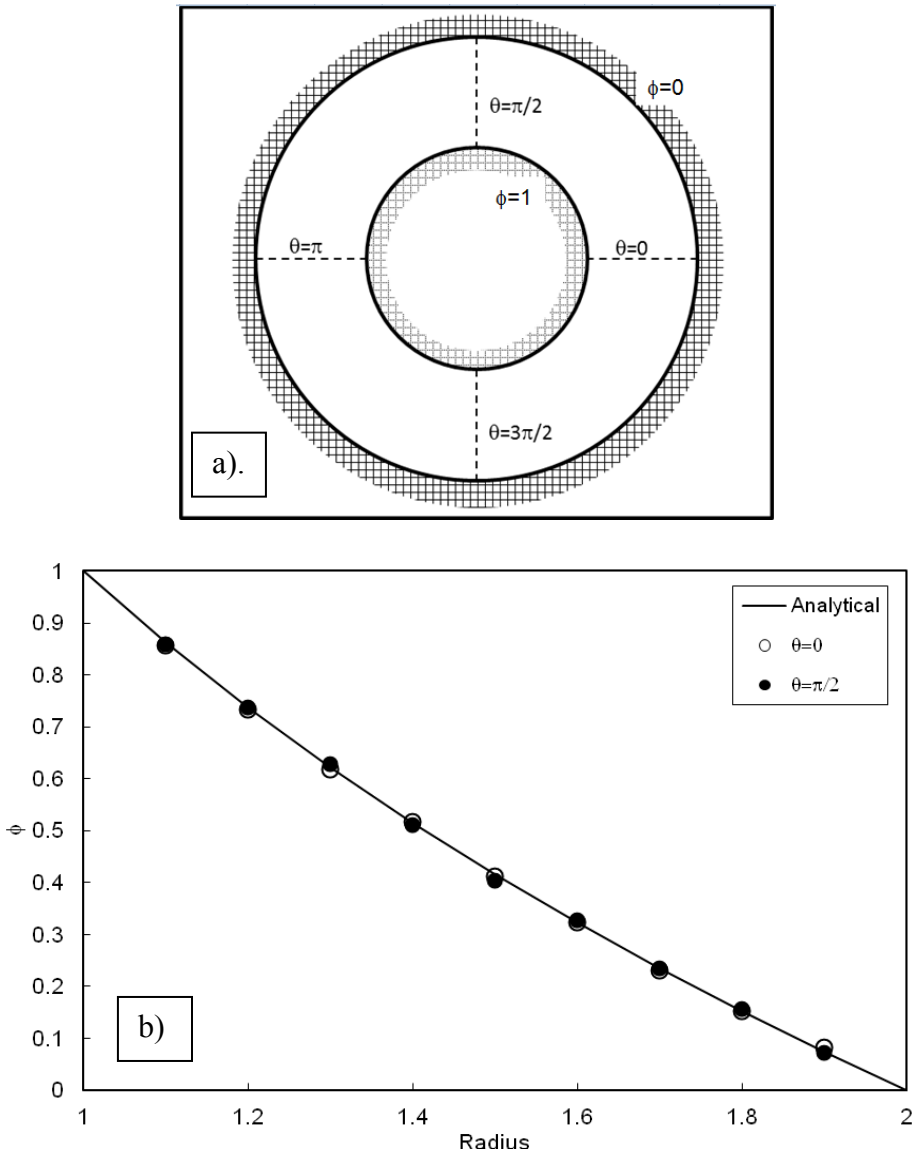

Figure E-6. Circular annulus problem a). domain and boundary conditions and b.) comparison of domain shifting random walk scheme ($\gamma = 0.0001, N = 4000$) predicted profiles and analytical solution for integer diffusion case—$\alpha_x = \alpha_y = 1$.

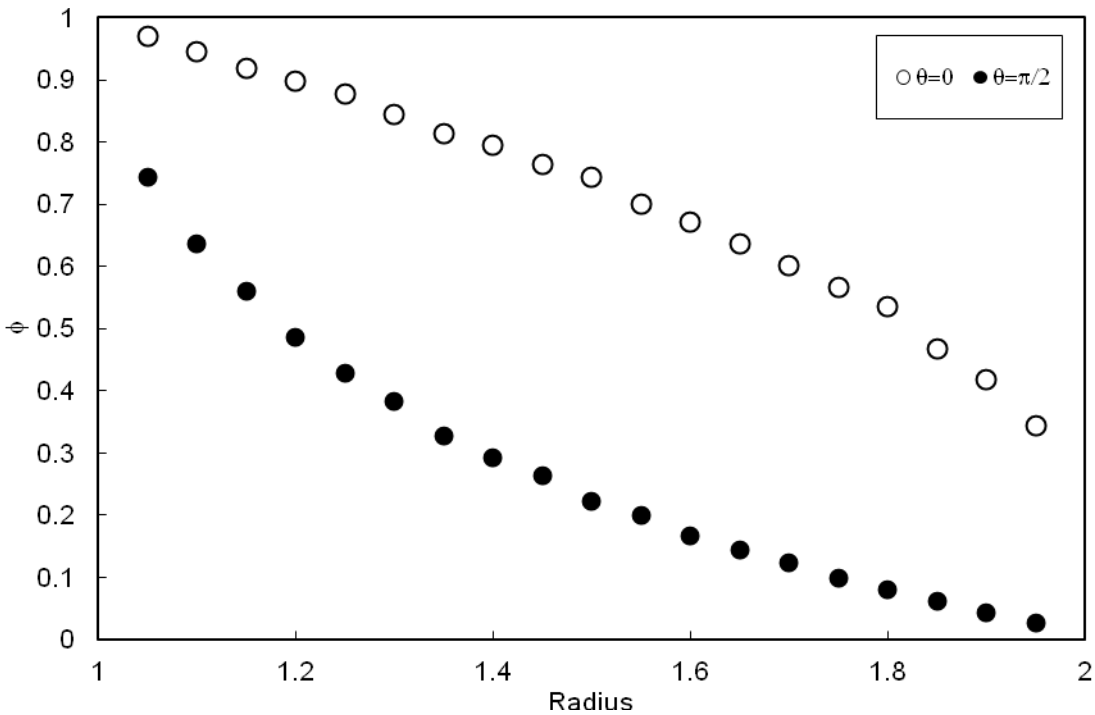

Figure E-7. Profiles for annulus problem along $\theta = \pi / 2$ and $\theta = 0$ radii with domain shifting random walk scheme ($\gamma = 0.0005, N = 4000$) for fractional diffusion case $\alpha_x = 0.3, \alpha_y = 0.7$ and $\beta_x = -1, \beta_y = 1$.

Appendix F: The control volume weighted flux scheme (CVWFS) for two-dimensional, two-sided Caputo fractional diffusion equations

Submitted as: Zielinski, D.P., Voller, V.R. (2013), The control volume weighted flux scheme (CVWFS) for two-dimensional, two-sided Caputo fractional diffusion equations, *Advances in Engineering Software*

A standard model for non-local diffusive transport, applicable when the distribution of heterogeneity length scales has infinite variance, is to represent the flux in terms of a fractional derivative. Here, a recently proposed scheme for fractional diffusive transport — the Control Volume Weighted Flux Scheme (CVWFS)—which is based on Caputo fractional derivatives, is extended to operate in two or more dimensions. The essential feature in the CVWFS is the representation of the flux at a point as a weighted sum of gradients operating up- and down-stream of that point. Following presentation of the scheme, the convergence and accuracy of the CVWFS, using alternative weightings, is demonstrated and its accuracy illustrated by comparing numerical predictions with two-dimensional analytical solutions.

1 Introduction

In a diffusion process an initial pulse will spread with a length scale $\ell \sim t^n$,where $n = ½$ in the case of normal diffusion. In some processes, however, due to the presence of heterogeneities, the time exponent for the spreading length scale can differ from the value of $n = ½$. Such a process is referred to as anomalous diffusion, with the exponent $1 > n > ½$ called super-diffusion and $n < ½$ called sub-diffusion (Voller, 2010; Lynch et al., 2003). As heterogeneities scale up to the domain length, the impact of resulting long waiting times – leading to sub-diffusive transport – and short paths – leading to super-diffusive transport – cannot be homogenized. In this context it is difficult to accept that at some scales, non-local and non-instantaneous effects will not be favored. With the frequency at which transport in disorded (i.e. heterogeneous) systems is studied, it is not surprising that anomalous diffusion has been observed in a number of physical systems. A brief selection of these include solute transport in a porous media (Zhang et al, 2007a; Yong et al., 2006; Zhang et al., 2005;Bensen et al. 2000a; Bensen et al. 2000b), earth-surface sediment transport (Voller et al, 2012; Ganti et al., 2010; Voller and Paola, 2010; Schumer et al., 2009) stream solute transport (Shen and Phanikuman, 2009), heat transfer in porous media (Scherer et al., 2008), moving boundary problems in heat transfer (Voller, 2010 and Liu and Xu, 2009) drug release (Xicheng et al., 2007), and organism dispersal (Viswanathan et al, 2011).

In conventional diffusion processes, the flux at a point is proportional to the local gradient of the potential ϕ with the *x*-component given by

$$q_x = -\nu \frac{\partial \phi}{\partial x} \tag{1}$$

where ν is the suitably dimensioned diffusivity coefficient. In contrast, cases where the length scales of the heterogeneities in the system have a distribution with infinite variance – i.e. power-law distributions – the flux is controlled by non-local properties; a situation that leads to anomalous super-diffusion. A number of theoretical results (Voller, 2010; Schumer et al, 2009; Xigheng, et al., 2007; Metzler and Klafter, 2000) indicate that this non-local process can be effectively modeled in terms of derivatives of fractional

order $0 < \alpha = \frac{1-n}{n} \leq 1$. One such realization of this model is to express the flux as a combination of left and right-sided Caputo fractional derivatives

$$q_x = -\nu \frac{1+\beta_x}{2} \frac{\partial^{\alpha_x} \phi}{\partial x^{\alpha_x}} + \nu \frac{1-\beta_x}{2} \frac{\partial^{\alpha_x} \phi}{\partial (-x)^{\alpha_x}} = \frac{1+\beta_x}{2} q_x^L + \frac{1-\beta_x}{2} q_x^R \tag{2}$$

where $-1 \leq \beta_x \leq 1$ is a bias weighting between the left and the right-sided derivatives and $0 < \alpha_x \leq 1$ is the order of the derivative—which can also be viewed as a measure of the non-locality in the system. The left sided (L) and right sided (R) derivatives in Equation (2) are respectively defined by (Podlubny, 1998)

$$\frac{\partial^\alpha \phi}{\partial x^\alpha} = \frac{1}{\Gamma(1-\alpha)} \int_0^x (x-\xi)^{-\alpha} \frac{\partial \phi(\xi)}{\partial x} d\xi \tag{3a}$$

$$\frac{\partial^\alpha \phi}{\partial (-x)^\alpha} = \frac{-1}{\Gamma(1-\alpha)} \int_x^1 (\xi - x)^{-\alpha} \frac{\partial \phi(\xi)}{\partial x} d\xi \tag{3b}$$

where Γ is the gamma function. In the event that $-1 < \beta_x < 1$, Equation (2) is considered two-sided – i.e. non-local flux is governed by up- and down-stream contributions. Note that the Caputo definition in Equation (2) and Equation (3) is preferred over the alternative Reimann-Liouville definition because conditions at the boundaries can be more easily constructed to match physically meaningful conditions and the Caputo fractional derivative of a constant is zero Podlubny (1999).

Under the assumption that the heterogeneities in the coordinate directions are statistically independent (i.e. multi-scaled), see discussions by Tadjeran and Meerschaert (2007), and that the domain is scaled so $0 \leq x \leq 1$; $0 \leq y \leq 1$ a general fractional diffusion equation in two dimensions can be written as

$$\frac{\partial \phi}{\partial t} = -\frac{\partial q_x}{\partial x} - \frac{\partial q_y}{\partial y} + S \tag{4}$$

where S is a source term, and the definition of q_y is simply obtained by replacing y for x in Equation (2). It should be noted that in one-dimension, Equation (4) recovers the traditional diffusion equation, whose point source solution is the normal distribution, when $\alpha = 1$. In contrast, when $0 < \alpha < 1$, the one-dimensional fractional diffusion

equation results, whose point source solution is an α-stable Lévy distribution (Bensen et al., 2000) – of which the normal distribution is a subset. Since all fractal phenomena have intrinsic, scale-free, power laws associated with them, researchers are actively attempting to estimate values of α from actual data, which is made difficult due to the scale free properties. In contrast, normal diffusion processes do exhibit a characteristic scale and a well-defined physical interpretation (Viswananthan et al., 2011)).

In terms of finding approximate solutions of the form in Equation (4), previous research has been based on the so called one-shift Grünwald approximation (Yang, 2010; Schumer et al., 2009; Shen and Phanikumar, 2009; ; Zhang et al., 2007b; Tadjeran and Meerschaert, 2007; Meerschaert and Tadjeran, 2006; Podlubny, 1999) or the alternative L1/L2 approximation (Yang, 2010; Shen and Phanikumar, 2009; Zhang et al., 2007b; Ilic et al, 2005; Zhang et al., 2005; Diethelm et al., 2005; Lynch et al., 2003; Diethlam, 1997; Oldham and Spanier; 1974) for fractional derivatives. In particular, Meerschaert and Tadjeran used the one-shift Grünwald approximation with a fully implicit ADI (Meerschaert and Tadjeran, 2006) and Crank-Nicolson ADI (Tadjeran and Meerschaert, 2007) time stepping schemes and Yang et. al. (2011) used the L1/L2 approximation in both finite element and finite difference solutions.

Recently Voller et. al. (Voller et al., 2011) obtained a solution to the one-dimensional form of Equation (4) using a discrete control volume approach – called the Control Volume Weighted Flux Scheme (CVWFS). The novelty of the approach lies in modeling the local diffusion flux at local control volume face as the weighted average of gradients across the control volume faces up- and down-stream, and creates a physical analog for the non-local diffusion that can be implemented directly into a control volume discretization. Here, we will expand the CVWFS to find numerical solutions for the two-dimensional transient Caputo fractional diffusion problem in Equation (4). Where possible this approach will be verified by using available analytical solutions. This paper is based upon Zielinski and Voller (2012), but the current paper includes expanded discussion on alternative solution techniques to Equation (4) and further descriptions of physical analogues to fractional diffusion. In addition it includes an important test

problem that demonstrates how the proposed CVWFS can be used to solve problems that include both up- and down- stream contributions to the non-locality.

The paper is laid out as follows. In the next section a brief overview of the CVWFS approach applied to a one-dimensional version of Equation (4) is given. Through an example one-dimensional problem, an error analysis of this scheme and with comparison to alternative schemes from the literature is conducted. Following, the CVWFS approach is generalized to handle the full two-dimensional form of Equation (4). The work concludes with a number of test problems that demonstrate the relative accuracy of the CVWFS when compared to the one-shift Grünwald (Yang, 2010; Schumer et al., 2009; Shen and Phanikumar, 2009; ; Zhang et al., 2007b; Tadjeran and Meerschaert, 2007; Meerschaert and Tadjeran, 2006; Podlubny, 1999) and L1/L2 approximations approximation (Yang, 2010; Shen and Phanikumar, 2009; Zhang et al., 2007a; Ilic et al, 2005; Zhang et al., 2005; Diethelm et al., 2005; Lynch et al., 2003; Diethlam, 1997; Oldham and Spanier; 1974) ,and verify the application of the proposed two-dimensional form of the CVWFS.

2 Overview of the CVWFS

Before demonstrating the discretization of the CVWFS in two-dimensions, it is important to understand the main characteristics of the method in one-dimension. The CVWFS is a discrete control volume (or finite volume) method that was developed to numerically solve non-local diffusion transport problems in the scaled domain $0 \le x \le 1$, (Voller et al., 2011). In this approach a uniformly spaced grid of NX+1 nodes a distance $\Delta x = 1/NX$ apart is assumed—note this will place nodes on the boundary (see Figure F-1).

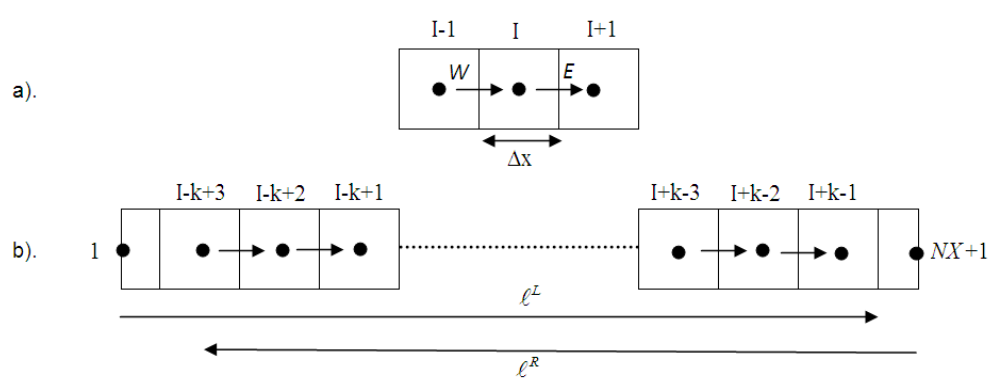

Figure F-1: Grids for calculating diffusion flux in one-dimension with a). local diffusion and b). non-local diffusion (Figure modified from Voller et al. Figure 1 (Voller et al., 2011)). Fluxes from the W-west and E-east are noted at node *I,J*.

In a standard approach the flux into the control volume about node *I* from the left, defined as q_{west_I}, would be estimated in terms of the potential gradient at the control volume face located at $x = x_I - \Delta x/2$. In a similar manner the flux out to the right, q_{east_I}, would be determined solely by the potential gradient at the face located at $x = x_I + \Delta x/2$. By contrast, in the CVWFS these fluxes are calculated in terms of a weighted average of the potential gradients across multiple control volume faces up- and down-stream of node *I* (see Figure F-1). There are two end-members in this treatment. In the first the flux on a given face of the control volume is calculated in terms of the potential gradients at and on all the neighboring control volume faces positioned to the *Right* of the given face. In this way the flux at the *east* and *west* faces of the Ith control volume are written as the weighted average

$$\begin{aligned} q^R_{west_I} &= \frac{\nu_{west_I}}{\Gamma(2-\alpha)} \sum_{k=1}^{NX+2-I} W_k \left[\frac{\phi_{I+k-2} - \phi_{I+k-1}}{\Delta x} \right] \\ q^R_{east_I} &= \frac{\nu_{east_I}}{\Gamma(2-\alpha)} \sum_{k=1}^{NX+1-I} W_k \left[\frac{\phi_{I+k-1} - \phi_{I+k}}{\Delta x} \right] \end{aligned} \tag{5}$$

where W_k are appropriately selected flux weights. Note, in Equation (5), only faces that lie within the domain $0 \le x \le 1$ are included in the weighted sum and that the upper limit of the summation differ by one; a device, as detailed in Voller et. al. (2011), that leads to desirable numerical properties. The opposite of Equation (5) is to write the face fluxes as a weighted sum of gradients at the faces that lie to the *Left* of the given face, i.e.

$$\begin{aligned} q^L_{west_I} &= \frac{\nu_{west_I}}{\Gamma(2-\alpha)} \sum_{k=1}^{I-1} W_k \left[\frac{\phi_{I-k} - \phi_{I+1-k}}{\Delta x} \right] \\ q^L_{east_I} &= \frac{\nu_{east_I}}{\Gamma(2-\alpha)} \sum_{k=1}^{I} W_k \left[\frac{\phi_{I+1-k} - \phi_{I+2-k}}{\Delta x} \right] \end{aligned} \tag{6}$$

In applying Equations (5) and (6) to solve fractional diffusion problems, Voller et. al. (2011) proposed using the power law weights

$$W_k = (1-\alpha)[(k-\mu)]^{-\alpha}\,\Delta x^{1-\alpha}$$

$$0 < \mu = \left[1 - \Gamma(1-\alpha)^{-\frac{1}{\alpha}}\right] < 1 \tag{7}$$

The following comments are made

1. As shown in (2011), a connection to the Caputo derivate definition in Equation (3) is established by noting that the components in Equations (5) and (6) are respectively formal approximations of q_x^R and q_x^L defined in Equation (2) when a constant of $\frac{1}{(1-\alpha)\Gamma(1-\alpha)} = \frac{1}{\Gamma(2-\alpha)}$ is multiplied by the weights generated by Equation (7).
2. The form of the correction μ allows for the recovery of the correct local approximation for the flux as $\alpha \to 1$.
3. A discrete flux balance over a control volume, using Equations (5) and/or (6), will lead to a system of discrete equations that, in a steady state case, will be diagonally dominant.

3 Alternative Weights

The power-law weights in Equation (7) can be replaced by alternative weighting schemes derived from other fractional derivative algorithms developed in the literature. One example is the L1/L2 algorithm for approximation of Caputo derivatives (Yang, 2010; Shen and Phanikumar, 2009; Zhang et al., 2007a; Ilic et al., 2005; Zhang et al., 2005; Diethelm et al., 2005; Lynch et al., 2003; Diethelm, 1997; Oldham and Spanier, 1974). The L1/L2 weights are derived from the first –order approximation of Equation (3a) or (3b) in a finite volume method (Oldham and Spanier, 1974). When applied to the CVWFS framework the L1/L2 weights are given by

$$W_k^{L1/L2} = \left[k^{1-\alpha} - (k-1)^{1-\alpha}\right]\Delta x^{1-\alpha}, \quad 1 \le k \le NX \tag{8}$$

Another example are weights obtained from the classical Grünwald approximation for a fractional derivative (Schumer et al., 2009; Shen and Phanikumar, 2009; Zhang et al., 2007b; Podlubny, 1999), which can be manipulated to the CVWFS

form in Equations (5) and (6) to provide the following alternative definition for the weights in Equation (7)

$$W_k^G = \Gamma(2-\alpha)\sum_{i=1}^{k} g_i \Delta x^{1-\alpha} \quad 1 \le k \le NX \tag{9}$$

where

$$g_1 = 1$$
$$g_i = \frac{i-2-\alpha}{i-1} g_{i-1}, \quad i = 2,3,...k \tag{10}$$

Note when these weights are used in the CVWFS the resulting scheme will match the so called one-shift Grünwald schemes for fractional diffusion previously reported in the literature (Voller et al., 2011; Yang, 2010; Schumer et al., 2009; Shen and Phanikumar, 2009; Tadjeran and Meerschaert, 2007; Zhang et al., 2007b; Meerschaert and Tadjeran, 2006; Meerschaert et al., 2006; Podlubny, 1999).

Table F-1 compares values of $\Delta x^{\alpha-1} W_k / \Gamma(2-a)$ (k=1 .. 5) for the case $\alpha = 0.3$, using all three methods. Observe the close match between the CVWFS weights (Equation (7)) and the Grünwald weights (Equation (9)) for all k=1,2… and the initial differences in the L1/L2 weights (Equation (8)). In respect to the first observation, it is noted that close agreement between the Grünwald and CVWFS weights is achieved through the choice of the correction factor μ in Equation (7); which enforces an exact match for the first weight, k=1.

Table F-1: Alternative normalized weights for CVWFS

k	CVWFS	Grünwald	L1/L2
1	1.0000	1.0000	1.1005
2	0.6936	0.7000	0.6873
3	0.5910	0.5950	0.5868
4	0.5328	0.5355	0.5297
5	0.4933	0.4953	0.4910

4 Extension of CVWFS to 2D Caputo Fractional Diffusion Equations

The approximate solution of the 2-D fractional diffusion problem in Equation (4) requires a straight forward extension of the 1-D CVWFS (Voller et al., 2011) outlined above. The key idea is to treat the *y* derivative approximations to the *north* (above) and *south* (below) of node *I,J* in the same fashion as the left and right hand *x* derivative approximations defined by Equations (5) and (6). The starting point is to assume a scaled domain of $(NX+1)\times(NY+1)$ nodes, where node *I,J* is located on the Ith column and J^{th} row of the discretization displayed in Figure F-2.

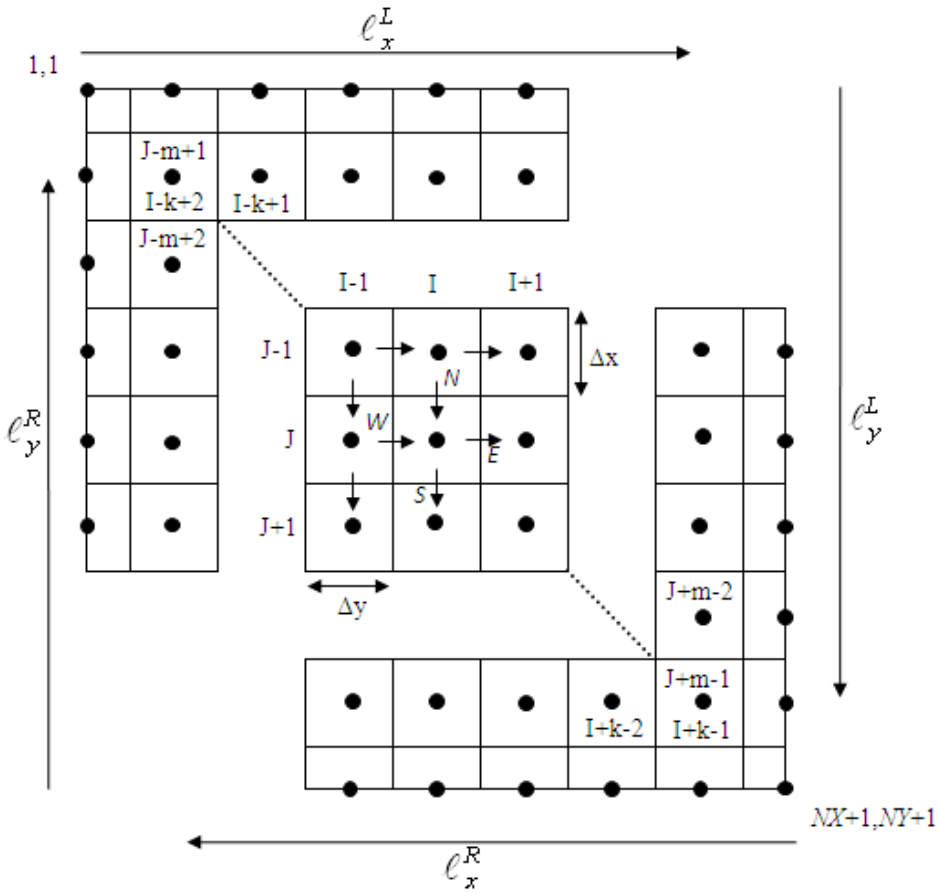

Figure F-2: Grid for calculating diffusion flux in two-dimensions. Subscripts on ℓ indicate direction of non-localities. Fluxes from N-north, S-south, E-east, W-west are noted at node *I,J*.

Then, following directly from Equations (5) and (6), the fluxes in the x-direction on the *east* and *west* faces of the control volume around node *I,J* can be written as the weighted averages

$$q^{R}_{west_{I,J}} = \frac{\nu_{west_{I,J}}}{\Gamma(2-\alpha_x)} \sum_{k=1}^{NX+2-I} W_k^x \left[\frac{\phi_{I+k-2,J} - \phi_{I+k-1,J}}{\Delta x} \right]$$
$$q^{R}_{east_{I,J}} = \frac{\nu_{east_{I,J}}}{\Gamma(2-\alpha_x)} \sum_{k=1}^{NX+1-I} W_k^x \left[\frac{\phi_{I+k-1,J} - \phi_{I+k,J}}{\Delta x} \right] \tag{11}$$

$$q^{L}_{west_{I,J}} = \frac{\nu_{west_{I,J}}}{\Gamma(2-\alpha_x)} \sum_{k=1}^{I-1} W_k^x \left[\frac{\phi_{I-k,J} - \phi_{I+1-k,J}}{\Delta x} \right]$$
$$q^{L}_{east_{I,J}} = \frac{\nu_{east_{I,J}}}{\Gamma(2-\alpha_x)} \sum_{k=1}^{I} W_k^x \left[\frac{\phi_{I+1-k,J} - \phi_{I+2-k,J}}{\Delta x} \right] \tag{12}$$

The weighted average of fluxes in the y-direction is restricted to that of gradients across the faces of control volumes along column *I*. The *north* and *south* flux at node *I,J* based on the derivatives from the left and right of the control volume can then be written as:

$$q^{R}_{north_{I,J}} = \frac{\nu_{north_{I,J}}}{\Gamma(2-\alpha_y)} \sum_{m=1}^{NY+2-J} W_m^y \left[\frac{\phi_{I,J+m-2} - \phi_{I,J+m-1}}{\Delta y} \right]$$
$$q^{R}_{south_{I,J}} = \frac{\nu_{south_{I,J}}}{\Gamma(2-\alpha_y)} \sum_{m=1}^{NY+1-J} W_m^y \left[\frac{\phi_{I,J+m-1} - \phi_{I,J+m}}{\Delta y} \right] \tag{13}$$

$$q^{L}_{north_{I,J}} = \frac{\nu_{north_{I,J}}}{\Gamma(2-\alpha_y)} \sum_{m=1}^{J-1} W_m^y \left[\frac{\phi_{I,J-m} - \phi_{I,J+1-m}}{\Delta y} \right]$$
$$q^{L}_{south_{I,J}} = \frac{\nu_{south_{I,J}}}{\Gamma(2-\alpha_y)} \sum_{m=1}^{J} W_m^y \left[\frac{\phi_{I,J+1-m} - \phi_{I,J+2-m}}{\Delta y} \right] \tag{14}$$

Here, $NX\Delta x = NY\Delta y$ and W_k^x and W_m^y are the flux weight at each control volume face defined by Equation (7) using α_x and α_y, respectively.

Using the approximations of Equation (11-14) the components of divergence of the fractional diffusion on the right hand side of Equation (4) can be approximated as

$$-\left.\frac{\partial q_x}{\partial x}\right|_{I,J} \approx \frac{1+\beta_x}{2}\frac{q^L_{west_{I,J}} - q^L_{east_{I,J}}}{\Delta x} + \frac{1-\beta_x}{2}\frac{q^R_{west_{I,J}} - q^R_{east_{I,J}}}{\Delta x}$$

$$-\left.\frac{\partial q_y}{\partial y}\right|_{I,J} \approx \frac{1+\beta_y}{2}\frac{q^L_{north_{I,J}} - q^L_{south_{I,J}}}{\Delta y} + \frac{1-\beta_y}{2}\frac{q^R_{north_{I,J}} - q^R_{south_{I,J}}}{\Delta y} \tag{15}$$

Hence, on using an explicit approximation in time, the following first order accurate in time and second order accurate in space scheme can be generated for the governing Equation (4)

$$\phi_{I,J}{}^{new} = \phi_{I,J} + \Delta t\left[-\left.\frac{\partial q_x}{\partial x}\right|_{I,J} - \left.\frac{\partial q_y}{\partial y}\right|_{I,J}\right] + \Delta t S_{I,J} \tag{16}$$

where *new* denotes the new temperature at node *I,J* at time $t + \Delta t$. Note, a steady state solution of Equation (4) would also be based on Equation (16). In this case, however, *new* would designate a pseudo-time step in an iterative solution.

As noted in (Voller et al., 2011) the CVWFS can naturally handle fixed value boundary conditions by simple substitution of the given values at the extrema of the summations in Equations (11) and (14). An appropriate substitution is also made to account for the prescription of a fixed flux condition. For example if a fixed flux q is applied on the right boundary $x = 1$, an iterative update of the boundary values is made to ensure a correct boundary flux calculation, see (Voller et al., 2011)

$$-\left.\frac{\partial q_x}{\partial x}\right|_{NX+I,J} = \frac{1+\beta_x}{2}\frac{q^L_{west_{NX+1,J}} - q}{0.5\Delta x} + \frac{1-\beta_x}{2}\frac{q^R_{west_{NX+1,J}} - q}{0.5\Delta x} \tag{17}$$

where the factor of 0.5 in the denominator accounts for the half sized control volume at the boundary.

While Equation (16) is the preferred form for computations it is worthwhile for analysis to expand Equation (16) using Equations (11-15) to arrive at the following point scheme

$$\phi_{I,J}{}^{new} = a_{I,J}\phi_{I,J} + \sum_{k=1,k\neq I}^{NX+1} a_{k,J}\phi_{k,J} + \sum_{m=1,m\neq J}^{NY+1} a_{I,m}\phi_{I,m} + \Delta t S_{I,J} \tag{18}$$

where the a's are coefficients as defined in (Voller et al., 2011) for one-dimension. In Equation (18) it is noted, assuming a diffusivity of 1.0 for notational convenience that the only possible negative coefficient is

$$a_{I,J} = 1 + \Delta t\left[\frac{\Delta x^{\alpha_x - 1}}{\Gamma(2-\alpha_x)\Delta x^{1+\alpha_x}}\left(-2W_1^x + W_2^x\right) + \frac{\Delta y^{\alpha_y - 1}}{\Gamma(2-\alpha_y)\Delta y^{1+\alpha_y}}\left(-2W_1^y + W_2^y\right)\right] \tag{19}$$

Consistent with known behaviors in numerical solutions of normal diffusion, Equation (18) shall provide a stable solution provided all the coefficients on the right-hand side are positive. Therefore, setting $a_{I,J} \geq 0$ allows for derivation of stability criteria. In this way using the observation from Table 1 that, for all α's $W_1 = \Gamma(2-\alpha)\Delta x^{1-\alpha}$ and $W_2 \approx (1-\alpha)\Gamma(2-\alpha)\Delta x^{1-\alpha}$ a stability criterion for Equation (16) sets the time step as

$$\Delta t < \left[\frac{1+\alpha_x}{\Delta x^{\alpha_x+1}} + \frac{1+\alpha_y}{\Delta y^{\alpha_y+1}}\right]^{-1} \tag{20}$$

consistent with stability criteria for the one-dimensional CVWFS (Voller et al., 2011) and other explicit fractional transient diffusion schemes in the literature (Meerschaert and Tadjeran, 2006).

It should be noted that the current form of the two-dimensional CVWFS is restricted for use on uniform, rectangular, structured grids. However, recent work by Ervin and Roop (Ervin and Roop, 2006; Roop, 2006) led to the developed of a theoretical framework for a Galerkin finite element approximation for fractional advection diffusion equations (FADEs) on unstructured grids in Cartesian domains.

5 Testing and Results

5.1 Comparison of Weighting Schemes

As noted above with the proposed CVWFS, three alternative weighting schemes can be used: the original weights suggested by Voller et al (Voller et al., 2011) (Equation (7)), weights based on the L1/L2 algorithm (Equation (8)), and weights derived from the Grünwald approximation (Equation (9)). To provide an illustration on the

relative accuracy of these three alternatives we consider the following one-dimensional Caputo fractional diffusion equation

$$\frac{\partial}{\partial x}\left(\frac{\partial^{\alpha}\phi}{\partial x^{\alpha}}\right)=0\,,\ 0\le x\le 1 \tag{21}$$

With

$$\phi(0)=1\text{, and }\ \phi(1)=0 \tag{22}$$

The analytical solution to Equation (21) with Equation (22) is

$$T=1-x^{\alpha} \tag{23}$$

The accuracy of each respective flux weight system is analyzed by inserting each weight into the 1-D steady state problem in the x-direction of Equation (16) using the pseudo time stepping CVWFS approach. The L-infinity norm—maximum absolute error—was calculated for each weighting scheme for varying grid sizes and α 's (see Table F-2).

As might be expected from the close match between the weights in Table F-1, similar values of the relative error between the Grünwald and CVWFS weights is observed, with both methods more accurate than predictions obtained with the L1/L2 weights. Based on the above tests, the remaining applications of the CVWFS will all use the original weights suggested by Voller et al. (2011) given in Equation (7) and will be implemented on grids of size $\Delta x, \Delta y \le 0.00625$.

Table F-2: L-infinity norm for CVWFS approximate solution to the one-dimensional fractional diffusion problem in Equation (25) utilizing each alternative weight in Equations (7)-(9)

Δx	CVWFS	Grünwald	L1/L2
	$\alpha = 0.3$		
0.1000	0.0482	0.0466	0.0859
0.0500	0.0407	0.0398	0.0725
0.0250	0.0336	0.0331	0.0600
0.0125	0.0275	0.0272	0.0491
0.0063	0.0224	0.0222	0.0401
	$\alpha = 0.7$		
0.1000	0.0176	0.0163	0.0321
0.0500	0.0114	0.0106	0.0212
0.0250	0.0071	0.0067	0.0135
0.0125	0.0044	0.0042	0.0084
0.0063	0.0027	0.0026	0.0052

5.2 2D Steady State Problems

The initial test problem for the two-dimensional CVWFS is a steady state problem with constant diffusivity $\nu = 1$ and fixed boundary conditions. The general Caputo fractional diffusion equation for this problem is Equation (4) with the transient and source term neglected, i.e.

$$\frac{\partial}{\partial x}\left(-q_x\right)+\frac{\partial}{\partial y}\left(-q_y\right)=0$$
$$q_x=-\frac{1+\beta_x}{2}\frac{\partial^{\alpha_x}\phi}{\partial x^{\alpha_x}}+\frac{1-\beta_x}{2}\frac{\partial^{\alpha_x}\phi}{\partial(-x)^{\alpha_x}} \tag{24}$$
$$q_y=-\frac{1+\beta_y}{2}\frac{\partial^{\alpha_y}\phi}{\partial x^{\alpha_y}}+\frac{1-\beta_y}{2}\frac{\partial^{\alpha_y}\phi}{\partial(-x)^{\alpha_y}}$$

Two alternative boundary conditions are considered. The first sets

$$\begin{aligned}&\phi(x,0)=1-x^{\alpha_x}\\&\phi(0,y)=1-y^{\alpha_y}\\&\phi(x,1)=\phi(1,y)=0\end{aligned} \tag{25}$$

The second sets

$$\begin{aligned}&\phi(x,0)=(1-x)^{\alpha_x}\\&\phi(0,y)=(1-y)^{\alpha_y}\\&\phi(x,1)=\phi(1,y)=0\end{aligned} \tag{26}$$

In the limit case of $\beta_x = \beta_y = 1$ (only selecting the left-hand fractional derivatives) the solution to Equations (24) and (25) is

$$\phi(x,y)=\left(1-x^{\alpha_x}\right)\left(1-y^{\alpha_y}\right) \tag{27}$$

In the alternative limit case of $\beta_x = \beta_y = -1$ (only selecting the right-hand derivatives) the solution to Equations (24) and (26) is

$$\phi(x,y)=(1-x)^{\alpha_x}(1-y)^{\alpha_y} \tag{28}$$

Solutions that may be verified by direct differentiation and substitution in Equation (24) using the following standard Caputo fractional derivatives relationships

$$\frac{\partial^{\alpha}}{\partial x^{\alpha}} A x^{\alpha} = A\Gamma(\alpha+1), \quad A = f(y) \tag{29}$$

$$\frac{\partial^{\alpha}}{\partial(-x)^{\alpha}} f(x) \equiv \frac{\partial^{\alpha}}{\partial x^{\alpha}} f(1-x); \quad x \subset [0,1] \tag{30}$$

The CVWFS solutions of the above problems are achieved using the approximations of Equations (11)-(15) in the pseudo time step iterative solver of Equation (16). The CVWFS solution to each set of boundary conditions was solved using $\alpha_x = \alpha_y = 0.3$, $\beta_x = \beta_y = 1$ and $\alpha_x = \alpha_y = 0.7$, $\beta_x = \beta_y = -1$; a grid spacing of $\Delta x = \Delta y = 0.025$ and a pseudo time $\Delta t = 0.0005$—sufficient for stability in both cases—were also selected.

Table F-3 provides the maximum absolute error for each problem using all three weighting schemes. Again, the CVWFS and Grünwald weights are in close agreement. Figure F-3 displays the CVWFS values along the line of symmetry (x=0, y=0 to x=1, y =1) with the available analytical solutions. The results in Figure F-3 are sufficient to verify that the proposed CVWFS can produce accurate solutions to two-dimensional fractional diffusion equations utilizing the weights provided by Equations (7)-(9).

Table F-3: Maximum absolute error of CVWFS approximation using alternative weights on grid spacing of $\Delta x = \Delta y = 0.025$

Equations	CVWFS	Grünwald	L1/L2
(24),(25),(27)	0.0294	0.0282	0.0512
(24),(26),(28)	0.0057	0.0053	0.0105

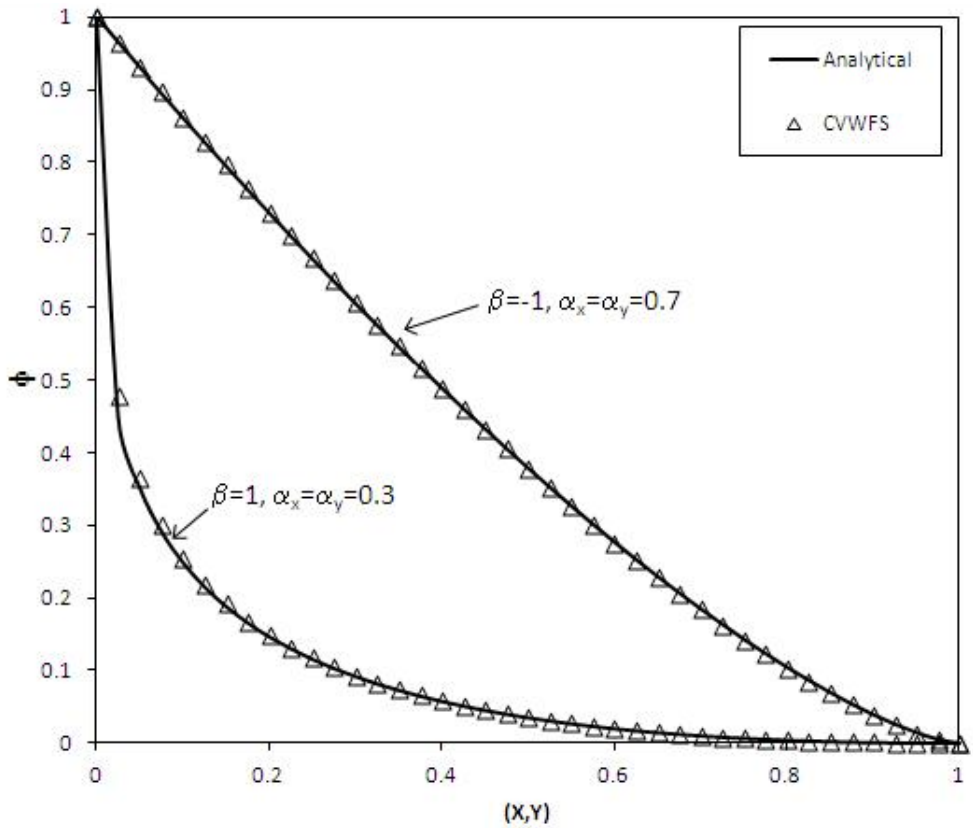

Figure F-3: CVWFS and random walk solution to steady state problems. Values presented along the line of symmetry (x=0, y=0 to x=1,y=1).

5.3 A Transient Problem

Similar to work in (Tadjeran and Meerschaert, 2006; Meerschaert et al., 2006) the following left-hand only fractional diffusion transient problem is posed

$$\frac{\partial \phi}{\partial t} = \frac{\partial}{\partial x}\left(\nu_x \frac{\partial^{\alpha_x} \phi}{\partial x^{\alpha_x}} \right) + \frac{\partial}{\partial y}\left(\nu_y \frac{\partial^{\alpha_y} \phi}{\partial y^{\alpha_y}} \right) + S \tag{31}$$

with boundary and initial conditions

$$\begin{aligned} &\phi(x,0,t) = \phi(0,y,t) = 0 \\ &\phi(1,y,t) = e^{-t} y^{3.6} \\ &\phi(x,1,t) = e^{-t} x^{3} \\ &\phi(x,y,0) = x^{3} y^{3.6} \end{aligned} \tag{32}$$

and a source term set as

$$S(x,y,t) = -(1+2xy)e^{-t}x^3y^{3.6} \tag{33}$$

Setting the diffusivities to

$$\begin{aligned} \nu_x &= \frac{\Gamma(4-\alpha_x)}{30}x^{2+\alpha_x}y \\ \nu_y &= \frac{6}{(5+\alpha_y)\Gamma(4+\alpha_y)}y^{2+\alpha_y}x \end{aligned} \tag{34}$$

Leads to the following analytical solution for Equations (31)-(34)

$$\phi(x,y,t) = e^{-t}x^3y^{3.6} \tag{35}$$

Which is readily verified by direct differentiation and substitution in Equation (31) using the following standard Caputo fractional derivative relationship

$$\frac{\partial^\alpha}{\partial x^\alpha}x^\eta = \frac{\Gamma(\eta+1)}{\Gamma(\eta+1-\alpha)}x^{\eta-\alpha} \tag{36}$$

Here in addition to testing the ability of the CWVFS to deal with transient problems its ability to deal with different localities in the coordinate directions is also tested by setting $\alpha_x = 0.8$ and $\alpha_y = 0.6$. In the CVWFS solution (see scheme defined by Equation (16)) the spatial and temporal grid spaces were set at $\Delta x = \Delta y = 0.025$ and $\Delta t = 0.0005$, choices that satisfy the stability criteria of Equation (20). Prediction of the profile along the line of symmetry (x=0, y=0 to x=1, y=1) at time t = 1 are compared with the analytical solution in Figure F-4. The maximum absolute error for this grid size is 5.77E-4. The maximum error, at the same time, for a grid size set at $\Delta x = \Delta y = 0.0125$ and $\Delta t = 0.0001$ drops to 4.98E-5. Both maximum errors were found to be consistent with those reported in the literature using alternative solution schemes [19,21].

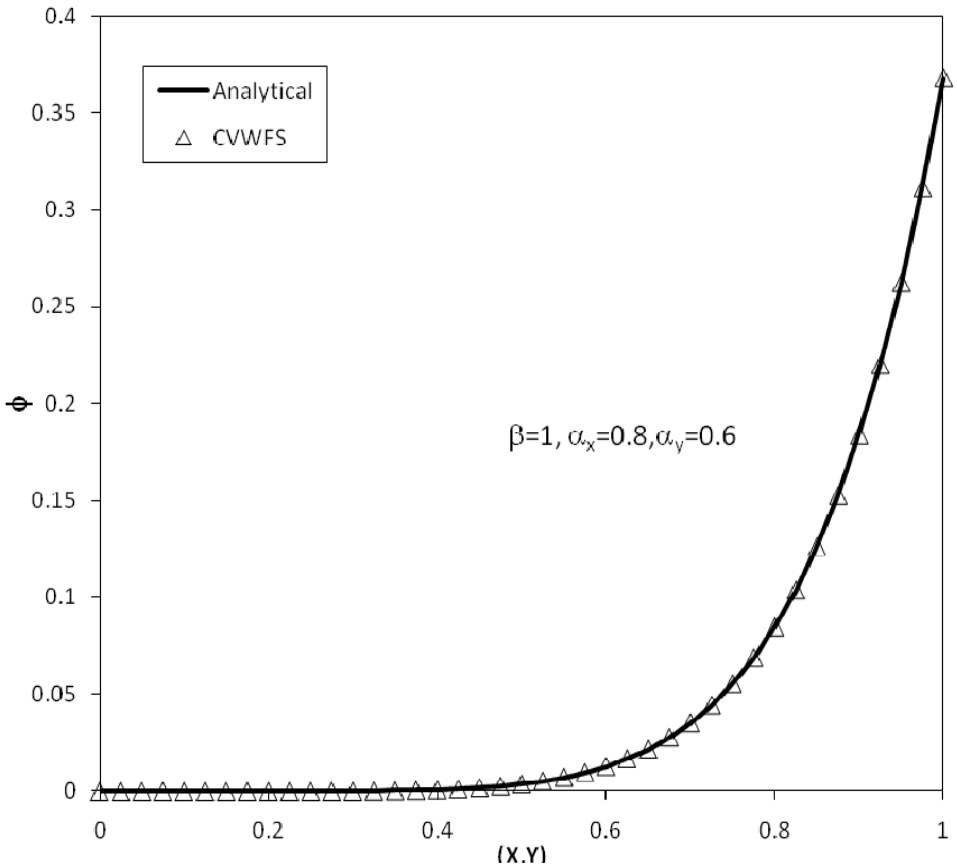

Figure F-4: CVWFS and exact solution to transient problem. Values presented along the line of symmetry (x=0, y=0 to x=1, y=1).

5.4 Two-Sided Problem

Finally, we demonstrate how the proposed CVWFS can be used to solve problems that include both up- and down- stream contributions to the non-locality. The test problem mirrors the steady state problem addressed in Section 5.2 with governing Equation (24); however, the bias term is appropriately selected to make the problem two-sided. To do this, we select $\beta_x = \beta_y = 0$ and set Dirichlet boundary conditions

$$\begin{aligned} &\phi(x,0) = 1 \\ &\phi(0,y) = 1 \\ &\phi(x,1) = \phi(1,y) = 0 \end{aligned} \tag{37}$$

The major difficulty of investigating this two-sided, two-dimensional fractional diffusion equation is that there is no known analytical solution. Therefore, we propose using a new

Monte Carlo random walk scheme developed by Zielinski and Voller (2013a) to provide an approximate solution to compare our results. This random walk – or so-called domain shifting – scheme operates similarly to traditional random walk processes except the domain is shifted about the point of interest and the step distributions are chosen from α-stable Lévy distributions (Zielinski and Voller, 2013a). An approximate solution using the domain-shifting method is generated by selecting an appropriate scaling parameter, γ, and non-locality measures— α and β.

The CVWFS solution was achieved using $\alpha_x = \alpha_y = 0.5$, $\beta_x = \beta_y = 0$; a grid spacing of $\Delta x = \Delta y = 0.025$ and a pseudo time $\Delta t = 0.0005$ —sufficient for stability — was also selected. Prediction of the profile along the line of symmetry (x=0, y=0 to x=1, y=1) are compared with the approximate solution generated by the domain-shifting scheme (Zielinski and Voller, 2013a) in Figure F-5. The domain-shifting solution at $\Delta x = \Delta y = 0.1$ was obtained by selecting $\gamma = 0.0005$, and performing $N = 4000$ Monte Carlo simulations at each point of interest. The approximate solution provided in Figure F-5 illustrates that the CVWFS is consistent with the domain-shifting scheme solution for a two-dimensional, two-sided fractional diffusion problem.

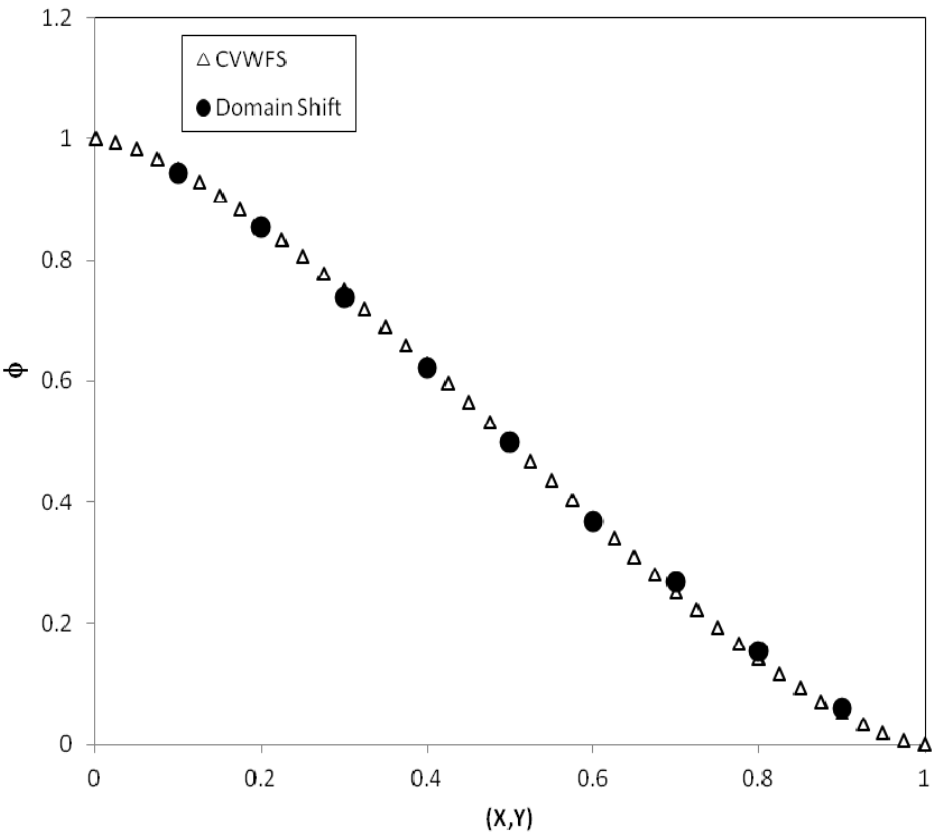

Figure F-5: CVWFS and domain-shifting scheme solution to two-sided problem. Values presented along the line of symmetry (x=0, y=0 to x=1, y=1).

6 Conclusions

Systems exhibiting non-local transport possess an intrinsic power law quality associated with them – e.g. the distribution of heterogeneity length scales or step size distribution of an organism. Whether non-local and non-instantaneous behavior is environment or organism motivated, the governing equation for so called anomalous transport is the fractional diffusion equation. With increased interest in non-local transport studies, development of numerical analysis techniques for handling fractional diffusion equations in multiple dimensions is needed.

Recent work introduced the so-called Control Volume Weighted Flux Scheme (CVWFS) for solving one-dimensional steady and transient diffusion equations in which the flux term is expressed in terms of a fractional derivative of order $0 < \alpha \leq 1$ (Voller et

al., 2011). An approach that can be viewed as an alternative to methods based on the one-shift Grünwald (Yang, 2010; Schumer et al., 2009; Shen and Phanikumar, 2009; Zhang et al., 2007a; Tadjeran and Meerschaert, 2006; Meerschaert and Tadjeran, 2006; Meerschaert et al., 2006; Podlubny, 1999) or L1/L2 (Yang, 2010; Shen and Phanikumar, 2009; Zhang et al., 2007b; Ilic et al., 2005; Zhang et al., 2005; Diethelm et al., 2005; Lynch et al., 2003; Diethelm, 1997; Oldham and Spanier, 1974) approximations. The main contributions of this paper have been to:

1. Explicitly test the relative accuracy of the previously proposed CVWFS.
2. Demonstrate that the CVWFS can also operate with weights derived from previous literature schemes.
3. Extend and verify the CVWFS for the solution of two-dimensional transient and steady-state fractional diffusion equations.

In the context of a particular one-dimensional test problem, it is clearly demonstrated that the accuracy of the CVWFS using the proposed weights is on the same order as the scheme operating with the Grünwald weights. Further, for a full range of multi-scaled (different non-locality values in the coordinate directions) and two-sided (up- and down-stream contributions to non-local flux) problems, solutions of the extended two-dimensional CVWFS are in good agreement with available analytical solutions and alternative random walk solutions (Zielinski and Voller, 2013a). A multi-dimensional CVWFS can be derived for use on a uniform, structured grid by simply expanding the approximations of Equations (11-16) to higher dimensions.

Currently, the CVWFS is not equipped to handle problems in non-Cartesian domains. A major difficulty in developing such schemes is the lack of analytical solutions to use in accuracy or consistency evaluations. However, this obstacle can be avoided by using an alternative solution technique like the recently developed domain-shifting scheme (Zielinski and Voller, 2013a), which provides accurate numerical solutions for steady state fractional diffusion equations in Cartesian and non-Cartesian domains. Therefore further work will focus on extending the CVWFS to operate on unstructured finite element grids.

Appendix G: A Control Volume Finite Element Method with Spines for Two-Dimensional Fractional Diffusion Equations

Most numerical treatments for space-fractional diffusion equations (FDEs) are constructed to function on structured grids in Cartesian domains, making solutions in arbitrarily shaped domains difficult. In this paper, we present a control volume finite element method (CVFEM) with spines for a class of two-dimensional fractional diffusion equations using unstructured grids, which is better suited for solutions in non-Cartesian domains. This scheme differs from previous finite element models in that the fractional diffusion flux across control volumes faces is approximated by using a generalized form of the recently developed control volume weighted flux scheme (CVWFS) along orthogonal spines extending from the control volume faces towards the boundaries. This creates a straightforward framework to construct the coefficient matrix, which as a result of non-local transport is mostly dense. Accuracy of the new approach is established by comparing solutions with known analytical solutions for a one-sided FDE at a range of orders of non-locality, α. Additionally, a two-sided ($-1 < \beta < 1$) FDE and fractional diffusion in a circular annulus domain were used to demonstrate the full utility of the CVFEM with spines.

1 Introduction

The classical diffusion equation is the long time limit approximation of an isotropic random walk employing normally distributed step sizes, characterized by a Gaussian propagator and linear in time growth of particle displacement variance. An assumption in using the classical diffusion equation is that heterogeneities be smaller than the domain length scale, allowing for homogenization and evaluation of diffusion fluxes in terms of local gradients. In the presence of heterogeneities, however, transport may exhibit non-Gaussian propagators and non-linear in time growth of variance. At some heterogeneity scale, transport processes become dominated by non-local or non-instantaneous effects, leading to anomalous diffusion. Similar to classical models, anomalous diffusion may be modeled by random walks employing particle step sizes chosen from power-law distributions, which are approximated at the stable limit by space-fractional diffusion equations (FDE's) (Meerschaert, 2012). Here, non-locality is accounted for by modeling the diffusion fluxes in terms of fractional (non-integer) gradients, rather than their integer-order counterparts. Anomalous transport behavior has been observed in numerous physical systems, including contaminant transport in heterogeneous aquifers (Wang, 2013; Zhang et al., 2007b; Yong et al., 2006; ; Zhang et al., 2005;Benson et al., 2000a; Benson et al., 2000b), earth-surface sediment transport (Voller et al., 2012; Voller and Paola 2010; Ganti et al., 2010; Foufoula-Georgiou et al., 2010; Schumer et al., 2009), stream solute transport (Shen and Phanikumar, 2009), moving boundary problems in heat transfer (Voller, 2010; Liu and Xu, 2009), and organism dispersal (Viswanathan et al. 2011; Zhang et al., 2007). Thus, there is a need for sophisticated and generally applicable numerical analysis techniques for anomalous transport described by fractional diffusion equations.

The diffusion flux at a given point, in a classical diffusion process, can be expressed in terms of the local potential, $\phi(x, y, t)$, gradient, given by:

$$q = \left(\nu_x \frac{\partial \phi}{\partial x}, \nu_y \frac{\partial \phi}{\partial y} \right) \tag{1}$$

where ν is a suitably dimensioned diffusivity coefficient. On setting the divergence of the flux equal to transient terms, the classical diffusion equation in two-dimensions can be formed:

$$\frac{\partial \phi}{\partial t} = \frac{\partial}{\partial x} \nu_x \frac{\partial \phi}{\partial x} + \frac{\partial}{\partial y} \nu_y \frac{\partial \phi}{\partial y} \tag{2}$$

Through the use of finite elements (Voller, 2009; Zienkiewicz and Taylor, 1989) or boundary element methods (Beer et al., 2008; Wrobel and Aliabadi, 2002) solving equation (2) in arbitrarily shaped domains is a simple exercise. In contrast, cases where heterogeneities in the system are power-law distributed, the diffusion flux is controlled by non-local properties and numerical treatments can be developed in terms of fractional derivatives (Schumeret al., 2009; Podlubny, 1999). Therefore, the non-local diffusion flux at a given point is expressed in terms of the fractional potential gradient, leading to a fractional Fick's law (Schumer et al., 2009; Schumer et al. 2001)

$$\begin{aligned} q_x^{\alpha_x} &= -\nu_x \left(\frac{1+\beta_x}{2} \right) \frac{\partial^{\alpha_x} \phi}{\partial x^{\alpha_x}} + \nu_x \left(\frac{1-\beta_x}{2} \right) \frac{\partial^{\alpha_x} \phi}{\partial (-x)^{\alpha_x}} \\ q_y^{\alpha_y} &= -\nu_y \left(\frac{1+\beta_y}{2} \right) \frac{\partial^{\alpha_y} \phi}{\partial y^{\alpha_y}} + \nu_y \left(\frac{1-\beta_y}{2} \right) \frac{\partial^{\alpha_y} \phi}{\partial (-y)^{\alpha_y}} \end{aligned} \tag{3}$$

In equation (3), the parameter $0 < \alpha \leq 1$ is the order of the derivative and associated with the measure of non-locality in coordinate directions in the system, and $-1 \leq \beta \leq 1$ is the bias weighting between left and right-sided derivatives. There are a number of alternative definitions of the fractional derivatives in equation (3); however, the Caputo definition is preferred over the alternative Reimann-Liouville definition because boundary conditions can be more easily constructed to match physically meaningful conditions and that the Caputo fractional derivative of a constant is zero. The left and right sided Caputo fractional derivatives in equation (3) take the form

$$\begin{aligned} \frac{\partial^{\alpha} \phi}{\partial x^{\alpha}} &= \frac{1}{\Gamma(1-\alpha)} \int_0^x (x-\xi)^{-\alpha} \frac{\partial \phi(\xi)}{\partial x} d\xi \\ \frac{\partial^{\alpha} \phi}{\partial (-x)^{\alpha}} &= \frac{-1}{\Gamma(1-\alpha)} \int_x^1 (\xi - x)^{-\alpha} \frac{\partial \phi(\xi)}{\partial x} d\xi \end{aligned} \tag{4}$$

where Γ is the gamma function. In equation (4) it is observed that the flux at a given point is no longer determined by the local gradient but rather a non-local representation comprised of a weighted sum of gradients up- or down-stream.

Again, setting the divergence of the flux in equation (3) equal to the transient term, and assuming that the heterogeneities in the coordinate directions are statistically independent (i.e. multi-scaled), see discussions by Meerschaert and authors (Tadjeran and Meerschaert, 2007; Meerschaert et al., 2001), the two-dimensional ($d = 2$) space-fractional diffusion equation can be written, in the general form:

$$\frac{\partial \phi}{\partial t} = \sum_{\ell=1}^{d} \left[\frac{\partial}{\partial x_\ell} \nu_\ell \left(\frac{(1+\beta_\ell)}{2} \frac{\partial^{\alpha_\ell} \phi}{\partial x_\ell^{\alpha_\ell}} - \frac{(1-\beta_\ell)}{2} \frac{\partial^{\alpha_\ell} \phi}{\partial (-x_\ell)^{\alpha_\ell}} \right) \right] \tag{5}$$

Note that in the event $\alpha = 1$, the diffusion flux in equation (3) is locally controlled and the classical diffusion equation is recovered. Additionally, if $-1 < \beta < 1$ equation (5) is considered to be two-sided, meaning the fractional diffusion flux is controlled by some ratio of up- and down-stream contributions.

Certainly, non-local transport imposes a number of computational constraints, namely dense matrices. A number of approaches have been considered for numerical treatment of space-fractional diffusion equations including finite difference methods (Wang and Wang, 2011; Yang et al., 2010; Tadjeran and Meerschaert, 2007; Meerschaert et al., 2006; Meerschaert and Tadjeran, 2006), finite element methods (Burrage et al., 2012; Yang et al., 2011; Ervin and Roop, 2006; Roop, 2006), finite volume/control volume methods (Zielinski and Voller, 2013b; Voller et al., 2011; Zhang et al., 2007a), radial base function methods (Piret and Hanert, 2013), and spectral methods (Bueno-Orovio et al., 2012) each suitably modified for specific FDEs. Of the numerical treatments listed, most are based on structured Cartesian grids, making solutions in arbitrarily shaped domains difficult. Although finite element approaches proposed by Burrage et al. (2012) and Yang et al. (2011) have each been successfully employed on unstructured grids, neither is able to solve two-sided FDEs in two-dimensions at this time. In contrast, Maroney and Yang (2013a, 2013b) have proposed a numerical

treatment for two-sided, two-dimensional FDEs, but use a finite difference scheme requiring a structured grid.

Voller at al. (2011) recently presented a new modeling technique with physical analog for modeling non-local diffusion that can be readily implemented into a control volume approach. The so called Control Volume Weighted Flux Scheme (CVWFS) models the diffusion flux at a local control volume face as the weighted average of gradients across the control volume faces up- and down-stream. The CVWFS has since been extended to two-dimensions and its accuracy demonstrated using one-shift Grünwald, L1-L2, and power-law weighting schemes (Zielinski and Voller, 2013b). The intuitive nature and flexibility to employ alternative weighting schemes in two-sided FDE's has motivated us to further develop the CVWFS approach towards unstructured grids and arbitrarily shaped domains. In this study, we introduce a control volume finite element method (CVFEM) with spines to solve the two-dimensional, two-sided, and multi-scaled form of equation (4) using the CVWFS to approximate non-local fluxes across control volume faces.

The paper is laid out as follows. A brief overview of the CVWFS approach and weighting scheme is given. In the next section, the framework of a control volume finite element method for fractional diffusion equations using the CVWFS on orthogonal-spines is demonstrated. Next, the accuracy and flexibility of the new approach is demonstrated by solving a one- and two-sided two-dimensional FDE on an unstructured grid in a Cartesian domain. Finally, the wider utility of the scheme is demonstrated by solving a fractional diffusion problem in a circular annulus domain with fixed conditions imposed on the inner and outer radii; a problem that is beyond the reach of existing finite element, finite difference, or alternative matrix transfer methods.

2 Overview of CVWFS

Before solving equation (5) using the control volume finite element method on an unstructured grid, it is important to understand the main characteristics of the CVWFS in one-dimension and give the formulation of alternative weighting schemes. The CVWFS is a discrete control volume method that was developed to numerically solve non-local

diffusion transport problems in the scaled domain $0 \le x \le 1$ (Voller et al., 2011). In this approach, the domain is divided into N equal elements each with size of Δx (note this will place nodes on the boundary). At a given control volume, centered about node *I*, the diffusion flux into and out of the control volume are calculated in terms of a weighted average of potential gradients across multiple control volume faces up- and down-stream of node *I*. In each coordinate direction there are two end-members in this treatment where the potential gradient at and on all neighboring control volume faces positioned to the *left* and *right* of the given face. In this way, the general form of the fractional diffusive flux at the *west* ($x_{west} = x_I - 0.5$) and *east* ($x_{east} = x_I + 0.5$) face of the Ith control volume is written as weighted averages of the local diffusion flux

$$
\begin{aligned}
q^R_{west_I} &= -\nu_{west_I} \sum_{k=1}^{N-I-1} W_k \left.\frac{d\phi}{dx}\right|_{x_{west}+(k-1)\Delta x} \\
q^L_{west_I} &= -\nu_{west_I} \sum_{k=1}^{I-1} W_k \left.\frac{d\phi}{dx}\right|_{x_{west}-(k-1)\Delta x} \\
q^R_{east_I} &= -\nu_{east_I} \sum_{k=1}^{N-I} W_k \left.\frac{d\phi}{dx}\right|_{x_{east}+(k-1)\Delta x} \\
q^L_{east_I} &= -\nu_{east_I} \sum_{k=1}^{I} W_k \left.\frac{d\phi}{dx}\right|_{x_{east}-(k-1)\Delta x}
\end{aligned}
\tag{6}
$$

where W_k are appropriately selected flux weights. Similarly, Zielinski and Voller (2013b) demonstrated that in two-dimensions, the flux at the *north* and *south* faces can be written in a similar fashion. For structured grids, like that considered by Zielinski and Voller (2013b), the numerical scheme can be written in an elegantly simple discrete form, see equation (18) in (Zielinski and Voller, 2013b), where volume *I* is supported by elements in the same row and column. For unstructured grids, however, a straightforward discrete form is more difficult to derive because support elements are not explicitly known *a priori*. In the next section, we will describe how orthogonal spines in the coordinate direction are used to locate support elements.

Recently, it was demonstrated that a number of alternative weighting schemes, derived from power-law relationships observed in non-local transport or other fractional derivative algorithms developed in the literature, can be used in the CVWFS treatment

(Zielinski and Voller, 2013b). Voller et al. (2011), initially proposed using a corrected power-law weighting scheme that enables a CVWFS to be diagonally dominant and recover locality when $\alpha \to 1$. Voller and others (Zielinski and Voller, 2013b ; Voller et al., 2011) have shown that the power-law weighting scheme is a close match to the so called one-shift Grünwald approximation derived by Meerschaert and Tadjeran (2006), a scheme with direct relation to the Reimann-Liouville fractional derivative, that can be manipulated to fit the CVWFS in the following manner

$$W_k = \Gamma(2-\alpha)\sum_{i=1} g_i \Delta x^{1-\alpha} \quad 1 \le k \le N \tag{7a}$$

where

$$g_1 = 1$$
$$g_i = \frac{i-2-\alpha}{i-1} g_{i-1} \quad i = 2,3,...k \tag{7b}$$

Although power law weights (Voller et al., 2011) and L1/L2 approximation (Zielinski and Voller, 2013b; Oldham and Spanier, 1974) can be sufficiently employed in the CVWFS, the one-shift Grünwald approximation in equation (7) is used throughout this study due to the improved accuracy and well established relationship to fractional derivatives in the literature (Podlubny, 1999).

3 Numerical approach for a fractional CVFEM

The control volume finite element method presented here is based on a spatial discretization of the domain Ω by a mesh of two-dimensional triangular elements (Figure G-1a). A control volume is constructed around each node by connecting the element centroids to face midpoints, as described in Voller (2009). In this construct, each control volume, which has area V_i, is comprised of n_i regions of support - the list of nodes that share a common element with node *i*, which have area ΔV_i (Figure G-1b) (Voller, 2009). Within each element, the continuous potential field will be expressed as a linear combination of the nodal values

$$\phi(x,y) = \sum_{i=1}^{3} N_i(x,y)\phi_i \tag{8}$$

where N_i are linear shape functions.

In order to discretize equation (5) using the control volume finite element method, the integral form must be derived. Integrating equation (5) over a control volume and applying conservation of mass to the transient term and divergence theorem to the diffusion terms, we obtain

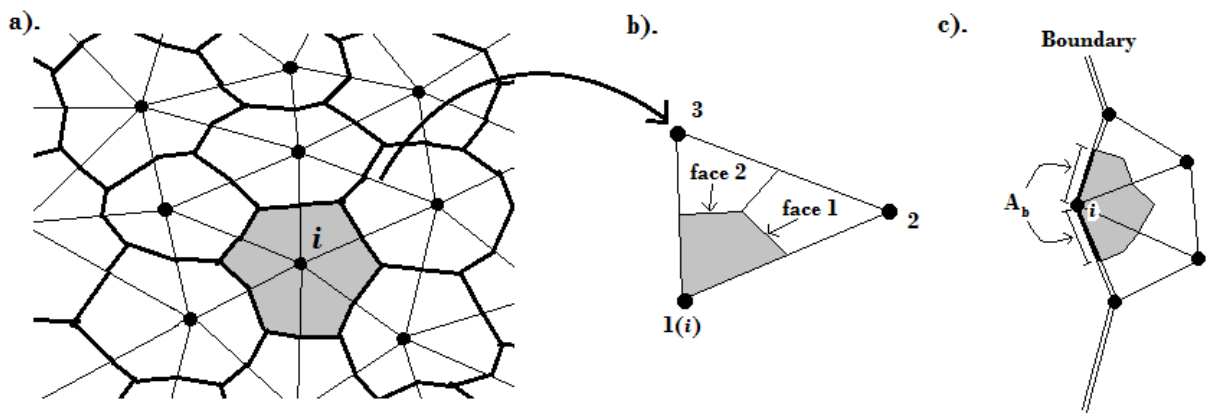

Figure G-1. Unstructured mesh of linear triangular elements with (a) control volume for node *i* inside the domain, (b) typical region of support in element *P*, and (c) control volume for node *i* on the boundary.

$$\frac{\partial}{\partial t}\int_{V_i}\phi dV=\sum_{j=1}^{n_i}\int_{A_j}\sum_{\ell=1}^{d}\left[\nu_\ell\left(\frac{(1+\beta_\ell)}{2}\frac{\partial^{\alpha_\ell}\phi}{\partial x_\ell{}^{\alpha_\ell}}-\frac{(1-\beta_\ell)}{2}\frac{\partial^{\alpha_\ell}\phi}{\partial(-x_\ell)^{\alpha_\ell}}\right)\right]\cdot\boldsymbol{n}dA \tag{9}$$

where A_j is the area of the control volume faces in the jth element of support and $\boldsymbol{n}$ is the unit outward normal.

The terms on the right hand side of equation (9) can be approximated by the sum of midpoint rule approximations over each face

$$\begin{aligned}\int_{A_1}\sum_{\ell=1}^{d}\left[\nu_\ell\left(\frac{(1+\beta_\ell)}{2}\frac{\partial^{\alpha_\ell}\phi}{\partial x_\ell{}^{\alpha_\ell}}-\frac{(1-\beta_\ell)}{2}\frac{\partial^{\alpha_\ell}\phi}{\partial(-x_\ell)^{\alpha_\ell}}\right)\right]\cdot\boldsymbol{n}dA=&\\ \int_{face1}\sum_{\ell=1}^{d}\left[\nu_\ell\left(\frac{(1+\beta_\ell)}{2}\frac{\partial^{\alpha_\ell}\phi}{\partial x_\ell{}^{\alpha_\ell}}-\frac{(1-\beta_\ell)}{2}\frac{\partial^{\alpha_\ell}\phi}{\partial(-x_\ell)^{\alpha_\ell}}\right)\right]\cdot\boldsymbol{n}dA&\\ +\int_{face2}\sum_{\ell=1}^{d}\left[\nu_\ell\left(\frac{(1+\beta_\ell)}{2}\frac{\partial^{\alpha_\ell}\phi}{\partial x_\ell{}^{\alpha_\ell}}-\frac{(1-\beta_\ell)}{2}\frac{\partial^{\alpha_\ell}\phi}{\partial(-x_\ell)^{\alpha_\ell}}\right)\right]\cdot\boldsymbol{n}dA&\end{aligned} \tag{10}$$

Now each term on the right hand side of equation (10) can be approximated by expanding the outward unit normal term to achieve

$$\int_{face1} \sum_{\ell=1}^{d} \left[\nu_\ell \left(\frac{(1+\beta_\ell)}{2} \frac{\partial^{\alpha_\ell} \phi}{\partial x_\ell^{\alpha_\ell}} - \frac{(1-\beta_\ell)}{2} \frac{\partial^{\alpha_\ell} \phi}{\partial (-x_\ell)^{\alpha_\ell}} \right) \right] \cdot \boldsymbol{n} dA$$
$$\approx \nu_x \left(\frac{(1+\beta_x)}{2} \frac{\partial^{\alpha_x} \phi}{\partial x^{\alpha_x}} - \frac{(1-\beta_x)}{2} \frac{\partial^{\alpha_x} \phi}{\partial (-x)^{\alpha_x}} \right) \Delta \vec{y}_{f1} \tag{11}$$
$$- \nu_y \left(\frac{(1+\beta_y)}{2} \frac{\partial^{\alpha_y} \phi}{\partial y^{\alpha_y}} - \frac{(1-\beta_y)}{2} \frac{\partial^{\alpha_y} \phi}{\partial (-y)^{\alpha_y}} \right) \Delta \vec{x}_{f1}$$

and

$$\int_{face2} \sum_{\ell=1}^{d} \left[\nu_\ell \left(\frac{(1+\beta_\ell)}{2} \frac{\partial^{\alpha_\ell} \phi}{\partial x_\ell^{\alpha_\ell}} - \frac{(1-\beta_\ell)}{2} \frac{\partial^{\alpha_\ell} \phi}{\partial (-x_\ell)^{\alpha_\ell}} \right) \right] \cdot \boldsymbol{n} dA$$
$$\approx \nu_x \left(\frac{(1+\beta_x)}{2} \frac{\partial^{\alpha_x} \phi}{\partial x^{\alpha_x}} - \frac{(1-\beta_x)}{2} \frac{\partial^{\alpha_x} \phi}{\partial (-x)^{\alpha_x}} \right) \Delta \vec{y}_{f2} \tag{12}$$
$$- \nu_y \left(\frac{(1+\beta_y)}{2} \frac{\partial^{\alpha_y} \phi}{\partial y^{\alpha_y}} - \frac{(1-\beta_y)}{2} \frac{\partial^{\alpha_y} \phi}{\partial (-y)^{\alpha_y}} \right) \Delta \vec{x}_{f2}$$

where $\Delta\vec{x}$ and $\Delta\vec{y}$ are the change in *x*- and *y*-values along each face. Here, the fractional CVFEM differs from the integer-order case in that the potential gradient at each face can no longer be approximated locally. Instead, the fractional gradient is approximated using the CVWFS approach by taking the weighted average of local fluxes up- and down-stream of the ith control volume.

A two-point scheme is used to approximate the fractional gradient across each face, because unlike the integer-order case, fractional gradients are not constant over each face. Thus, the fractional gradient across a given control volume face is calculated by averaging the fractional gradients at the two Gauss-nodes, GP1 (x_{GP1}, y_{GP1}) and GP2 (x_{GP2}, y_{GP2}), of each face (Figure G-2). The two Gauss nodes are located a distance of $\pm\sqrt{3}/6$ away from the midpoint, along the face. Using a general form of the CVWFS approach in equation (6), the left- and right-sided fractional gradients in coordinate directions can be written in the following form

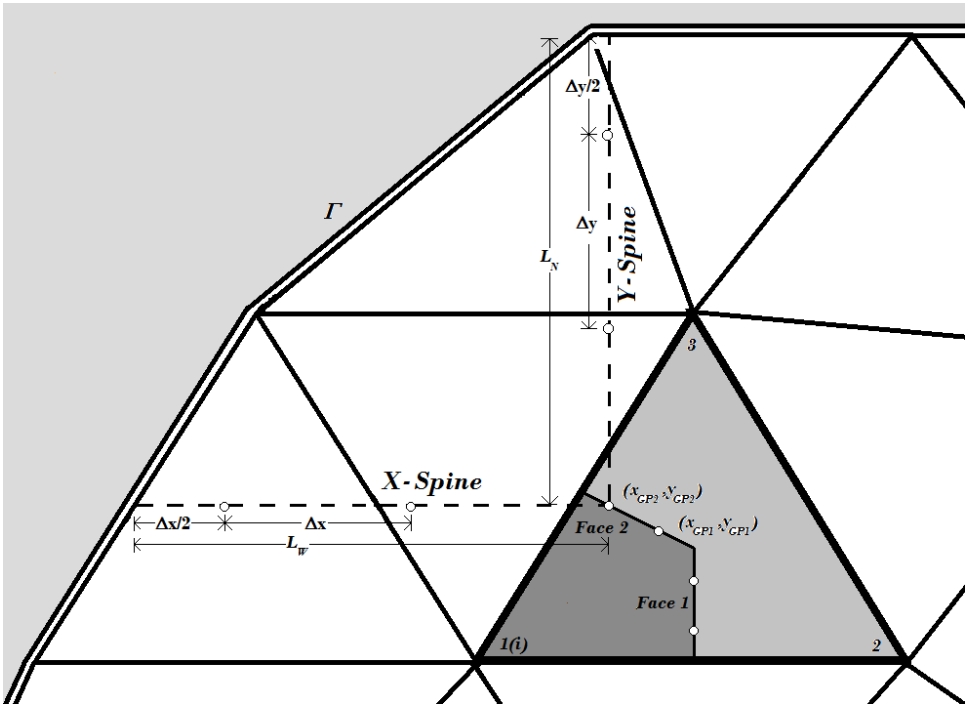

Figure G-2. Evaluation of fractional gradient at Gauss Point (GP2), on face 2 of a region of support (dark shaded area) about control volume *i* using method of spines in the coordinate directions. Δx and Δy denote the spacing between evaluation points (O) where the local gradient is calculated and used in the CVWFS to approximate the fractional gradient. Domain boundary is labeled as Γ. Only the left sided fraction derivative is considered (i.e. weighted sum of local gradients to the *west* and *north* of GP2).

$$
\begin{aligned}
\frac{\partial^\alpha \phi}{\partial x^\alpha} &\approx \frac{\nu_x}{2}\sum_{k=1}^{NS_w} W_k - \frac{\partial \phi}{\partial x}\bigg|_{P(x_{GP1}-(k-1)\Delta x_w,\, y_{GP1})} + \frac{\nu_x}{2}\sum_{k=1}^{NS_w} W_k - \frac{\partial \phi}{\partial x}\bigg|_{P(x_{GP2}-(k-1)\Delta x_w,\, y_{GP2})} \\
\frac{\partial^\alpha \phi}{\partial (-x)^\alpha} &\approx \frac{\nu_x}{2}\sum_{k=1}^{NS_e} W_k - \frac{\partial \phi}{\partial x}\bigg|_{P(x_{GP1}+(k-1)\Delta x_e,\, y_{GP1})} + \frac{\nu_x}{2}\sum_{k=1}^{NS_e} W_k - \frac{\partial \phi}{\partial x}\bigg|_{P(x_{GP2}+(k-1)\Delta x_e,\, y_{GP2})} \\
\frac{\partial^\alpha \phi}{\partial y^\alpha} &\approx \frac{\nu_y}{2}\sum_{k=1}^{NS_n} W_k - \frac{\partial \phi}{\partial y}\bigg|_{P(x_{GP1},\, y_{GP1}+(k-1)\Delta y_n)} + \frac{\nu_y}{2}\sum_{k=1}^{NS_n} W_k - \frac{\partial \phi}{\partial y}\bigg|_{P(x_{GP2},\, y_{GP2}+(k-1)\Delta y_n)} \\
\frac{\partial^\alpha \phi}{\partial (-y)^\alpha} &\approx \frac{\nu_y}{2}\sum_{k=1}^{NS_s} W_k - \frac{\partial \phi}{\partial y}\bigg|_{P(x_{GP1},\, y_{GP1}-(k-1)\Delta y_s)} + \frac{\nu_y}{2}\sum_{k=1}^{NS_s} W_k - \frac{\partial \phi}{\partial y}\bigg|_{P(x_{GP2},\, y_{GP2}-(k-1)\Delta y_s)}
\end{aligned}
\tag{13}
$$

where the local gradient within each triangular element can be calculated using equation (8)

$$\left.\frac{\partial \phi}{\partial x}\right|_P = \frac{\partial N_1}{\partial x}\phi_1 + \frac{\partial N_2}{\partial x}\phi_2 + \frac{\partial N_3}{\partial x}\phi_3$$
$$\left.\frac{\partial \phi}{\partial y}\right|_P = \frac{\partial N_1}{\partial y}\phi_1 + \frac{\partial N_2}{\partial y}\phi_2 + \frac{\partial N_3}{\partial y}\phi_3 \tag{14}$$

where the spatial derivatives of the linear shape functions are constant over the element P. In equation (13) the local gradient is evaluated using equation (14) in the element P containing the evaluation point (x, y), and the number of steps, *NS*, where local gradients are evaluated, is given by

$$\sum_{r=w,e,n,s} NS_r = \left\lceil \frac{L_r}{\delta} \right\rceil \tag{15}$$

where $L_{w,e,n,s}$ is the distance between the boundary and Gauss-node being evaluated in each direction, δ is the minimum side length of mesh elements, and the ceiling function $\lceil\ \rceil$ denotes the smallest integer that is larger than the function evaluated. The step sizes, Δx and Δy, between evaluation points are selected such that the last point falls within an element near the boundary and no consecutive points fall in the same element (Figure G-2). Therefore step sizes in each direction are calculated by

$$\sum_{r=w,e} \Delta x_r = \frac{L_r}{NS_r - 0.5}$$
$$\sum_{r=n,s} \Delta y_r = \frac{L_r}{NS_r - 0.5} \tag{16}$$

In this way, the fractional gradient at each Gauss-point is evaluated along orthogonal spines extending towards the boundaries in the coordinate directions of length L (Figure G-2) with evaluation points located on the spines at a constant spacing of Δx and Δy.

Imposing equation (10) on each mesh node using equations (11-16) results in the general discrete form for relating node *i* to its neighbors (nb)

$$a_i \phi_i = \sum_{nb} a_{nb}\phi_{nb} + b_i \tag{17}$$

where a_i and a_{nb} are coefficients for the unknown nodal values and b_i accounts for boundaries, sources, and transients. Special care must be taken in the data structure to

define the nodal coefficients of a_{nb} for the fractional order case because nodes in support of node *i* extend along the x- and y-spines, not just neighboring nodes. For each Gauss-point GP_j on face l about node *i* in element *I*, the nodal coefficients are updated using the following steps

(1) Calculate NS_r, Δx_r, and Δy_r and initialize evaluation point (x_{GPj}, y_{GPj})

(2) Loop through evaluation points along each spine ($k = 1$ to NS_r)

(3) Find element *P* containing current evaluation point, with vertex nodes at S_1, S_2, and S_3

(4) Update nodal coefficients using

$$
\begin{aligned}
a_{i,S_1} &= a_{i,S_1} + \frac{(1 \pm \beta_x)}{2} W_k \frac{\Delta \vec{y}_{fl_i}}{2} \frac{\partial N_1}{\partial x}\bigg|_P \\
a_{i,S_2} &= a_{i,S_2} + \frac{(1 \pm \beta_x)}{2} W_k \frac{\Delta \vec{y}_{fl_i}}{2} \frac{\partial N_2}{\partial x}\bigg|_P \\
a_{i,S_3} &= a_{i,S_3} + \frac{(1 \pm \beta_x)}{2} W_k \frac{\Delta \vec{y}_{fl_i}}{2} \frac{\partial N_3}{\partial x}\bigg|_P
\end{aligned}
\tag{18}
$$

In the x-direction, and

$$
\begin{aligned}
a_{i,S_1} &= a_{i,S_1} + \frac{(1 \pm \beta_y)}{2} W_k \frac{\Delta \vec{x}_{fl_i}}{2} \frac{\partial N_1}{\partial y}\bigg|_P \\
a_{i,S_2} &= a_{i,S_2} + \frac{(1 \pm \beta_y)}{2} W_k \frac{\Delta \vec{x}_{fl_i}}{2} \frac{\partial N_2}{\partial y}\bigg|_P \\
a_{i,S_3} &= a_{i,S_3} + \frac{(1 \pm \beta_y)}{2} W_k \frac{\Delta \vec{x}_{fl_i}}{2} \frac{\partial N_3}{\partial y}\bigg|_P
\end{aligned}
\tag{19}
$$

In the y-direction

(5) Update evaluation point by Δx_r or Δy_r and repeat

Once all elements and nodes are cycled through, a_{nb} becomes a dense coefficient matrix, thus preventing the use of classical matrix solver techniques (e.g. tri-diagonal solvers). The coefficients for node *i* are then defined as $a_i = -diag(a_{nb})$, and a_{nb} is updated such that $diag(a_{nb}) = 0$ For simplicity, a fully explicit approximation in time is applied using

equation (10-19). The resulting equation for nodes that lie *inside* the domain, assuming no source terms, is as follows

$$(V_i)\phi_i^{new} = V_i\phi_i + \Delta t\left(\sum_{j=1}^{M} a_{i,j}\phi_j - a_i\phi_i\right) \tag{20}$$

where *new* denotes the new nodal value at node i at time $t = t + \Delta t$, and M is the number of nodes in the domain. A steady state solution to equation (20) can also be found by substituting *new* with a pseudo-time step in an iterative solution.

Specific treatments must be defined for nodes on the boundaries of the calculation domain. Assuming the net flux entering a boundary segment of area, A_b, about node i on the boundary is specified by a transfer coefficient, $h \geq 0$, and ambient field variable, ϕ_{amb} (Voller, 2009). The resulting integral approximation for the convective boundary conditions is

$$\int_l q_{in}\, dA_b = \int_l h(\phi_{amb} - \phi)\, dA_b \approx -B_{C_i}\phi_i + B_{B_i} \tag{21}$$

where $B_{C_i} = hA_{b_i}$ is the coefficient contribution and $B_{B_i} = hA_{b_i}\phi_{amb}$ is the constant contribution. In equation (21) A_b is defined as the sum of midpoint distances between neighboring boundary nodes of uniform thickness (Figure G-3). The values of h and ϕ_{amb} can be appropriately set to accommodate insulated ($h = 0$), fixed value ($h = 10^{16}, \phi_{amb} = \phi_{fix}$), and fixed flux ($h = 10^{-16}, \phi_{amb} = q_{fix}/h$) conditions (Voller, 2009). Settings for h are chosen such that the fixed value and fixed flux choices are forced at the boundary.

Adding the boundary condition treatments to equation (20), the explicit in time scheme for all nodes in the domain can be written as

$$(V_i + B_{c_i})\phi_i^{new} = V_i\phi_i + \Delta t\left(\sum_{j=1}^{M} a_{i,j}\phi_j - a_i\phi_i\right) + B_{b_i} \tag{22}$$

The solution to equation (22) shall be stable provided the coefficients for ϕ_i on the right-hand side are positive. In this way, a stability criterion for equation (22) sets the time step as

$$\Delta t < \min\left(\frac{V_i}{a_i}\right) \tag{23}$$

4 Testing and Results

4.1 2D Steady State Problem

The initial test problem investigated is a simple two-dimensional steady state fractional diffusion problem in a one-unit square domain, with fixed boundary conditions, and constant diffusivity $\nu = 1$. The general Caputo fractional diffusion equation and boundary conditions for this problem at the limit case $\beta_x = \beta_y = 1$ (only selecting the left-sided fractional derivatives) are

$$\begin{aligned}
&\frac{\partial}{\partial x}\left(\frac{\partial^{\alpha_x}\phi}{\partial x^{\alpha_x}}\right) + \frac{\partial}{\partial y}\left(\frac{\partial^{\alpha_y}\phi}{\partial y^{\alpha_y}}\right) = 0 \\
&\phi(x,0) = 1 - x^{\alpha_x} \\
&\phi(0,y) = 1 - y^{\alpha_y} \\
&\phi(x,1) = \phi(1,y) = 0
\end{aligned} \tag{24}$$

By direct differentiation and substitution of the standard Caputo fractional derivative relationships

$$\frac{\partial^\alpha}{\partial x^\alpha} A x^\alpha = A\Gamma(\alpha+1), \quad A = f(y) \tag{25}$$

$$\frac{\partial^\alpha}{\partial(-x)^\alpha} f(x) \equiv \frac{\partial^\alpha}{\partial(x)^\alpha} f(1-x), \quad x \subset (0,1) \tag{26}$$

the analytic solution to equation (24) is

$$\phi(x,y) = \left(1 - x^{\alpha_x}\right)\left(1 - y^{\alpha_y}\right) \tag{27}$$

Equation (24) is solved using the fractional CVFEM with spines and the one-shift Grünwald weights of equation (7). Solutions are arrived at by using the fully explicit solver in equation (22) and marching to steady state through pseudo-time. The pseudo-time step is chosen to satisfy the stability criteria in equation (23). The fractional

CVFEM solution was solved using $\alpha = 0.3, 0.5, 0.7$ and minimum triangular element edge length, δ, of 2^{-2} to 2^{-6}.

In addition, we considered solving equation (24) using one, two, and three Gauss nodes (quantity of evaluation points on volume faces) and increasing evaluation step size, Δx and Δy, by setting the numerator in equation (15) to 1δ, 2δ, and 4δ. The first Gauss node is located at the midpoint of the face, and the three Gauss node scheme places the nodes at the midpoint and distance $\pm\sqrt{3/20}$ away from midpoint. Unlike the two Gauss node scheme, each point is not weighted the same (e.g. the midpoint weight is 4/9 and the remaining nodes receive 5/18).

The solutions obtained by the fractional CVFEM with spines, setting $\delta = 2^{-5}$, are in good agreement with the analytical solution for each value of α along the line of symmetry ($x = 0, y = 0$ to $x = 1, y = 1$) (Figure G-3). The L^1, L^2, and L^∞ norm of the error for each solution, provided in Table G-1, are calculated using

$$\begin{aligned}
\left\|\phi_{CVFEM} - \phi_{ana}\right\|_{L^1} &= \sum_{i=1}^{M} \left|\phi_{CVFEM}\left(x_i, y_i\right) - \phi_{ana}\left(x_i, y_i\right)\right| \delta^2 \\
\left\|\phi_{CVFEM} - \phi_{ana}\right\|_{L^2} &= \sqrt{\sum_{i=1}^{M} \left|\phi_{CVFEM}\left(x_i, y_i\right) - \phi_{ana}\left(x_i, y_i\right)\right|^2 \delta^2} \\
\left\|\phi_{CVFEM} - \phi_{ana}\right\|_{L^\infty} &= \max_{1 \le i \le M} \left|\phi_{CVFEM}\left(x_i, y_i\right) - \phi_{ana}\left(x_i, y_i\right)\right|
\end{aligned} \tag{28}$$

Table G-1. The L^1, L^2, and L^∞ errors, following equation (28), of the fractional CVFEM with spines for equation (24) with $\alpha = 0.3, 0.5, 0.7$.

δ	L^1 Error	L^2 Error	L^∞ Error
$\alpha = 0.7$			
2^{-2}	0.52×10^{-2}	1.70×10^{-3}	2.19×10^{-2}
2^{-3}	0.39×10^{-2}	6.02×10^{-4}	1.86×10^{-2}
2^{-4}	0.27×10^{-2}	1.89×10^{-4}	1.17×10^{-2}
2^{-5}	0.18×10^{-2}	6.06×10^{-5}	8.00×10^{-3}
2^{-6}	0.10×10^{-2}	1.77×10^{-5}	5.00×10^{-3}
$\alpha = 0.5$			
2^{-2}	0.48×10^{-2}	2.10×10^{-3}	3.12×10^{-2}
2^{-3}	0.42×10^{-2}	8.28×10^{-4}	3.94×10^{-2}
2^{-4}	0.39×10^{-2}	2.89×10^{-4}	2.48×10^{-2}
2^{-5}	0.30×10^{-2}	1.11×10^{-4}	2.18×10^{-2}
2^{-6}	0.20×10^{-2}	3.67×10^{-5}	1.63×10^{-2}
$\alpha = 0.3$			
2^{-2}	0.10×10^{-1}	4.20×10^{-3}	4.61×10^{-2}
2^{-3}	0.56×10^{-2}	1.20×10^{-3}	5.14×10^{-2}
2^{-4}	0.40×10^{-2}	3.17×10^{-4}	2.69×10^{-2}
2^{-5}	0.35×10^{-2}	1.46×10^{-4}	3.53×10^{-2}
2^{-6}	0.25×10^{-2}	5.36×10^{-5}	3.80×10^{-2}

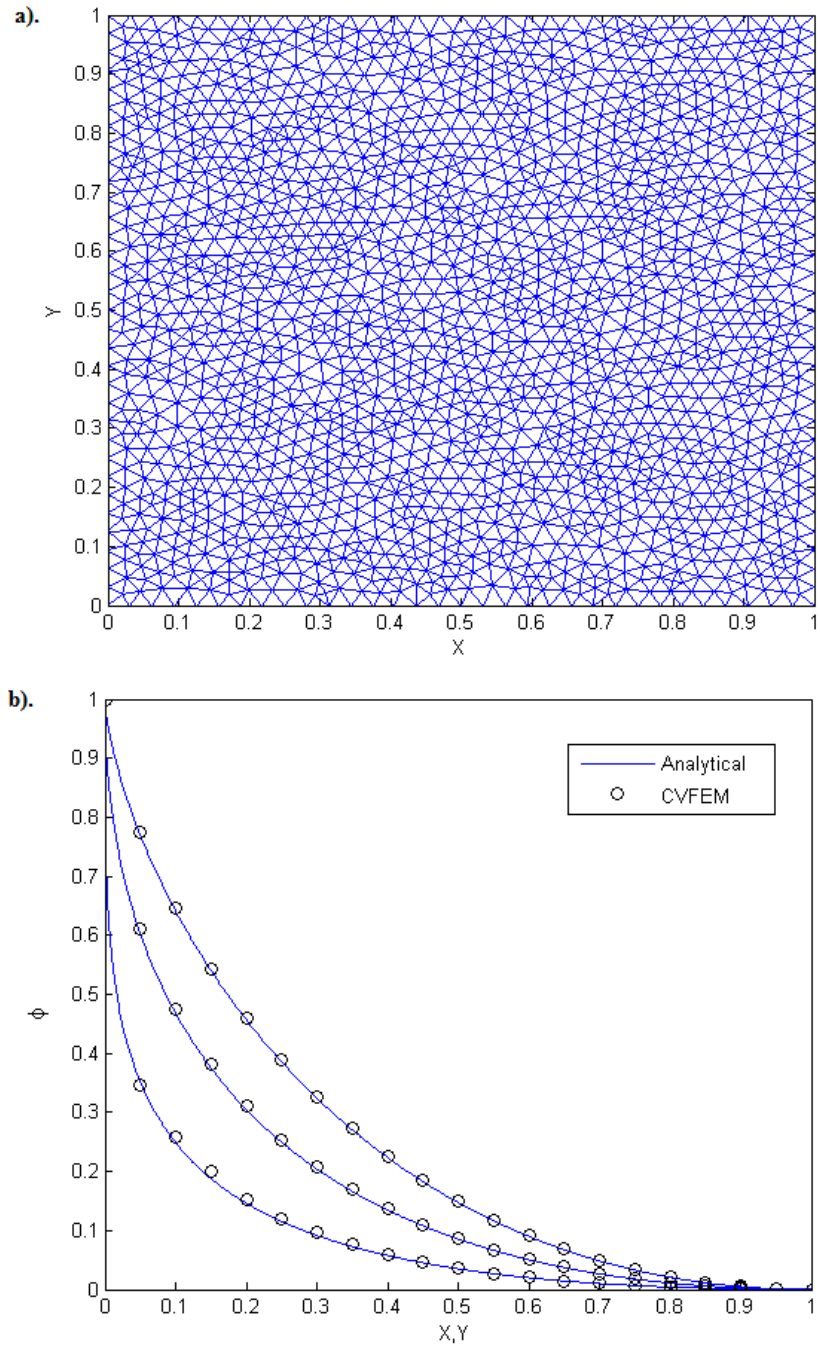

Figure G-3. a) Unstructured mesh with $\delta = 2^{-5}$ (2048 elements) used for the fractional CVFEM and b). profiles of CVFEM with spines and analytical solution – equation (27) – for two-dimensional fractional diffusion problem described by equation (24). Values presented along the line of symmetry (x=0, y=0 to x=1, y=1) for non-locality measures $\beta_x, \beta_y = 1$ and $\alpha_x, \alpha_y = 0.3, 0.5, 0.7$.

The fractional CVFEM with spines is stable and convergent for solving equation (24); however, as α decreases, or the degree of non-locality increases, the L^{∞} norm no longer decreases for subsequent grid refinements. These errors are induced by increasingly sharp gradients near the boundaries. Overall performance (stability and convergence) of the numerical method is not negatively impacted, as evidenced by the convergence of L^1 and L^2 norms while the L^{∞} norm plateaus for $\alpha = 0.3$. The convergence rate of the L^2 error approaches 1.4, 1.6, and 1.8 for the solutions of $\alpha = 0.3, 0.5, 0.7$, respectively

In Table G-2, the L^{∞} norm of the error and CPU time required to reach steady state for the solution to equation (24) using variable evaluation point step size are presented. In Table G-3, the L^{∞} norm of the error and CPU time required to reach steady state for the solution to equation (24) using one, two, and three Gauss nodes are presented. As expected, the CPU time is reduced, at the cost of accuracy, as the step sizes increase. Similarly, using a greater Gauss node scheme decreases error at the cost of CPU time. The error decreased at a greater rate between the two and three node schemes for $\alpha = 0.3$ because the additional Gauss node improved resolution in the region of high curvature near the boundaries.

Table G-2. The L^1, L^2, and L^{∞} errors and CPU time (s) of the fractional CVFEM with spines for equation (24) with $\alpha = 0.3, 0.5, 0.7$ for $\delta = 2^{-5}$ for increasing evaluation step size, Δx and Δy, by setting the numerator in equation (15) to 1δ, 2δ, and 4δ.

Step Size	L^1 Error	L^2 Error	L^{∞} Error	CPU(s)
$\alpha = 0.7$				
4δ	0.91×10^{-3}	4.56×10^{-5}	1.00×10^{-2}	419
2δ	0.96×10^{-3}	4.66×10^{-5}	9.70×10^{-3}	440
1δ	0.18×10^{-2}	6.06×10^{-5}	8.00×10^{-3}	465
$\alpha = 0.5$				
4δ	0.38×10^{-2}	1.41×10^{-4}	3.66×10^{-2}	251
2δ	0.16×10^{-2}	9.15×10^{-5}	3.43×10^{-2}	263
1δ	0.30×10^{-2}	1.11×10^{-4}	2.18×10^{-2}	298
$\alpha = 0.3$				
4δ	0.67×10^{-2}	2.90×10^{-4}	9.81×10^{-2}	178
2δ	0.33×10^{-2}	1.90×10^{-4}	9.01×10^{-2}	191
1δ	0.35×10^{-2}	1.46×10^{-4}	3.53×10^{-2}	214

Table G-3. The L^1, L^2, and L^∞ errors and CPU time (s) of the fractional CVFEM with spines for equation (24) with $\alpha = 0.3, 0.5, 0.7$ and $\delta = 2^{-5}$ using one, two, and three Gauss-node evaluation points.

Step Size	L^1 Error	L^2 Error	L^∞ Error	CPU(s)
$\alpha = 0.7$				
1	0.18 x 10^{-2}	6.03 x 10^{-5}	8.30 x 10^{-3}	345
2	0.18 x 10^{-2}	6.06 x 10^{-5}	8.00 x 10^{-3}	465
3	0.18 x 10^{-2}	6.00 x 10^{-5}	7.90 x 10^{-3}	588
$\alpha = 0.5$				
1	0.30 x 10^{-2}	1.11 x 10^{-4}	2.32 x 10^{-2}	205
2	0.30 x 10^{-2}	1.11 x 10^{-4}	2.18 x 10^{-2}	298
3	0.30 x 10^{-2}	1.11 x 10^{-4}	2.10 x 10^{-2}	437
$\alpha = 0.3$				
1	0.35 x 10^{-2}	1.39 x 10^{-4}	3.96 x 10^{-2}	160
2	0.35 x 10^{-2}	1.46 x 10^{-4}	3.53 x 10^{-2}	214
3	0.35 x 10^{-2}	1.41 x 10^{-4}	3.14 x 10^{-2}	398

4.2 Two Sided Problem

The next test problem was chosen to demonstrate the flexibility of the fractional CVFEM with spines for two-sided $(\beta_x, \beta_y = 0)$, multi-scaled problems $(\alpha_x \neq \alpha_y)$. For this problem, the fractional CVFEM with spines is applied to a similar problem as the first test problem, except both left- and right-sided fractional derivatives are considered. The general Caputo fraction diffusion equation and boundary conditions for this problem are

$$\begin{aligned}
&\frac{\partial}{\partial x}\left(\frac{(1+\beta_x)}{2}\frac{\partial^{\alpha_x}\phi}{\partial x^{\alpha_x}} - \frac{(1-\beta_x)}{2}\frac{\partial^{\alpha_x}\phi}{\partial(-x)^{\alpha_x}}\right) + \frac{\partial}{\partial y}\left(\frac{(1+\beta_y)}{2}\frac{\partial^{\alpha_y}\phi}{\partial y^{\alpha_y}} - \frac{(1-\beta_y)}{2}\frac{\partial^{\alpha_y}\phi}{\partial(-y)^{\alpha_y}}\right) = 0 \\
&\phi(x,0) = 1 \\
&\phi(0,y) = 1 \\
&\phi(x,1) = \phi(1,y) = 0
\end{aligned} \tag{29}$$

No known analytical solution exists for the two-sided, two-dimensional fractional diffusion problem described by equation (29). In lieu of this, we use the two-dimensional CVWFS on a structured grid (Zielinski and Voller, 2013b) to provide an approximate solution to compare with our results.

The fractional CVFEM solution was solved for $\alpha_x = 0.8, \alpha_y = 0.6$ and $\beta_x, \beta_y = 0$, using $\delta = 2^{-5}$ (2048 elements) on an unstructured mesh, and CVWFS solution was found using a structured mesh of 1600 elements $(\Delta x = \Delta y = 0.025)$. The fractional CVFEM with spines solution along the line of symmetry ($x = 0, y = 0$ to $x = 1, y = 1$) is consistent with that of the CVWFS on a structured grid (Figure G-4).

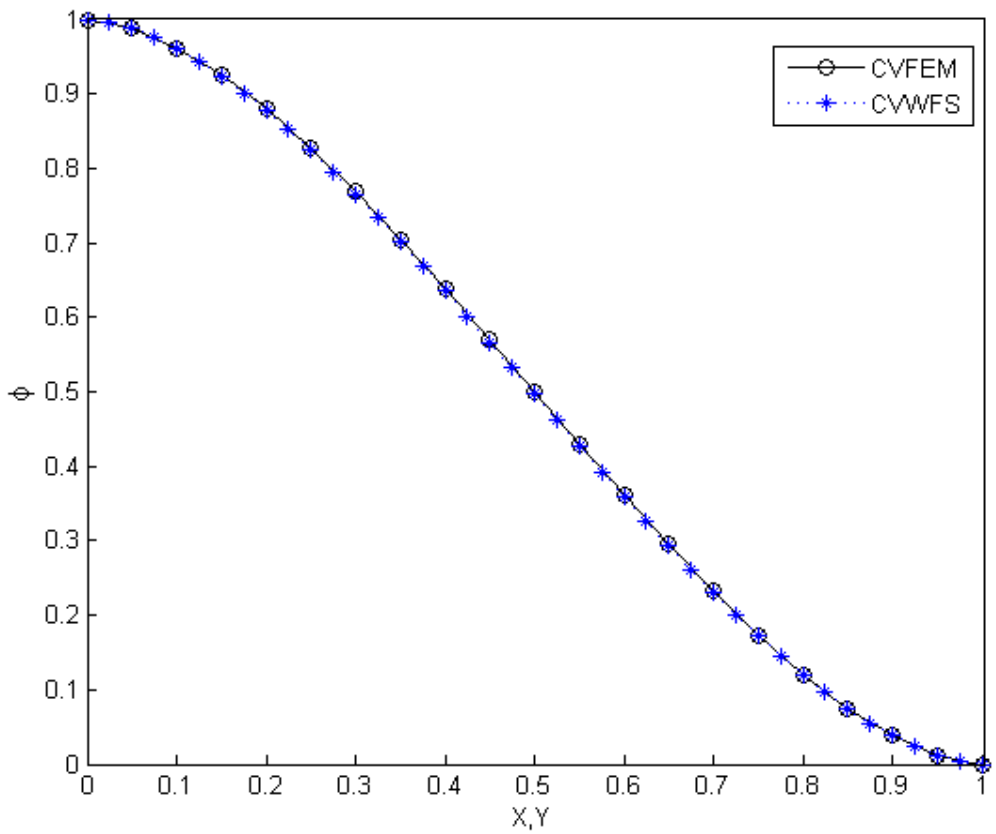

Figure G-4. Fractional CVFEM with spines and CVWFS solution to a two-sided problem, equation (29) with $\alpha_x = 0.8, \alpha_y = 0.6$ and $\beta_x, \beta_y = 0$. Values presented along the line of symmetry (x=0, y=0 to x=1, y=1).

4.3 Annulus Problem

The final test problem of fractional diffusion in a circular annulus domain, consisting of an inner radius $r = 1$ at $\phi = 1$, and outer radius $r = 2$ at $\phi = 0$ (Figure G-5a),

was chosen to demonstrate the full utility of the proposed numerical scheme. The general Caputo fractional derivative for this test problem is modeled by equation (29), but the boundary conditions are adjusted for the annulus geometry.

No known analytical solution exists for two-dimensional fractional diffusion in a circular annulus domain. In lieu of this, we use a recently developed Monte Carlo random walk – or so-called domain shifting – scheme (Zielinski and Voller, 2013a) to provide an approximate solution to compare with our results. This scheme functions much like a traditional random walk process except the domain boundary shifts about the point of interest and step distributions are chosen from appropriate α -stable Lévy distributions (Zielinski and Voller, 2013a). The approximate solution using the domain-shifting method is produced by selecting appropriate scaling parameter, γ, and non-locality measures, α and β.

The fractional CVFEM solution was solved for $\alpha_x = 0.8, \alpha_y = 0.6$ and $\beta_x = -1, \beta_y = 1$, using $\delta = 2^{-4}$ (8192 elements) on an unstructured mesh, and the domain-shifting solution was found using $\gamma = 0.0001$ and performing 4000 Monte Carlo simulations are each point of interest. Three separate domain shift predictions of the profile along the radii $\theta = 0$ and $\theta = \pi/2$ are compared with the approximate solution produced by the domain-shifting scheme in Figure G-5b. Consistent with the two-sided problem in a Cartesian domain, the CVFEM approximation closely matches that of the domain shifting scheme.

5 Conclusions

When heterogeneities within a system reach a scale that cannot be homogenized, non-local and non-instantaneous effects dominate transport processes. Modeling systems that exhibit such anomalous diffusion requires the use of fractional derivatives to replace their integer order counterpart to approximate non-local diffusion fluxes. Although numerous schemes have been identified to solve particular fractional diffusion equations, few are equipped to handle two-sided, two-dimensional problems on unstructured grids in arbitrarily shaped domains. In this paper, we introduce a control volume finite element

method (CVFEM) with spines as a generally applicable numerical scheme for a particular class of space-factional diffusion equations suited for unstructured grids in non-Cartesian domains.

The accuracy of the proposed scheme was demonstrated by comparing the solution of the CVFEM with spines with available analytical solutions of an one-sided fractional diffusion equation across a range of non-locality measures, α . Additionally, higher order Gauss-node approximations on each control volume face and step sizes that scale with δ improves accuracy of the scheme, but at the expense of computational effort. Solutions of the CVFEM with spines were also shown to be consistent with that of an alternative random walk solution (Zielinski and Voller, 2013a) for a two-sided, multi-scaled fractional diffusion problem on a Cartesian domain. Furthermore, the full capabilities of the proposed scheme are demonstrated by the close agreement between CVFEM with spines and random walk solution for a multi-scaled fractional diffusion equation over a circular annulus domain.

The proposed scheme differs from previous finite element and matrix transfer methods (Burrage et al., 2012; Yang et al., 2011; Ervin and Roop, 2006;Roop, 2006) by approximating fractional gradients at each control volume by applying a generalized version of the control volume weighted flux scheme (CVWFS) (Voller et al., 2011) along orthogonal spines, extending from control volume faces to the boundaries. This allows for straightforward identification of nodal support across the domain and construction of the coefficient matrix. Overall, the CVFEM with spines provides a generic framework for approximating space-fractional diffusion equations in unstructured grids, desirable traits for numerical schemes to model anomalous transport in physically realistic domains.

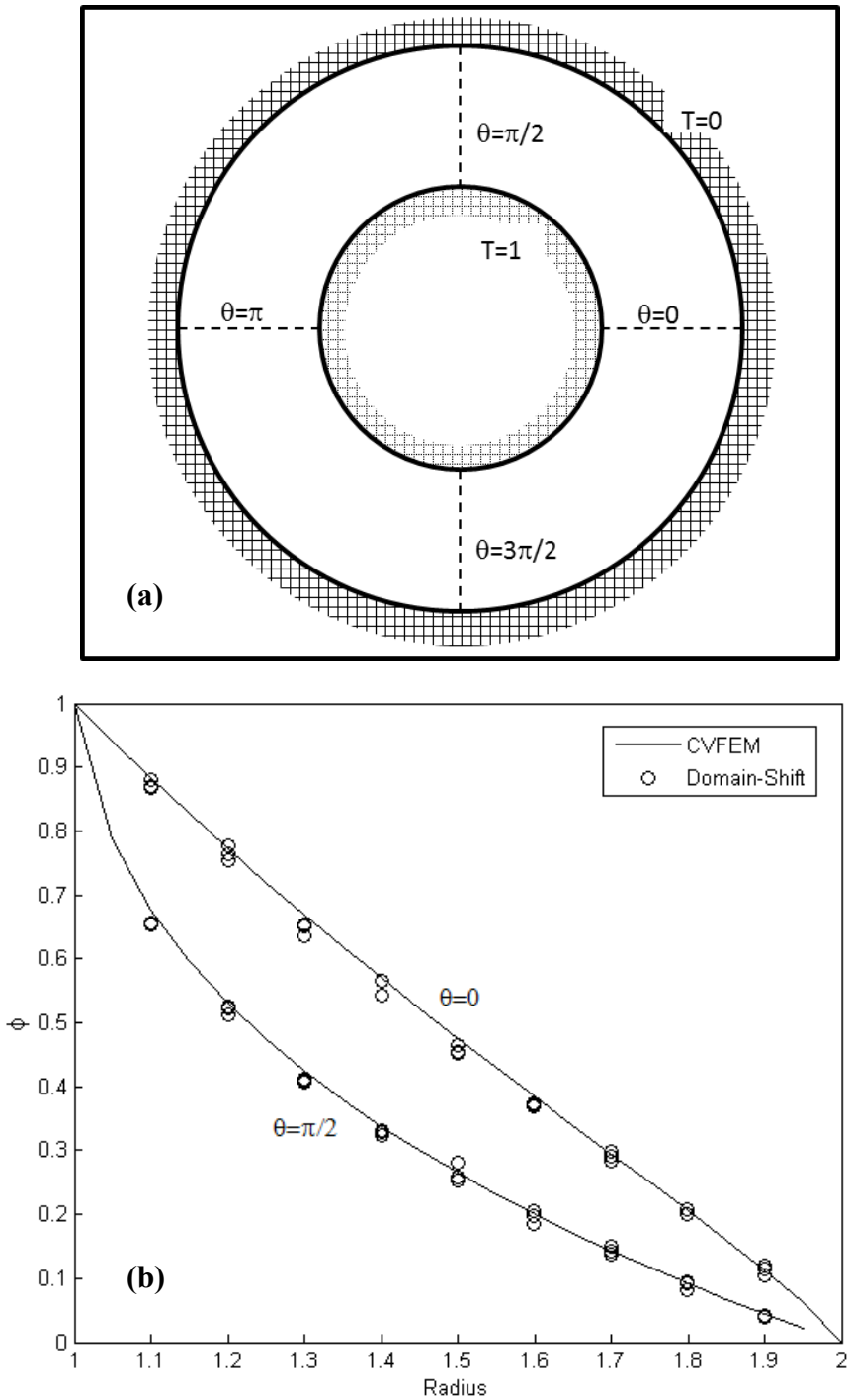

Figure G-5. (a) Domain and boundary conditions for the circular annulus problem – adapted from Zielinski and Voller (2013a) – and (b) solution profiles along radii $\theta = 0$ and $\theta = \pi/2$, with domain shifting scheme ($\gamma = 0.00025$) and CVFEM for the fractional diffusion case $\alpha_x = 0.8, \alpha_y = 0.6$ and $\beta_x = -1, \beta_y = 1$.